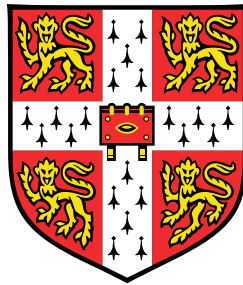


# The Dynamics of Geophysical and Astrophysical Turbulence



**Laura Cope**

Department of Applied Mathematics and Theoretical Physics  
University of Cambridge

This dissertation is submitted for the degree of  
*Doctor of Philosophy*



## **Declaration**

This thesis is the result of my own work and includes nothing which is the outcome of work done in collaboration except as declared in the Preface and specified in the text. It is not substantially the same as any that I have submitted, or, is being concurrently submitted for a degree or diploma or other qualification at the University of Cambridge or any other University or similar institution except as declared in the Preface and specified in the text. I further state that no substantial part of my thesis has already been submitted, or, is being concurrently submitted for any such degree, diploma or other qualification at the University of Cambridge or any other university or similar institution except as declared in the Preface and specified in the text. It does not exceed the prescribed word limit for the relevant Degree Committee.

Laura Cope

July 2021



## **Acknowledgements**

First and foremost, I would like to thank my PhD supervisor, Peter Haynes, with whom it has been a pleasure to work over the last four years. It is without question that I would not be where I am now without his support, guidance and encouragement as I traverse the academic roadmap. I would also like to thank the NERC doctoral training programme who have provided substantial financial support during my studies, in addition to a comprehensive professional training environment that has complemented my research.

Having had the opportunity to participate as a fellow at the Woods Hole Oceanographic Institute summer GFD programme in 2018, I would like to extend my thanks to all those who helped to create an unforgettable summer. In particular, I am very grateful to both Pascale Garaud and Colm-cille Caulfield for their joint supervision of my project, which extended beyond the summer school, resulting in a publication and the constitution of the second part of this thesis.

The last four years have offered ample opportunities for travel to workshops and conferences which have had an immeasurable impact on my work. I would like to acknowledge the friendships made during these trips, and for the wonderful memories shared. Closer to home, I would also like to thank my research group for providing a stimulating and supportive environment, and for the many individuals in DAMTP and Murray Edwards College with whom I have formed close and lasting friendships.

Last, but certainly not least, I would like to say a huge thank you to my family and friends for their endless support during this journey. In particular, I pay tribute to my late grandfather who shared my determination and strong willpower to succeed regardless of the circumstances. I would also like to thank my parents for their enduring support, despite having no clue what it is that I actually do. Finally, my sincere thanks go to everyone who has held my hand on this exciting, but uncertain, journey.



## Abstract

Turbulence is ubiquitous within geophysical and astrophysical fluid flows. Its interaction with physical ingredients such as rotation and stratification gives rise to spectacular dynamics, including the layering of material properties, which in turn influence the transport and distribution of heat, momentum and tracers. We consider the effects of rotation and stratification individually in the study of two different problems of scientific interest, using idealised models which retain only the essential ingredients.

Our first problem investigates the role of rotation in geophysical flows. We consider a barotropic, stochastically-forced turbulent flow on a beta-plane, which is well known to exhibit the spontaneous formation and equilibration of persistent zonal jets. The equilibrated jets are not steady and the focus here is on their time variability, which is of interest both because of its relevance to the behaviour of naturally occurring jet streams and for the insights it provides into the dynamical mechanisms operating in these systems. We compare the behaviour of a nonlinear (NL) system to a quasilinear (QL) model in which eddy-eddy interactions are neglected. Both systems reveal a rich zoology of dynamics, nevertheless, key differences exist. The NL model admits the formation of systematically migrating jets, a phenomenon that has not been previously identified. Jets migrate north or south with a speed of translation that is a function of the Rhines scale and the frictional damping rate, occasionally changing their direction of migration. The QL model does not exhibit jet migration, but a generalised quasilinear (GQL) model, in which certain eddy-eddy interactions are systematically restored, does, demonstrating that long waves, generated by such interactions, play a key dynamical role. The importance of these waves, in addition to the role of random fluctuations, is affirmed using a statistical formulation in which the flow statistics are solved for directly.

Our second problem considers the interaction of a stable density stratification with a background velocity distribution, which can develop into stratified turbulence. Geophysical flows, in which the diffusivities of momentum and heat are commensurate, are often very strongly stratified, nevertheless, turbulence still occurs. Density layering is key to understanding the properties of this ‘layered anisotropic stratified turbulence’ (LAST) regime. On the other hand, astrophysical flows are typically characterised by strong thermal diffusion, inhibiting the formation of density layers. This suggests that LAST dynamics cannot occur, raising the interesting question of whether analogous or fundamentally different regimes exist in the limit of strong thermal diffusion. This thesis addresses this question for the case of a vertically stratified, horizontally-forced Kolmogorov flow. Using linear stability theory, we show that three-dimensional perturbations of the horizontal shear are always unstable in the limit of strong stratification and strong thermal diffusion, causing the flow to develop vertical layers, and hence vertical shear, in the velocity field, thereby allowing vertical shear instabilities to develop. The subsequent nonlinear evolution and transition to turbulence is studied numerically using direct numerical simulations, where four distinct dynamical regimes emerge, depending upon the strength of the background stratification. By considering dominant balances in the governing equations, we derive scaling laws which explain the empirical observations.



# Contents

<b>List of figures</b>	<b>xiii</b>
<b>List of tables</b>	<b>xvii</b>
<b>Nomenclature</b>	<b>xix</b>
<b>1 General Introduction</b>	<b>1</b>
1.1 Jet stream variability in beta-plane turbulence . . . . .	1
1.2 Turbulent mixing in stratified, thermally diffusive shear flows . . . . .	3
<b>2 Introduction to beta-plane turbulence</b>	<b>5</b>
2.1 Motivation . . . . .	5
2.2 A framework of idealised models of zonal jets . . . . .	8
2.2.1 On the validity of idealised models . . . . .	10
2.3 Towards an understanding of the dynamics of zonal jets . . . . .	12
2.3.1 A brief review of Rossby waves . . . . .	13
2.3.2 Zonostrophic turbulence and general scaling arguments . . . . .	14
2.3.3 Zonal jet formation mechanisms . . . . .	16
2.3.3.1 Turbulent energy cascades . . . . .	16
2.3.3.2 Potential vorticity staircases . . . . .	18
2.3.3.3 Wave-mean flow interactions . . . . .	19
2.3.4 The zonostrophy parameter as a measure of zonation . . . . .	20
2.3.5 Dynamical insights from two-layer models . . . . .	22
2.4 Insights from reduced models . . . . .	22
2.4.1 Statistical closure models . . . . .	23
2.4.1.1 Second order closures and the quasilinear approximation . . . . .	24
2.4.1.2 Higher order closures and the generalised quasilinear approximation . . . . .	25
2.4.2 Zonostrophic instability . . . . .	26
2.4.3 Zonostrophic saturation . . . . .	27
2.4.4 Zonal jet dynamics: fluctuations and rare events . . . . .	28
2.5 Research questions . . . . .	29
<b>3 A mathematical model of beta-plane turbulence</b>	<b>31</b>
3.1 Introduction . . . . .	31
3.2 Mathematical formulation . . . . .	31

3.2.1	Nonlinear (NL) mathematical model . . . . .	31
3.2.2	Quasilinear (QL) approximation . . . . .	33
3.2.3	A simple model of turbulence forcing . . . . .	35
3.3	Numerical formulation . . . . .	36
3.3.1	Numerical implementation . . . . .	36
3.3.2	Stochastic forcing . . . . .	37
3.3.3	Hyperviscosity . . . . .	39
3.4	Numerical simulation of zonal flows . . . . .	40
3.4.1	Direct numerical simulation of zonal jet formation and equilibration . . . . .	40
3.4.2	Numerical properties of the stochastic forcing wavenumber . . . . .	41
3.4.3	Computation of velocity profiles and eddy momentum flux convergences . . . . .	43
3.5	Discussion . . . . .	45
<b>4</b>	<b>The variability of stochastically forced, beta-plane zonal jets</b>	<b>47</b>
4.1	Introduction . . . . .	47
4.2	The zoology of beta-plane zonal jet dynamics . . . . .	47
4.2.1	Fundamental types of variability . . . . .	48
4.2.2	The zoology of non-migrating zonal jets . . . . .	51
4.2.2.1	Single jet dynamics . . . . .	51
4.2.2.2	Zonal jet spacings and strengths . . . . .	53
4.2.3	The zoology of migrating zonal jets . . . . .	55
4.2.3.1	Fast zonal jet migration . . . . .	55
4.2.3.2	Slow zonal jet migration . . . . .	56
4.3	The dependence of variability on system parameters . . . . .	58
4.3.1	Parameter space and zonostrophic flow regimes . . . . .	58
4.3.2	Relationship between the Rhines scale and jet spacings . . . . .	61
4.3.3	Influence of the zonostrophy parameter on jet strengths . . . . .	62
4.3.4	Influence of the forcing wavenumber on jet widths . . . . .	64
4.4	Hysteresis, non-uniqueness and spontaneous regime transitions . . . . .	65
4.4.1	Hysteresis as $\beta$ varies . . . . .	65
4.4.2	Existence of multiple stable attractors . . . . .	66
4.4.3	The dynamics of spontaneous regime transitions . . . . .	67
4.4.4	Analogy of multiple stochastic potential wells . . . . .	69
4.5	Discussion . . . . .	71
<b>5</b>	<b>The dynamics of zonal jet migration</b>	<b>73</b>
5.1	Introduction . . . . .	73
5.2	Mathematical formulation . . . . .	74
5.2.1	Generalised quasilinear (GQL) approximation . . . . .	74
5.2.2	Generalised quasilinear (GQL) model . . . . .	76
5.3	Generalised quasilinear theory: the sufficiency of $\Lambda \geq 1$ . . . . .	77
5.4	A new theory for zonal jet migration . . . . .	80
5.4.1	Identification of zonons . . . . .	80

5.4.2	Partition of energy between jets and zonons . . . . .	84
5.4.3	Organisational role of zonons . . . . .	86
5.4.4	Necessity of small-scale eddies . . . . .	87
5.4.5	Summary of the zonal jet migration mechanism . . . . .	89
5.5	The translation speed of migrating zonal jets . . . . .	89
5.5.1	Self-similarity of velocity profiles and eddy momentum flux convergences . . . . .	90
5.5.2	Dependence of translation speeds on eddy momentum flux convergences . . . . .	91
5.5.3	Dependence of translation speeds on system parameters . . . . .	92
5.6	Discussion . . . . .	97
<b>6</b>	<b>Direct statistical simulation of zonal jet dynamics</b>	<b>99</b>
6.1	Introduction . . . . .	99
6.2	Mathematical formulation . . . . .	99
6.2.1	Cumulant expansion truncated at second order (CE2) methodology . . . . .	100
6.2.2	Cumulant expansion truncated at second order (CE2) model . . . . .	101
6.3	Direct statistical simulations (DSS) . . . . .	104
6.3.1	Numerical formulation . . . . .	104
6.3.2	Numerical comparison between DNS and DSS models . . . . .	107
6.4	The zoology of CE2 beta-plane zonal jet dynamics . . . . .	109
6.4.1	Fundamental types of solutions . . . . .	109
6.4.2	Time-dependency of CE2 solutions . . . . .	111
6.5	Hysteresis, non-uniqueness and spontaneous regime transitions . . . . .	111
6.5.1	Hysteresis as $\beta$ varies . . . . .	112
6.5.2	Existence of multiple stable attractors . . . . .	113
6.5.3	The dynamics of unforced regime transitions . . . . .	114
6.6	A further look at zonal jet migration . . . . .	115
6.7	Discussion . . . . .	117
<b>7</b>	<b>Introduction to stratified turbulence</b>	<b>119</b>
7.1	Motivation . . . . .	119
7.2	Stratified turbulence in geophysical flows . . . . .	120
7.2.1	A framework of idealised models of stratified flows . . . . .	120
7.2.2	Stratified turbulence and general scaling arguments . . . . .	121
7.2.3	Towards an understanding of the sustainment of stratified turbulence . . . . .	122
7.3	Stratified shear instabilities in astrophysical flows . . . . .	123
7.4	Research questions . . . . .	126
<b>8</b>	<b>The dynamics of stratified horizontal shear flows at low Péclet number</b>	<b>127</b>
8.1	Introduction . . . . .	127
8.2	Mathematical formulation . . . . .	127
8.2.1	Mathematical model . . . . .	127
8.2.2	Non-dimensionalisation and model parameters . . . . .	129
8.2.3	Low-Péclet number approximation . . . . .	129

8.3	Linear stability analysis of a horizontal shear flow . . . . .	130
8.3.1	Standard equations . . . . .	130
8.3.1.1	Comparison with previous results at $Pr = 1$ . . . . .	132
8.3.1.2	Linear stability at low $Pr$ . . . . .	133
8.3.2	Low-Péclet number equations . . . . .	134
8.3.3	Critical Reynolds number for the onset of linear instability . . . . .	135
8.4	Direct numerical simulations . . . . .	136
8.4.1	Numerical formulation . . . . .	136
8.4.2	Typical simulations: early phase . . . . .	138
8.4.3	Typical simulations: nonlinear saturation . . . . .	139
8.4.4	Data extraction . . . . .	141
8.5	Scaling regimes for nonlinear saturation . . . . .	143
8.5.1	Effects of stratification on mixing and the vertical scale of eddies . . . . .	143
8.5.2	Derivation of scaling regimes . . . . .	145
8.5.2.1	Unstratified regime . . . . .	145
8.5.2.2	Stratified turbulent regime . . . . .	146
8.5.2.3	Stratified viscous regime . . . . .	148
8.5.2.4	Stratified intermittent regime . . . . .	149
8.5.3	A regime diagram . . . . .	150
8.6	Discussion . . . . .	151
8.6.1	Comparison between stratified mixing in geophysical and astrophysical flows . . . . .	151
8.6.2	Implications for mixing in stars . . . . .	153
<b>9</b>	<b>Conclusions and future work</b>	<b>155</b>
9.1	Jet stream variability in beta-plane turbulence . . . . .	155
9.2	Turbulent mixing in stratified, thermally diffusive shear flows . . . . .	158
	<b>References</b>	<b>159</b>
	<b>Appendix A Shallow water quasi-geostrophic equations</b>	<b>171</b>
	<b>Appendix B Implementation of the stochastic forcing</b>	<b>173</b>
B.1	Continuous formulation . . . . .	173
B.2	Discrete DNS formulation . . . . .	174
B.3	Discrete DSS formulation . . . . .	177
B.4	Proof of the relation $\overline{\zeta'_1 \xi_2} + \overline{\zeta'_2 \xi_1} = \Xi$ . . . . .	177
	<b>Appendix C Numerical integration of the DNS and DSS systems</b>	<b>179</b>
C.1	Numerical integration of the NL, GQL and QL systems . . . . .	179
C.2	Numerical integration of the CE2 system . . . . .	180
	<b>Appendix D Zonal jet migration in the presence of strong vortices</b>	<b>183</b>
	<b>Appendix E Generalisation of linear stability analyses</b>	<b>185</b>

# List of figures

2.1	Geophysical observations of jet streams . . . . .	6
2.2	Geophysical observations of jet stream variability . . . . .	7
2.3	Observational evidence of eddy-driven jet streams . . . . .	11
2.4	Numerical simulations highlighting the bifurcation between jets and vortices . . . . .	15
2.5	Idealistic and numerically-simulated kinetic energy spectra in beta-plane turbulence . . . . .	16
2.6	Theoretical and time-evolving energy spectra in forced-dissipative beta-plane turbulence . . . . .	17
2.7	Numerical simulation of the formation of zonal jets in beta-plane turbulence . . . . .	17
2.8	The evolution of idealised potential vorticity staircases on a turbulent beta-plane . . . . .	18
2.9	A regime diagram of possible zonal flow states; the consistency of zonon phase speeds . . . . .	21
2.10	A series of idealised models investigating the formation of zonal jets . . . . .	25
2.11	The probability density function of eddy momentum flux convergence fluctuations . . . . .	29
3.1	Illustration of wave-mean flow triad interactions . . . . .	34
3.2	Forcing distributions in Fourier space and physical space . . . . .	38
3.3	Selecting the hyperviscosity parameters . . . . .	39
3.4	An example numerical integration of the NL model . . . . .	41
3.5	The effect of the forcing wavenumber on the distribution of kinetic energy . . . . .	42
3.6	The effect of the forcing wavenumber on hyperviscosity . . . . .	42
3.7	The effect of the forcing wavenumber on the energy injection rate . . . . .	43
3.8	Computation of the jet velocity profile . . . . .	44
3.9	Measuring the latitudinal translation speed of a jet . . . . .	44
3.10	Computation of the eddy momentum flux convergence profile . . . . .	45
4.1	Fundamental types of zonal jet variability in the NL model . . . . .	48
4.2	Fundamental types of zonal jet variability in the QL model . . . . .	49
4.3	Zonal jet variability regimes observed via parameter continuation . . . . .	50
4.4	Single zonal jet dynamics in the NL model . . . . .	51
4.5	Single zonal jet dynamics in the QL model . . . . .	52
4.6	Zonal jet spacings and strengths in the NL model . . . . .	53
4.7	Zonal jet spacings and strengths in the QL model . . . . .	55
4.8	Fast zonal jet migration in the NL model . . . . .	56
4.9	Slow zonal jet migration in the NL model . . . . .	57
4.10	Slow zonal jet migration in the QL model . . . . .	58
4.11	The NL and QL parameter spaces defined in terms of $k_{Rh}$ and $R_\beta$ . . . . .	59

4.12	Zonostrophic flow regimes in the NL and QL models . . . . .	60
4.13	The relationship between the number of jets and the Rhines wavenumber . . . . .	62
4.14	The relationship between the zonostrophy parameter and the zonal mean flow index . . . . .	64
4.15	The effect of the forcing wavenumber on the jet velocity profile . . . . .	65
4.16	Hysteresis observed via parameter continuation . . . . .	66
4.17	The existence of multiple stable attractors . . . . .	67
4.18	The dynamics of merging behaviour . . . . .	68
4.19	The dynamics of regime transitions . . . . .	68
4.20	The influence of the zonostrophy parameter on the frequency of regime transitions . . . . .	69
4.21	The influence of abrupt eddy field changes on regime transitions . . . . .	70
4.22	The analogy of multiple stochastic potential wells . . . . .	71
5.1	Geophysical examples of jet stream migration . . . . .	73
5.2	Illustration of generalised quasilinear triad interactions . . . . .	75
5.3	A comparison of kinetic energy spectra in the NL, QL and GQL models . . . . .	77
5.4	The influence of the GQL partition wavenumber on zonal jet migration . . . . .	78
5.5	The influence of the GQL partition wavenumber during parameter continuation . . . . .	79
5.6	The coexistence of jets and zonons during fast zonal jet migration . . . . .	80
5.7	The coexistence of jets and zonons in two-jet configurations . . . . .	81
5.8	The zonal phase speed of jets and zonons . . . . .	83
5.9	Streamlines in the frame of reference moving with the zonons . . . . .	84
5.10	The partition of energy between jets and zonons . . . . .	85
5.11	Decomposition of the eddy momentum flux convergence . . . . .	86
5.12	The dependence of jet migration behaviour on the existence of small-scale forcing . . . . .	87
5.13	The dependence of jet migration behaviour on the forcing wavenumber . . . . .	88
5.14	The velocity profiles and eddy momentum flux convergences of migrating zonal jets . . . . .	90
5.15	The dependence of jet translation speeds on eddy momentum flux convergence biases . . . . .	92
5.16	The dependence of jet translation speeds on characteristic flow velocities . . . . .	94
5.17	The dependence of jet translation speeds on system parameters . . . . .	95
5.18	The relationship between the Rhines scale and the number of jets . . . . .	96
6.1	The DNS and DSS forcing distributions . . . . .	104
6.2	Time step dependence within the CE2 model . . . . .	105
6.3	An example numerical integration of the CE2 model . . . . .	106
6.4	The NL, QL and CE2 parameter spaces defined in terms of $k_{Rh}$ and $R_\beta$ . . . . .	107
6.5	A comparison of solutions between the NL, QL and CE2 models . . . . .	108
6.6	A comparison between properties of the QL and CE2 models . . . . .	109
6.7	The zoology of zonal jet variability in the CE2 model . . . . .	110
6.8	The time-dependence of CE2 solutions . . . . .	111
6.9	Hysteresis observed via parameter continuation in the CE2 model . . . . .	112
6.10	The existence of multiple stable attractors in the CE2 model . . . . .	113
6.11	Unforced regime transitions in the CE2 model . . . . .	114
6.12	Zonal jet migration in the CE2 model . . . . .	115

---

6.13	A comparison between zonal jet translation speeds in the CE2 and NL models . . . . .	116
7.1	Differential rotation in the Sun . . . . .	124
8.1	Schematics of the basic state temperature distribution and velocity profile . . . . .	128
8.2	Linear stability results from the standard set of equations . . . . .	132
8.3	A comparison of linear stability results from the standard and LPN equations . . . . .	133
8.4	Linear stability results from the LPN equations . . . . .	135
8.5	The early time evolution of horizontal shear instabilities . . . . .	139
8.6	Snapshots illustrating the four dynamical regimes in the nonlinear evolution . . . . .	140
8.7	Computation of the vertical length scales using the autocorrelation function method . . . .	142
8.8	Theoretical and numerical comparison of the regime scalings . . . . .	144
8.9	A diagram illustrating the dynamical regimes in parameter space . . . . .	150
9.1	A taxonomy of the zoology of zonal jet dynamics . . . . .	156
D.1	Zonal jet migration in the presence of strong vortices . . . . .	183



# List of tables

2.1	Parameter estimates in various planetary environments . . . . .	20
6.1	The effect of hyperviscosity on the kinetic energy and Rhines scale . . . . .	106
8.1	Summary of direct numerical simulation data using the standard set of equations . . . . .	137
8.2	Summary of direct numerical simulation data using the LPN equations . . . . .	138



# Nomenclature

## Acronyms

ACC	Antarctic Circumpolar Current
AMS	Adaptive multilevel splitting algorithm
CE <sub>n</sub>	Cumulant expansion with truncation at $n$ -th order
CHM	Charney–Hasegawa–Mima equation
CMIP5	Coupled Model Intercomparison Project: Phase 5
DNS	Direct numerical simulation
DSS	Direct statistical simulation
EENL	Eddy eddy nonlinearity terms
EP	Eliassen-Palm flux
GCM	General circulation model
GQL	Generalised quasilinear
HHNL	High high nonlinearity terms
HST	Hubble Space Telescope
IID	Independent, identically distributed
LAST	Layered anisotropic stratified turbulence
LDT	Large deviation theory
LPN	Low Péclet number
LPNST	Low Péclet number stratified turbulence
NL	Nonlinear
PDF	Probability density function
PV	Potential vorticity
QG	Quasi-geostrophic
QL	Quasilinear
RGB	Red Giant Branch
SSST	Stochastic structural stability theory

## Mathematical Symbols

$\langle \bullet \rangle$	Ensemble or volume average
$\bar{\bullet}$	Zonal average

---

$\Delta t$	Time step
$B$	Buoyancy parameter
$\beta$	Latitudinal gradient of potential vorticity
$D_{\text{turb}}$	Vertical turbulent transport diffusivity
$\varepsilon$	Energy injection rate; dimensional dissipation rate
$\epsilon$	Non-dimensional dissipation rate
$f$	Coriolis parameter
$Fr$	Froude number
$\text{gzmf}$	Generalised zonal mean flow index
$k_f$	Forcing wavenumber
$k_{\text{jet}}$	Number of jets in domain
$k_{\text{max}}$	Largest resolved wavenumber
$\Lambda$	Partition wavenumber in GQL approximation
$L_d$	Rossby radius of deformation
$L_D$	Domain size
$L_\varepsilon$	Wave-turbulence cross-over scale
$L_O$	Ozmidov scale
$L_{Rh}$	Rhines scale
$L_v$	Kolmogorov scale
$\eta$	Mixing efficiency
$N$	Numerical grid point resolution
$\Omega$	Planetary rotation rate
$Pe$	Péclet number
$Pr$	Prandtl number
$R_b$	Buoyancy Reynolds number
$R_\beta$	Zonostrophy parameter
$Re$	Reynolds number
$Ri$	Richardson number
$Ro$	Rossby number
$\theta$	Planetary latitude
$\mu$	Frictional damping rate
$U$	Jet velocity profile
$\mathcal{V}$	Translation speed of zonal jets
$\xi$	Stochastic forcing
$\Xi$	Two-point correlation function of stochastic forcing
$\Psi$	Two-point correlation function of eddy streamfunction
$\mathcal{Z}$	Two-point correlation function of eddy vorticity
$\text{zmf}$	Zonal mean flow index

# Chapter 1

## General introduction

Geophysical and astrophysical fluid dynamics is the study of naturally occurring fluid flows. Examples include planetary atmospheres, oceans and stellar interiors in which physical ingredients such as rotation, stratification and magnetism permit a variety of wave motions. Turbulence, which is often described as being unsteady, irregular and chaotic, is ubiquitous within these flows, occurring across a wide range of spatial and temporal scales and exists alongside the waves. In some flows, the turbulence excites waves which, in turn, reshape the structure of the turbulence by dispersing its energy into particular patterns; in others, the waves excite new turbulence through instabilities. Such interactions lie at the heart of fields such as meteorology, oceanography and astrophysics, giving rise to the complex and spectacular dynamics that are often observed.

A hierarchy of mathematical models spanning a wide spectrum of complexity are used to study geophysical and astrophysical flows, incorporating varying degrees of realism depending on the approximations made. At one end of the spectrum, state-of-the-art general circulation models (GCMs), run on the world's largest supercomputers, are used for forecasting and the prediction of future states. Their complexity, however, impedes the study of phenomena in isolation, and thus a series of simpler models serve this purpose. At the other end of the spectrum lie those models which retain only the essential ingredients necessary to study a particular phenomenon of interest. Such *toy models*, whilst having no forecasting capabilities, require substantially less computational power in addition to offering the viability for analytical exploration, thereby enabling the fundamental physics to be probed in detail.

In this thesis, we consider the effects of rotation and stratification individually through the study of two different problems, both of which share the theme of *layering* of material properties in turbulence. We adopt a mathematical approach in each case, choosing to study idealised models that retain only the essential ingredients. In addition, we probe the complex nature of the resulting nonlinear dynamics using further model reductions that permit additional insights to be made. Each of these problems, which we now proceed to describe, have important consequences for the associated turbulent transport properties.

### 1.1 Jet stream variability in beta-plane turbulence

In our first problem, which forms the basis of Chapters 2 – 6, we focus on the role of rotation within geophysical fluids. Viewed from a distance, planetary atmospheres and oceans are *shallow* turbulent fluid layers on a rotating sphere, a consequence of their large horizontal extent compared with their depth. The quasi-two-dimensional nature of their planetary scale motions gives rise to fascinating dynamics, including

the formation of jet streams and cyclones, with particularly spectacular images of each captured by the recent Juno mission to Jupiter showing jets dominating at lower latitudes and vortices close to the poles (Bolton et al., 2017). These features, which are maintained by smaller scale fluctuations, or *eddies*, due to the tendency of energy in two-dimensional space to continuously transfer into larger scales, are remarkably robust and they dramatically reshape the structure of the flows.

Focussing our attention on these former structures, jet streams are strong and persistent, longitudinally-aligned, alternating currents that arise spontaneously in planetary atmospheres and oceans. They are observed in a wide range of geophysical flows, including those of the terrestrial atmosphere and oceans and, perhaps most strikingly, the atmospheres of the gas giant planets. Acting like fast-moving rivers, jet streams play a key role in the transport of heat, momentum and tracers, including chemically and thermodynamically important quantities such as ozone and water vapour. Following the celebrated paper of Rhines (1975), lively argument has focussed on the mechanisms by which they form and are maintained, with the underlying theme in each case being linked to the natural tendency of potential vorticity, a quantity comprising in the simplest case the relative vorticity plus a component due to the planetary rotation, to be mixed into layers or *staircases* (see Dritschel and McIntyre, 2008; Srinivasan and Young, 2012; Vallis and Maltrud, 1993, and many others).

Nevertheless, equilibrated jet streams are inherently unsteady, and a current leading order question concerns their time variability. Observations have revealed that the gas giant planets are enveloped in a series of remarkably steady jet streams (Asay-Davis et al., 2011; Tollefson et al., 2017), while their terrestrial counterparts exhibit a multitude of types of variability, including latitudinal shifts, strength changes and jet mergers (Sokolov and Rintoul, 2007; Woollings et al., 2010). The reasons for these differences between the planetary systems are not fully understood, and a complete categorisation of jet variability regimes has yet to be accomplished. In addition, understanding how the atmospheric jet streams change as concentrations of greenhouse gases increase is an important aspect of understanding the implications of climate change for regional weather patterns, going beyond the zeroth-order effect of increased global temperature. In order to address these questions, GCMs are often employed, however, computational constraints prevent the simulation of all scales of motion. Instead, smaller spatial scale interactions and fast time scale dynamics are parameterised, raising the question of which physical mechanisms should be retained in order to maintain the fidelity of these models.

Seeking to understand the fundamental aspects of the underlying dynamics, in this study we examine jet stream variability using a framework of idealised models. We follow the inspiration of many before us (see Danilov and Gurarie, 2004; Galperin et al., 2006; Vallis and Maltrud, 1993; Williams, 1978, and many others) by neglecting stratification in a single layer model and we incorporate the effects of planetary rotation by adopting a beta-plane approximation, which is a simple device used to represent the latitudinal variation in the vertical component of the planetary rotation. The jets are not directly driven; instead, they arise spontaneously from a forcing comprising a parameterisation of small-scale eddies or fluctuations. Within this simple framework, we seek to explore jet stream dynamics and, in particular, variability, using a series of model reductions in which the fundamental ingredients are isolated.

We begin in Chapter 2, where we introduce the concept of these idealised models and conduct a literature review of the present understanding of the formation mechanisms of jet streams and their equilibrated dynamical regimes. This is followed in Chapter 3 with the mathematical formulation of two models that will lie at the heart of our studies. Comprising a fully nonlinear model and a quasilinear version in which

eddy-eddy interactions are neglected, these models are then contrasted and compared in Chapter 4 in order to illuminate the differences between the fundamental physics that is captured in each. Further exploration of these differences is investigated in Chapter 5, where we seek to elucidate the physical processes that are relevant for a newly identified type of variability by the systematic restoration of eddy-eddy interactions to the quasilinear model. Finally, in Chapter 6 we adopt a statistical approach in order to assess the role of random fluctuations and gain a deeper understanding of our earlier findings.

## 1.2 Turbulent mixing in stratified, thermally diffusive shear flows

Our second problem shifts gear in Chapters 7 and 8 with a study of stratification in astrophysical fluids. Stratified flows, in which buoyant fluid overlays dense fluid, are ubiquitous; examples in geophysics include atmospheres and oceans, while they also occur on astrophysical scales in planetary and stellar interiors. The interaction of a stable stratification with a background velocity distribution can develop into so-called stratified turbulence, key to transport processes in geophysical flows and also thought to play a crucial role in stellar interiors. Atmospheric and oceanic flows, in which the diffusivities of momentum and heat are commensurate, are often strongly stratified, nevertheless, turbulence still occurs. *Density layering* is key to understanding the properties of this ‘layered anisotropic stratified turbulence’ (LAST) regime (Falder et al., 2016) that is characterised by anisotropic length scales and also anisotropy in the velocity field, and hence the associated turbulence (Lindborg, 2006). On the other hand, astrophysical flows are typically characterised by strong thermal diffusion, achieved physically through radiative transfer, inhibiting the formation of density layers. This suggests that LAST dynamics cannot occur, raising the interesting question of whether analogous or fundamentally different regimes exist in the limit of strong thermal diffusion.

Whilst turbulent mixing in geophysical (atmospheric and oceanic) GCMs has received much attention, it is usually either neglected or poorly parameterised in stellar evolution models. However, there is growing theoretical and observational evidence that such mixing is present and can affect the life cycle of a star, participating in the transport of both angular momentum and chemical elements. Inspired by the work of Jean-Paul Zahn (Zahn, 1974, 1992), shear instabilities are conjectured to provide one such source of turbulent mixing in stars, with the origin of the shear attributed to the star’s differential rotation. Indeed, the advent of helio- and astero-seismology have enabled the internal structure of the sun and Red Giant Branch (RGB) stars to be probed, including the direct measurement of shear (see Beck et al., 2012; Benomar et al., 2018; Christensen-Dalsgaard and Schou, 1988; Thompson et al., 1996, and many others).

The unexpected discovery of the *solar tachocline* (see Hughes et al., 2007; Spiegel and Zahn, 1992), which constitutes an abrupt transition (4% of the solar radius) between the differentially rotating outer convection zone and the uniformly rotating radiative inner zone, is clear evidence that shear in stellar interiors does not have a fixed orientation. Observations highlight components in both the vertical direction (radial shear) and horizontal direction (latitudinal shear), however, the majority of theoretical studies of shear-induced mixing to date have focussed purely on the effect of vertical shear. The fact that vertical shear instabilities directly generate vertical fluid motion makes them natural choices as a source of vertical mixing, nevertheless, they do have a tendency to be suppressed by stratification (Garaud et al., 2015a). This study aims to address these questions for the case of stratified horizontal shear instabilities. Neglecting the effects of rotation and magnetism and focussing on the thermally-diffusive limit, we seek to identify

mechanisms for the transition to turbulence, with a view towards determining the resulting contributions from horizontal shear instabilities to vertical turbulent mixing.

We begin in Chapter 7 with a literature review of stratified turbulence and horizontal shear instabilities, focussing initially on geophysically-motivated studies before taking a look at the current state of affairs in the astrophysical literature. In Chapter 8 we present the results of our research. After describing the mathematical model, we discuss the results from a linear stability analysis of the problem. Shifting to focus on the subsequent nonlinear evolution, we then describe some characteristic numerical simulations and identify four separate dynamical regimes. By studying the dominant balances in the governing equations, we derive scaling laws that are compared with the numerical data, enabling a quantitative description of each of the regimes. Finally, our results are compared with theoretical predictions from Zahn (1992), where we highlight the potential importance of horizontally-oriented shears compared with their vertically-aligned counterparts for the turbulent mixing and transport properties in stellar interiors.

## Chapter 2

# Introduction to beta-plane turbulence

### 2.1 Motivation

Planetary atmospheres and oceans are *shallow* fluid layers on a rotating sphere, a consequence of their large horizontal extent compared with their depth. They are in constant motion and their circulations, which are primarily driven by heat radiation due to the relative excess of heating in equatorial regions compared to higher latitudes, are complex. The fundamental dynamics of these flows are dominated by the effects of stable stratification and planetary rotation which, at the largest scales, give rise to quasi-two-dimensional dynamics. Turbulence, which is often described as being unsteady, irregular and chaotic, is ubiquitous. Owing to the tendency of energy in two dimensions to transfer to larger spatial scales, these *turbulent* flows are shaped by the spontaneous emergence of long-lived, coherent structures.

Jet streams are one of the primary constituents of planetary flows. They characteristically manifest themselves as a banded structure of fluctuating, alternating jets with a mild asymmetry in form between sharper eastward jets and broader westward flows (Vallis, 2017). Predominantly flowing in the east-west or *zonal* direction, they are frequently referred to as *zonal jets* or *zonal flows*, terms that will be used interchangeably throughout this thesis. Zonal jets influence the transport properties of planetary systems; thus, their unsteadiness and the nature of their time variability is of great interest.

Terrestrial examples have been well studied since their discovery in the early twentieth century. In the Earth's atmosphere, the alternating pattern of easterlies and westerlies is a permanent feature, visible in the annual mean tropospheric winds (see Figure 2.1(a)). Close to the tropopause, each hemisphere contains an eddy-driven, or polar, jet located at  $50 - 60^\circ$  latitude and 9 – 12 km above sea level, and a subtropical jet at about  $30^\circ$  latitude and 10 – 16 km altitude. Multiple modes of variability have been observed, with timescales ranging from intraseasonal to interdecadal. Despite having a preferred location, these jets naturally fluctuate about their average position on a synoptic time scale, as can be seen in Figure 2.2(a). They are also known, for example, to exhibit bistability between a double-jet regime, in which two distinct jets are well-separated, and a single-jet regime, in which the jets are merged. Eichelberger and Hartmann (2007) suggested that the single-jet regime is more related to pulsing, i.e. the acceleration and deceleration of the zonal wind, while the double-jet regime is more related to latitudinal shifting of the eddy-driven jet. Another prominent form of variability is the poleward propagation of zonal mean flow anomalies, which has been observed in both hemispheres (Feldstein, 1998; Riehl et al., 1950).

The jets in the Earth's oceans are somewhat narrower, a consequence of a smaller Rossby radius of deformation (a measure of the length scale at which rotational effects become important - see Section 2.2).

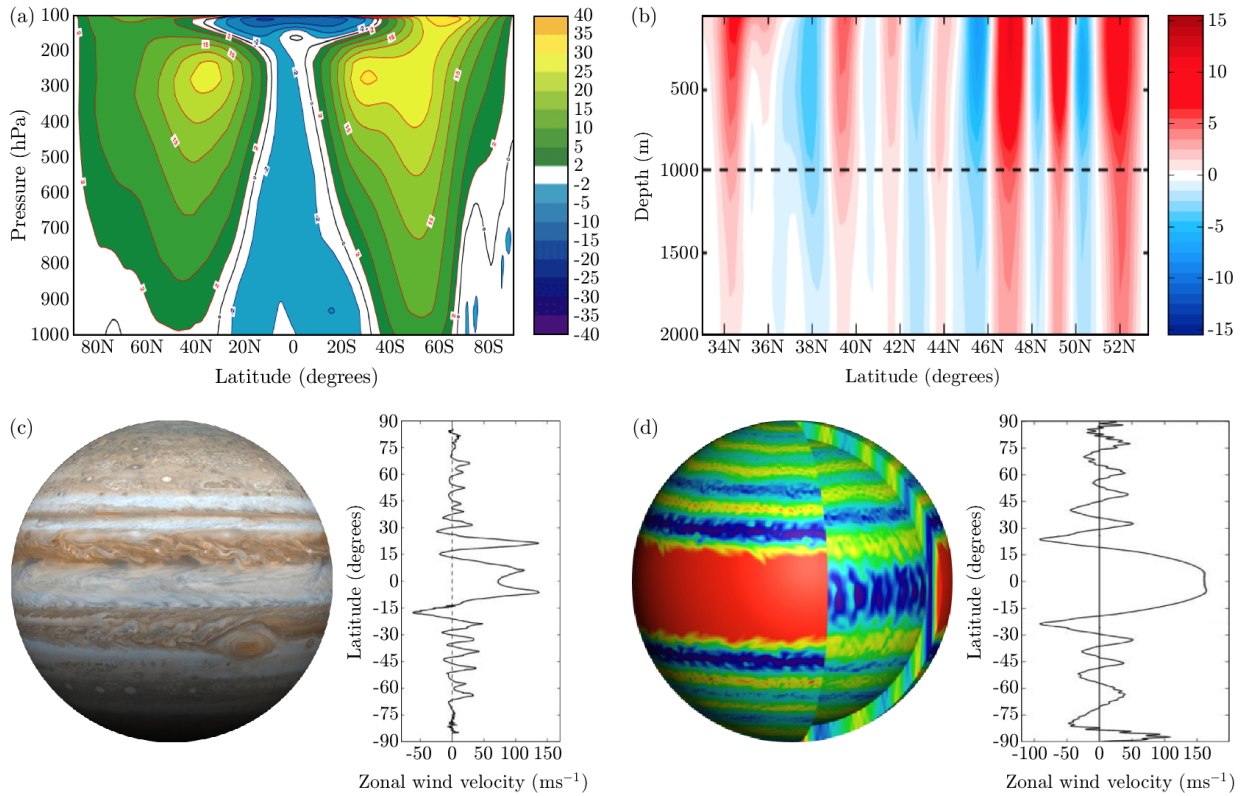


**Figure 2.1** Geophysical observations of jet streams. (a) *Earth's atmosphere*: latitude-pressure projection showing the annual mean values of the mean zonal winds from the ECMWF ERA-40 Atlas. (b) *Earth's oceans*: vertical cross section at 20°W showing vertically-coherent patterns of alternating positive and negative velocity from Argo data from 2004-2006 (adapted from van Sebille et al., 2011). (c) *Jupiter*: image of Jupiter's zonal jets and the zonally averaged zonal winds, both from the NASA Cassini mission. (d) *Jupiter model*: the zonal winds (left) and the zonally averaged zonal winds (right) from a numerical model of Jupiter's atmosphere (adapted from Heimpel et al., 2005).

Their existence is often difficult to establish, partly due to the fact that they are weak relative to the eddies (defined as departures from the mean) and tend to be observable only after time-averaging, a property referred to as *latency* by Berloff et al. (2011). Nevertheless, observations record multiple zonal jets in the equatorial regions, in the subtropics, and in the Antarctic Circumpolar Current (ACC) (see Cravatte et al., 2017; Maximenko et al., 2005, 2008, and many others). Oceanic zonal jets can be deep-reaching, as shown in Figure 2.1(b) in which strong *barotropic* (depth-independent) structures are detectable down to depths on the orders of kilometres. Despite their positions often being tied to topographical features, the Southern Ocean jets display considerable spatial and temporal variability (Sokolov and Rintoul, 2007) with jets observed to merge, nucleate (generate) and reorganise along the path of the ACC (see Figure 2.2(b)).

The most striking examples of zonal jets are those that are clearly visible in the atmospheres of the gas giant planets (see Figure 2.1(c)). These jets are profoundly strong and their influence on the distribution of clouds is visible even through amateur telescopes. Despite being observed for hundreds of years, with the first zonal wind measurements recorded in the twentieth century, the wind systems of these planets remained poorly known until Voyagers 1 and 2 flew past Jupiter in 1979 and Saturn in 1980–81. Jupiter's zonally averaged zonal wind profile, as observed by Cassini (plotted in Figure 2.1(c)), is not hemispherically symmetrical; it contains between seven and eight jets per hemisphere and is dominated by a strong equatorial jet with maximum velocities of 140 ms<sup>-1</sup>. A hierarchy of complexity of models have attempted to replicate the structure, including the relatively complex numerical model of Heimpel

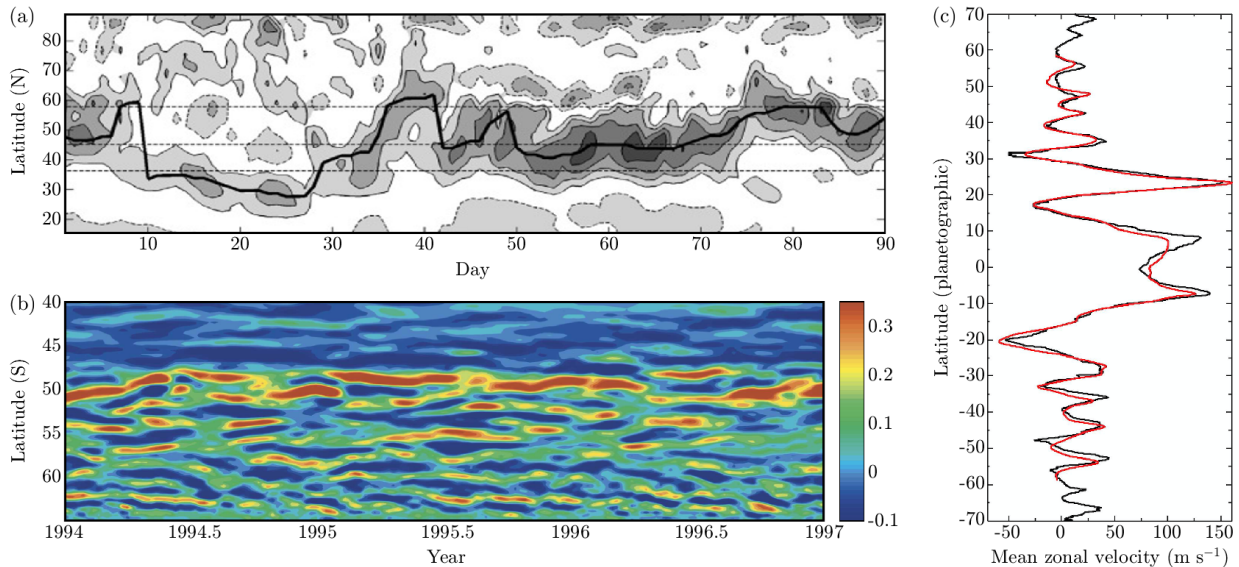


**Figure 2.2** Geophysical observations of jet stream variability. (a) *Earth's atmosphere*: Hovmöller diagram of the zonal wind averaged over 925–700 hPa and 0–60°W for the winter of 2001–2002. The black line shows the latitude of the jet core. Contours are drawn every  $5 \text{ m s}^{-1}$  with negative contours dashed and the zero contour omitted (adapted from Woollings et al., 2010). (b) *Earth's oceans (ACC)*: meridional gradient of sea surface height [ $\text{m (100km)}^{-1}$ ] at 130°E between 1994 and 1997 (adapted from Sokolov and Rintoul, 2007). (c) *Jupiter*: mean zonal velocities from (red) Hubble Space Telescope images taken on May 10, 2008, and (black) Voyager 2 measurements from Limaye (1986) in March 1979 (adapted from Asay-Davis et al., 2011).

et al. (2005) shown in Figure 2.1(d). In contrast to their terrestrial equivalents, Jupiter's jets are remarkably stable over long time intervals (see García-Melendo et al., 2011; Tollefson et al., 2017, and others). This is evident by comparing data from space missions spanning nearly 40 years alongside observations from the Hubble Space Telescope (HST), which show remarkably good agreement, as highlighted in Figure 2.2(c).

Zonal jets play a fundamental role in the climate system, transporting geophysically-important quantities, such as momentum and heat, that determine patterns of weather and climate. Regions of strong alternating currents suppress eddy diffusivities and act as effective barriers to north-south, or *meridional*, transport (Berloff et al., 2009; Dritschel and McIntyre, 2008; Haynes et al., 2007; Naveira Garabato et al., 2011). On Earth, modifications in the structure or the position of the tropospheric jet streams, which account for about half of the total kinetic energy, may induce dramatic changes in regional weather patterns. This was the cause of the 2003 and 2010 European heat waves which occurred when a slow-moving high-pressure system caused an *atmospheric blocking* of the eastward winds, preventing the normal transport of mid-latitude weather systems. It is no coincidence, therefore, that systematic changes in the positions and strengths of the jet streams are a central theme in climate change research. Recent climate change projections from Phase 5 of the Coupled Model Intercomparison Project (CMIP5) generally show a poleward shift of the eddy-driven jets and storm tracks in both hemispheres (Barnes and Polvani, 2013; Chang et al., 2012). Other studies (based on ERA-Interim reanalysis data or individual CMIP5 model projections) predict a future weakening of the tropospheric jet streams due to a reduction in the pole-to-equator temperature gradient (see e.g. Coumou et al., 2015), which is hypothesised to invoke a higher degree of variability.

As we have seen, zonal jets exhibit a rich assortment of behaviours which differ substantially between different planetary systems. However, the reasons for these differences are not fully understood. Thus, the topic of zonal jet variability is of considerable interest and forms the focus of the first part of this thesis.

## 2.2 A framework of idealised models of zonal jets

From a theoretical viewpoint, the advantages of using idealised, simplified models of geophysical phenomena are the facility to retain and study only the essential physics inherent within a system. We begin with a formulation of a generic mathematical model lying at the heart of much of the literature that will be reviewed in this chapter and which will subsequently form the basis of the models used within this study. It is a convenient framework that has been widely adopted due to the facility with which it can shed light on important properties such as the formation and dynamics of zonal jets.

Large scale geophysical flows are strongly influenced by two effects: rotation and stratification. These lead respectively to dominant balances between the pressure gradient and the Coriolis force (geostrophic balance) in the horizontal direction, and the pressure gradient and gravity (hydrostatic balance) in the vertical direction. The underlying equations can be simplified by exploiting these balances, filtering out modes such as gravity waves and sound waves which are unimportant in the study of certain phenomena. Atmospheric and oceanic flows are often modelled using the shallow water equations in which, in the simplest *barotropic* formulation, a single-fluid layer of constant density is considered:

$$\frac{\partial \mathbf{u}}{\partial t} + (\mathbf{u} \cdot \nabla) \mathbf{u} + \mathbf{f} \times \mathbf{u} = -g \nabla h, \quad \frac{\partial h}{\partial t} + \nabla \cdot (h \mathbf{u}) = 0. \quad (2.1)$$

Within this unstratified model, coordinates  $x$  and  $y$  correspond to the zonal and latitudinal directions respectively,  $\mathbf{u}(x, y, t) = (u, v)$  is the horizontal velocity field,  $h(x, y, t)$  denotes the total fluid depth,  $\mathbf{f} = f \hat{\mathbf{z}}$  is the local vertical component of the planetary rotation vector and  $\nabla = (\partial_x, \partial_y)$  is the two-dimensional gradient operator. The Coriolis parameter is given by  $f = 2\Omega \sin \theta$  at latitude  $\theta$  for a planet with radius  $a$  rotating with angular velocity  $\Omega$ . For simplicity, this is often approximated using a truncated Taylor series,  $f = f_0 + \beta y$ , with a constant latitudinal gradient  $\beta = (2\Omega/a) \cos \theta_0$  close to latitude  $\theta_0$ . This known as the *beta-plane approximation*, first introduced by Rossby (1939).

The ratio of the magnitude of the advective term,  $(\mathbf{u} \cdot \nabla) \mathbf{u}$ , to the Coriolis term,  $\mathbf{f} \times \mathbf{u}$ , is a key parameter called the *Rossby number*. For a characteristic horizontal velocity,  $U_c$ , a characteristic horizontal length scale,  $L_c$ , and a characteristic Coriolis frequency,  $f_c$ , this is given by

$$Ro = \frac{U_c}{f_c L_c}, \quad (2.2)$$

where  $Ro \ll 1$  implies the importance of rotation. Typical values for large-scale mid-latitude flows in the Earth's atmosphere and ocean are 0.1 and 0.01 respectively, implying that rotational effects are significant.

The smallness of this parameter can be exploited to simplify the shallow water equations in the limit in which there is an approximate balance between the pressure gradient and the Coriolis force. Known as *quasi-geostrophic (QG) motion*, this was first formulated by Charney (1948). The procedure, outlined in Appendix A, can be found in many standard text books, including Vallis (2017), and involves scaling equations (2.1) before performing an asymptotic analysis. Remarkably, this leads to dynamics that are completely determined by a single dynamical variable, namely the streamfunction,  $\psi(x, y, t) = (g/f_0)h$ , or the vorticity,  $\zeta = \nabla^2 \psi$ . The resulting shallow water quasi-geostrophic potential vorticity equation is

$$\frac{\partial}{\partial t} \left( \nabla^2 \psi + \beta y - \frac{1}{L_d^2} \psi \right) + (\mathbf{u}_g \cdot \nabla) \left( \nabla^2 \psi + \beta y - \frac{1}{L_d^2} \psi \right) = 0, \quad (2.3)$$

which is sometimes known as the Charney–Hasegawa–Mima (CHM) equation (Galperin and Read, 2019). Here,  $\mathbf{u}_g$  denotes the geostrophic velocity field and  $L_d = \sqrt{gH}/f$  is the *Rossby radius of deformation*, i.e. the length scale at which the geostrophic balance becomes important. The quantity inside the parentheses,

$$q = \nabla^2 \psi + \beta y - \frac{1}{L_d^2} \psi, \quad (2.4)$$

is known as the shallow water quasi-geostrophic potential vorticity (PV). We note that the vortex stretching term that is present in three-dimensional flows, acting as a mechanism for transferring turbulent energy to smaller scales by enhancing vorticity through stretching processes, is identically zero in equation (2.3), leading to qualitatively different flow evolution. Consequently, the potential vorticity is materially conserved,  $Dq/Dt = 0$  (provided external forcing and dissipation are neglected), a property that is widely used in theoretical studies of the atmosphere and ocean. In the limit in which the characteristic scales of motion are much smaller than  $L_d$ , the potential vorticity reduces to  $q = \nabla^2 \psi + \beta y = \zeta + f$  and the dynamics become *two-dimensional*. This is one of the simplest fully nonlinear models with which to study the effects of rotation on turbulence, including the formation of zonal jets.

In three-dimensional, stratified configurations, turbulence naturally arises as a result of dynamical instabilities such as baroclinic instability, however, there is no such underlying instability in the two-dimensional case. Consequently, it is common to artificially force two-dimensional turbulence through an exogenous, statistically homogeneous, forcing function,  $\mathcal{F}$ , and associated forcing scale,  $k_f$ . In doing so, it is assumed that the barotropic and baroclinic interactions are decoupled and that the baroclinic eddies can be represented by an external force added to the barotropic model. A state of equilibration can then be achieved by the inclusion of dissipation terms,  $\mathcal{D}$ , representing physical processes such as radiative cooling (Scott and Polvani, 2008) or Ohmic dissipation (Liu et al., 2008). Incorporating these approximations, the resulting two-dimensional beta-plane potential vorticity equation for this forced-dissipative system is

$$\frac{\partial \zeta}{\partial t} + J(\psi, \zeta) + \beta \frac{\partial \psi}{\partial x} = \mathcal{F} + \mathcal{D}, \quad (2.5)$$

where we note that  $J$  is the Jacobian determinant, defined by  $J(A, B) = A_x B_y - A_y B_x$ . This single equation encapsulates the entire dynamics governing the evolution of the flow. Numerous versions of equation (2.5) have been used to study the spontaneous formation of zonal jets, including a recent study by Constantinou et al. (2014) in which a stochastic forcing function was used to parameterise small scale turbulence. An example numerical solution from this study can be seen in Figure 2.10(a), illustrating a configuration in which three sharp eastward jets undergo small latitudinal fluctuations.

Motivated by the study of zonally-orientated flows, it is instructive to seek an equation governing the evolution of the zonally averaged zonal velocity field. To do this, we begin by applying an eddy-zonal mean decomposition (denoted by a prime and an overbar respectively) to the streamfunction:

$$\psi(x, y, t) = \bar{\psi}(y, t) + \psi'(x, y, t), \quad (2.6)$$

with corresponding decompositions of the other variables. For convenience with notation, we represent the zonal mean zonal velocity (which we call the jet velocity profile) as  $U(y, t) = \bar{u}(y, t)$ . Applying this decomposition to the variables in the vorticity equation and taking a zonal average (noting that when  $\mathcal{F}$  is prescribed to be statistically homogeneous in space then  $\bar{\mathcal{F}} = 0$ ), we derive an equation governing the

evolution of the zonal mean zonal flow (related to the zonal mean vorticity by  $\bar{\zeta}(y, t) = -\partial_y U(y, t)$ ):

$$\frac{\partial U}{\partial t} + \frac{\partial}{\partial y} (\overline{u'v'}) = \mathcal{D}, \quad (2.7)$$

with corresponding dissipation terms on the right-hand side denoted by  $\mathcal{D} = -\int \overline{\mathcal{D}} dy$ . For heterogeneous flow solutions in which  $U(y, t) \neq 0$ , this equation is non-trivial and describes the evolution of jet velocity profiles which, in a statistically steady state with linear damping  $\mathcal{D} \propto -\zeta$ , are given by  $U(y) \propto -\partial_y (\overline{u'v'})$ . It can be seen that eddy-driven zonal jets are forced and maintained by the *eddy momentum flux* convergence (sometimes called the Reynolds stress divergence),  $-\partial_y (\overline{u'v'})$ , which is a key quantity in the study of the large scales of turbulent flows. This implies that eastward (westward) jets form where eddy momentum fluxes converge (diverge). A remarkable fact, given by the Taylor identity (see Bühler, 2014),

$$-\frac{\partial}{\partial y} (\overline{u'v'}) = \overline{v'\zeta'}, \quad (2.8)$$

is that the eddy momentum flux convergence equals the meridional flux of eddy potential vorticity, allowing jet formation to be described in terms of the latitudinal transfer of potential vorticity (see Section 2.3.3.2). The exact form of the eddy momentum flux is integral to understanding the formation and variability of zonal jets and will be discussed in detail throughout this thesis.

It is also useful to consider the evolution of a couple of quadratic quantities, notably the kinetic energy of the fluid per unit mass,  $E = \frac{1}{2} \langle |\nabla\psi|^2 \rangle$ , and the enstrophy of the fluid per unit mass,  $Z = \frac{1}{2} \langle (\nabla^2\psi)^2 \rangle$ , where the angular brackets  $\langle \bullet \rangle$  represent a volume average over the domain. An evolution equation for the former can be derived by multiplying the vorticity equation (2.5) by the streamfunction,  $\psi$ , and integrating:

$$\frac{dE}{dt} = -\langle \psi \mathcal{F} \rangle - \langle \psi \mathcal{D} \rangle, \quad (2.9)$$

where the energy input rate by the forcing,  $\mathcal{F}$ , is given by  $\varepsilon = -\langle \psi \mathcal{F} \rangle$ . This expression is independent of the value of  $\beta$  and we observe that, in the absence of forcing and dissipation, energy is conserved,  $dE/dt = 0$ . Enstrophy, unlike in three-dimensional flows where vortex stretching is present, is another conserved quantity in the unforced, undissipated case, where  $dZ/dt = 0$  can be shown by multiplying the vorticity equation (2.5) by the vorticity,  $\zeta = \nabla^2\psi$ , and integrating. The relevance of these quadratic invariants is demonstrated by their profound impacts on the nature of the flows, as we shall discuss in Section 2.3.

Within this idealised model there are at least three external parameters, in addition to those associated with the forcing, that control the dynamics: the strength of the background gradient of potential vorticity,  $\beta$ , the rate of energy injection by the forcing,  $\varepsilon$ , and a rate of damping associated with  $\mathcal{D}$ . As will be seen, these parameters play a fundamental role in the ensuing dynamics.

### 2.2.1 On the validity of idealised models

Variations of this two-dimensional model encapsulated by equation (2.5) have been used in a wide range of studies investigating large-scale planetary flows (Nozawa and Yoden, 1997; Scott and Dritschel, 2012; Williams, 1978, to name a few). With the choice of such an idealised representation, however, it is natural to enquire about the validity of the modelling assumptions. The shallowness of planetary atmospheres and oceans could be argued as a legitimate reason to consider only the horizontal components of the large-scale

velocity field, but to what extent do naturally-occurring jet streams have a barotropic (depth-independent) structure, and to what extent are they driven by turbulence?

Hadley (1735) first recognised that the Earth's rotation is responsible for the alternating patterns of tropospheric winds. Driven by differential equator-to-pole heating, he envisaged an atmospheric overturning circulation, symmetric about the Equator, in which air parcels are upwelled in the tropics, transported poleward in the upper troposphere and finally downwelled in the subtropics as they lose heat. Due to the conservation of absolute angular momentum of air parcels, which is given by

$$M = \Omega a^2 \cos^2 \theta + ua \cos \theta, \quad (2.10)$$

for a planet with radius  $a$ , such poleward transportation induces eastward momentum, driving zonal flows (Hide, 1969). Bounded by the equatorial angular momentum,  $M_0 = \Omega a^2$ , the corresponding wind profile is

$$u_{max}(\theta) = \Omega a \frac{\sin^2 \theta}{\cos \theta}, \quad (2.11)$$

which is an increasing function of the latitude,  $\theta$ . This poleward transport of angular momentum by the Hadley circulation drives the terrestrial subtropical jet streams which, correspondingly, have a baroclinic (stratified) structure with vertical shear and are therefore not well modelled using equation (2.5).

In contrast to the thermodynamically-driven tropical circulations, the polar jet streams are predominantly maintained by the convergence of eddy momentum fluxes due to turbulent motions. This idea was first suggested by Jeffreys (1926), who realised that the large-scale eddies in the mid-latitudes are not perturbations of an idealised axisymmetric circulation but instead are often of similar amplitude to the mean flow and thus play an essential role in the transport of heat and angular momentum. Broadly speaking, the meridional overturning circulation in the mid-latitudes, termed the Ferrel Cells, is significantly weaker than its tropical equivalent, and flows in the reverse direction. In contrast to the Hadley Cells, the Ferrel Cells are dominated by wave-like flows and are driven by eddies in order to balance a convergence of horizontal eddy momentum fluxes. The net effect of these eddies reduces the pole-to-equator temperature gradient and,

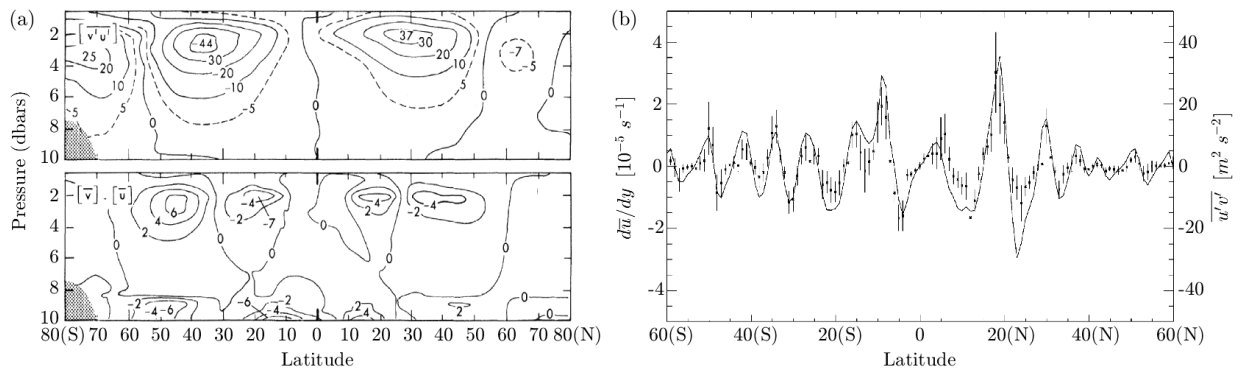


**Figure 2.3** Observational evidence of eddy-driven jet streams: (a) Zonal mean cross sections in Earth's atmosphere of (top) the northward flux of momentum by eddies,  $\overline{u'v'}$  ( $m^2 s^{-2}$ ), and (bottom) the northward flux of momentum by mean meridional circulations,  $\overline{uv}$  ( $m^2 s^{-2}$ ), for annual mean conditions (adapted from Peixoto and Oort, 1984); (b) Jovian observations from Cassini showing  $\overline{u'v'}$  and  $\overline{d\bar{u}/dy}$  plotted together as a function of latitude.  $\overline{u'v'}$ , corresponding to the right of the two axes, is plotted as dots with error bars corresponding to 2 standard deviations from the mean.  $\overline{d\bar{u}/dy}$  is shown as a solid line and corresponds to the left of the two axes. There is a distinct positive correlation between the two curves, and their correlation coefficient is 0.86 (adapted from Salyk et al., 2006).

correspondingly, the baroclinic shear of the mean flow. Thus, the Polar jets are more barotropic, evidence for which can be seen in Figure 2.1(a), and have a better chance of being relevant to equation (2.5).

Atmospheric observations giving weight to these ideas are shown in Figure 2.3(a). Peixóto and Oort (1984) decomposed the zonally-averaged momentum flux,  $\overline{uv}$ , into the components due to the axisymmetric motions in the meridional circulations,  $\overline{u\bar{v}}$ , and the components due to the eddies,  $\overline{u'v'}$ :

$$\overline{uv} = \overline{u\bar{v}} + \overline{u'v'}. \quad (2.12)$$

Within each hemisphere, the eddy momentum fluxes,  $\overline{u'v'}$ , in the top of Figure 2.3(a) have larger magnitudes than those from the meridional circulations,  $\overline{u\bar{v}}$ , and can be seen to converge at latitudes of 50-60° where the Polar jet is located, highlighting the role of turbulence. In contrast, momentum convergence due to the overturning circulation at the location of the subtropical jet (30°) confirms the thermodynamic forcing mechanism in this case. The turbulent motions responsible for the maintenance of the Polar jet, sometimes referred to as *macroturbulence* (Held, 1999; Schneider and Walker, 2006), consist of large-scale eddies with typical length scales of 1000 km. Baroclinic instability is the typical generation mechanism of these eddies which transport angular momentum into the latitudes in which they form (Held and Hoskins, 1985; Simmons and Hoskins, 1978).

What is missing in the Earth's atmosphere is the multiplicity of zonal jets that emerge in the Earth's oceans and the atmospheres of the gas giant planets. The zonal jets in the ACC are deep-reaching with bottom velocities typically having an eastward component (Heywood et al., 1999), implying that the orientation of the jets is relatively uniform throughout the water column. On Jupiter, it was not possible until recently to determine whether the observed cloud level winds penetrate deep into the planet or are relatively shallow. This conundrum has apparently been resolved by Kaspi et al. (2018) using measurements from the Juno spacecraft, in which the jet depth is inferred to be 2000–3000 km, although the uniqueness of this interpretation has been challenged (Kong et al., 2018). Nevertheless, it is agreed that their structure it is likely to include both deep and shallow processes (see Vasavada and Showman, 2005, and others).

In terms of dynamical mechanisms, observations have confirmed that the Jovian jets are predominantly eddy-driven (Beebe et al., 1980; Galperin et al., 2014; Ingersoll et al., 1981), where the small-scale forcing is generated by baroclinic instability or convection (Ingersoll et al., 2000; Read et al., 2020). Salyk et al. (2006) plotted the eddy momentum flux,  $\overline{u'v'}$ , alongside the latitudinal shear of the zonal mean flow,  $d\bar{u}/dy$ , noting a strong correlation between the two (see Figure 2.3(b)). From equation (2.7), this implies that

$$\frac{\partial U}{\partial t} \approx -\frac{\partial}{\partial y} (\overline{u'v'}) \propto -\frac{\partial^2 U}{\partial y^2}, \quad (2.13)$$

illustrating the anti-diffusive effect of the eddies due to the negative prefactor in the diffusion term. The phenomenon of energy being transferred upgradient into larger scale mean flows has been observed in a wide range of settings and is sometimes referred to as *negative viscosity* (Starr, 1953, 1968).

## 2.3 Towards an understanding of the dynamics of zonal jets

It is well known that rotating systems with a meridional gradient of the Coriolis parameter, such as that arising from differential rotation or varying topography, have a natural tendency to develop zonal flows, a phenomenon that is sometimes called *zonation*. Lively debate over the last few decades has produced a

multitude of theories in order to explain the spontaneous emergence and persistence of these zonal jets using a hierarchy of models of varying complexity. Whilst this is still an ongoing area of research, it is understood that jets form via the interaction of two-dimensional turbulence and *Rossby-wave* dynamics. In this section we will review several of these theories, with consideration primarily given to zonal jets using a beta-plane formulation and an infinite Rossby radius of deformation.

We begin with a brief review of the fundamental theory of Rossby waves, which are perhaps the most important large-scale waves in the atmosphere and the ocean. This is followed by establishing a conceptual basis for expecting the formation of large-scale structures in beta-plane turbulence and a discussion of a selection of popular zonation mechanisms. Thinking beyond jet formation, we present a classification of different zonostrophic regimes on a beta-plane using a diagnostic known as the zonostrophy parameter, which is a measure of the strength, or the variability, of jets once they have saturated. Finally, we depart from barotropic models and discuss some dynamical insights that have been inferred from two-layer, or baroclinic, systems, restricting attention to horizontally-periodic domains and no imposed topography.

### 2.3.1 A brief review of Rossby waves

Rossby waves owe their existence to a background gradient of potential vorticity, a natural source of which is the latitudinal gradient of the Coriolis parameter. As discussed in Section 2.2, potential vorticity is a materially conserved quantity, which, on a barotropic beta-plane, is given by  $q = \zeta + \beta y$ . The equation of motion, written in terms of the streamfunction, and in the absence of forcing and dissipation, is given by

$$\frac{\partial}{\partial t} \nabla^2 \psi + J(\psi, \nabla^2 \psi) + \beta \frac{\partial \psi}{\partial x} = 0. \quad (2.14)$$

By considering small perturbations,  $\psi'(x, y, t)$ , away from a basic state comprising a generic background zonal flow, i.e.  $\psi(x, y, t) = \bar{\psi}(y) + \psi'(x, y, t)$ , where  $U(y) = -\partial \bar{\psi} / \partial y$ , the linearised perturbation equation is

$$\frac{\partial}{\partial t} \nabla^2 \psi' + \left( U \nabla^2 + \beta - \frac{\partial^2 U}{\partial y^2} \right) \frac{\partial \psi'}{\partial x} = 0, \quad (2.15)$$

where the operator inside the parentheses is called the Rayleigh-Kuo operator. In the special case when the background flow,  $U$ , is constant, this equation admits plane wave solutions of the form

$$\psi' = \text{Re} \tilde{\psi} e^{i(k_x x + k_y y - \omega t)}, \quad (2.16)$$

with wavenumber  $\mathbf{k} = (k_x, k_y)$ , frequency  $\omega$  and amplitude  $\tilde{\psi}$ , where substitution of (2.16) into (2.15) yields

$$\left[ -(U k_x - \omega)(k_x^2 + k_y^2) + \beta k_x \right] \tilde{\psi} = 0. \quad (2.17)$$

For non-trivial solutions, we obtain the *dispersion relation* for this family of barotropic Rossby waves,

$$\omega = U k_x - \frac{\beta k_x}{k_x^2 + k_y^2}, \quad (2.18)$$

where the constant mean flow,  $U$ , Doppler shifts the frequency by amount  $U k_x$ . These waves are inherently anisotropic, as illustrated by the lack of symmetry between the zonal and latitudinal wavenumbers in this

dispersion relation. For example, purely zonal ( $k_y = 0$ ) propagation is permitted, whilst purely latitudinal propagation is not ( $\omega = 0$  when  $k_x = 0$ ).

The corresponding phase velocity,  $c_p$ , and group velocity,  $c_g$ , are found to be, respectively,

$$c_p = \frac{\omega}{|\mathbf{k}|} \frac{\mathbf{k}}{|\mathbf{k}|} = \left( U(y) - \frac{\beta}{k_x^2 + k_y^2}, \frac{\beta k_x}{k_y(k_x^2 + k_y^2)} \right), \quad (2.19)$$

$$c_g = \frac{\partial \omega}{\partial \mathbf{k}} = \left( U(y) + \frac{\beta(k_x^2 - k_y^2)}{k_x^2 + k_y^2}, \frac{2\beta k_x k_y}{(k_x^2 + k_y^2)^2} \right). \quad (2.20)$$

It is evident from the phase velocity that Rossby waves propagate westward relative to the mean flow, and that waves with longer wavelengths travel faster. In addition, their zonal group velocity is eastward relative to the mean flow if  $|k_x| > |k_y|$  and westward if  $|k_x| < |k_y|$ .

### 2.3.2 Zonostrophic turbulence and general scaling arguments

Following the seminal contributions by Kolmogorov (1941, 1962) to the development of a mathematical theory of three-dimensional turbulence, in which energy and enstrophy both cascade from large scales down to small scales (see Chapter 7), Fjørtoft (1953) recognised that two-dimensional flows on the surface of a sphere behave in a profoundly different way, with energy culminating instead at the largest scales. The pioneering works of Kraichnan (1967), Leith (1968) and Batchelor (1969) later established a theory of two-dimensional turbulence, in which eddies interact and evolve towards larger scales.

On the grounds of dimensional arguments, and by invoking the *locality hypothesis*, which says that the fluxes of energy or enstrophy at a particular scale depend only on the processes occurring at or near that scale, two inertial ranges were predicted. The energy inertial range, in which energy preferentially transfers to larger scales (familarly known as the *inverse energy cascade*) and the enstrophy inertial range, in which enstrophy transfers to smaller scales, were hypothesised to depend only on the local isotropic wavenumber,  $k = (k_x^2 + k_y^2)^{1/2}$ , and the respective rates of production of energy,  $\varepsilon$ , and enstrophy,  $\eta$ , by the forcing. Consequently, the associated energy spectrum,  $\mathcal{E}(k)$ , for wavenumbers smaller than the scale of the forcing,  $k_f$ , was predicted to be

$$\mathcal{E}(k) = C_\varepsilon \varepsilon^{2/3} k^{-5/3}, \quad (2.21)$$

while for wavenumbers larger than the scale of the forcing, it was predicted to be

$$\mathcal{E}(k) = C_\eta \eta^{2/3} k^{-3}, \quad (2.22)$$

where  $C_\varepsilon$  and  $C_\eta$  are constants. Experimental and numerical evidence for the existence of these inertial ranges is vast, with further discussion on this topic provided by Boffetta and Ecke (2012).

In non-rotating two-dimensional turbulence, energy is *isotropically* transferred to the largest scales, resulting in the formation of isotropically-distributed coherent vortices (see McWilliams, 1984; Oetzel and Vallis, 1997, and many others), provided that the aspect ratio of the two-dimensional domain is unity (Frishman et al., 2017; Guervilly and Hughes, 2017; Tobias and Marston, 2017). However, the effect of rotation, i.e. the beta-effect, induces anisotropy into the system, resulting in zonally-orientated flows with significantly different dynamics. A comparison between these two regimes showing the dichotomy between jets and vortices is presented in Figure 2.4. To understand why these differences emerge, let us consider

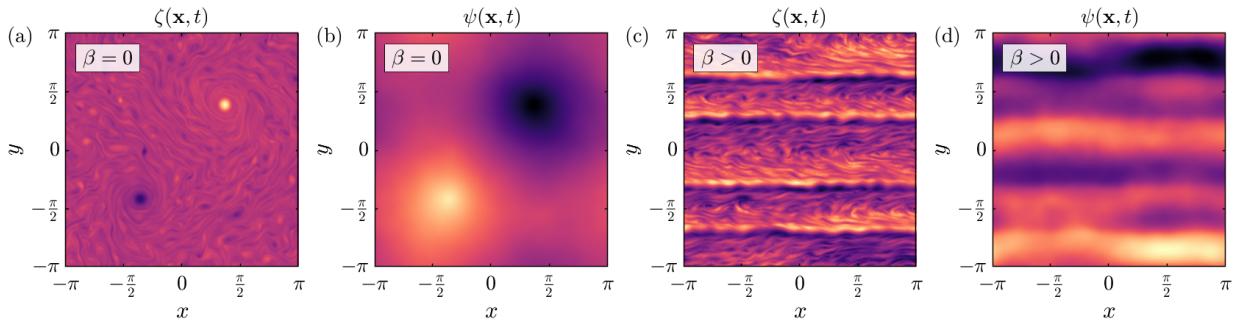


**Figure 2.4** Numerical simulations using the nonlinear model described in Chapter 3 highlighting the bifurcation between (a-b) the formation of coherent vortices in the absence of rotation (parameters:  $\beta = 0$ ,  $\mu = 0.0005$ ,  $\varepsilon = 10^{-5}$ ,  $k_f = 16$ ,  $N = 256$ ), and (c-d) zonal jets in the presence of rotation (parameters:  $\beta = 8.5$ ,  $\mu = 0.0005$ ,  $\varepsilon = 10^{-5}$ ,  $k_f = 16$ ,  $N = 256$ ,  $R_\beta = 3.29$ ). Figures (a) and (c) plot the relative vorticity,  $\zeta$ , while (b) and (d) plot the streamfunction,  $\psi$ .

a beta-plane in which Rossby waves and two-dimensional turbulence may interact. By considering the magnitudes of the advective term ( $\mathbf{u} \cdot \nabla \zeta \sim U_c^2 / L_c^2$ ) and the beta-term ( $\beta v \sim \beta U_c$ ) in the beta-plane vorticity equation (2.5), we observe that for large scales, the beta-term will dominate, while for smaller scales, the advective term will dominate. The cross-over scale,  $L_{Rh}$ , given by

$$L_{Rh} = \left( \frac{2U}{\beta} \right)^{1/2}, \quad (2.23)$$

with corresponding wavenumber  $k_{Rh} = L_{Rh}^{-1}$ , is popularly known as the *Rhines scale* (Hide, 1966; Rhines, 1975). Here,  $U$  can be interpreted as the root-mean-square (r.m.s) velocity and the factor of  $\sqrt{2}$  is often included by convention. The Rhines scale is believed to be linked to the latitudinal scale of the emerging zonal jets (Chemke and Kaspi, 2015a; Sukoriansky et al., 2007), however, the precise nature of the relationship is still an active area of research.

Another important length scale emerges by examining the wave-turbulence cross-over using the phenomenology of two-dimensional turbulence. If the characteristic time scale of turbulence, i.e. the eddy-turnover time, is given by  $\tau_t = \varepsilon^{-1/3} k^{-2/3}$ , and the time scale of linear Rossby waves is given by  $\tau_w = k/\beta$ , then turbulent processes dominate on small scales where  $\tau_t < \tau_w$  and conversely, waves dominate on large scales. By equating these time scales, Maltrud and Vallis (1991) deduced that the transitional scale at which the turbulence first begins to feel the beta-term in the vorticity equation, synonymous with the Ozmidov scale in stably stratified fluids (see Chapter 7), is given by

$$L_\varepsilon = 2 \left( \frac{\varepsilon}{\beta^3} \right)^{1/5}, \quad (2.24)$$

with corresponding wavenumber  $k_\varepsilon = L_\varepsilon^{-1}$ . Here, we note that the prefactor of 2 has been widely adopted following an analysis of numerical simulations (Galperin et al., 2008), however, estimates from an analysis of observational data from Jupiter do give slightly different values (Galperin et al., 2014). The length scale  $L_\varepsilon$  marks the threshold of the beta-effect induced anisotropisation of the inverse energy cascade.

Provided that the scales  $L_{Rh}$  and  $L_\varepsilon$  are sufficiently well separated, then it is predicted that a *zonostrophic inertial range* will develop in the interval (Galperin et al., 2008), extending the classical theories of two-dimensional turbulence to flows with a beta-effect. In this range, we might hypothesise, following the arguments used in the theory of isotropic two-dimensional turbulence, that the energy spectrum is

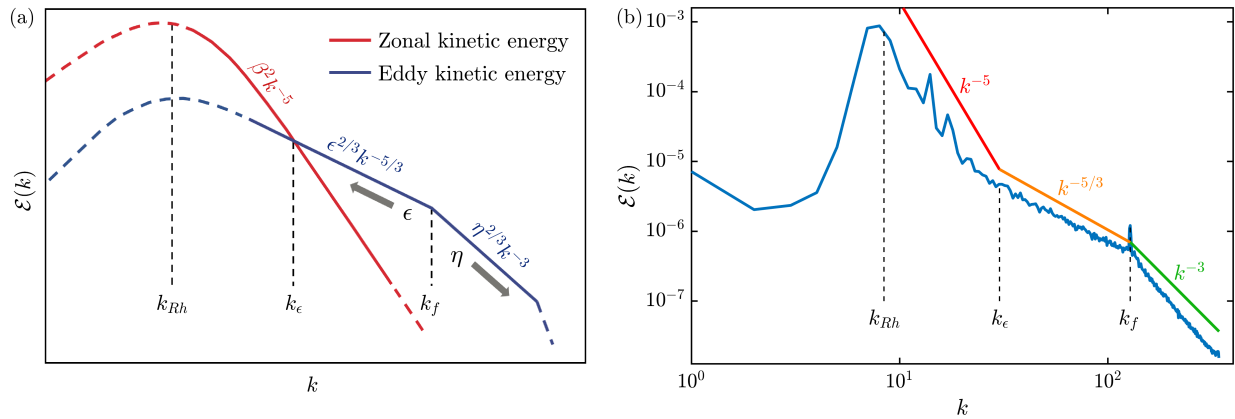


**Figure 2.5** The kinetic energy spectra,  $\mathcal{E}(k)$ , in beta-plane turbulence. Energy that is injected at wavenumber  $k_f$  isotropically cascades to larger scales, forming a  $k^{-5/3}$  spectrum, until it reaches the transitional wavenumber  $k_\epsilon$ . The energy in the zonal modes then forms a zonostrophic  $k^{-5}$  spectrum which extends as far as the Rhines wavenumber,  $k_{Rh}$ , believed to be related to the latitudinal scale of the jets. These spectra are shown using (a) an idealised illustration (adapted from Vallis, 2017) and (b) a numerical simulation using the nonlinear model described in Chapter 3, where we plot only the total kinetic energy spectra for greater visual clarity (parameters:  $\beta = 20$ ,  $\mu = 0.0005$ ,  $\varepsilon = 10^{-5}$ ,  $k_f = 128$ ,  $N = 1024$ ,  $R_\beta = 3.59$ ).

determined only by  $\beta$  and  $k$ . This results in a predicted spectrum given by:

$$\mathcal{E}(k) = C_\beta \beta^2 k^{-5}, \quad (2.25)$$

where  $C_\beta$  is a constant. Turbulence in this range is known as *zonostrophic* (Galperin et al., 2006), with most of the energy accumulated in the largest *zonal* scales, as we will argue in the next section, due to the steepness of the slope. Multiple theoretical (Chekhlov et al., 1996; Galperin et al., 2008; Huang et al., 2001) and observational (Barrado-Izagirre et al., 2009; Galperin et al., 2001, 2014; Sukoriansky et al., 2002) studies have sought to demonstrate the validity of this scaling with some success, giving weight to these theoretical arguments. A schematic illustrating the spectra from zonostrophic and two-dimensional turbulence is shown in Figure 2.5(a), whilst Figure 2.5(b) shows evidence of their existence from a numerical simulation using the nonlinear model described in Chapter 3.

### 2.3.3 Zonal jet formation mechanisms

It is important to point out that the scaling arguments just discussed do not take into account the anisotropic nature of Rossby waves that is evident from their dispersion relation (2.18), and thus by themselves do not predict the formation of zonally orientated flows. We now proceed to describe three different jet formation mechanisms, all of which are likely to be important, and where it is understood that the dominant mechanism in a particular situation will depend on the underlying parameters.

#### 2.3.3.1 Turbulent energy cascades

Continuing for the moment our discussion in spectral space, we begin by focussing on the idealised scenario in which the forcing is spatially homogeneous. Vallis and Maltrud (1993) postulated that the wave-turbulence boundary, given by  $k_\epsilon$ , should incorporate the anisotropy of the Rossby wave dispersion relation into its definition. By assuming that the turbulent part of the flow remains isotropic, they equated the characteristic frequency of turbulence,  $\omega_t = \varepsilon^{1/3} k^{2/3}$ , with the Rossby wave frequency in the absence of

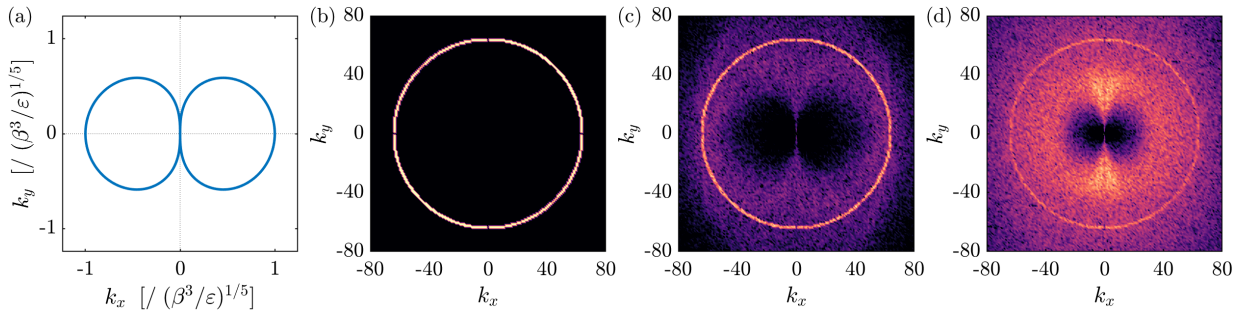


**Figure 2.6** (a) The theoretical wave-turbulence boundary,  $k_\varepsilon$ , in spectral space; (b-d) The time evolution, in spectral space, of the kinetic energy spectrum in forced-dissipative beta-plane turbulence using the nonlinear model described in Chapter 3, plotted on a logarithmic scale at times (b)  $\mu t = 0$ , (c)  $\mu t = 0.5$  and (d)  $\mu t = 4$  (parameters:  $\beta = 60$ ,  $\mu = 0.02$ ,  $\varepsilon = 10^{-5}$ ,  $k_f = 64$ ,  $N = 512$ ,  $R_\beta = 1.59$ ).

a mean flow,  $\omega_R = -\beta k_x/k^2$ , to give the expression

$$\varepsilon^{1/3} k^{2/3} = \frac{\beta k_x}{k^2}. \quad (2.26)$$

The solution,  $k_\varepsilon$ , which is plotted in Figure 2.6(a), defines the anisotropic cross-over wavenumber which can be written in terms of its zonal,  $k_{\varepsilon,x}$ , and latitudinal,  $k_{\varepsilon,y}$ , components as

$$k_{\varepsilon,x} = \left(\frac{\beta^3}{\varepsilon}\right)^{1/5} \cos^{8/5} \theta, \quad k_{\varepsilon,y} = \left(\frac{\beta^3}{\varepsilon}\right)^{1/5} \sin \theta \cos^{3/5} \theta, \quad (2.27)$$

where the polar coordinate is parameterised by  $\theta = \tan^{-1}(k_x/k_y)$ .

Physically, if we assume that the forcing wavenumber is larger than  $k_\varepsilon$ , then the injected energy will cascade via localised interactions to larger scales lying on the outside of this *dumbbell* shape, unaffected by rotation. Since the region inside the dumbbell is dominated by Rossby waves, which have a higher frequency, then the turbulent cascade preferentially excites modes which lie on the outside. The tendency of energy to seek the largest scales results in a build-up of energy close to the  $k_x = 0$  axis, reorganising the flow into the zonally-orientated flow structures (including jets) that are frequently observed.

The anisotropic dumbbell shape predicted by these analytic scaling arguments has been observed in a number of studies (Bakas and Ioannou, 2013; Vallis and Maltrud, 1993), including the models used within this thesis. Figures 2.6(b-d) demonstrate the time evolution, in Fourier space, of the kinetic energy spectrum

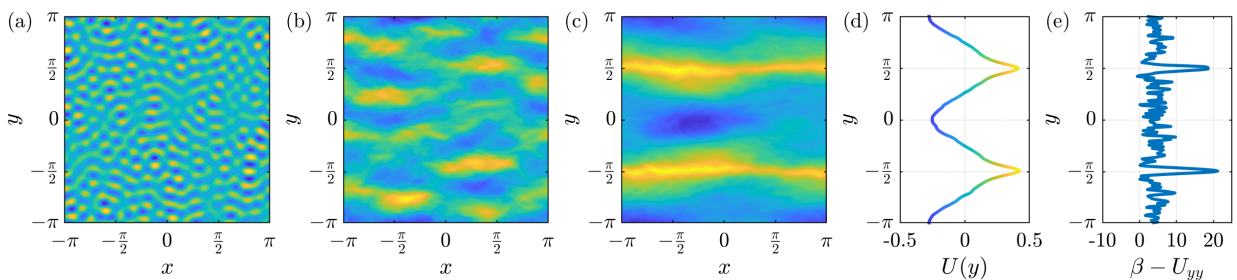


**Figure 2.7** The temporal evolution of a pair of zonal jets within a numerical simulation using the nonlinear model described in Chapter 3 showing the zonal velocity field,  $u$ , at time (a)  $\mu t = 0$ , (b)  $\mu t = 0.1$  and (c)  $\mu t = 16$ . We also plot (d) the equilibrated zonal mean zonal velocity,  $U(y)$ , and (e) the corresponding meridional potential vorticity gradient,  $\beta - U_{yy}$  (parameters:  $\beta = 5$ ,  $\mu = 0.0002$ ,  $\varepsilon = 10^{-5}$ ,  $k_f = 16$ ,  $N = 256$ ,  $R_\beta = 3.93$ ).

for a numerical simulation using the nonlinear model described in Chapter 3, where we observe that an initial narrow-band forcing spectrum implodes, creating the classic dumbbell shape with a concentration of energy in the vicinity of the  $k_x = 0$  axis. These ideas are also visible in physical space, as depicted in Figures 2.7(a-c), in which small-scale forcing drives the formation of larger scale structures which become zonally elongated prior to the formation of strong jets.

### 2.3.3.2 Potential vorticity staircases

Having a conceptual basis for expecting the emergence of zonal structures does not necessarily explain the underlying physical mechanisms involved, nor the expected equilibrated structures. A complementary approach, providing an intuitive understanding of the mechanisms of jet formation, considers a physical argument involving ideas of potential vorticity mixing. This theory was first introduced by Kuo (1951) and is clearly reviewed by Dritschel and McIntyre (2008) and Dritschel and Scott (2011).

The local homogenisation of scalar quantities over finite regions due to turbulent mixing, leading to layering and the formation of *staircases*, is a generic phenomenon in geophysical and astrophysical fluids. For example, the spontaneous layering of a stably stratified fluid in which homogeneous stirring produces an inhomogeneous layering of the background buoyancy distribution, which was first reported by Phillips (1972) and discussed further by Ruddick et al. (1989), has since become known as the *Phillips effect*. It is believed that an analogous effect, in particular the mixing of potential vorticity into a set of zonally-orientated layers or staircases, for which a positive feedback mechanism is responsible, leads to the formation and sharpening of zonal jets. Similar ideas are also mirrored in the development of other coherent structures such as vortices (Turner et al., 2009).

Figure 2.8 illustrates this mechanism for the situation in which a turbulent flow coexists with a background potential vorticity gradient. Eddies seek to mix potential vorticity, which leads to regions of higher and lower gradients. Rossby waves are weakened in mixed regions, encouraging further mixing, and conversely strengthened in regions of higher potential vorticity gradients between mixed regions, discouraging further mixing due to advection and shearing mechanisms. This leads to the large-scale potential vorticity gradient becoming weakened in some regions and sharpened in others, as shown in Figure 2.8(b), and in extreme cases the formation of a *staircase* distribution (Figure 2.8(c)), the condition for which was determined by Scott and Tissier (2012) to require  $L_{Rh}/L_\epsilon \geq 6$ . The corresponding velocity field reveals the creation and sharpening of zonal jets, with steep potential vorticity gradients being co-located with the jet core and mixed regions on the jet flanks (see Figures 2.8(d-f)). In fact, as briefly mentioned, these ideas are reflected in the Taylor identity, (2.8), in which meridional fluxes of potential vorticity lead to the formation and maintenance of mean zonal velocities.

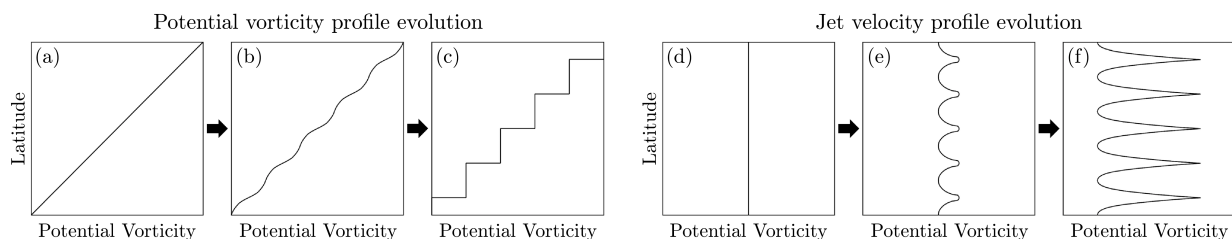


**Figure 2.8** Schematic diagrams depicting the idealistic time evolution of the zonally averaged potential vorticity field into a staircase distribution showing (a) the initial time, (b) an intermediate time, (c) the long-term equilibrium distribution. The corresponding jet velocity profiles are shown in figures (d), (e) and (f).

These ideas can be quantified analytically by considering an infinite potential vorticity staircase with latitudinal layer heights  $L$ . In the idealised limit, the distribution is piecewise continuous and is given by  $\zeta + \beta y = q_0 + n\beta L$  within a layer, such that  $nL < y < (n+1)L$  where  $n \in \mathbb{Z}$  and  $q_0$  is a constant. If we assume that the flow is predominantly zonal, i.e.  $\zeta \approx \partial u / \partial y$ , and we require the continuity of  $u$  across the layers, then we obtain parabolic solutions with sharp eastward jets and broad westward flows:

$$u \approx \frac{1}{2}\beta \left( y - \left( n + \frac{1}{2} \right) L \right)^2 + \text{constant}, \quad nL < y < (n+1)L, \quad (2.28)$$

which bear some resemblance to the zonal jets observed in nature and in numerical simulations (see Figure 2.7(d)). This asymmetry in jet structure is also predicted by the Rayleigh-Kuo stability criterion (see Vallis, 2017) which states that a necessary condition for barotropic instability is that the meridional potential vorticity gradient,  $\beta - U_{yy}$ , does not change sign within the domain, thus limiting the curvature of the westward jets. Figure 2.7(e) demonstrates these ideas numerically, in which we observe a strictly positive potential vorticity gradient, close to zero between jets and with sharp spikes aligned with the jet cores.

### 2.3.3.3 Wave-mean flow interactions

The previous two arguments discussed zonal jet formation using two complementary approaches - one in spectral space and the other in physical space. However, in both cases we assumed that the forcing was statistically homogeneous, in which case the emerging jets have no preferred latitude. This is not always the case in nature; for example, observations of the terrestrial atmosphere show that, despite its variability, the Polar jet does in fact have a preferred average location. For completeness, we feel that it is useful to briefly mention a mechanism that takes these factors into consideration.

It is well known that the production and radiation of Rossby waves can cause momentum convergence and hence the production of zonal jets. Following significant advances in the theory of wave-mean flow interactions in the 1960s and 1970s, starting from the work of Eliassen and Palm (1960) and Dickinson (1969), and later generalised by Andrews and McIntyre (1976), the transfer of angular momentum by waves was quantified in terms of a simple diagnostic: the *Eliassen-Palm (EP) flux*. This mechanism is ubiquitous in planetary atmospheres, and it is perhaps the most common of all mechanisms of jet production.

Maintaining focus on the simplest case, that of a barotropic flow on a beta plane, we can understand this mechanism by considering a disturbance that is localised in latitude. The stirring of fluid parcels excites Rossby waves which propagate away from the disturbance. Let us imagine that the waves do not interact and that each wave has the form  $\psi' = \text{Re} \tilde{\psi} e^{i(k_x x + k_y y - \omega t)}$  with dispersion relation given by equation (2.18). From (2.20), the meridional component of the group velocity is given by

$$c_{g,y} = \frac{2\beta k_x k_y}{(k_x^2 + k_y^2)^2}. \quad (2.29)$$

Since the energy flux associated with the waves travels at the group velocity, then the group velocity must be directed away from the source of the disturbance. Hence, north of the source, where  $c_{g,y} > 0$ , we see that  $k_x k_y > 0$ , while south of the source,  $c_{g,y} < 0$  implies that  $k_x k_y < 0$ . Since the zonal and latitudinal components of the velocity associated with the Rossby waves are, respectively,

$$u' = -\frac{\partial \psi'}{\partial y} = -\text{Re} \tilde{\psi} i k_y e^{i(k_x x + k_y y - \omega t)}, \quad v' = \frac{\partial \psi'}{\partial x} = \text{Re} \tilde{\psi} i k_x e^{i(k_x x + k_y y - \omega t)}, \quad (2.30)$$

this gives an eddy momentum flux (associated with the meridional component of the Eliassen-Palm flux) as

$$\overline{u'v'} = -\frac{1}{2}|\tilde{\psi}|^2 k_x k_y. \quad (2.31)$$

Consequently, north of the source the momentum flux is southward ( $\overline{u'v'} < 0$ ) and south of the source the momentum flux is northward ( $\overline{u'v'} > 0$ ) due to the relative signs of  $k_x k_y$ . This corresponds to a convergence of momentum associated with the Rossby waves towards the source of the disturbance, thereby supplying kinetic energy which produces a net eastward flow (by consideration of (2.7)). As the waves dissipate elsewhere, they deposit negative angular momentum and decelerate the flow (Andrews and McIntyre, 1976), producing weaker westward flow on the jet flanks.

### 2.3.4 The zonostrophy parameter as a measure of zonation

As we have seen, turbulent motions under the influence of rotation have a tendency to self-organise into a series of zonally-orientated flows. However, the mechanisms responsible for their formation cannot explain their long-time dynamics. As mentioned in Section 2.1, observations reveal substantially different tendencies across different systems, ranging from the latency of the oceanic jets to the robustness and quasi-steadiness of the Jovian jets. We now proceed to review some ideas which provide useful insights into expected behaviours once a system has reached a statistically steady state.

In Section 2.3.2, we saw that a forced-dissipative two-dimensional beta-plane system possesses at least two intrinsic length scales:  $L_{Rh}$ , which depends on the energy per unit mass,  $E$ , and  $L_\varepsilon$ , which depends on the energy injection rate,  $\varepsilon$ . The ratio of these two scales, termed the *zonostrophy parameter*,

$$R_\beta \equiv \frac{L_{Rh}}{L_\varepsilon} = \frac{U^{1/2} \beta^{1/10}}{2^{1/2} \varepsilon^{1/5}}, \quad (2.32)$$

may be regarded as a measure of the anisotropy of the flow, which in turn is associated with the strength of the emergent jets (Galperin et al., 2006; Sukoriansky et al., 2007). Acting as a measure of the width of the zonostrophic inertial range ( $k_{Rh}, k_\varepsilon$ ), it allows the classification of various flow regimes along with the quantisation of their thresholds. As  $R_\beta$  increases, so does the width of this range, steepening the energy spectrum as it approaches the  $\mathcal{E}(k) = C_\beta \beta^2 k^{-5}$  law. Consequently, for large  $R_\beta$ , the system equilibrates with strong, or *manifest*, zonal jets which are associated with well-defined potential vorticity staircases (Scott and Dritschel, 2012). It turns out to be the case that most of the kinetic energy is contained within the mean flow in this case, therefore the eddies are typically not strong enough to perturb the dynamics away from equilibrium, leading to very steady jets. However, when  $R_\beta$  is small, the natural variability of the system is

Environment	$\beta$ [ $m^{-1} s^{-1}$ ]	$\varepsilon$ [ $m^2 s^{-3}$ ]	$U$ [ $ms^{-1}$ ]	$L_\varepsilon$ [ $m$ ]	$L_{Rh}$ [ $m$ ]	$R_\beta$
Earth's atmosphere	$1 \times 10^{-11}$	$1 \times 10^{-4}$	15	$7 \times 10^6$	$1.1 \times 10^7$	1.6
Earth's oceans	$1 \times 10^{-11}$	$1 \times 10^{-9}$	0.1	$6 \times 10^5$	$8 \times 10^5$	1.4
Jupiter	$3 \times 10^{-12}$	$5 \times 10^{-5}$	50	$7 \times 10^6$	$4 \times 10^7$	5
Saturn	$3 \times 10^{-12}$	$1 \times 10^{-6}$	40	$6 \times 10^6$	$3.2 \times 10^7$	5.3

**Table 2.1** Estimates of key parameters in various planetary environments in which zonal jets are observed, where it is noted that there will be a certain amount of variability around these values (Galperin et al., 2019).

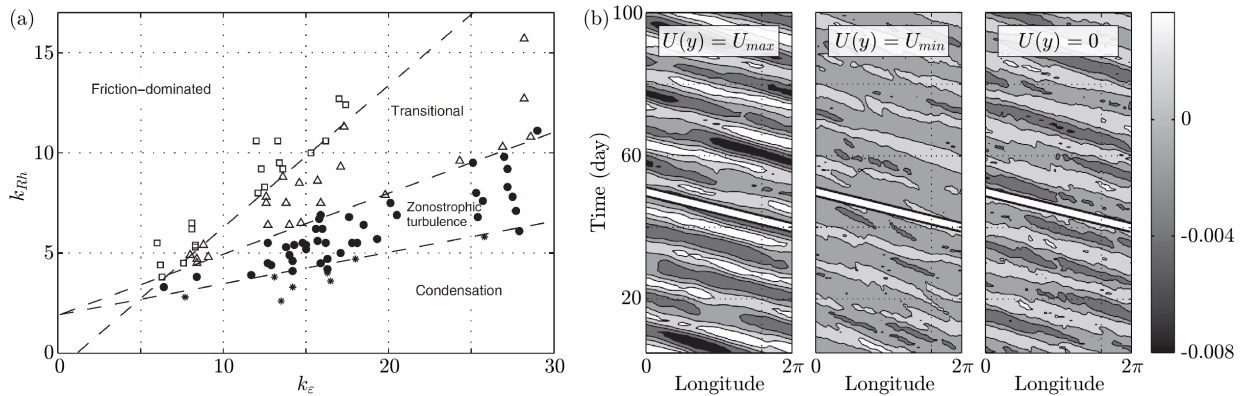


**Figure 2.9** (a) Regime diagram showing four possible flow regimes in the  $(k_{Rh}, k_e)$ -parameter space (adapted from Galperin et al., 2010); (b) Hovmöller diagrams of the stream function at three different latitudes in the zonostrophic regime corresponding to where the zonal jets have their maximum, minimum and zero velocity; the white lines show the slope of the diagrams used to calculate the velocities of the eddies (adapted from Sukoriansky et al., 2008).

dominated by the forcing and hence weak, or latent, jets form which are found to be highly unsteady. As  $R_\beta$  decreases between these limits, the time-scale separation between the evolution time of the mean flow and the eddy turnover time reduces, with the eddies playing a significantly stronger role in the resulting dynamics. Consequently, the zonostrophy parameter is a useful measure of jet variability.

Various parameter estimates are provided in Table 2.1 for planetary systems in which zonal jets have been observed. The smaller values of  $R_\beta$  relating to the terrestrial jets compared with those that have been observed in the atmospheres of the gas giant planets correlate well with observations. Indeed, the eddy-driven jets in the Earth's oceans are thought to be relatively weak or *latent* in the sense that they are no stronger than the eddies; this is in contrast with the very prominent, striking jets observed, for example, in Jupiter's atmosphere.

By analysing a series of idealised numerical simulations which had reached a statistically steady state, Galperin et al. (2006) and Sukoriansky et al. (2007) constructed a regime diagram, shown in Figure 2.9(a), identifying four distinct flow regimes delineated by the zonostrophy parameter. In the *friction-dominated regime* ( $R_\beta \lesssim 1.5$ ), the flow is nearly isotropic with the kinetic energy spectra closely following the scalings, (2.21) and (2.22), predicted for classical two-dimensional turbulence. The lack of anisotropy implies that no jets form within this regime. The *transitional regime* ( $1.5 \lesssim R_\beta \lesssim 2$ ) allows for the onset of anisotropisation, however, the zonal jets that emerge are typically only visible after averaging the flow field. The regime that is most applicable to the gas giant planets is the *zonostrophic regime* ( $R_\beta \gtrsim 2$ ), characterised by strong anisotropy and strong jets. The authors observed that the zonostrophic regime broke down in the limit of weak friction, in which energy condensed in the largest scales; they termed this the *condensation regime* (small  $k_{Rh}$ ).

Another property of the zonostrophic regime is the emergence of a new class of waves, referred to as *satellite modes* (Danilov and Gurarie, 2004) or *zonons* (Galperin et al., 2010; Sukoriansky et al., 2008, 2012). These waves are regarded as being nonlinear because their only source is nonlinear interactions. It was noted by Sukoriansky et al. (2008) that, specifically within the zonostrophic regime, certain non-zonal (but small zonal wavenumber) modes may accrue as much energy as the most energetic zonal ( $k_x = 0$ ) modes. This gave rise to the discovery of these coherent structures which will henceforth be referred to as zonons. Further analysis deduced that zonons are forced oscillations that are comprised of waves associated with a set of latitudinal wavenumbers,  $k_y$ , and a single zonal wavenumber,  $k_x$ . Only one of these waves,

with  $k_y = L$ , was found to satisfy the Rossby wave dispersion relation,  $\omega_R(k_x, L)$ , which they termed the *master* Rossby wave. The remaining *slave* waves with latitudinal wavenumbers  $k_y$  were found to share this same frequency,  $\omega(k_x, k_y) = \omega_R(k_x, L)$ , as the master waves. Accordingly, zonons are packets of long waves given by  $\mathbf{k} = (k_x, k_y)$  that share the same zonal wavenumbers,  $k_x$ , and the same zonal phase speeds,  $c_{p,x}$ .

These properties can be observed in physical space, in which zonons are manifest as westward-propagating anomalies or long waves. For example, Sukoriansky et al. (2008) plotted longitude-time plots (see Figure 2.9(b)) of the streamfunction (with the zonal mean removed) at latitudes corresponding to where the zonal jets have their maximum, minimum and zero velocity. The white lines, which have slopes given by the phase speeds of the master Rossby waves, matched the propagation speeds of the observed features, confirming that these anomalies may be associated with the zonons that appeared as spikes in the corresponding energy spectra.

Further studies have since confirmed the existence of non-zonal coherent structures (Bakas and Ioannou, 2013, 2014; Constantinou et al., 2016) with a view towards understanding their formation. However, the relevance of zonons on the long-term evolution of the flow and their role in shaping the dynamics of the zonal jets with which they coexist is still an open question.

### 2.3.5 Dynamical insights from two-layer models

In addition to the barotropic beta-plane model described in Section 2.2, there have also been a number of studies that have investigated the formation and long-time behaviours of zonal jets using two-layer models which incorporate a natural eddy-generating mechanism via baroclinic instability (thereby eliminating the need for stochastic forcing). For example, Panetta (1993) studied the long-time persistence and low-frequency variability of zonal flows within a horizontally-periodic domain, noting the importance of internal dynamics rather than externally-imposed mechanisms due to the long time scales involved. Panetta found that when the domain size is an integral multiple of the latitudinal jet scale, the jets evolve independently of each other, meandering on long time scales. In addition, jet interactions were prevalent and found to be predominantly pairwise when the domain scale was not an integral multiple of the jet scale.

Also opting for a horizontally-periodic domain such that the jets were not influenced by zonal boundary conditions, Lee (1997) chose to study these pairwise interactions by considering the transition from a persistent one-jet state to a persistent two-jet state that occurs when the latitudinal width of the baroclinically-unstable region within the domain is increased. After the transition, the two-jet state was found to be characterised by a larger fraction of kinetic energy in the zonal mean flow than that for the one jet state, resulting from a barotropic energy conversion from the eddies to the jets. It should be noted, however, that these studies have focussed on narrow parameter regimes and a full classification of zonal jet dynamics is yet to be accomplished.

## 2.4 Insights from reduced models

We now shift gear in order to spend some time reviewing an alternative type of modelling that has proven effective in studies of turbulent phenomena and which is a powerful tool in the study of zonal jets. It is widely recognised that the problem of understanding homogeneous and isotropic turbulence is one of the most difficult challenges in physics. Fortunately, the fact that many naturally occurring flows are instead anisotropic and inhomogeneous makes them more tangible in the sense that we have additional

characteristics with which to study these systems. It was recognised over a century ago by Taylor (1915) that whilst the motions of individual eddies in turbulent flows may be virtually impossible to predict, their macroscopic behaviour is relatively steady and is therefore best described using statistical approaches. In the presence of mean flows such as zonal jets, the turbulence becomes heterogeneous, providing an ideal starting point from which to develop a systematic treatment of statistical quantities. We begin this section with a review of some fundamental *reduced models* which have become popular starting points from which to study geophysical turbulence. This is followed by a discussion of some insights that have been obtained from such models regarding the formation, equilibration and finally the dynamics of zonal jets.

### 2.4.1 Statistical closure models

Geophysical and astrophysical flows evolve over a very wide range of spatial and temporal scales. Despite advances in computing, the parameter regimes of physical relevance (for example large zonostrophy in the case of the jets observed in the atmospheres of the gas giant planets) will remain out of reach by direct numerical simulations (DNS) for the foreseeable future. Consequently, mathematicians have sought to find new ways of simulating these flows such that the statistics relevant to the largest scales remain accurate whilst the smallest scales are parameterised. One such approach that has gained popularity over the last decade is called *Direct Statistical Simulation* (DSS), in which the low-order statistics of the flow are solved for directly. In addition to overcoming computational constraints, statistical approaches such as DSS are also useful for seeking physical understanding of turbulent phenomena due to their analytical capabilities, in addition to the systematic manner in which certain ingredients can be retained or eliminated.

In Section 2.3.3.1 we considered the mechanism of zonal jet formation using a spectral approach, discussing energy cascades in which, by construction, there is a local energy transfer from one wavenumber to another. Whilst in practice it is widely recognised that this does play a part in the formation and maintenance of jets, it is useful to take a step back and question the necessity of the scale-by-scale transfer of energy associated with the inverse cascade. Observational evidence suggests that a significant proportion of the turbulent momentum transfers are in fact non-local (Salyk et al., 2006), being the result of two-way interactions between eddies and the mean flow. In addition, numerical simulations suggest that zonal jets are primarily maintained by the shear-straining mechanism involving large-scale jets and small-scale eddies (Huang and Robinson, 1998; Kaspi and Flierl, 2007). These findings, together with ideas from wave-mean flow theory (see Section 2.3.3.3), have led to speculation as to whether zonal flows emerge in simplified models that are constructed such that eddy-eddy interactions are either systematically neglected or else are parameterised. The fact that they do (see Srinivasan and Young, 2012, and many others) means that the study of zonal flows lends itself very well to the application of DSS, as we shall now begin to describe.

The objective behind this approach is the derivation of a tractable set of equations that successfully describe the statistical properties of a nonlinear system. Consider such a system described by a state vector of variables  $\mathbf{q}(\mathbf{x}, t)$  satisfying the equation of motion

$$\frac{\partial \mathbf{q}}{\partial t} = \mathcal{L}[\mathbf{q}] + \mathcal{N}[\mathbf{q}, \mathbf{q}], \quad (2.33)$$

where  $\mathcal{L}$  is a linear operator and  $\mathcal{N}$  includes nonlinear terms of quadratic order. Performing a standard Reynolds decomposition of the state vector into its mean (for example zonal mean) and fluctuating parts, we obtain  $\mathbf{q} = \bar{\mathbf{q}} + \mathbf{q}'$ , satisfying the rules  $\overline{\bar{\mathbf{q}}} = \bar{\mathbf{q}}$ ,  $\overline{\mathbf{q}'} = 0$  and  $\overline{\mathbf{q}'\mathbf{q}'} = \overline{\mathbf{q}'\mathbf{q}'}$ . Upon averaging equation (2.33), we

derive the evolution equation for the mean, which we term the first cumulant:

$$\frac{\partial \bar{\mathbf{q}}}{\partial t} = \mathcal{L}[\bar{\mathbf{q}}] + \overline{\mathcal{N}[\mathbf{q}, \mathbf{q}]}.$$
 (2.34)

The second term on the right-hand side of equation (2.34), involving the evaluation of nonlocal correlations of the form  $\overline{\mathbf{q}'(\mathbf{x}_1)\mathbf{q}'(\mathbf{x}_2)}$ , which we shall term second cumulants, is an unknown quantity. Proceeding to determine equations for these second cumulants in turn introduces nonlocal cubic correlations, which we shall term third cumulants. If we continue in this fashion, we generate an infinite hierarchy of equations in which the rate of change of the  $n$ -th cumulants requires knowledge of the  $(n + 1)$ -th cumulants, which clearly has no advantage over the original formulation. The challenge, therefore, is to express one of the cumulants in terms of lower orders so that the hierarchy becomes finite; this is known as the *closure problem* (Vallis, 2017).

Several attempts have been made to truncate such sets of equations in order to formulate closed systems that accurately describe the statistical properties of nonlinear systems and which are amenable to mathematical analysis. One such approach involves truncating the equations governing the evolution of the cumulants at second order by parameterising the terms involving the third cumulant, requiring radical ad hoc simplifying assumptions (DelSole, 2004; DelSole and Farrell, 1996). Alternatively, and particularly in the context of zonal jet formation, simpler closures are usually preferred which, although physically incomplete, nevertheless capture the basic nonlinear interactions and which are capable of dealing with inhomogeneous statistics. The most popular of these involve setting the third cumulants to zero due to their simplicity and ability to recover many features of planetary circulation (O’Gorman and Schneider, 2007). Known as the *quasilinear approximation*, this has been widely used in physics for more than half a century owing to its use in making systems more accessible analytically.

#### 2.4.1.1 Second order closures and the quasilinear approximation

Marston et al. (2008) and Tobias et al. (2011) developed a system which naturally lends itself to this problem, providing a systematic way of approximating the system whilst conserving quadratic quantities such as energy and enstrophy (in the absence of forcing and dissipation). Based upon the assumption that the mean flow (first cumulant) is dominant and fluctuations about the mean flow are small, the system is perturbatively expanded in equal-time cumulants. The resulting hierarchy of equations is then truncated at order  $n$  by neglecting the  $(n + 1)$ -th and higher order cumulants in order to close system, which is subsequently known as CE $n$ . The systematic manner in which the system can be approximated makes it ideal for identifying the root causes of emerging phenomena. Closure at second order in the cumulant expansion, termed CE2, is the coarsest truncation, with the phenomenological interpretation being the removal of the interactions between eddies unless such interactions involve the mean flow. Potential vorticity is *not* materially conserved in this closure scheme, which raises questions about the necessity of potential vorticity mixing as a jet formation mechanism, nevertheless, the fact that this simplest model is capable of reproducing zonal jet formation confirms the non-necessity of eddy-eddy interactions and makes it a convenient model for further analysis (Tobias et al., 2011).

The attraction of reduced mathematical models such as CE2 is the way in which they simplify a complex, fully nonlinear system into a tractable set of equations that retain the essential features of the original system. A closely related approximation, mathematically equivalent to CE2, which has been coined

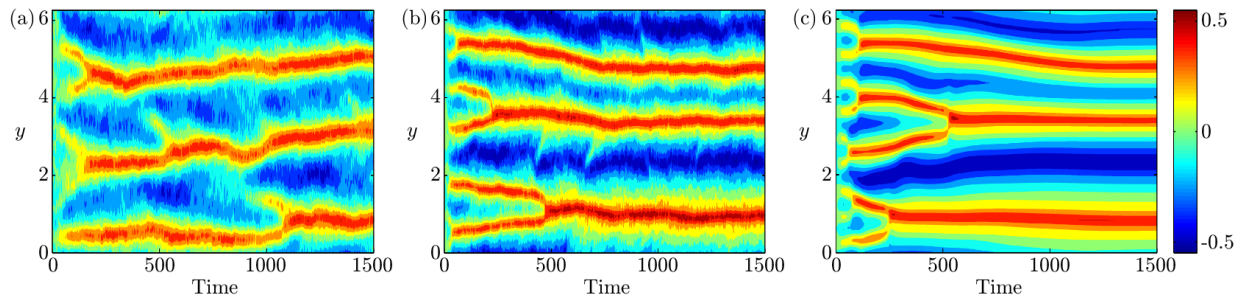


**Figure 2.10** Latitude-time plots showing the zonal mean zonal velocity field from numerical integrations of (a) a nonlinear model, (b) a quasilinear model, (c) a SSST model. Identical parameters were used in all three models in which we observe the spontaneous formation of 3 eastward jets (adapted from Constantinou et al., 2014).

stochastic structural stability theory (SSST), was developed by Farrell and Ioannou (2003, 2007). SSST is a statistical theory that succeeds in analytically deriving a closed set of equations, with the exception being that the equation of motion for the first cumulants retains a term representing the internal nonlinear noise. Just like CE2, the SSST model forms a dynamical system that captures the mean and covariance properties and which can be used to test the stability and analyse the structure of flow solutions such as zonal jets.

We note that it is also possible to employ a single-realisation formulation of the quasilinear approximation whose statistics are described by the CE2 model under certain assumptions, as demonstrated in a recent study by Srinivasan and Young (2012) who developed a *quasilinear model* of zonal jets on a two-dimensional beta-plane. Their model removes interactions between eddies directly from the original vorticity equation and in doing so, derives a closed system for a single realisation of the coupled evolution of the zonal mean flow and the eddies. The CE2 and SSST models are mathematically equivalent to this quasilinear model according to Srinivasan and Young (2012), with the additional assumption of an infinite ensemble of eddies replacing the single realisation that appears within the quasilinear model. Consequently, the CE2 and SSST systems provide a predictive theory of the dynamics of the statistical mean state whilst the quasilinear model allows for a single realisation to be simulated in which some variability is retained whilst eddy-eddy interactions are removed. Both approaches offer advantages in different situations. Thus, the quasilinear model can be viewed as an intermediate model lying between fully nonlinear models and statistical models such as CE2 and SSST. Example simulation results from all three model types (fully nonlinear, quasilinear and SSST) are shown in Figure 2.10.

#### 2.4.1.2 Higher order closures and the generalised quasilinear approximation

Whilst CE2 and SSST are formally exact in the limit of large zonostrophy, a result that was proven by Bouchet et al. (2013), second order truncations become less effective as the zonostrophy decreases. This was demonstrated by Tobias and Marston (2013) in which comparisons were made between the statistics derived from fully nonlinear DNS and CE2, showing that CE2 fails to reproduce the number and strength of the jets and the structure of the second cumulant as  $R_\beta$  becomes small. One approach to resolving these issues is to adopt higher order truncations which include *some* eddy-eddy interactions. Marston et al. (2019) investigated the inclusion of higher order corrections by truncating the hierarchy of cumulants at third (CE3) order and an intermediate (CE2.5) order (in which only some of the terms in the equations for the third cumulants are retained), noting that both of these systematically improve the qualitative agreement in the statistics of weaker jets. The downside is that these schemes have a significantly higher computational

cost and they cannot be implemented as single realisations, as is the case with second order closures and the quasilinear approximation.

It has been argued (Marston et al., 2016) that a better approach instead involves generalising the original quasilinear approximation so that it still supports a single-realisation formulation but also lays the groundwork for a new statistical approach. In an attempt to construct a new method of improving the accuracy of predicted jet statistics for weaker jets, Marston et al. (2016) developed the Generalised Quasilinear (GQL) approximation. Rather than performing a standard Reynolds decomposition on the state vector of variables  $\mathbf{q}(\mathbf{x}, t)$  into its mean and fluctuations, this decomposition is generalised by separating the state variables into large and small scales (termed low and high modes) via a spectral filter (see Chapter 5). The standard quasilinear (or second-order closure) approximation would then be equivalent to retaining just the zeroth mode in the low modes. Equations of motion for the statistics are then derived as before, with truncation at second order forming a closed system. This allows fully nonlinear interactions between the largest scales of motion, but, more importantly, the small-scale eddies can now exchange energy through their interaction with the large scales, thereby redistributing energy to all scales via a *scattering* mechanism. GQL provides a systematic way of improving CE2 by bridging the gap between quasilinear and exact nonlinear dynamics and has been shown to significantly improve the statistics by the retention of just one additional wavenumber in the low modes.

The additional advantage of using a generalised quasilinear scheme is that, by allowing the largest scales to nonlinearly interact, zonons can be captured. This was the motivation which inspired Constantinou et al. (2016) to extend the SSST framework using an approach similar to one described above. They developed a statistical theory for the coexistence of jets and large scale waves by separating these largest scales (which they termed coherent motions) from the smaller-scale motions that constitute the incoherent component. The inclusion of zonons in their model revealed how these large-scale waves can tap into the energy of the jets, thereby acting as a destabilising mechanism during jet formation and providing the first insights into the role that zonons play in planetary turbulence.

### 2.4.2 Zonostrophic instability

With these models in our toolbox, we now return to thinking about the dynamics of planetary scale zonal flows. A variety of mechanisms have already been discussed which attempt to explain the spontaneous emergence of zonal jets (see Section 2.3.3). Here, we describe a different perspective, invoking insights that have been obtained from reduced models.

It has been shown that the laminar stability of zonally varying meridional flows on a beta-plane are unstable to random initial perturbations which reorganise the flow into a series of zonally orientated jets (Connaughton et al., 2010; Manfroi and Young, 1999). This is known as modulational instability, which is ubiquitous in nature, and offers one route to zonal jet formation. Nevertheless, planetary atmospheres and oceans are turbulent fluids, comprised of a broad spectrum of waves. Consequently, a number of studies have sought to demonstrate that zonation can be understood as a symmetry-breaking bifurcation of an isotropic, homogeneous beta-plane flow, which is now understood to be a generalisation of modulational instability (Bakas et al., 2015; Parker and Krommes, 2013).

A stationary state of beta-plane flow is that of a homogenous, isotropic, turbulent state in which there are no jets. Farrell and Ioannou (2007) used the SSST model to investigate the linear stability of this state, finding it to be unstable for sufficiently strong turbulence. In addition, an analysis of the structure

of the subsequent zonal jet formation revealed that for weak forcing, the latitudinal scale of the jets was determined by the most unstable linear mode in the system, however, stronger forcing caused the jets to adjust in structure until they reached their most stable latitudinal wavenumber, approximated by the Rhines scale. These findings helped to confirm that jets initially arise as a linear instability of an infinitesimal jet perturbation, while finite amplitude jets are the result of nonlinear equilibria developing from these linear instabilities.

Srinivasan and Young (2012) continued the study of this initial symmetry-breaking bifurcation, which they termed *zonostrophic instability*. They used the CE2 model to derive analytical expressions for the growth rates of the most unstable linear modes, with findings being broadly in agreement with those from the earlier work by Farrell and Ioannou (2007). It was subsequently noted by Constantinou et al. (2014) that quantitative differences in the predicted location of the jet formation bifurcation exist between second order statistical closure models, the quasilinear model and the fully nonlinear model. These differences were found to be due to a modification of the turbulence spectrum in the nonlinear model resulting from the formation of coherent non-zonal structures, i.e. zonons, providing some of the first insights that these long waves play in zonostrophic turbulence. Nevertheless, the fact that these reduced models replicate at least some of the essential physics of zonal flow formation demonstrates their utility for further analysis.

### 2.4.3 Zonostrophic saturation

Thinking beyond the initial stages of the instability, an important finding by Farrell and Ioannou (2007) demonstrated that, once a statistically steady state has been reached, SSST can exhibit non-unique solutions, where the number of jets in the steady state depends on the initial conditions. Parker and Krommes (2013) later proved this result with their analogy between zonal jet formation and the dynamics of pattern formation. They extended the previous instability analyses with a weakly nonlinear analysis about the zonostrophic instability threshold, revealing an amplitude equation for the resulting zonal flow (the real Ginzburg-Landau equation). Motivated by the way in which zonal flows *saturate* into a steady state, they revealed behaviours such as the existence of multiple solutions with different latitudinal scales and the phenomenon of jets merging to reach a stable solution, features which have been observed in direct numerical simulations.

Whilst numerical simulation can be insightful, a longstanding challenge in the study of turbulent flows is the theoretical prediction of equilibrated states, such as the velocity profiles of zonal flows and the eddy momentum fluxes driving these flows. Srinivasan and Young (2014) considered the problem of predicting the eddy momentum flux convergence analytically for a stochastically-forced, linearised beta-plane flow with a background mean shear (a Couette flow) along with the assumption of a spatially homogeneous steady solution. The forcing was homogeneous but anisotropic, with eddies elongated either zonally or latitudinally (with the motivation being that the physical processes parameterised by the forcing, such as baroclinic instability in the ocean, are typically not isotropic). On assuming that the statistical properties of the solution are spatially homogeneous, explicit analytic results for the eddy momentum flux were derived. Findings showed that for eddies elongated latitudinally, the eddy momentum flux has an antifrictional effect (energy is transferred from small to large scales), while for eddies elongated zonally, the reverse is true.

For the case of coherent structures in two-dimensional flows, the first theoretical predictions of the profiles of large-scale turbulent vortices and associated eddy momentum fluxes were derived by Laurie et al. (2014) which agreed well with numerical simulations. Woillez and Bouchet (2017) went a step further by investigating the situation with zonal jets. In an equivalent manner to Srinivasan and Young (2014), they

used the quasilinear approximation and exploited the large time-scale separation between the evolution of the mean flow and the eddies by choosing to treat the zonal mean flow (first cumulant) as temporally constant in the evolution equation for the eddies. In the limit of small amplitude forcing and weak friction, they were able to derive an equation for this stationary profile of the zonal mean flow, along with the eddy momentum flux. The solution was not fully satisfactory, however, since it predicted diverging profiles at the jet extrema which they argued should be regularised by a cusp at the eastward jet maxima and a parabolic profile at the westward jet minima. These results are the first known computations of eddy momentum fluxes and self-consistent velocity profiles for zonal jets from turbulent dynamics; clearly there is scope to improve upon the current solutions.

#### 2.4.4 Zonal jet dynamics: fluctuations and rare events

Despite the lively discussions that have taken place over the last few decades concerning the formation and structure of zonal flows, the problem of characterising their fluctuations or dynamical behaviours has received much less attention in the theoretical literature, with the few existing studies focussing on the probabilities associated with fluctuations rather than associated mechanisms.

Bouchet et al. (2013, 2014) took some of the first steps towards understanding zonal jet fluctuations with their construction of a kinetic theory of zonal jet dynamics, in which the study of microscopic behaviours permits the deduction of macroscopic properties. Using slightly different terminology to that already defined in this thesis, they identified a small parameter in the system to be  $\alpha = R\beta^{-5}$  (Bouchet and Simonnet, 2009; Bouchet and Venaille, 2012), in which  $\alpha \ll 1$  corresponds to a divergence in time scales between the slow evolution of the jet and the rapid evolution of the small scale eddies. Using ideas from kinetic theory, they perturbatively expanded the system around  $\alpha$ , going beyond classical statistical closure schemes by formulating a closed quasilinear system describing both the spatial structure of the covariance of the noise and the resulting variance of the jet velocity profile. The resulting formulation, comprising an equation governing the slow evolution of the velocity profile,  $U(y)$ , which gives an effective description of zonal jet dynamics, is able to describe the relaxation towards and typical fluctuations around zonal jet attractors.

As is sometimes observed in physical systems, large fluctuations can sometimes lead to abrupt changes, such as spontaneous transitions between  $n$  and  $n + 1$  jets ( $n \in \mathbb{N}$ ) via jet mergers and nucleations. For large zonostrophy, or correspondingly small  $\alpha$ , such events are sometimes called *rare transitions* because the system has a tendency to remain in one attractor for a very long time compared with other time scales such as the dissipative time scale. Rare events can be very challenging to study directly using numerical simulations, and the kinetic theory developed by Bouchet et al. (2013) is not able to describe them. Instead, Bouchet et al. (2018) investigated the probabilities of arbitrarily large fluctuations associated with the eddy momentum flux convergence in zonal jet dynamics using large deviation theory (LDT) (see Bouchet et al., 2016, for a more rigorous introduction). They developed theoretical and numerical tools with which to calculate the probabilities associated with fluctuations in the eddy momentum flux, opening up the possibility of studying rare transitions between attractors in turbulent flows. Consequently, the probability density functions for the eddy momentum flux convergence were computed for the first time (see Figure 2.11), showing that both quasilinear and fully nonlinear dynamics have exponential tails, with greater variance associated with quasilinear dynamics.

In extreme cases where it is virtually impossible to collect statistics for these rare events using direct numerical simulations, other numerical methods such as the Adaptive Multilevel Splitting (AMS) algorithm

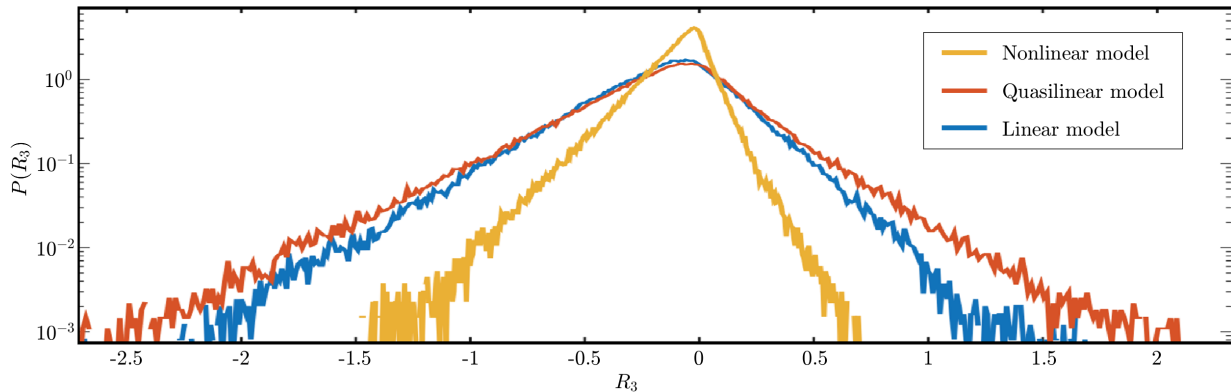


**Figure 2.11** Probability density functions of  $R_3$ , the third component in the spherical harmonics decomposition of the eddy momentum flux convergence, from direct numerical simulations of the fully nonlinear barotropic beta-plane vorticity equation (yellow), the quasilinear vorticity equation (orange) and a linear system in which  $U(y)$  is held fixed (blue) (adapted from Bouchet et al., 2018).

(see, for example, Cérou et al., 2019; Rolland and Simonnet, 2015) have been employed with some success. The recent development and application of such methods have allowed for the estimation of quantities such as the probability of transitions between different configurations, but also, and crucially, they offer insights into the typical paths of such transitions (Bouchet et al., 2019), opening up additional possibilities for the exploration of the associated dynamics.

## 2.5 Research questions

As we have seen, there has been much discussion over the last few decades regarding mechanisms governing the formation and maintenance of zonal jets, with theories ranging from anisotropic inverse cascades to phenomenological arguments involving ideas of potential vorticity mixing and finally instability mechanisms of turbulent states. Simplified models such as the turbulent beta-plane model have formed the basis of many of these theories, retaining only the essential ingredients necessary for the spontaneous formation and equilibration of persistent zonal jets. However, the equilibrated jets are not steady and the nature of the time variability in the equilibrated phase is of interest both because of its relevance to the behaviour of naturally occurring jet streams and for the insights it provides into the dynamical mechanisms operating in these systems.

Due to the significant role that zonal jets play in the climate system, their time variability is a topic of great interest. However, their fundamental properties and the physical mechanisms governing their dynamics are not well understood. These include questions relating to the dynamical equivalence of single and multiple-jet regimes and the interactions between jets and eddies. In addition, there are questions relating to jet strengths, as defined by the zonostrophy parameter, in particular whether latent and manifest jets share similar characteristics. As we have seen (for example in Figures 2.2 and 2.10), observations and simulations reveal a variety of behaviours, including low-frequency fluctuations, or wandering behaviour, transitions between persistent  $n$ - and  $(n + 1)$ -jet states via mergers and nucleations, and the poleward propagation of zonal mean flow anomalies. However, these behaviours differ substantially between different planetary systems and the reasons for these differences are not clear.

Of course, there are various broader motivations for gaining an understanding of the fundamental physics of zonal jet variability. For example, parameterisations in non-eddy-resolving general circulation

models (GCMs) need to capture the effects of the important interactions between jets and eddies and, alongside this, it is important to understand which flow features must be measured in order to test the accuracy of these parameterisations. In addition, there continues to be association of the signal-to-noise paradox (that climate models are better at predicting observations than themselves) in seasonal forecasting with the characteristic of many models to simulate variability with memory time that is too short and alongside that to fail to capture eddy-mean flow feedbacks (see e.g. Scaife et al., 2019). This aspect of climate models may improve at very high resolution, which leaves open the question of exactly what physical mechanisms are not being captured when the models are run at lower resolution.

The novelty in the first part of this thesis, therefore, is to take some steps towards understanding fundamental aspects of jet variability within the context of barotropic beta-plane models, arguably the simplest systems which exhibit the relevant variability. With the help of additional reduced formulations, which provide a natural framework for studying variability due to the way in which their complexity can be systematically varied, we seek an understanding of the minimal ingredients required for different types of jet variability. For example, the quasilinear model derived by Srinivasan and Young (2012) allows for the spontaneous formation and equilibration of fluctuating zonal jets, and is therefore instructive as an indication of the role that nonlinear interactions between eddies play in permitting, or not permitting, different physical processes relevant to zonation.

In Chapter 4, we study zonal jet variability side-by-side using a fully nonlinear model and a quasilinear version (both of which are formulated theoretically and numerically in Chapter 3), comparing and contrasting the dynamical behaviour in order to examine the role of eddy-eddy interactions. A thorough categorisation of the zoology of different types of variability has never, to our knowledge, been documented before, therefore this forms the objective of our initial investigations. Our primary focus is the zonostrophic regime defined by Galperin et al. (2008) in which robust, persistent jets naturally develop alongside other coherent structures such as zonons.

Our study proceeds in Chapter 5 by further investigating features which are not captured using quasilinear dynamics, in particular a new type of zonal jet variability. A natural choice for further investigation is a single-realisation version of the generalised quasilinear formulation described by Marston et al. (2016). By systematically restoring *some* eddy-eddy interactions to the quasilinear model, we seek to understand the mechanisms which are essential for certain aspects of variability, with a view towards formulating some insights which may be applicable in more complex, geophysically-relevant systems.

It has also been observed that second order statistical closure models such as CE2 and SSST exhibit zonal flows that can merge and reach statistically steady states, demonstrating that these models possess some of the interesting and relevant nonlinear behaviour. Consequently, we finish our study of zonal jet variability in Chapter 6 by investigating the statistical properties of regimes that are identified in earlier chapters. As predicted, the elimination of eddy-eddy interactions restricts the dynamical behaviour in line with observations from its single-realisation counterpart, the quasilinear model, nevertheless, some additional insights can be illuminated by the neglect of certain aspects of random fluctuations.

## Chapter 3

# A mathematical model of beta-plane turbulence

### 3.1 Introduction

From a theoretical viewpoint, the advantages of using idealised, simplified models of geophysical phenomena are the facility to retain and study only the essential physics inherent within a system. In this chapter, we describe the mathematical models that will form the basis of our study of zonal jet variability. We begin with a description of a fully nonlinear model, arguably the simplest system in which the spontaneously emerging jets exhibit behaviour that is relevant to planetary scale flows. This is followed by the introduction of a quasilinear formulation in which eddy-eddy interactions are excluded. Both of these models form the basis of a numerical study of zonal jet dynamics, therefore we proceed by describing their numerical formulation and discretisation. Finally, we discuss parameter choices and provide numerical verifications of key assumptions that will be used in later chapters.

### 3.2 Mathematical formulation

#### 3.2.1 Nonlinear (NL) mathematical model

Exploiting the quasi-two-dimensional nature of large-scale geophysical flows and an assumed small Rossby number, we adopt the modelling framework described in Section 2.2. Specifically, we use a quasi-geostrophic approximation and consider the limit in which the characteristic scales of motion are much smaller than the Rossby radius of deformation,  $L_d$ . This simplifies the study to the dynamics of a barotropic flow on a beta-plane with potential vorticity  $q = \zeta + f$ , Coriolis parameter  $f = f_0 + \beta y$ , and a constant background gradient of potential vorticity  $\beta$ .

We artificially force an idealisation of two-dimensional turbulence via a stochastic vorticity forcing function  $\xi(\mathbf{x}, t)$ , assumed to be a random function of both space and time, in which energy is injected homogeneously and isotropically at a constant rate  $\varepsilon$  (see Section 3.2.3). As discussed in Section 2.3.2, energy has a tendency to transfer to larger scales in two-dimensional turbulence, while enstrophy has a tendency to transfer to smaller scales. Consequently, energy is predominantly dissipated at the largest spatial scales using linear damping with rate  $\mu$ , modelling, for example, Ekman friction in planetary atmospheres. In addition, the build-up of enstrophy at the smallest scales is removed using hyperviscosity of order  $n$

and rate  $\nu_n$ , where  $n \in \mathbb{N}$ . Doubly periodic geometry is imposed on a square domain of size  $L_D$  such that  $(x, y) \in [0, 2\pi L_D) \times [0, 2\pi L_D)$  in order to select the simplest possible boundary conditions. Incorporating these choices, the two-dimensional beta-plane vorticity equation (2.5) becomes

$$\frac{\partial \zeta}{\partial t} + J(\psi, \zeta) + \beta \frac{\partial \psi}{\partial x} = \xi - \mu \zeta + \nu_n \nabla^{2n} \zeta, \quad (3.1)$$

for relative vorticity  $\zeta = \nabla^2 \psi$  and corresponding velocity field  $(u, v) = (-\partial_y \psi, \partial_x \psi)$ .

The entire dynamics governing the evolution of the flow are encapsulated in this equation, which can be re-expressed using a single variable,  $\psi$  or  $\zeta$ . This model, which will henceforth be referred to as the *nonlinear* (NL) model, permits *all* interactions between eddies. We mention that when  $\xi$  is specified to be statistically homogeneous, equation (3.1) admits the latitudinal symmetry

$$(t, x, y, \psi, \zeta) \mapsto (t, x, -y, -\psi, -\zeta), \quad (3.2)$$

however, there are no zonal or time-reversal symmetries in the presence of dissipation.

As before, we seek an equation governing the evolution of the zonally averaged zonal velocity. By applying a Reynolds decomposition to each variable, such as the streamfunction,

$$\psi(x, y, t) = \bar{\psi}(y, t) + \psi'(x, y, t), \quad (3.3)$$

in which the overbar denotes a zonal mean and the prime denotes fluctuations away from the mean, and following the steps described in Section 2.2, we derive the evolution equation for the jet velocity profile,

$$\frac{\partial U}{\partial t} + \frac{\partial}{\partial y} (\overline{u'v'}) = -\mu U + \nu_n \frac{\partial^{2n}}{\partial^{2n} y} U. \quad (3.4)$$

Here, we have assumed that  $\bar{\xi} = 0$  since  $\xi$  is prescribed to be spatially homogeneous in a statistical sense, and we choose to write  $U(y, t) = \bar{u}(y, t)$  as before for convenience. In planetary flows, viscosity is often negligible in the global energy balance. Thus, in the inviscid limit ( $\nu_n \rightarrow 0$ ), the diffusion term on the right hand side is negligible, leading to steady state solutions given by  $U(y) \approx -\mu^{-1} \partial_y (\overline{u'v'})$ .

An equation governing the evolution of the total kinetic energy per unit mass,  $E = \frac{1}{2} \langle |\nabla \psi|^2 \rangle$ , can be derived by multiplying the vorticity equation (3.1) by the streamfunction,  $\psi$ , and computing a volume average, denoted by  $\langle \bullet \rangle$ , over the periodic domain. This equation is given by

$$\frac{dE}{dt} = -\langle \psi \xi \rangle - 2\mu E - \nu_n \langle |\nabla^{n-1} \zeta|^2 \rangle, \quad (3.5)$$

where the energy injection rate by the forcing is  $\varepsilon = -\langle \psi \xi \rangle$ . In practice,  $\varepsilon$  shall be regarded as an externally imposed constant, with justification given in Section 3.3.2. In the inviscid limit, changes in the total kinetic energy are balanced by the forcing and the large-scale energy dissipation:

$$\frac{dE}{dt} = \varepsilon - 2\mu E. \quad (3.6)$$

Thus, for solutions which have reached a statistically steady state, we see that

$$E = \frac{\varepsilon}{2\mu} \quad (3.7)$$

in this limit, giving a convenient expression for the total kinetic energy density, or equivalently the root mean square velocity, in terms of the model parameters. This assumption of negligible viscosity is useful because it enables, for example, the Rhines scale and the zonostrophy parameter, given by expressions (2.23) and (2.32) respectively, to be written entirely in terms of external parameters.

Using the notation  $[\bullet]$  to indicate dimensions, the set of externally defined parameters which govern the dynamics in this system include:

$$[\varepsilon] \sim L^2 T^{-3}, \quad [\beta] \sim L^{-1} T^{-1}, \quad [\mu] \sim T^{-1}, \quad (3.8)$$

along with two externally imposed length scales,  $k_f^{-1}$  and  $L_D$ , associated with the respective scales of the forcing and the domain. Systems that are damped by large-scale drag are associated with a frictional scale,  $L_{fr} = U/\mu$ , defined as the length scale at which the characteristic friction time is equal to that of the flow (noting that  $L_{fr} = 4(L_{Rh}/L_\varepsilon)^5 \gg 1$  in the zonostrophic regime). This means that, together with the Rhines scale,  $L_{Rh}$ , and the cross-over scale between wave and turbulence-dominated regimes,  $L_\varepsilon$ , both of which were introduced in Section 2.3.2, the system is associated with at least five different length scales:

$$k_f^{-1}, \quad L_D, \quad L_{Rh} = \frac{2^{1/2} \varepsilon^{1/4}}{\beta^{1/2} \mu^{1/4}}, \quad L_\varepsilon = 2 \left( \frac{\varepsilon}{\beta^3} \right)^{1/5}, \quad L_{fr} = \left( \frac{\varepsilon}{\mu^3} \right)^{1/2}, \quad (3.9)$$

where we note that the characteristic velocity,  $U$ , has been re-written using equation (3.7). As mentioned in Section 2.3.4, the zonostrophy parameter is often used as a measure of the strength of the emergent zonal jet solutions. With the assumption of negligible viscosity, it is a pre-defined, dimensionless parameter:

$$R_\beta = \frac{\varepsilon^{1/20} \beta^{1/10}}{2^{1/2} \mu^{1/4}}. \quad (3.10)$$

Another convenient measure of the strength of zonal jets relative to the fluctuating eddy field was defined by Srinivasan and Young (2012). Termed the zonal mean flow index,  $\text{zmf}(t)$ , it is also a dimensionless quantity, equal to the fraction of the total kinetic energy that is distributed in the zonal mean zonal flow,

$$\text{zmf}(t) = \frac{\langle |\nabla \psi| \rangle^2}{\langle |\nabla \psi|^2 \rangle}, \quad (3.11)$$

with time-average denoted by  $\text{zmf}$ . Henceforth referred to as the  $\text{zmf}$  index, this diagnostic also represents a ratio of dissipation rates, since energy that is injected into the system by the forcing subsequently flows into, and is dissipated from, the mean flow and the eddies according to the forcing balance (3.5). As we will demonstrate, both the zonostrophy parameter and the  $\text{zmf}$  index turn out to be systematically related to jet variability and will be discussed throughout this thesis.

### 3.2.2 Quasilinear (QL) approximation

In our quest for a mathematically tractable, or at least the simplest possible, model of zonal jets, we adopt the methodology of Srinivasan and Young (2012) in our formulation of a reduced model, which we shall refer to as the *quasilinear* (QL) model. The quasilinear approximation has been widely used in previous studies of turbulent motions, owing to its utility in the derivation of analytical theories governing the

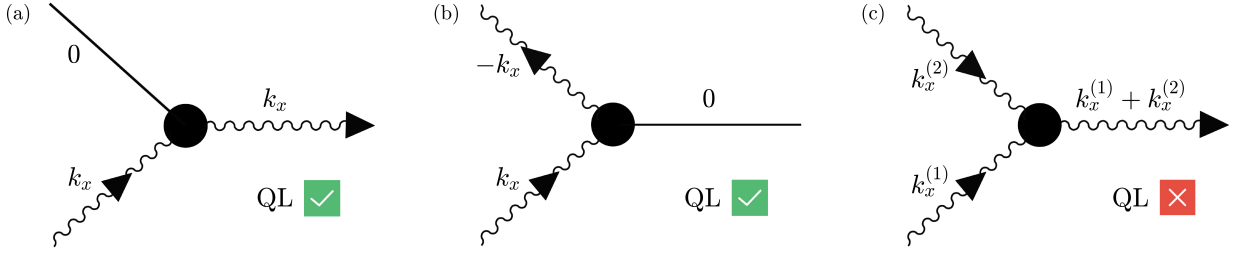


**Figure 3.1** Illustrations of the possible interactions between zonal eddies and the zonal mean flow in the fully nonlinear system. Note that only (a) and (b) are possible in the quasilinear system. (a) Wave-mean flow interaction: an eddy of zonal wavenumber  $k_x$  interacts with the zonal mean flow (wavenumber 0) to produce an eddy of zonal wavenumber  $k_x$ . (b) Reynolds stress on the zonal mean flow: two waves of equal but opposite wavenumbers  $k_x$  and  $-k_x$  interact, leaving the zonal mean flow (wavenumber 0). (c) General interaction between two waves of wavenumbers  $k_x^{(1)}$  and  $k_x^{(2)}$  to give a new wave of wavenumber  $k_x^{(1)} + k_x^{(2)}$ . Inspiration for the figures came from Marston et al. (2019).

interactions between waves and mean flows. At the most fundamental level, it is instructive with respect to the exploration of the relevant physical mechanisms associated with zonal flows.

To begin, we apply an eddy-zonal mean decomposition (denoted by a prime and overbar respectively) to the streamfunction, as demonstrated in equation (3.3), with corresponding decompositions of the other variables. Applying this decomposition to the variables in the NL vorticity equation (3.1) and taking a zonal average, we derive respectively the zonal mean vorticity equation and the eddy vorticity equation:

$$\frac{\partial \bar{\zeta}}{\partial t} + \frac{\partial}{\partial y} (\overline{v' \zeta'}) = -\mu \bar{\zeta} + \nu_n \frac{\partial^{2n} \bar{\zeta}}{\partial y^{2n}}, \quad (3.12)$$

$$\frac{\partial \zeta'}{\partial t} - \frac{\partial \bar{\psi}}{\partial y} \frac{\partial \zeta'}{\partial x} + \left( \beta + \frac{\partial \bar{\zeta}}{\partial y} \right) \frac{\partial \psi'}{\partial x} + \left[ \frac{\partial \psi'}{\partial x} \frac{\partial \zeta'}{\partial y} - \frac{\partial \psi'}{\partial y} \frac{\partial \zeta'}{\partial x} - \frac{\partial}{\partial y} \left( \frac{\partial \psi'}{\partial x} \zeta' \right) \right] = \xi - \mu \zeta' + \nu_n \nabla^{2n} \zeta'. \quad (3.13)$$

The QL model is then obtained by defining the terms inside the square brackets in equation (3.13) to be zero, leaving a quasilinear partial differential equation.

Following earlier comments, this is consistent with the removal of eddy-eddy interactions, whilst retaining the coupling between the mean flow and the eddies, as can be seen in equation (3.12) where the eddy momentum flux convergence,  $\partial_y (\overline{v' \zeta'})$ , interacts with the large-scale mean flow. Figure 3.1 illustrates these ideas, showing all possible interactions in the fully nonlinear system. Only interactions shown in Figures 3.1(a) and 3.1(b) are possible under the quasilinear approximation, leading Tobias et al. (2011) to describe the QL model as an approximation to the NL model.

Provided that ergodicity in the zonal direction is assumed such that a zonal average is equivalent to an ensemble average, the QL model is mathematically equivalent to the CE2 system (see Chapter 6 for further discussion). However, an advantage to studying this single realisation formulation over CE2 is that, rather than working with equations governing the evolution of statistical quantities, the quasilinear approximation can be incorporated directly inside the original NL vorticity equation, thereby retaining aspects of the variability of the flow which can be simulated using DNS. The quantities inside the square brackets in equation (3.13) were called the *eddy-eddy nonlinearity* (EENL) terms by Srinivasan and Young (2012). Adopting this convention here, the QL beta-plane vorticity equation is

$$\frac{\partial \zeta}{\partial t} + J(\psi, \zeta) + \beta \frac{\partial \psi}{\partial x} - \text{EENL} = \xi - \mu \zeta + \nu_n \nabla^{2n} \zeta, \quad (3.14)$$

which, as before, is a single equation encapsulating the entire dynamics. In the absence of forcing and dissipation, the QL model respects the conservation of energy and enstrophy that was demonstrated for the NL model in Section 2.2, however, it should be noted that it destroys the exact material conservation of potential vorticity. Both the NL and QL vorticity equations can be solved alongside the elliptic equation,  $\zeta = \nabla^2 \psi$ , subject to the prescription of the vorticity forcing  $\xi$ .

### 3.2.3 A simple model of turbulence forcing

In contrast to three-dimensional stratified environments where baroclinic instabilities or convection can occur, there is no natural generation mechanism for turbulence in two-dimensional configurations. Consequently, it is conventional to parameterise the effects of small-scale eddies acting on a barotropic flow. A common choice, which we shall adopt here, excites an idealisation of two-dimensional turbulence using a rapidly decorrelating, spatially homogeneous, stochastic force which is assumed to be a random function of both space and time. In particular, energy and enstrophy are typically injected into a narrow band of wavenumbers in Fourier space. This choice of forcing was first used by Lilly (1969) and has since become a standard convention in many studies of forced-dissipative, two-dimensional models of zonal jets. Williams (1978) considered a spatial distribution in which the forced wavenumbers lie in a narrow rectangular band, however, we follow the example of Scott and Polvani (2007), choosing instead to impose an isotropic distribution with a well-defined forcing wavenumber  $k_f$ .

Ensuring that zonal flows arise spontaneously rather than being directly forced, we choose to stir the fluid in both the NL and QL models using a stochastic vorticity force  $\xi(x, y, t)$  with zero mean,  $\langle \xi(\mathbf{x}, t) \rangle = 0$ , and a two-point, two-time correlation function described by  $\Xi$ ,

$$\langle \xi(\mathbf{x}_1, t_1) \xi(\mathbf{x}_2, t_2) \rangle = \Xi(\mathbf{x}_1, \mathbf{x}_2, t_2 - t_1), \quad (3.15)$$

where the angular brackets here denote an ensemble average. This forcing is associated with a decorrelation time  $\tau_f$  in which the limit  $\tau_f \rightarrow 0$  corresponds to white noise,  $\tau_f \rightarrow \infty$  corresponds to steady forcing, and finite (but non-zero)  $\tau_f$  corresponds to red noise. Motivated by topographic excitations, Scott and Tissier (2012) implemented red noise forcing in which the decorrelation time was equal to the inverse Rossby wave frequency of the forcing wavenumber. Using this approach, the forcing was implemented as a time-varying topography in which the forcing and the system maintain a correlation, leading to a unsteady rate of energy injection into the system. Preferring a steady rate of energy injection, we follow the example of many before us (Constantinou et al., 2014; Srinivasan and Young, 2012, and many others) by opting for a simpler approach. We shall consider the white noise limit in which the forcing and the system are uncorrelated. Within this approximation, the correlation function becomes delta-correlated in time:

$$\langle \xi(\mathbf{x}_1, t_1) \xi(\mathbf{x}_2, t_2) \rangle = \Xi(\mathbf{x}_1, \mathbf{x}_2) \delta(t_2 - t_1). \quad (3.16)$$

As a further idealisation, we shall restrict attention to spatially homogeneous and isotropic forcing distributions such that  $\Xi$  depends only on the two-point separation distance

$$r = |\mathbf{x}_1 - \mathbf{x}_2| = \sqrt{(x_1 - x_2)^2 + (y_1 - y_2)^2}. \quad (3.17)$$

Consequently, the correlation functions considered in this study will take the form

$$\langle \xi(\mathbf{x}_1, t_1) \xi(\mathbf{x}_2, t_2) \rangle = \Xi(r) \delta(t_2 - t_1), \quad (3.18)$$

where  $\Xi(r)$  is related to its Fourier modes,  $\tilde{\Xi}(k)$ , according to the relations

$$\tilde{\Xi}(k) = 2\pi \int_0^\infty \Xi(r) J_0(kr) r dr, \quad \Xi(r) = \frac{1}{2\pi} \int_0^\infty \tilde{\Xi}(k) J_0(kr) k dk, \quad (3.19)$$

using the fact that the two-dimensional Fourier transform of a circularly symmetric function is equivalent to a Hankel transform of order zero. Here,  $k = \sqrt{k_x^2 + k_y^2}$  is the isotropic wavenumber in Fourier space,  $J_0$  is the Bessel function of order zero and  $\tilde{\Xi}$  is Hermitian (i.e.  $\tilde{\Xi}(\mathbf{k}) = \tilde{\Xi}^*(-\mathbf{k})$ ) so that  $\Xi$  is real-valued.

Many previous studies of beta-plane turbulence and zonation have focussed on *narrow-band* forcing in which an annulus of wavevectors is excited in Fourier space, with mean radius  $k = k_f$  and thickness  $2\delta k \ll k_f$  (see Bakas and Ioannou, 2014; Scott and Polvani, 2007; Srinivasan and Young, 2012, and many others). We shall consider the further idealization of *ring forcing*, taking the limit  $\delta k \rightarrow 0$ , in which energy is injected onto the circle  $k = k_f$  in Fourier space. By assuming ergodicity such that volume averages of single realisations are equivalent to ensemble averages, the corresponding correlation function can be derived from the relation  $\varepsilon = -\langle \xi \psi \rangle$ . Written respectively in Fourier and physical space, it is given by

$$\tilde{\Xi}(k) = 4\pi k_f \varepsilon \delta(k - k_f), \quad \Xi(r) = 2\varepsilon k_f^2 J_0(k_f r), \quad (3.20)$$

with the precise details of the derivation presented in Appendix B.1.

Spectral theories of zonal jet formation require a separation of scales between the forcing wavenumber,  $k_f$ , and the scale at which the jets equilibrate in order that a steep zonostrophic inverse cascade can develop with a large accumulation of energy at the largest zonal scales. However, it has recently been demonstrated that zonal jet formation itself does not require this separation (see, for example, Scott and Tissier (2012) and the discussion in Section 2.4.1.1), suggesting that this cascade is not necessary. With a view towards underpinning those factors relevant to zonal jet variability, we investigate a broad range of forcing wavenumbers, as we describe in the next section.

### 3.3 Numerical formulation

The nonlinear and quasilinear models described in Sections 3.2.1 and 3.2.2 are solved numerically using direct numerical simulation (DNS). We begin with a discussion of the numerical algorithm, followed by a more detailed discussion of the implementation of the stochastic forcing and the hyperviscosity.

#### 3.3.1 Numerical implementation

DNS of both the NL (3.1) and QL (3.14) vorticity equations is implemented using a pseudo-spectral algorithm together with a standard 2/3 dealiasing rule (Orszag, 1971). Spectral methods have several advantages over finite-difference schemes within our simple geometry, including exponential rather than algebraic convergence of errors with increasing resolution in addition to their ability to give exact derivatives with precision restricted only by truncation errors. Adopting this set-up, time integration is performed in Fourier space using a second-order Runge-Kutta scheme, while nonlinear terms are evaluated in physical

space. The vorticity equation is used to integrate the vorticity,  $\zeta$ , forwards in time, while the elliptic equation  $\zeta = \nabla^2\psi$  is used to determine the streamfunction,  $\psi$ , from the vorticity field. Further details of the numerical algorithm are presented in Appendix C.1.

We integrate over a two-dimensional, doubly-periodic, square domain such that  $(x, y) \in [0, 2\pi L_D) \times [0, 2\pi L_D)$ , with domain size  $L_D$ . The numerical resolution is selected such that there is a balance between the retention of small-scale details and computational practicality, i.e. the need to run 100's of simulations over long time periods. Consequently, our simulations in Chapters 4 and 5 are run with a grid resolution of  $N = 256$  in each spatial direction, which, due to dealiasing, equates to a maximum allowed wavenumber of  $k_{max} = 85$ . The time-step,  $\Delta t$ , is held fixed within each simulation but varies between the simulations, with smaller values required for larger zonestrophy. In each case, we select an optimal value within the limits of numerical stability, with this typically lying in the range  $0.0025 \leq \Delta t \leq 0.01$ . As a verification, some numerical integrations were performed using half the chosen time-step or double the spatial resolution, producing statistically identical results. The numerical implementation of the stochastic forcing,  $\xi(\mathbf{x}, t)$ , and the hyperviscosity,  $\nu_n \nabla^{2n} \zeta$ , are discussed in detail in Sections 3.3.2 and 3.3.3 respectively.

All simulations were initialised with  $\mathbf{u} = \zeta = 0$  and all parameters were held fixed within each simulation, unless stated otherwise. It was found that the time taken for the total kinetic energy to reach a statistically steady state during the initial spin-up period depends on the linear damping rate,  $\mu$ . This is usually achieved by time  $\mu t = 2 - 3$  (see Section 3.4), after which the simulations were integrated for a long time (typically between  $10 - 1000\mu t$  depending on parameters) in order to capture the long-time behaviour of the system.

We explore via systematic variation a broad combination of parameters in order to simulate an assortment of dynamical behaviours. For example, we vary the background potential vorticity gradient over the range  $\beta \in [0.1, 20]$ ; the linear damping rate is varied over two orders of magnitude,  $\mu \in [0.00005, 0.01]$ ; and we explore three different energy injection rates covering two orders of magnitude,  $\varepsilon \in \{10^{-6}, 10^{-5}, 10^{-4}\}$ . This equates to a spectrum of Rhines wavenumbers in the range  $0 < k_{Rh} < 8$  and zonestrophy parameters lying in the interval  $1 < R_\beta < 6$ . The domain size,  $L_D$ , is chosen to be unity in all simulations.

### 3.3.2 Stochastic forcing

The forcing that we numerically implement, a first-order Markov process, has been widely adopted in many studies of forced-dissipative two-dimensional models of zonal jets (Maltrud and Vallis, 1991; Scott and Tissier, 2012, etc) over the last few decades. We approximate  $\xi(\mathbf{x}, t)$  to be piecewise constant on discrete time steps  $t_n < t < t_{n+1}$ . Applying the discretised Fourier theorem,

$$\tilde{\xi}(\mathbf{k}, t) = \sum_{\mathbf{x}} \xi(\mathbf{x}, t) e^{-i\mathbf{k}\cdot\mathbf{x}}, \quad \xi(\mathbf{x}, t) = \frac{1}{N^2} \sum_{\mathbf{k}} \tilde{\xi}(\mathbf{k}, t) e^{i\mathbf{k}\cdot\mathbf{x}}, \quad (3.21)$$

the Fourier coefficients  $\tilde{\xi}(\mathbf{k}, t)$  are given by  $\tilde{\xi}(\mathbf{k}, t) = \mathcal{A} \tilde{\eta}(\mathbf{k}, t)$  with constant amplitude  $\mathcal{A} \in \mathbb{R}$  and Markovian coefficients  $\tilde{\eta}(\mathbf{k}, t)$  satisfying the Hermitian property  $\tilde{\eta}(-\mathbf{k}, t) = \tilde{\eta}^*(\mathbf{k}, t)$  to ensure that the forcing function  $\xi(\mathbf{x}, t)$  is real. These coefficients are updated at each time step  $t_n$  using the scheme

$$\tilde{\eta}(\mathbf{k}, t_0) = X_0, \quad \tilde{\eta}(\mathbf{k}, t_n) = \gamma \tilde{\eta}(\mathbf{k}, t_{n-1}) + \sqrt{1 - \gamma^2} X_n, \quad (3.22)$$

where the  $X_n$  are independent, identically distributed (IID) random variables given by  $X_n = e^{i\theta_n}$  with uniformly distributed random phase  $\theta_n \in [0, 2\pi)$ , mean  $\langle X_n \rangle = 0$  and covariance  $\langle X_m X_n^* \rangle = \delta_{mn}$ . The

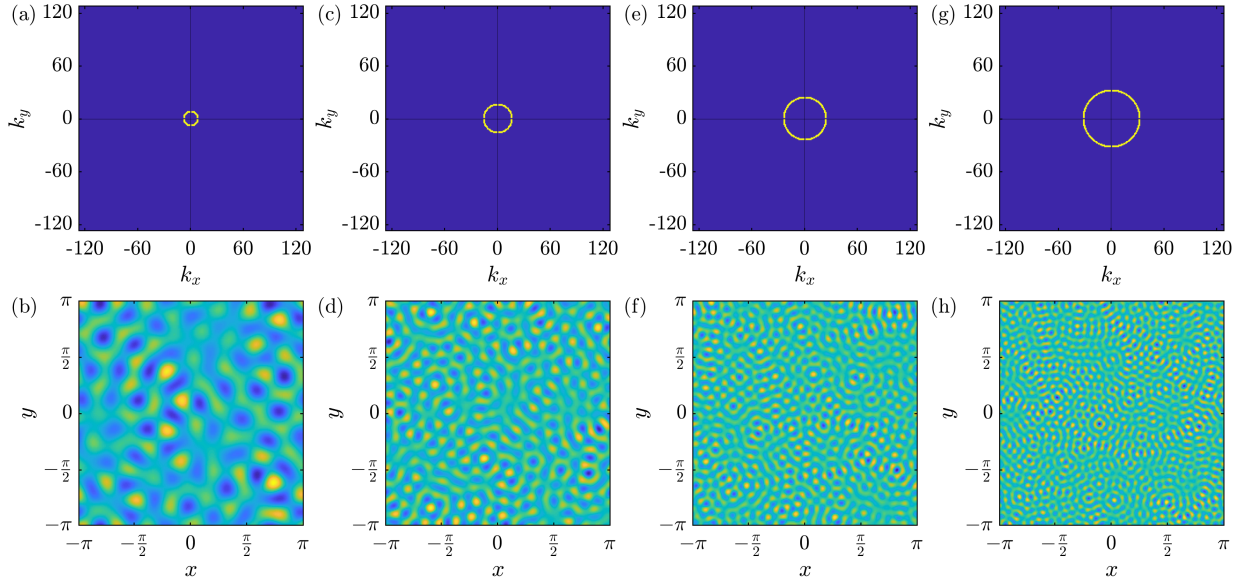


**Figure 3.2** Forcing distributions for  $\xi$  in (top) Fourier space and (bottom) example realisations in physical space for forcing wavenumbers (a-b)  $k_f = 8$ , (c-d)  $k_f = 16$ , (e-f)  $k_f = 24$ , (g-h)  $k_f = 32$ .

parameter  $0 \leq \gamma \leq 1$  is related to the decorrelation time  $\tau_f$  of the forcing by  $\gamma = 1 - \Delta t / \tau_f$ , where  $\gamma = 0$  (corresponding to  $\tau_f = \Delta t$ ) approximates Gaussian white noise using a Markov process,  $\gamma = 1$  corresponds to deterministic forcing, and  $0 < \gamma < 1$  represents forcing with a Markovian time-dependence. As shown in Appendix B.2, this forcing scheme ensures that the variance of its Fourier coefficients remains constant over time, given by  $\langle \tilde{\xi}(\mathbf{k}, t) \tilde{\xi}(\mathbf{k}, t) \rangle = \mathcal{A}^2$ .

We numerically implement isotropic ring forcing with wavenumber  $k_f$  by forcing only those wavevectors such that  $|k - k_f| < \delta k$  (where  $\delta k \ll k_f$ ) and specifying that all non-zero Fourier coefficients have equal amplitude. For short decorrelation times, we can assume that the stochastic forcing is independent of the state of the system, allowing the rate of energy injection,  $\varepsilon$ , to be prescribed via the amplitudes  $\mathcal{A}$  of the Fourier coefficients of the forcing function. If, in addition, we assume ergodicity such that spatial and ensemble averages are equivalent, then the relationship between  $\varepsilon$  and  $\mathcal{A}$  can be derived from  $\varepsilon = -\langle \xi \psi \rangle$ :

$$\varepsilon = \frac{1}{2} \left( \frac{1+\gamma}{1-\gamma} \right) \frac{\mathcal{N} \mathcal{A}^2 \Delta t}{N^4 k_f^2}, \quad \mathcal{A} = \sqrt{\frac{2\varepsilon N^4 k_f^2 (1-\gamma)}{N \Delta t (1+\gamma)}}, \quad (3.23)$$

with further details presented in Appendix B.2. The stochastic forcing function is thus defined as

$$\xi(\mathbf{x}, t) = \sqrt{\frac{2\varepsilon k_f^2 (1-\gamma)}{N \Delta t (1+\gamma)}} \sum_{|k-k_f| < \delta k} \tilde{\eta}(\mathbf{k}, t) e^{i\mathbf{k} \cdot \mathbf{x}}. \quad (3.24)$$

In these expressions,  $\mathcal{N}$  corresponds to the number of wavevectors that are forced in Fourier space and  $N$  is the spatial resolution in the zonal and latitudinal directions. The dependence  $\mathcal{A} \propto 1/\sqrt{\Delta t}$  ensures that the forcing is delta-correlated in the limit  $\Delta t \rightarrow 0$ . Clearly these expressions break down in the limit  $\gamma \rightarrow 1$  (corresponding to steady forcing), therefore we emphasize their applicability purely in the regimes of short decorrelation time  $\tau_f = \Delta t / (1 - \gamma)$ . In this study, we restrict attention to the case  $\gamma = 0$ , although we note that a number of simulations were run with  $\gamma > 0$  (but  $\tau_f \leq 10\Delta t$ ) in order to verify these relations.

We implement idealised ring forcing numerically by forcing an annulus of wavevectors in Fourier space centred around a mean radial wavenumber  $k_f$  with thickness  $2\delta k = 2$ . In order to avoid forcing purely zonal or purely meridional flows, we choose not to force wavevectors of the form  $\mathbf{k} = (0, k)$  and  $\mathbf{k} = (k, 0)$ . Whilst we explore a range of forcing wavenumbers lying in the interval  $k_f \in [2, 32]$ , the majority of simulations focus on four cases:  $k_f \in \{8, 16, 24, 32\}$ . These are illustrated in Figure 3.2, in which each distribution is plotted in Fourier space alongside an example realisation in physical space.

### 3.3.3 Hyperviscosity

Hyperviscosity has a long history of being used as a tool for maintaining numerical stability by acting as a sink for the build-up of energy in small scale fluctuations whilst largely unaffected the larger scales. There is no theoretical basis for selecting the optimum parameters; instead, as mentioned by Smith and Hammett (1997), they are typically chosen on an experimental basis such that a dissipation range appears within the resolved modes. We incorporate hyperviscosity,  $\nu_n \nabla^{2n} \zeta$ , in each of our models with the aim of removing the build-up of enstrophy in the vicinity of the largest retained wavenumber,  $k_{max}$ . The resolution-dependent prefactor of this hyperviscosity term is implemented as

$$\nu_n = \frac{(-1)^{n+1} \nu}{k_{max}^{2n}}, \quad (3.25)$$

where  $\nu$  is the amplitude and  $n$  is the hyperviscosity index. Within this scheme, suitable choices for  $\nu$  and  $n$  must be made in order to fully define the numerical models. If  $n$  is too small then significant damping at smaller wavenumbers will occur which will affect the numerical results. Conversely, if  $n$  is too large then there will be virtually no damping for almost all of the modes except for those closest to  $k_{max}$  which will be damped significantly. Consequently, a trade-off is necessary between these competing goals.

A useful measure of the role of hyperviscosity can be inferred from the equation for the evolution of the domain-averaged total kinetic energy  $E$  given by (3.5). In a steady state, the idealised inviscid limit leads to a balance between the energy injection rate by the forcing and the frictional dissipation rate:

$$E^{(i)} = \frac{\varepsilon}{2\mu}, \quad (3.26)$$

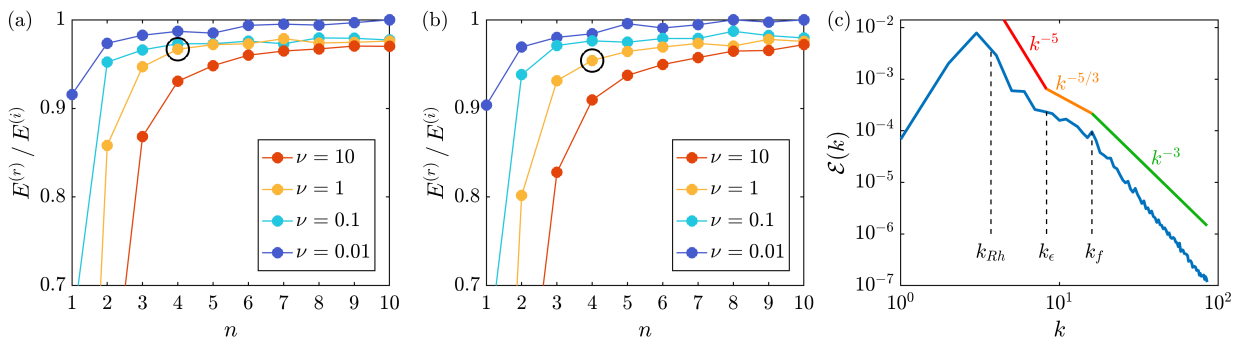


**Figure 3.3** Numerical simulation of different hyperviscosity indices  $n$  and amplitudes  $\nu$  within the (a) NL model and (b) QL model. Black circles indicate the values selected within all simulations in this thesis. (c) The corresponding kinetic energy spectrum  $\mathcal{E}(k)$  using  $\nu = 1$  and  $n = 4$  in the NL model with the zonal and two-dimensional inertial ranges shown above for comparison. The parameters used in each of the above simulations are:  $\beta = 5$ ,  $\mu = 0.0030$ ,  $\varepsilon = 10^{-4}$ ,  $k_f = 16$ ,  $N = 256$ ,  $R_\beta = 2.24$ .

where  $E^{(i)}$  is the idealised total kinetic energy. Hyperviscosity will act to reduce the amount of energy that is dissipated by frictional processes, thereby reducing the emergent total kinetic energy, a quantity which is computable and denoted  $E^{(r)}$ . The fraction  $E^{(r)}/E^{(i)}$  therefore provides a measure of the influence of hyperviscosity, with values close to unity being desirable.

In order to proceed, we run a series of numerical simulations using both the NL and the QL models in which different permutations of  $\nu \in \{10^{-2}, 10^{-1}, 10^0, 10^1\}$  and  $n \in \{1, 2, \dots, 10\}$  are selected, keeping all other parameters fixed. We compute time averages of the diagnostic  $E^{(r)}/E^{(i)}$  for each of these simulations once a statistically steady state has been reached, with the results presented in Figures 3.3(a,b). For each model, the simulations become increasingly inviscid as  $\nu \rightarrow 0$  and  $n \rightarrow \infty$ , with  $E^{(r)}/E^{(i)} \rightarrow 1$  as we would expect. However, it is apparent that  $E^{(r)}/E^{(i)}$  increases significantly between  $n = 1$  and  $n = 4$  whilst  $n > 4$  does not lead to further notable increases. In addition, there is a noticeable benefit to selecting  $\nu = 1$  rather than  $\nu = 10$ , however, further reductions in  $\nu$  are less significant. In keeping with our desire to maintain numerical stability, we therefore choose an amplitude of  $\nu = 1$  and we adopt  $n = 4$ , giving  $\nu_4 \nabla^8 \zeta$  (in line with Srinivasan and Young, 2012; Sukoriansky et al., 2008, etc). These choices are identified using black circles in Figures 3.3(a,b) and correspond to configurations in which the total energy equilibrates at approximately 95% of its ideal value.

Figure 3.3(c) shows the corresponding kinetic energy spectrum,  $\mathcal{E}(k)$ , for these parameters in the NL model, computed by discretising the wavenumbers into discrete bins of unit width:

$$\mathcal{E}(k) = \sum_{k-\frac{1}{2} \leq |\mathbf{k}| < k+\frac{1}{2}} \left\langle \left| \frac{k^2}{2N^2} \tilde{\psi}(\mathbf{k}, t) e^{i\mathbf{k} \cdot \mathbf{x}} \right|^2 \right\rangle. \quad (3.27)$$

There is clearly no build-up of energy in the largest resolved wavenumbers which adds confidence to our choice of hyperviscosity parameters in our simulations.

### 3.4 Numerical simulation of zonal flows

Having formulated discretised versions of the NL and QL models, we now discuss aspects of their simulation of zonal jets and discuss some key assumptions that will be used throughout this thesis. In addition, we describe our numerical procedures for computing the velocity profiles and corresponding eddy momentum flux convergences that we will present in subsequent chapters.

#### 3.4.1 Direct numerical simulation of zonal jet formation and equilibration

Numerical simulation of the NL and QL models captures the two-dimensional vorticity field at discrete time steps, from which the velocity field can be inferred by  $(u, v) = (-\nabla^{-2} \partial_y \zeta, \nabla^{-2} \partial_x \zeta)$ . In the interests of visualising the dynamics of zonal flows, we reduce the dimension at individual time steps by computing the zonally averaged zonal velocity field, denoted  $U(y, t)$ , and plot the evolution of this one-dimensional profile in time. These latitude-time, or *Hovmöller*, plots will form a significant part of the discussion in this thesis. An example numerical integration of the NL model is shown in Figure 3.4(a) in which the system equilibrates after about  $t = 5,000$  ( $\mu t = 2.5$ ) with between 5 and 6 eastward jets. Hereafter, we will drop the term ‘eastward’, instead inferring that jet numbers, unless stated otherwise, correspond to eastward jets.

The domain-averaged total kinetic energy, defined by  $E = \frac{1}{2} \langle |\nabla \psi|^2 \rangle$  and shown by the red curve in Figure 3.4(b), is relatively steady in time after equilibration. It can be decomposed into contributions from

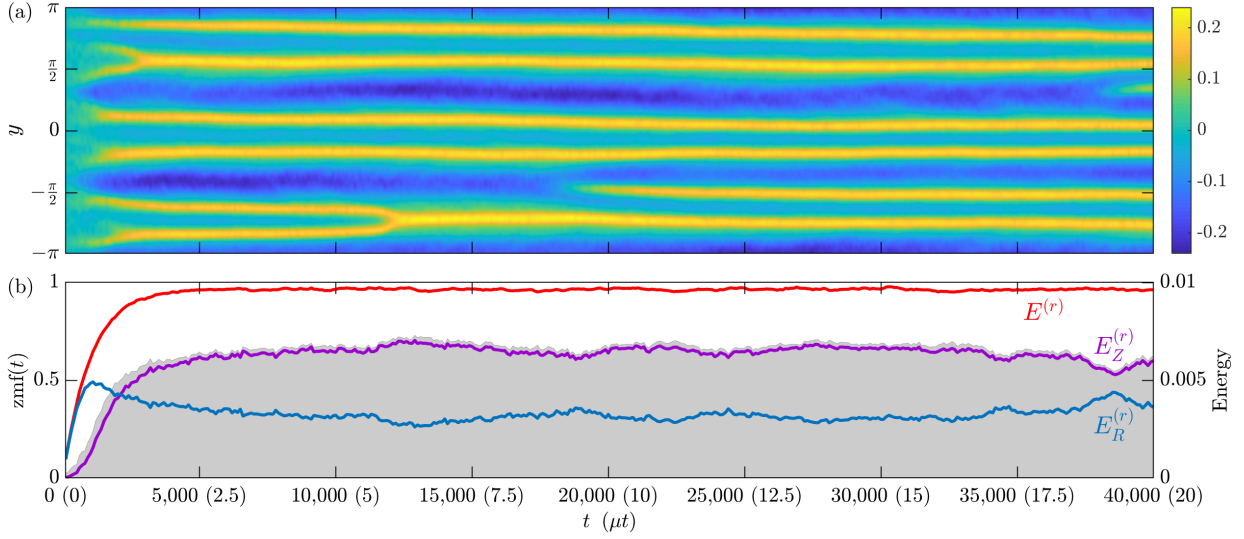


**Figure 3.4** (a) Latitude-time plot showing time evolution of the zonal mean zonal velocity field. The system reaches a statistically steady state after about  $t = 5,000$ . (b) The corresponding evolution of the total kinetic energy  $E^{(r)}$  (red), zonal mean kinetic energy  $E_Z^{(r)}$  (purple) and eddy kinetic energy  $E_R^{(r)}$  (blue) plotted alongside the zonal mean flow index  $\text{zmf}(t)$  (grey shading). The parameters used are:  $\beta = 11.5$ ,  $\mu = 0.0005$ ,  $\varepsilon = 10^{-5}$ ,  $k_f = 16$ ,  $N = 256$ ,  $R_\beta = 3.40$ .

the zonal mean zonal velocity field,  $E_Z$ , and the non-zonal, or *residual* eddy field,  $E_R$ , in which

$$\begin{aligned}
 E &= \frac{1}{2} \langle |\nabla\psi|^2 \rangle &= \sum_{k_x} \sum_{k_y} \left\langle \left| \frac{k^2}{2N^2} \tilde{\psi}(\mathbf{k}, t) e^{i\mathbf{k}\cdot\mathbf{x}} \right|^2 \right\rangle, \\
 E_Z &= \frac{1}{2} \langle |\overline{\nabla\psi}|^2 \rangle &= \sum_{k_x=0} \sum_{k_y} \left\langle \left| \frac{k^2}{2N^2} \tilde{\psi}(\mathbf{k}, t) e^{i\mathbf{k}\cdot\mathbf{x}} \right|^2 \right\rangle, \\
 E_R &= \frac{1}{2} \langle |\nabla\psi|^2 \rangle - \frac{1}{2} \langle |\overline{\nabla\psi}|^2 \rangle &= \sum_{k_x \neq 0} \sum_{k_y} \left\langle \left| \frac{k^2}{2N^2} \tilde{\psi}(\mathbf{k}, t) e^{i\mathbf{k}\cdot\mathbf{x}} \right|^2 \right\rangle,
 \end{aligned} \tag{3.28}$$

and  $E = E_Z + E_R$ . This decomposition is plotted in Figure 3.4(b) in which it can be seen that  $E_Z$  (purple) and  $E_R$  (blue) are not steady, with energy continuously redistributing between the different modes. The steadiness of  $E$  and the unsteadiness of  $E_Z$  and  $E_R$  suggest that, rather than reporting all three values, instead a more useful diagnostic, encapsulating these different ingredients, is the  $\text{zmf}$  index described by (3.11). The time evolution of this dimensionless quantity is shown in Figure 3.4(b) using grey shading, where it is clear that there is a very strong correlation between  $E_Z$  and  $\text{zmf}(t)$  once the system has reached a statistically steady state.

There is also evidence for the existence of the zonostrophic and two-dimensional inertial ranges within our simulations, even for relatively small forcing wavenumbers. Figure 3.3(c) shows the energy spectrum for a simulation with  $k_f = 16$  in which the  $k^{-5}$  and  $k^{-5/3}$  scalings show reasonably good fit, despite the short ranges of wavenumbers over which they exist.

### 3.4.2 Numerical properties of the stochastic forcing wavenumber

We are interested in simulating a wide range of wavenumbers  $k_f$  associated with the stochastic forcing distribution. Consequently, it is useful to understand how the numerical models respond to this variation. We begin with a consideration of hyperviscosity. In Section 3.3.3, the hyperviscosity parameters were selected using a simulation with forcing wavenumber  $k_f = 16$  in which the emergent total kinetic energy

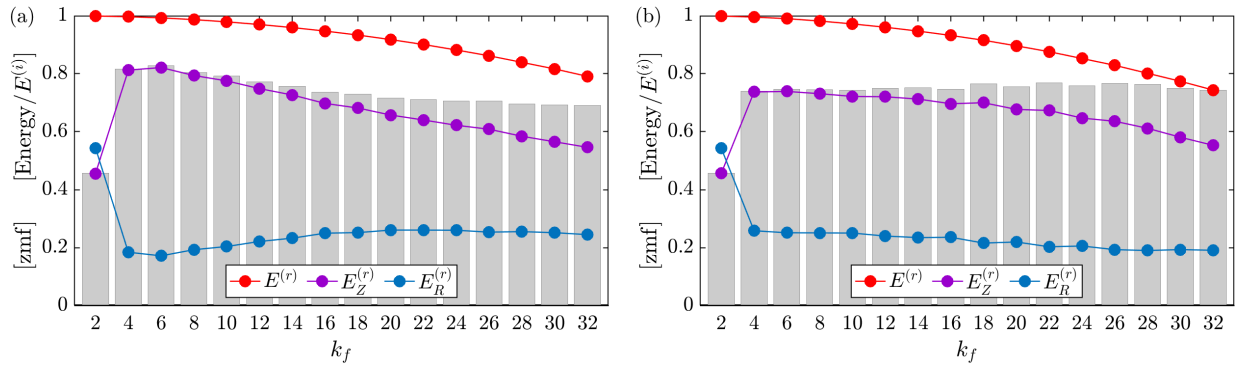


**Figure 3.5** The effect of the forcing wavenumber  $k_f$  on the distribution of equilibrated energy levels in the (a) NL model and (b) QL model. The total kinetic energy  $E^{(r)}$  (red), zonal mean kinetic energy  $E_Z^{(r)}$  (purple) and eddy kinetic energy  $E_R^{(r)}$  (blue), each normalised by the ideal total kinetic energy  $E^{(i)}$ , are plotted alongside the time averaged zmf index (grey bars). The parameters used are:  $\beta = 0.8$ ,  $\mu = 0.0002$ ,  $\varepsilon = 10^{-5}$ ,  $N = 256$ ,  $R_\beta = 3.27$ .

$E^{(r)}$  equilibrated at approximately 95% of its ideal value  $E^{(i)}$ . Here we explore this saturation fraction  $E^{(r)}/E^{(i)}$  for a range of wavenumbers lying in the range  $k_f \in [2, 32]$ , shown in Figure 3.5 using red circles. For both the NL and QL models, less than 1% of the energy is lost to hyperviscosity when  $k_f < 8$  while this figure drops to about 20% when  $k_f = 32$  due to its closer proximity to the largest retained wavenumber  $k_{max} = 85$  where the hyperviscosity acts most strongly. Analogous tendencies are plotted for the normalised zonal mean  $E_Z^{(r)}/E^{(i)}$  and eddy  $E_R^{(r)}/E^{(i)}$  kinetic energies, using the purple and blue series respectively, along with the time-averaged zmf index using grey bars. Aside from the smallest wavenumber  $k_f = 2$  where zonal jets struggle to form, the zmf index is relatively constant in both models, with perhaps a modestly decreasing trend between  $4 < k_f < 16$  in the NL model.

In order to examine the generality of these results, the analysis is extended in Figures 3.6(a,b) to include a much larger collection of numerical simulations. Here, we restrict attention to four forcing wavenumbers  $k_f \in \{8, 16, 24, 32\}$  and compute the average total kinetic energy as a fraction of its ideal value,  $E^{(r)}/E^{(i)}$ , (shown on the left hand axis of each figure) for simulations covering a broad range of zmf values. For any given wavenumber, there is very little variance around clearly defined average fractions corresponding to the values presented in Figure 3.5. Thus, we have confidence that the data presented in Figure 3.5 are representative of simulations using a broad range of parameters. Figure 3.6 also shows the measured Rhines

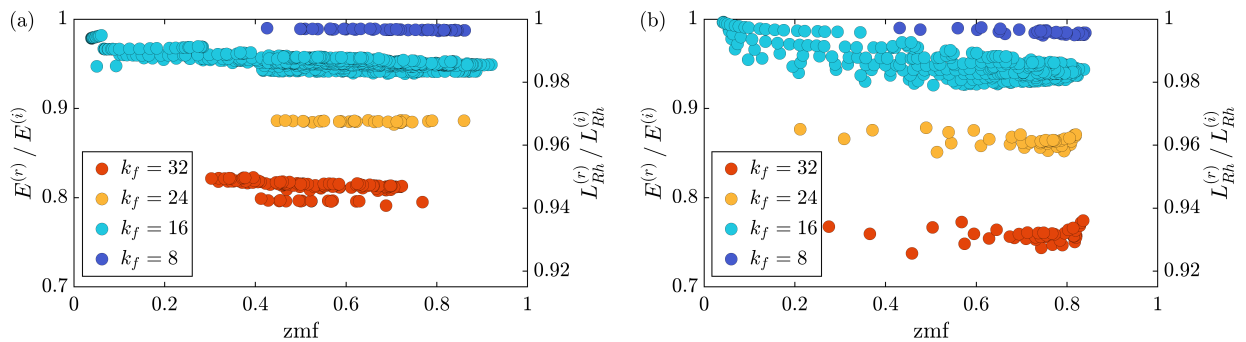


**Figure 3.6** The effect of the forcing wavenumber  $k_f \in \{8, 16, 24, 32\}$  on the measured total kinetic energy as a fraction of its ideal value  $E^{(r)}/E^{(i)}$  (left axis) and the corresponding measured Rhines scale as a fraction of its ideal value  $L_{Rh}^{(r)}/L_{Rh}^{(i)}$  (right axis) for the (a) NL model and (b) QL model. A large range of 826 NL and 547 QL simulations have been included such that  $N = 256$  and time averages were taken once the simulations had reached a statistically steady state.

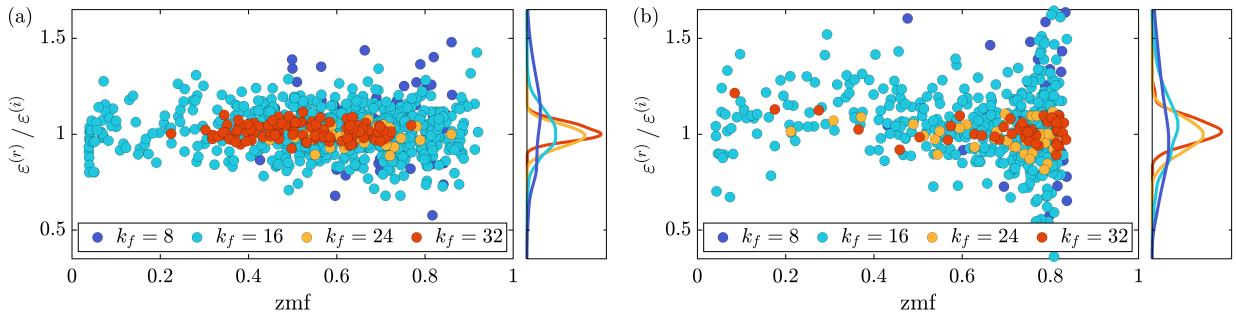


**Figure 3.7** The effect of the forcing wavenumber  $k_f \in \{8, 16, 24, 32\}$  on the measured energy injection rate  $\varepsilon^{(r)} = -\langle \xi \psi \rangle$  as a fraction of its ideal value  $\varepsilon^{(i)}$  for the (a) NL model and (b) QL model. A large range of 826 NL and 485 QL simulations have been included such that  $N = 256$  and time averages were taken once the simulations had reached a statistically steady state. The plots on the right show the corresponding probability density functions (PDFs).

scale as a fraction of its ideal value,  $L_{Rh}^{(r)}/L_{Rh}^{(i)}$ , on the right hand axes, computable using the simple relation

$$\frac{E^{(r)}}{E^{(i)}} = \left( \frac{L_{Rh}^{(r)}}{L_{Rh}^{(i)}} \right)^4. \quad (3.29)$$

This is equivalent to the measured zonestrophy parameter as a fraction of its ideal value,  $R_\beta^{(r)}/R_\beta^{(i)}$ . For the largest wavenumber  $k_f = 32$ , the emergent Rhines scale and zonestrophy parameter are approximately 95% of their ideal values in the NL model (or 93% in the QL model) while the fraction rises to over 98% for forcing wavenumbers  $k_f \leq 16$ . Consequently, hyperviscosity is considered to be negligible and we proceed to report only ideal values of these quantities in subsequent chapters.

It is also of interest to investigate the effectiveness of the stochastic forcing in maintaining a given energy injection rate, with statistical mean  $\varepsilon$  and associated variance due to random fluctuations. To verify this, we compute a time average of  $\varepsilon^{(r)} = -\langle \xi \psi \rangle$ , sampled every 10,000 time steps (corresponding to  $O(10^3)$  snapshots in total) over the entire equilibrated simulation, for a large range of simulations using both the NL and QL models. These values are then normalised by the corresponding ideal energy injection rates  $\varepsilon^{(i)}$ . The results are presented in Figures 3.7(a,b) for four different forcing wavenumbers  $k_f \in \{8, 16, 24, 32\}$  and a broad range of zmf values. Each circle represents a single simulation, coloured according to its forcing wavenumber, and the associated probability density functions (PDFs) for each wavenumber and model are displayed in order to visualise the overall means and variances.

Firstly, we note that the average energy injection rate across the ensemble of simulations is close to its ideal value, indicated by the approximate alignment of the peaks of the PDFs with the ratio  $\varepsilon^{(r)}/\varepsilon^{(i)} = 1$ . Secondly, the associated variance of  $\varepsilon$  due to random fluctuations at individual time steps increases as the forcing wavenumber decreases. Thus, forcing distributions with smaller characteristic scales are less likely to be correlated with the flow field and are therefore associated with smaller variances around the mean. Overall though, these results give us confidence in reporting the ideal values of the energy injection rate, bearing in mind that these are statistical averages with associated fluctuations.

### 3.4.3 Computation of velocity profiles and eddy momentum flux convergences

In our analysis of zonal jet variability, we shall be interested in computing the velocity profile,  $U(y)$ , associated with particular solutions. Fluctuations in the system lead to high frequency perturbations to the

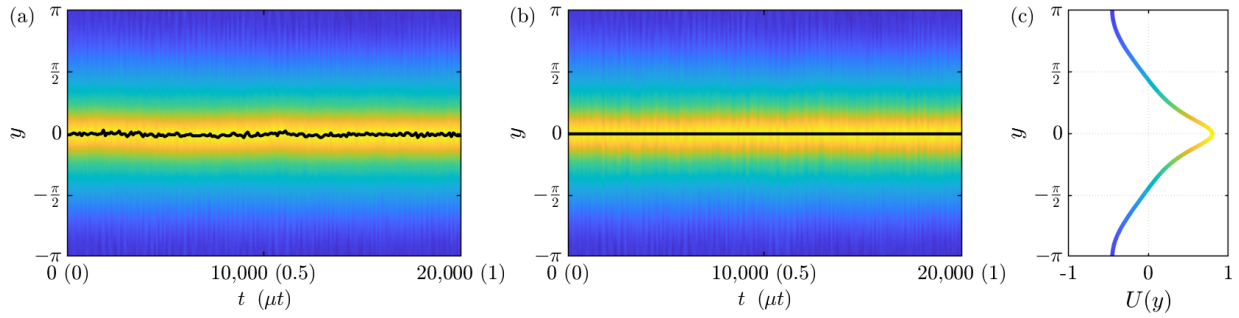


**Figure 3.8** The computation of the jet velocity profile,  $U(y)$ , for a relatively steady jet which exhibits small amplitude fluctuations. (a) Latitude-time plot of the zonal mean zonal velocity field, with the black line indicating the location of  $U_{\max}$ ; (b) same as (a) with the flow rearranged such that  $U_{\max}$  occurs at  $y = 0$ ; (c) the corresponding time-averaged jet velocity profile. For illustrative purposes, the NL model was used with parameters  $\beta = 0.6$ ,  $\mu = 0.00005$ ,  $\varepsilon = 10^{-5}$ ,  $k_f = 16$ ,  $N = 256$ ,  $R_\beta = 4.49$ .

structure of the jets, therefore it is necessary to compute an average over multiple time steps in order to cancel out the effects of these fluctuations. In addition, it is necessary to confine the averaging to a time period over which the system is ‘steady’ in the sense that its behaviour is not changing. This may, or may not, involve latitudinal drifting behaviour, as we shall discuss shortly. Within these limitations, there are no bounds on the length of such a period for averaging purposes.

To make ideas more concrete, we show an example simulation in Figure 3.8 in which a single jet is steady in the sense that it maintains an approximately constant latitude, although the same ideas apply to drifting behaviour. In Figure 3.8(a) we use a black line to track to the latitude of the maximum value of the zonal mean zonal velocity,  $U_{\max}$ , highlighting the location of the jet core. The small amplitude latitudinal fluctuations of the core (which are sometimes larger than those shown here) indicate the high frequency perturbations that we wish to average over. A Eulerian time average, i.e. at each fixed latitude  $y$ , would lead to a smoothing and broadening of the profile (and certainly wouldn’t work for drifting behaviour). Consequently, we adopt a simple Lagrangian time average using a jet-following procedure in which the zonal mean zonal flow is rearranged such that  $U_{\max}$  is centred at  $y = 0$ , as shown in Figure 3.8(b). A time average over this rearranged flow then gives the jet velocity profile, shown in Figure 3.8(c).

Another key diagnostic is the eddy momentum flux convergence,  $-\partial_y(\overline{u'v'}) = \overline{v'\zeta'}$ , which is responsible for driving and maintaining eddy-driven zonal jets. This is a rapidly-fluctuating quantity requiring time averages to cancel the noise and detect its structure. We are interested in the form of  $\overline{v'\zeta'}$  relative to a particular jet which may be drifting in the latitudinal direction. An example of a single jet drifting with

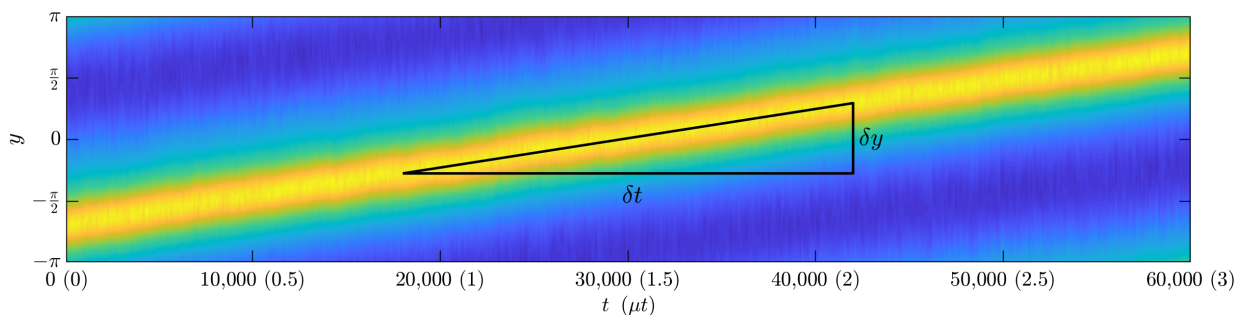


**Figure 3.9** The latitudinal translation speed  $\mathcal{V}$  of a jet, computed as the latitudinal shift  $\delta y$  divided by the elapsed time  $\delta t$ . For illustrative purposes, the NL model was used with parameters  $\beta = 0.6$ ,  $\mu = 0.00005$ ,  $\varepsilon = 10^{-5}$ ,  $k_f = 16$ ,  $N = 256$ ,  $R_\beta = 4.49$ .

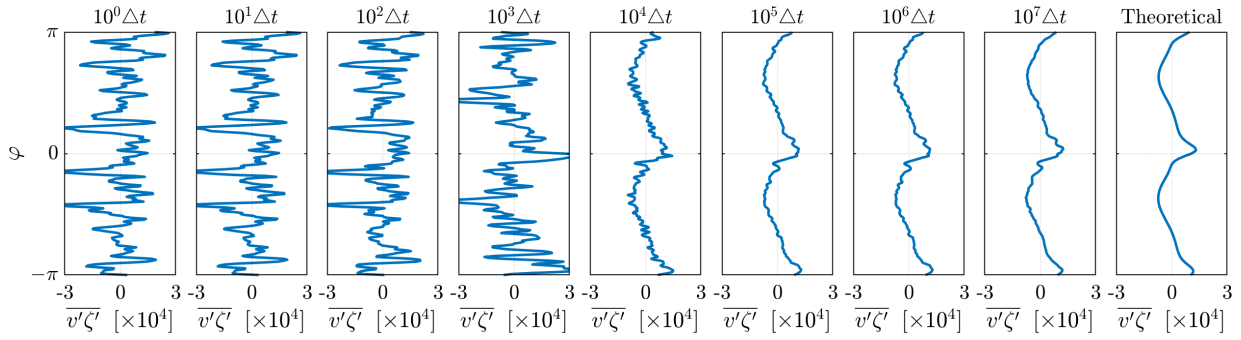


**Figure 3.10** The direct numerical computation of the eddy momentum flux convergence  $\overline{v'\zeta'}$  within a transformed domain in which a zonal jet with original latitudinal translation speed  $\mathcal{V}$  is steady at latitude  $\varphi = 0$ . Time averages of  $\overline{v'\zeta'}$  over different numbers of time steps are compared with a ‘theoretical’ profile derived from the momentum balance in order to test for convergence. The NL model was used with parameters  $\beta = 2.5$ ,  $\mu = 0.0004$ ,  $\varepsilon = 10^{-5}$ ,  $k_f = 16$ ,  $N = 256$ ,  $R_\beta = 3.08$ . For comparison, the frictional damping time scale is given by  $\mu t = 250,000\Delta t$ .

constant latitudinal speed is shown in Figure 3.9. Here, the speed of translation is computed as

$$\mathcal{V} = \frac{\delta y}{\delta t}, \quad (3.30)$$

where  $\delta y$  is the latitudinal displacement of the jet core and  $\delta t$  is the time that has elapsed during this displacement. Let us assume without loss of generality that a particular jet within a system has constant latitudinal translation speed  $\mathcal{V}$  and that we wish to compute  $\overline{v'\zeta'}$  in this jet’s frame of reference. The zonal mean momentum equation (3.4) can be recast by introducing the coordinate  $\varphi = y - \mathcal{V}t$ . This gives the transformed equation for the maintenance of the jet,

$$-\mathcal{V} \frac{d}{d\varphi} U(\varphi) = \overline{v'(x, \varphi)\zeta'(x, \varphi)} - \mu U(\varphi) + \nu_n \frac{d^{2n}}{d\varphi^{2n}} U(\varphi). \quad (3.31)$$

When  $\mathcal{V} = 0$ , the term on the left hand side is zero and we recover the steady version of (3.4). Numerically, the two-dimensional solution can be transformed as necessary in order that a particular jet maintains a constant latitude, as illustrated in Figure 3.8, then a Lagrangian time average of  $\overline{v'(\varphi)\zeta'(\varphi)}$  can be directly computed relative to the jet core. Alternatively, an estimate can be computed from the momentum balance in (3.31) using the velocity profile  $U(\varphi)$ , computed over a time average during which  $\mathcal{V}$  remains constant.

In Figure 3.10 we consider a simulation in which two jets have a constant drift speed. Direct numerical averaging over different numbers of time steps  $\Delta t$  is compared with an estimate of  $\overline{v'\zeta'}$  derived from the momentum balance in order to test for convergence. It is clear that at least  $10^3$  time steps are required in order to see any structure in the underlying noise, while convergence on the profile derived from the momentum balance is achieved by  $10^5$  or more time steps. For practical reasons, we will report the momentum balance profile unless stated otherwise, noting that this is indeed equivalent to the average of  $\overline{v'\zeta'}$  evaluated over a large number of individual time steps.

### 3.5 Discussion

The mathematical models that we have introduced in this chapter will lay the foundations for our study of zonal jet variability in Chapters 4–6. By retaining only the essential physical processes, these highly idealised models capture fundamental dynamics that may be applicable to zonal jets in planetary atmospheres and

oceans. We began with a description of the NL model, in which an idealisation of turbulence is forced using a stochastic vorticity forcing function. The quasilinear approximation then permitted the derivation of a QL model in which nonlinear interactions between eddies are excluded. Both of these models were formulated numerically, with special attention given to the stochastic forcing term. Finally, we demonstrated aspects of the simulation of zonal jets and provided some numerical justifications of key modelling assumptions that will be used throughout this thesis.

## Chapter 4

# The variability of stochastically forced, beta-plane zonal jets

### 4.1 Introduction

Naturally-occurring zonal jets are inherently unsteady, undergoing low-frequency latitudinal displacements, which, as previously mentioned, are manifested by a variety of behaviours that differ substantially between different planetary systems. Whilst several studies have attempted to document aspects of their dynamics (see e.g. Bouchet et al., 2013, 2014; Lee, 1997; Panetta, 1993), a thorough categorisation has yet to be completed. In this chapter we explore zonal jet variability using the NL and QL barotropic models defined in Chapter 3. The term *variability* shall be interpreted in the loose sense of the word, referring to the dynamical regimes, flow structures and regime transitions that exist once the system has equilibrated.

By studying zonal jet variability side-by-side using a fully nonlinear model and a quasilinear version, we endeavour to examine the necessity of the role of eddy-eddy interactions in aspects of variability. Our primary focus is the zonostrophic regime, defined by Galperin et al. (2008), in which robust, persistent jets naturally develop alongside other coherent structures such as zonons. We shall begin by attempting to categorise the zoology of different types of variability within these stochastically forced systems. This will be followed by more detailed investigations of the dependence of the system on key parameters. Finally, we will discuss some of the interesting complexities of these systems, such as the existence of multiple stable flow solutions and spontaneous regime transitions.

### 4.2 The zoology of beta-plane zonal jet dynamics

We have run a large number of 839 NL and 547 QL simulations across a broad range of parameters such that the Rhines wavenumber lies in the range  $0 < k_{Rh} < 8$ , the zonostrophy parameter is in the interval  $1 < R_\beta < 6$ , and the forcing wavenumber covers a broad range of scales,  $2 \leq k_f \leq 32$ . In each case, the simulations were spun up from a state of rest until statistical equilibrium was achieved, before being run for a long time as described in Section 3.3 in order to capture the dynamical regimes. Whilst a rich assortment of behaviours are observed, it is helpful to begin with a discussion of the fundamental types of variability that are defined on the basis of the zonal mean time evolution. This is followed by a deeper investigation of the flow structures associated with various subclasses of variability that fall under these parent categories.

### 4.2.1 Fundamental types of variability

Focussing initially on the NL model, we observe three distinct types of behaviour in the latitude-time plots, illustrated in Figure 4.1. Firstly, the jets are sometimes associated with latitudinal fluctuations that occur with low temporal frequency, or long time scales, compared with other time scales of motion, such as the Rossby wave time scale,  $\tau_w = k/\beta \sim O(1)$ , or the eddy-turnover time scale,  $\tau_t = \varepsilon^{-1/3} k^{-2/3} \sim O(10)$ . An example simulation is shown in Figure 4.1(a) in which a single zonal jet exhibits small amplitude fluctuations that are commensurate with the width of the jet. The magnitudes of the displacements vary considerably between simulations, with some simulations exhibiting larger amplitude fluctuations in which the displacements are comparable with the size of the domain. Unlike the terrestrial atmosphere (see Figure 2.2(a)), the zonal jets in our simulations do not have a preferred latitude because there is no imposed latitudinal structure, leading us to refer to this type of variability as *randomly wandering* behaviour.

The second fundamental type of variability involves spontaneous transitions between integral numbers of jets, such that the total number of jets typically oscillates between  $n$  and either  $n+1$  or occasionally  $n+2$  jets. An example simulation illustrating this behaviour is shown in Figure 4.1(b) in which the number of jets varies between two and four at any one time. Similar behaviour can also be seen in observations (Figure 2.2(b)) and in previous idealised studies (Figure 2.10). A reduction in the number of jets in the domain occurs when two neighbouring jets merge together to form a single jet. Similarly, an increase in the number of jets occurs when a new jet is generated, or *nucleated*. We note that these are the only mechanisms by which the number of jets can change; they are *never* observed to split or vanish, i.e. there is no time-reversal symmetry. Consequently, we refer to these transitions as *merging and nucleating* behaviour.

In addition to these two variability types, we report the discovery of a new type of zonal jet variability observed within the NL model. Rather than behaving randomly, or stochastically, we observe that, for certain sets of parameters, the jets behave deterministically to a first approximation. For example, they are

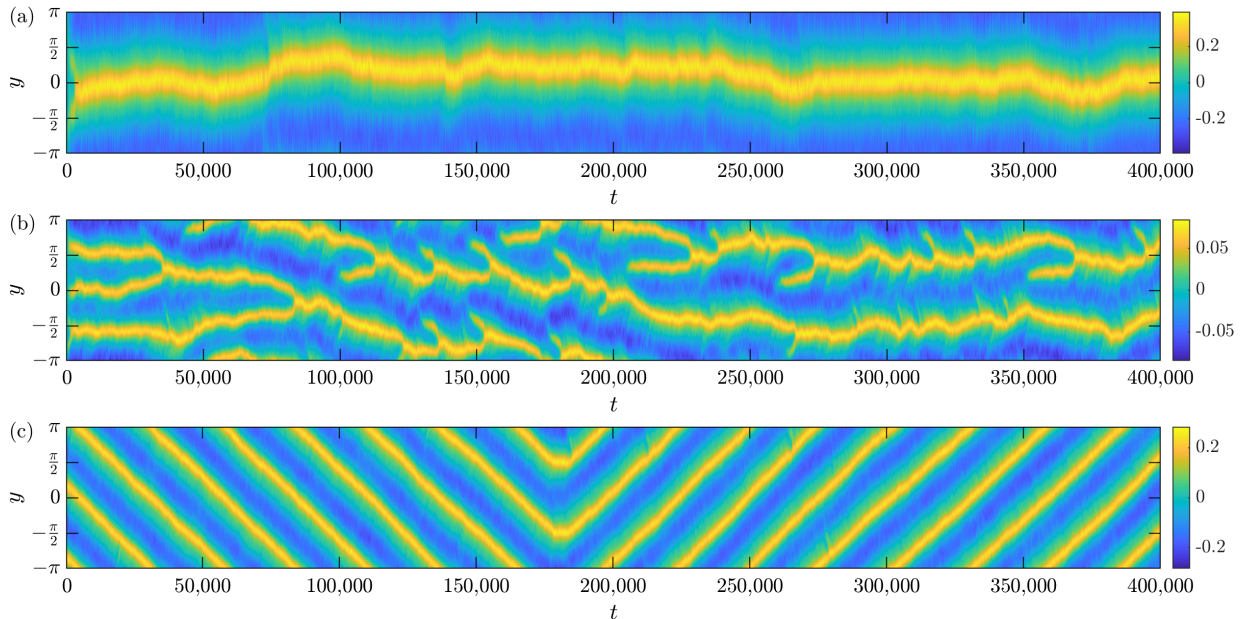


**Figure 4.1** Fundamental types of zonal jet variability regimes observed in the NL model described by equation (3.1). (a) Randomly wandering behaviour (parameters used:  $\beta = 0.6$ ,  $\mu = 0.0002$ ,  $\varepsilon = 10^{-5}$ ,  $k_f = 16$ ,  $N = 256$ ,  $R_\beta = 3.18$ ). (b) Merging and nucleating behaviour (parameters used:  $\beta = 0.9$ ,  $\mu = 0.0004$ ,  $\varepsilon = 10^{-6}$ ,  $k_f = 16$ ,  $N = 256$ ,  $R_\beta = 2.50$ ). (c) Migrating behaviour (parameters used:  $\beta = 2.2$ ,  $\mu = 0.0004$ ,  $\varepsilon = 10^{-5}$ ,  $k_f = 16$ ,  $N = 256$ ,  $R_\beta = 3.04$ ).

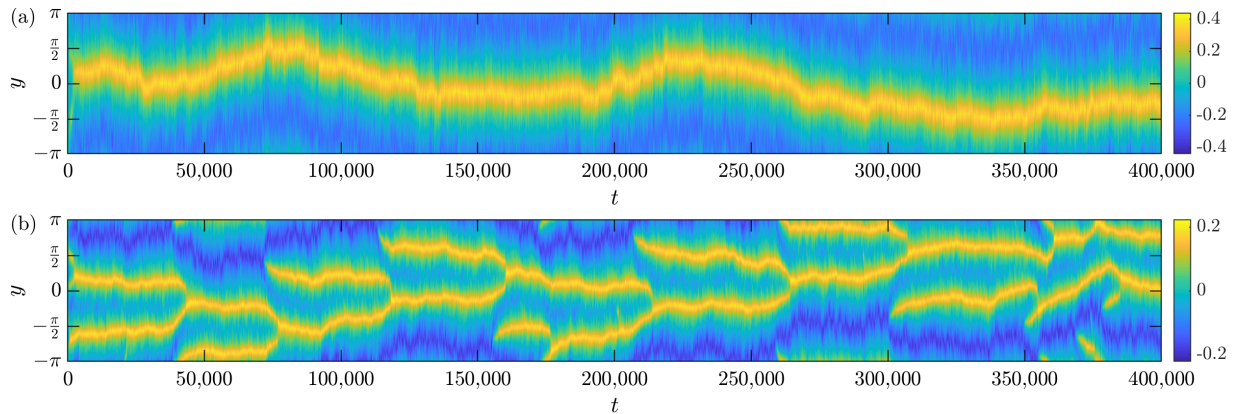


**Figure 4.2** Fundamental types of zonal jet variability regimes observed in the QL model described by equation (3.14). (a) Randomly wandering behaviour (parameters used:  $\beta = 0.3$ ,  $\mu = 0.0002$ ,  $\varepsilon = 10^{-5}$ ,  $k_f = 16$ ,  $N = 256$ ,  $R_\beta = 2.96$ ). (b) Merging and nucleating behaviour (parameters used:  $\beta = 1.2$ ,  $\mu = 0.0007$ ,  $\varepsilon = 10^{-5}$ ,  $k_f = 16$ ,  $N = 256$ ,  $R_\beta = 2.49$ ).

sometimes observed to systematically *translate* in the latitudinal direction with approximately constant speed. In this case, the latitudinal symmetry property (3.2) is spontaneously broken, with both northward and southward translation equally probable. In addition, the jets can spontaneously change direction as a result of internal dynamics, with no external stimulus. This is visible in Figure 4.1(c) in which the domain contains two jets that switch from a southward to a northward direction of translation at about  $t \approx 180,000$ . Wishing to maintain continuity with the existing literature in which similar behaviour has been observed in more complex systems where there is a preferred direction of translation (see e.g. Chemke and Kaspi, 2015b), we henceforth refer to this behaviour as *jet migration*.

The QL model, on the other hand, whilst exhibiting some interesting dynamics, fails to capture the full range of behaviours that its fully nonlinear counterpart is capable of simulating. The first two types of variability - randomly wandering and merging / nucleating behaviours - are observed in the QL simulations, as evidenced in Figure 4.2. However, jet migration, in which equally-spaced and equally-strong jets systematically translate, such as those visible in Figure 4.1(c), has not been observed in the QL framework despite exhaustive searches, leading us to conclude that the QL model does not permit this behaviour. This fundamental result implies that the nonlinear eddy-eddy interactions that are removed in the quasilinear approximation are relevant to jet migration behaviour, whilst they are not strictly necessary in other aspects of variability. It is worth also mentioning that in both systems, the jets may exhibit multiple types of variability for a given set of parameters, often with abrupt and spontaneous transitions between these regimes. This non-uniqueness of solutions will be discussed further in Section 4.4.2.

It is insightful to compare these fundamental types of variability within both models by performing a series of numerical simulations in which a parameter, in this case the Rhines wavenumber,  $k_{Rh}$ , is continuously varied in time in order to observe changes in jet behaviour (see Figure 4.3). For both models, we hold all parameters constant except for the value of  $\beta$ , systematically increasing or decreasing  $\beta^{1/2}$  (in accordance with (3.9)) such that the Rhines wavenumber varies linearly over the range  $0 \leq k_{Rh} \leq 5$ . As we would expect, increases (decreases) in  $k_{Rh}$  lead to increases (decreases) in the number of jets within the domain via jet mergers and nucleations, however, the number of jets that are visible in the NL and QL simulations do not match: four NL jets are apparent when  $k_{Rh} \approx 5$  while only two QL jets are visible for the same set of parameters. Whilst this is an extreme example, we note that in general the QL model does have a tendency to underestimate the numbers of jets relative to the NL model; we shall return to this point later.

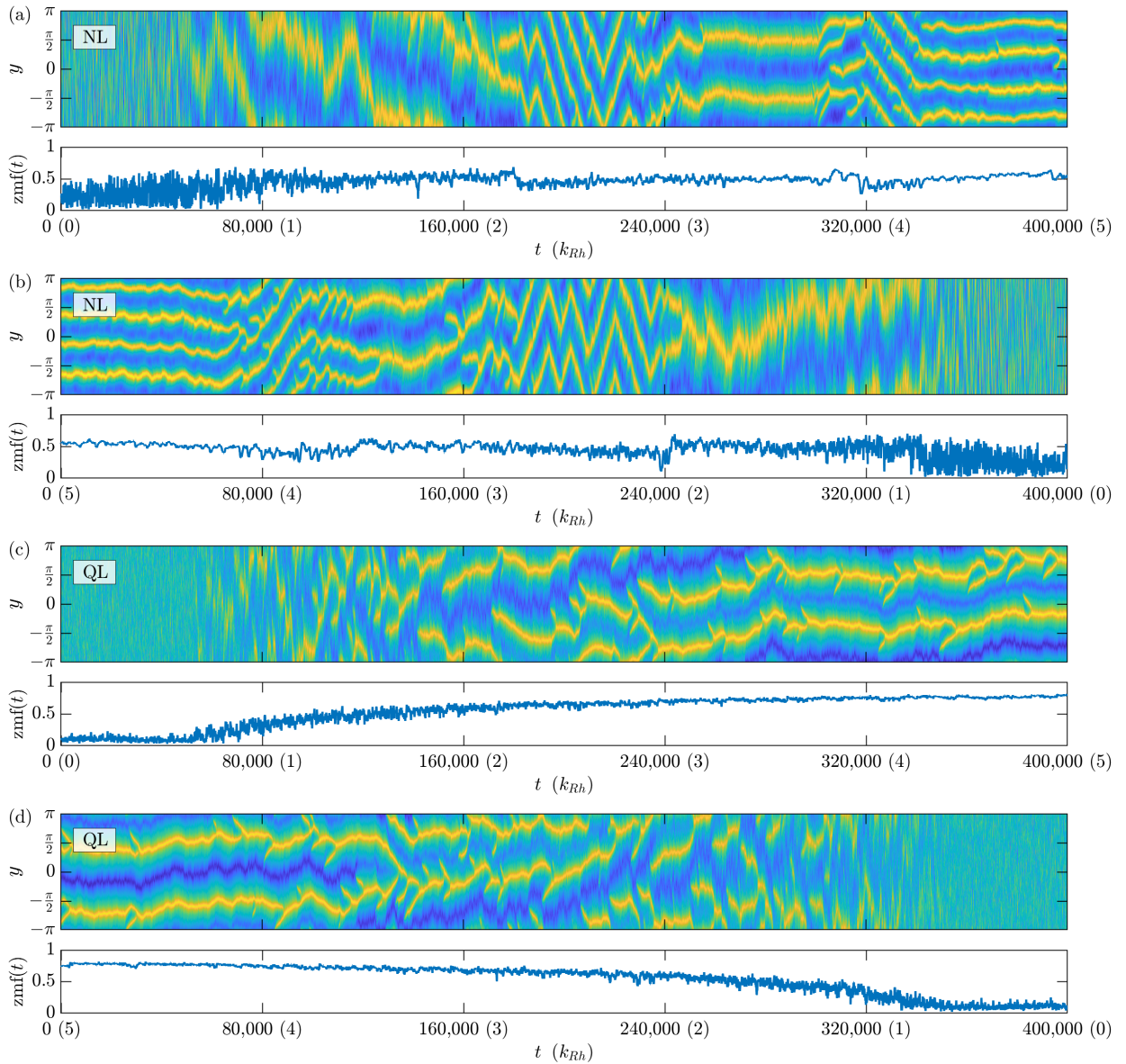


**Figure 4.3** Zonal jet variability regimes observed as the Rhines wavenumber is linearly varied in time over the range  $0 \leq k_{Rh} \leq 5$ . Figures (a) and (b) used the NL model while figures (c) and (d) used the QL model.  $k_{Rh}$  is linearly increased in figures (a) and (c) while in figures (b) and (d)  $k_{Rh}$  is linearly decreased. In each case, the top figure shows a latitude-time plot of the time evolution of the zonal mean zonal velocity field, while the bottom plot shows the corresponding evolution of the zmf index. The parameters used in all plots were:  $0 \leq \beta \leq 12.91$ ,  $\mu = 0.0015$ ,  $\varepsilon = 10^{-4}$ ,  $k_f = 32$ ,  $N = 256$ ,  $0 \leq R_\beta \leq 2.93$ .

Figure 4.3 also serves to highlight more clearly the existence of jet migration behaviour in the NL model, with relatively abrupt transitions into and out of this newly identified variability regime. The clear migration of two jets for  $k_{Rh} \approx 2.5$  and three jets for  $k_{Rh} \approx 4$  in the NL simulations suggests that this type of variability occurs for particular sets of parameters. Equivalent behaviour is not replicated in the QL simulations, in which the jets instead display merging and nucleating behaviour. The bottom panel within each figure displays the time evolution of the zmf index. Whilst there is a certain amount of high-frequency variability in this diagnostic, it does vary fairly consistently in the QL model with the Rhines wavenumber, and consequently, the zonostrophy parameter. On the other hand, the zmf index undergoes jumps in the NL simulations that coincide with the start (finish) of jet migration behaviours as  $k_{Rh}$  increases (decreases).

These jumps, which take place on time scales of  $O(\mu^{-1})$ , imply that the respective rates at which energy is dissipated from the mean flow and the eddies change when the jets migrate, hinting at the role of the nonlinear interactions. In their stable states, migrating jets are weaker relative to the eddies compared with non-migrating configurations.

## 4.2.2 The zoology of non-migrating zonal jets

Having set out the fundamental types of behaviour that exist in the NL and QL frameworks, we now attempt to delve deeper into the zoology of jet variability, going beyond the zonal mean time evolution analysis and focussing in more detail on the sub-range of quasi-steady solutions, or *stable attractors*, by examining the flow structures. We emphasize that the types of variability considered here are *not* exhaustive; it is instead our intention to give a flavour of the rich array of dynamical behaviours. Reserving further discussion of merging and nucleating behaviour to Section 4.4.4 where we discuss transitions more widely, zonal jets can either migrate, or not migrate. We begin with a discussion of (weakly fluctuating) non-migrating configurations; this is followed by a closer look in Section 4.2.3 at jet migration regimes. In each case, we examine the large scale properties of the flow field along with the structure of the underlying eddy field. The streamfunction is ideal for this purpose, helping to visualise coherent structures with its emphasis on the large scales.

### 4.2.2.1 Single jet dynamics

As the number of zonal jets within the domain increases, the taxonomy of solutions becomes ever more complex. This is because the number of possible permutations of configurations, such as the spacing between the jets and the relative strengths of the jets, increase in line with the number of jets. It is therefore instructive to begin with a discussion of the simplest case: that in which a single jet equilibrates. With this in mind, we observe two distinct dynamical regimes in the NL model: pulsing and meandering behaviours, illustrated in Figure 4.4. Whilst these are not distinguishable in the latitude-time plots, they are visible in the instantaneous flow fields.

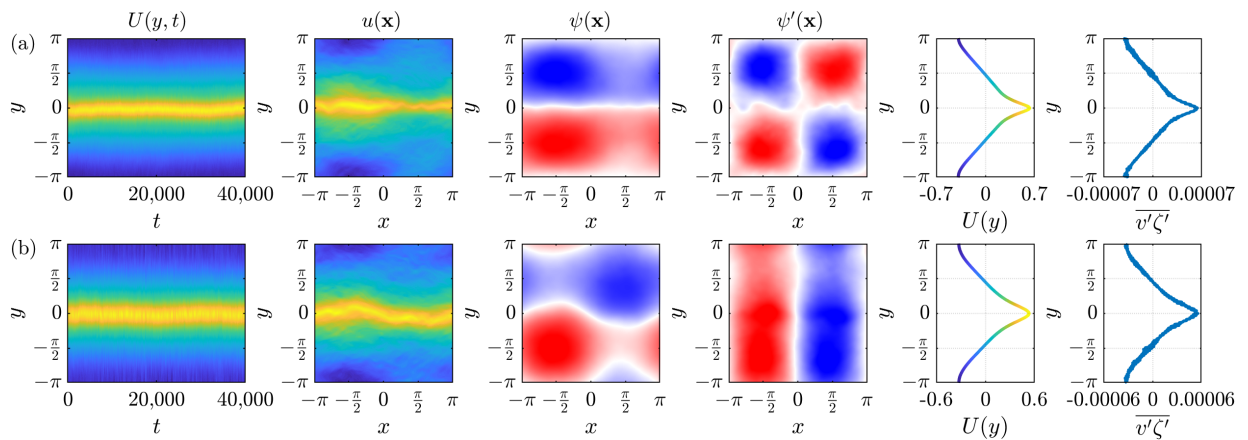


**Figure 4.4** Single zonal jet dynamics in the NL model. From left to right we show a latitude-time plot of the zonal mean zonal velocity field  $U(y, t)$ , a single snapshot of the zonal velocity field  $u(\mathbf{x})$ , the corresponding streamfunction  $\psi(\mathbf{x})$  and eddy streamfunction field  $\psi'(\mathbf{x})$ , the time-averaged jet velocity profile  $U(y)$  and the time-averaged eddy momentum flux convergence  $\overline{v'\zeta'}$ . (a) A pulsing jet with parameters  $\beta = 1.5$ ,  $\mu = 0.0001$ ,  $\varepsilon = 10^{-5}$ ,  $k_f = 16$ ,  $N = 256$ ,  $R_\beta = 4.14$ ; (b) A meandering jet with parameters  $\beta = 0.8$ ,  $\mu = 0.0001$ ,  $\varepsilon = 10^{-5}$ ,  $k_f = 16$ ,  $N = 256$ ,  $R_\beta = 3.89$ .

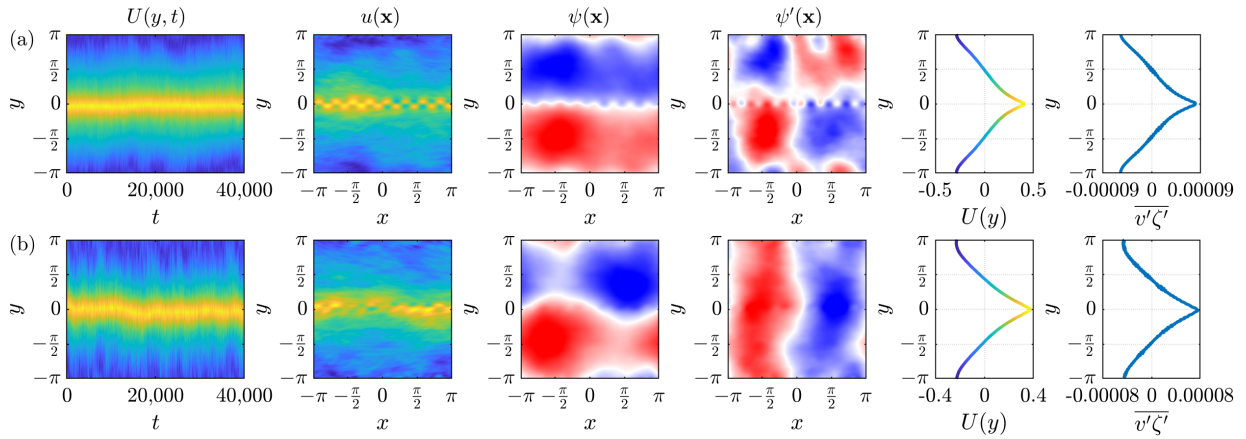


**Figure 4.5** Single zonal jet dynamics in the QL model. From left to right we show a latitude-time plot of the zonal mean zonal velocity field  $U(y, t)$ , a single snapshot of the zonal velocity field  $u(\mathbf{x})$ , the corresponding streamfunction  $\psi(\mathbf{x})$  and eddy streamfunction field  $\psi'(\mathbf{x})$ , the time-averaged jet velocity profile  $U(y)$  and the time-averaged eddy momentum flux convergence  $v'\zeta'$ . (a) A pulsing jet with parameters  $\beta = 1.2$ ,  $\mu = 0.0002$ ,  $\varepsilon = 10^{-5}$ ,  $k_f = 16$ ,  $N = 256$ ,  $R_\beta = 3.41$ ; (b) A meandering jet with parameters  $\beta = 0.4$ ,  $\mu = 0.0002$ ,  $\varepsilon = 10^{-5}$ ,  $k_f = 16$ ,  $N = 256$ ,  $R_\beta = 3.05$ .

Jet *pulsation* (sometimes referred to as varicose behaviour) is associated with the rhythmical strengthening and weakening of the jet along its core, visible in the zonal velocity field in Figure 4.4(a). The associated streamfunction, being symmetric about the jet axis, reveals the straightness of the path of the jet as it flows through the domain. In contrast, *meandering* jets (or sinuous behaviour) follow a winding course rather than flowing in a straight line. The streamfunction, plotted in Figure 4.4(b), reflects this behaviour, having rotational rather than north-south reflectional symmetry. Further insights are obtained by plotting the eddy streamfunction field, defined as  $\psi'(\mathbf{x}) = \psi(\mathbf{x}) - \bar{\psi}(\mathbf{x})$ . In both cases, this reveals a dominant structure with zonal wavenumber  $k_x = 1$  coinciding with the single pulse or meander that is observable in the corresponding zonal velocity field. Accordingly, pulsing behaviour is associated with a coherent wave, given by  $\mathbf{k} = (1, 1)$ , that coexists with the jet while meandering behaviour is associated with a wave given by  $\mathbf{k} = (1, 0)$ . It remains to be seen how these structures materialise in different geometries such as rectangular domains.

It is worth mentioning that each of these states represent idealised limits of dynamical regimes. Indeed, jets are often observed to be transitioning between pulsing and meandering behaviour, exhibiting characteristics of both, however, we make no attempts to classify this continuum of intermediate states. Focusing on situations in which a jet is closely aligned with one of these idealised regimes, we make the qualitative observation that pulsing jets are relatively steady in space and tend to immediately follow a jet merger (as we shall discuss later) while meandering jets are often (but not always) associated with latitudinal shifting or randomly wandering behaviour. Similar modes of variability were observed by Eichelberger and Hartmann (2007) who used a simple GCM to investigate the effects of the zonal jet structure on the variability in the Northern hemisphere. They found that when the Polar and subtropical jets are nearly merged, pulsing behaviour of the combined jet system dominates while the leading mode of variability when the jets are well separated is latitudinal shifting behaviour of the Polar jet. Our findings reinforce the pulsing observations and also suggest that the latitudinal shifting is associated with meandering behaviour.

Turning our attention to the QL model, we seek to ask whether these same dynamical regimes are replicated when eddy-eddy interactions are neglected. It turns out that they are (see Figure 4.5), with a number of caveats. Firstly, it is rare to observe a QL jet close to one of these idealised limits; their variability

usually comprises of a mixture of both. This is evident in Figure 4.5 in which the examples are more disordered due to perturbations away from the ideal structures. Moreover, multiple-jet QL systems are not usually associated with a large-scale coherent wave structure. Whilst the forcing distribution does include modes with  $k_x = 1$ , offering an explanation for these observations, we observe that the eddy streamfunction field becomes increasingly disorganised as the number of jets increase, with smaller scales dominating.

To conclude our discussion of single jet dynamics, we briefly compare the associated jet velocity profiles  $U(y)$  and eddy momentum flux convergences  $\overline{v'\zeta'}$  between the regimes and also the models, plotted in Figures 4.4 and 4.5. The shapes of these profiles are remarkably similar and it is not straightforward to identify differences. In each case, the profiles are latitudinally-symmetric and the eddy momentum flux convergences bear similar forms to the velocity profiles, as we would expect from the steady state momentum balance  $U(y) \approx \mu^{-1} \overline{v'\zeta'}$ . Nevertheless, the shapes of the QL jets are slightly sharper with more pointed cores. In addition, pulsing jets are associated with a narrower core and broader flanks on either side while meandering jets have a more well-rounded core (due to the zonal averaging of the meanders) along with more parabolic westward flows.

#### 4.2.2.2 Zonal jet spacings and strengths

The pulsing and meandering behaviours classified for a single jet state are also applicable to multiple-jet cases. In this case, the behaviour of each jet may independently be dominated by either mode of variability and the situation rapidly becomes complex as the number of jets increase. Of course, multiple jets are also associated with additional degrees of freedom, such as their relative latitudinal spacings and strengths,

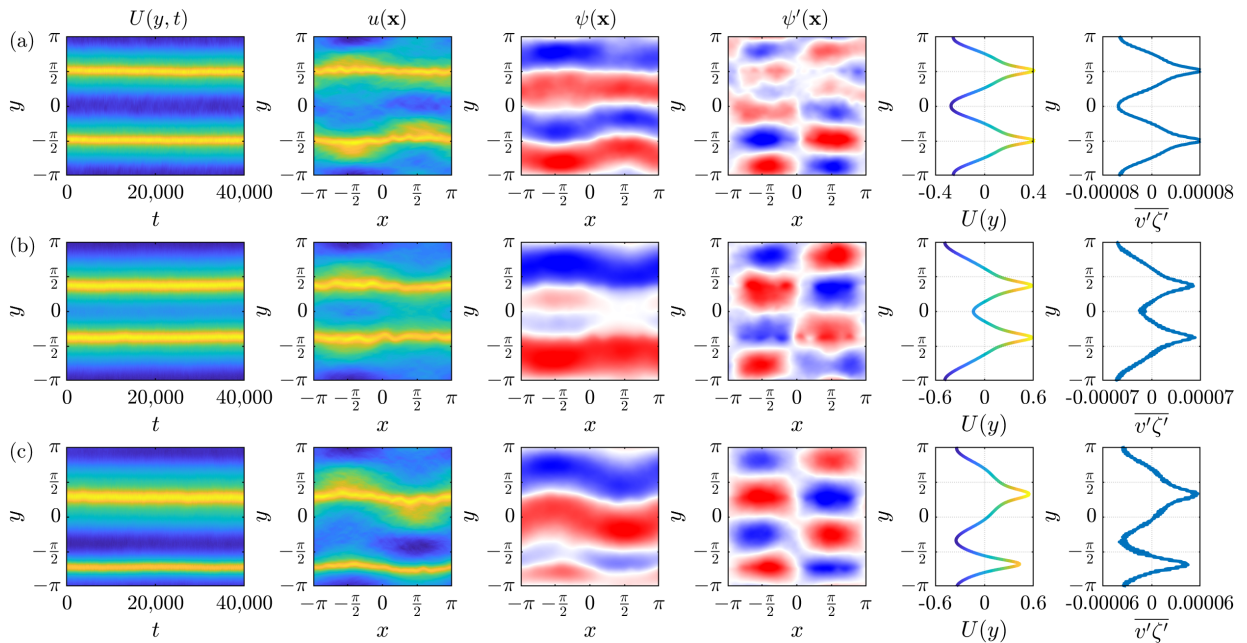


**Figure 4.6** Zonal jet spacings and strengths associated with two jets in the NL model. From left to right we show a latitude-time plot of the zonal mean zonal velocity field  $U(y,t)$ , a single snapshot of the zonal velocity field  $u(\mathbf{x})$ , the corresponding streamfunction  $\psi(\mathbf{x})$  and eddy streamfunction  $\overline{\psi'(\mathbf{x})}$ , the time-averaged jet velocity profile  $U(y)$  and the time-averaged eddy momentum flux convergence  $\overline{v'\zeta'}$ . (a) Two equally spaced and equally-strong jets with parameters  $\beta = 5.5$ ,  $\mu = 0.0002$ ,  $\varepsilon = 10^{-5}$ ,  $k_f = 16$ ,  $N = 256$ ,  $R_\beta = 3.97$ ; (b) Two unequally spaced but equally-strong jets with parameters  $\beta = 3.2$ ,  $\mu = 0.0001$ ,  $\varepsilon = 10^{-5}$ ,  $k_f = 16$ ,  $N = 256$ ,  $R_\beta = 4.47$ ; (c) Two equally spaced but unequally-strong jets with parameters  $\beta = 3.5$ ,  $\mu = 0.0001$ ,  $\varepsilon = 10^{-5}$ ,  $k_f = 24$ ,  $N = 256$ ,  $R_\beta = 4.51$ .

which contribute towards their dynamics. Our findings suggest that each of these aspects are interlinked and should not be considered in isolation. In our classification of variability, we therefore proceed with a discussion of the relative spacings and strengths of jets in multiple-jet configurations, which could be applicable to the Earth's oceans or the gas giant planets.

As before, it is instructive to focus on the simplest scenario which, in this case, is when two jets emerge in the domain. Our analysis of a large number of numerical simulations suggests that there are three distinct arrangements that emerge in the NL model, associated with the symmetries of the spacings and strengths of a pair of jets. Illustrated in Figure 4.6, these include two equally spaced and equally strong jets, two unequally spaced but equally strong jets, and two equally spaced but unequally strong jets. In each case, the jets are observed to meander rather than pulsate, as can be seen in the zonal velocity and streamfunction fields in addition to the relative positioning of  $\psi'(\mathbf{x})$  and the jets. Nevertheless, these cases differ in terms of the relative phases of the meanders, which, in turn, are associated with large-scale Rossby-like waves.

The fully symmetric solution, shown in Figure 4.6(a) in which the jets are equally spaced and equally strong, does not occur frequently. We might naively assume that this state should be the solution when the preferred jet spacing divides the periodic domain size such that two jets are stable; in reality, it is usually observed in configurations when both two and three jets persist, following the jump from three to two jets. The zonal velocity field shows that these jets meander with opposite phases, exhibiting north-south reflectional symmetries that are confirmed by the associated velocity profiles and eddy momentum flux convergences. The eddy streamfunction shows a structure with a very clear zonal wavenumber  $k_x = 1$  mode, and a latitudinal wavenumber  $k_y \approx 3$ , revealing that these jets coexist with an eddy field that is dominated by a coherent wave given by  $\mathbf{k} = (1, 3)$ .

On the other hand, stable two-jet states exhibit a symmetry breaking phenomenon associated with either their spacings or their strengths, as characterised by the other two arrangements shown in Figures 4.6(b-c). The case where the jets are unequally spaced but equally strong in Figure 4.6(b) shows jets meandering with opposite phases, while the equally spaced but unequally strong jets in Figure 4.6(c) meander with equal phases, as shown in their respective zonal velocity and streamfunction fields. These asymmetries are reflected in their respective velocity profiles and eddy momentum flux convergences. In particular, the stronger jet in Figure 4.6(c) has broad, prominent flanks on either side while its weaker neighbour is very narrow. In addition, each jet in Figure 4.6(b) is asymmetric about its own core, being broader on the side that is furthest from its neighbour. Despite these differences, similarities exist in the large-scale structures of their coexistent eddy fields, revealing that both configurations are dominated by a coherent wave given by  $\mathbf{k} = (1, 2)$ . As we will discuss in Chapter 5, we believe that these structures are related to the coexistence of jets with zonons in the NL model which indirectly influence the eddy momentum flux convergences and associated velocity profiles.

As the number of jets in the domain increases, so does the number of possible permutations of these asymmetries associated with their relative spacings and strengths. To be more explicit, we can formulate this symbolically by denoting a jet spacing or strength by  $S$  and assigning an index  $1, 2, \dots$  to refer to the *ordered* magnitude such that higher numbers correspond to larger magnitudes but do not quantify relative sizes. In this case, the spacings in Figures 4.6(a-c) can be represented as  $(S^1, S^1)$ ,  $(S^1, S^2)$  and  $(S^1, S^1)$  while the jet strengths are given by  $(S^1, S^1)$ ,  $(S^1, S^1)$  and  $(S^1, S^2)$ . Extrapolating to the case of three stable jets, the possibilities for each of the spacings and strengths include  $(S^1, S^1, S^1)$ ,  $(S^1, S^1, S^2)$ ,  $(S^1, S^2, S^2)$  and  $(S^1, S^2, S^3)$ . It is clear that as the number of jets increase, these permutations become increasingly

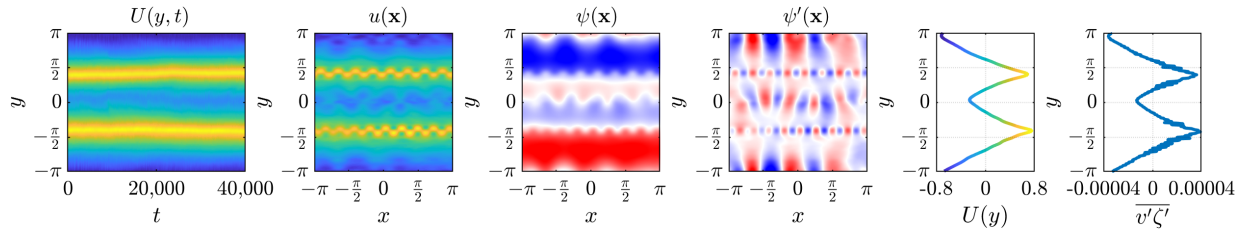


**Figure 4.7** Zonal jet spacings and strengths associated with two jets in the QL model. From left to right we show a latitude-time plot of the zonal mean zonal velocity field  $U(y, t)$ , a single snapshot of the zonal velocity field  $u(\mathbf{x})$ , the corresponding streamfunction  $\psi(\mathbf{x})$  and eddy streamfunction field  $\psi'(\mathbf{x})$ , the time-averaged jet velocity profile  $U(y)$  and the time-averaged eddy momentum flux convergence  $\overline{v'\zeta'}$ . The figure shows two unequally-spaced but equally-strong jets with parameters  $\beta = 6.0$ ,  $\mu = 0.00005$ ,  $\varepsilon = 10^{-5}$ ,  $k_f = 16$ ,  $N = 256$ ,  $R_\beta = 5.66$ .

numerous and so we choose not to proceed further. Nevertheless, we observe that the formulations illustrated in Figure 4.6 are combined in the presence of larger numbers of jets. Together with the single-jet modes of variability, these configurations form the building blocks of multiple-jet dynamical regimes.

The quasilinear approximation excludes some of these arrangements, as illustrated in Figure 4.7. For example, QL jets are *never* observed to be fully symmetric (with the exclusion of the single-jet state). In multiple-jet regimes, meanders are not typically observed and jets are not associated with coherent large-scale eddy fields. Analysis of simulations shows that, while two-jet QL systems only permit an asymmetry in jet spacings, asymmetries in jet strengths do exist, however, weaker jets always occur in pairs, excluding for example  $(S^1, S^2)$  or  $(S^1, S^2, S^2)$ -strength states. We are led to conclude that nonlinear eddy-eddy interactions are essential for the large-scale organisation of the eddy field that coexists with the jets, and that this coherent wave pattern is potentially associated with the existence of certain jet regimes.

### 4.2.3 The zoology of migrating zonal jets

Zonal jet migration has never, to our knowledge, been observed in idealised models in the absence of an imposed latitudinal symmetry-breaking mechanism, such as sloping topography, spherical geometry or statistically inhomogeneous forcing. Of course, latitudinal symmetries are broken when jets undergo fluctuations or randomly wandering behaviour. What is extraordinary is the time-persistence of the migration behaviour and the regularity with which the jets migrate at an apparently preferred translation speed, leading us to refer to both northward and southward migration as stable attractors of the system. There are two types of zonal jet migration that we observe in our simulations: fast migration, where the arrangement of jets obeys a kind of translational symmetry, and slow migration, associated with asymmetric arrangements (aside from the phenomenon described in Appendix D in which the presence of strong vortices leads to jet migration). Extending our previous discussion of non-migrating states, we now discuss in turn each of these types of migration in more detail.

#### 4.2.3.1 Fast zonal jet migration

We choose to term the migration behaviour illustrated in Figure 4.1(c), in which the jets are equally spaced and equally strong (i.e. translationally-symmetric), *fast migration*, short for *fast and symmetric*, because the speed of translation (which will be quantified in Chapters 5 and 6) is significantly faster than the second type, to be discussed shortly. Fast migration is a robust phenomenon that has so far been observed in NL systems with up to three jets. Despite extensive searches, however, it has not been observed in the QL

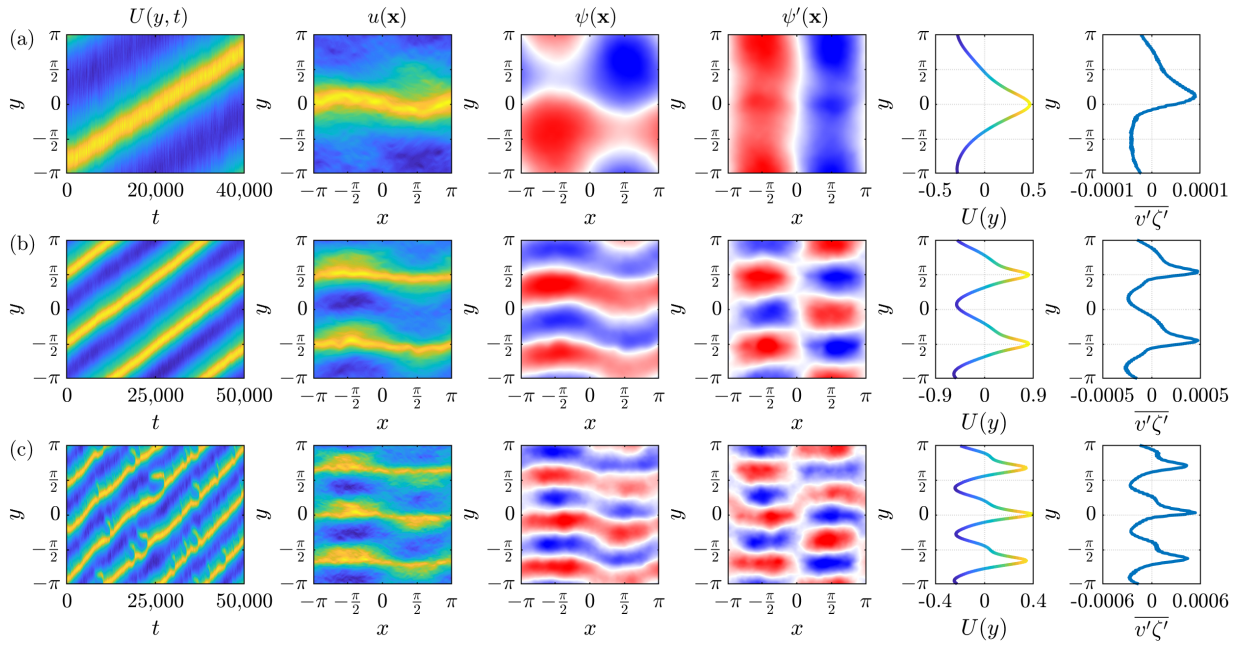


**Figure 4.8** Fast zonal jet migration in the NL model. From left to right we show a latitude-time plot of the zonal mean zonal velocity field  $U(y, t)$ , a single snapshot of the zonal velocity field  $u(\mathbf{x})$ , the corresponding streamfunction  $\psi(\mathbf{x})$  and eddy streamfunction field  $\psi'(\mathbf{x})$ , the time-averaged jet velocity profile  $U(y)$  and the time-averaged eddy momentum flux convergence  $\overline{v'\zeta'}$ . (a) A single migrating jet with parameters  $\beta = 0.45$ ,  $\mu = 0.0001$ ,  $\varepsilon = 10^{-5}$ ,  $k_f = 16$ ,  $N = 256$ ,  $R_\beta = 3.67$ ; (b) Two migrating jets with parameters  $\beta = 6.0$ ,  $\mu = 0.0004$ ,  $\varepsilon = 10^{-4}$ ,  $k_f = 16$ ,  $N = 256$ ,  $R_\beta = 3.77$ ; (c) Three migrating jets with parameters  $\beta = 10.0$ ,  $\mu = 0.001$ ,  $\varepsilon = 10^{-4}$ ,  $k_f = 32$ ,  $N = 256$ ,  $R_\beta = 3.16$ .

model. While migration speeds vary between parameters, each parameter group is associated with its own characteristic translation speed, regardless of the direction in which the jets migrate. Further discussion of jet migration speeds for this fast type of migration is reserved for Chapter 5.

Example simulations are shown in Figure 4.8 in which one, two and three jets are migrating north. In each of these examples, snapshots of the zonal velocity field and the streamfunction show that the jets are meandering, and the relative phases of these meanders are aligned in multiple-jet configurations. The eddy streamfunction is dominated by a coherent wave given by  $\mathbf{k} = (1, n)$  for  $n > 1$  jets, while the structure associated with the single migrating jet is instead given by  $\mathbf{k} = (1, 0)$ , reminiscent of Figure 4.4(b), implying that the meanders of the eastward jet are out of phase with those of the westward jet. The reason for this change of pattern between  $n = 1$  and  $n > 1$  jets is not clear, nevertheless, we will return to this point in Chapter 5. The velocity profiles in all three cases are asymmetric about each jet core, with each jet being broader on the side towards which it migrates. The peaks of the corresponding eddy momentum flux convergences have a small but not insignificant offset (in the direction of migration) from the corresponding jet cores, and their profiles show a marginally stronger north-south asymmetry than the jets themselves.

#### 4.2.3.2 Slow zonal jet migration

A second type of jet migration behaviour is also visible in our simulations, in which the jets have asymmetric strengths and sometimes asymmetric spacings too. These jets migrate with a significantly slower speed than the translationally-symmetric variants (a distinction that will be clarified in Chapter 6) which leads us to term this type of behaviour *slow migration*, short for *slow and asymmetric*. As discussed in Section 4.2.2.2, the breaking of asymmetries in jet strengths or spacings requires two or more jets to be present.

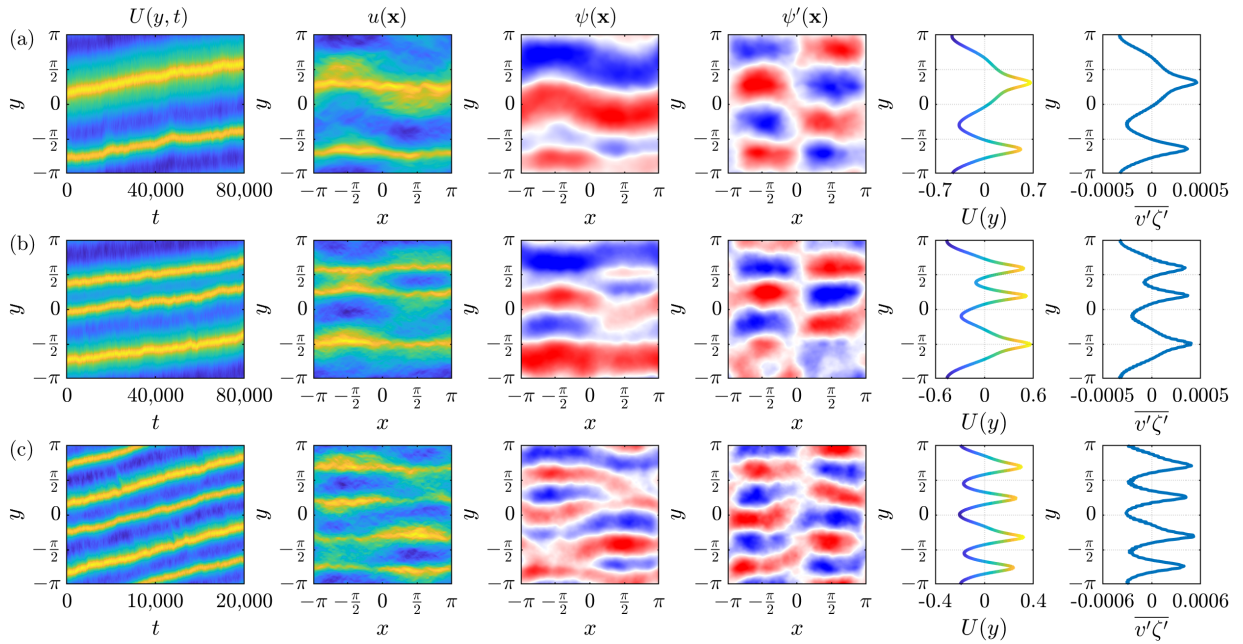


**Figure 4.9** Slow zonal jet migration in the NL model. From left to right we show a latitude-time plot of the zonal mean zonal velocity field  $U(y,t)$ , a single snapshot of the zonal velocity field  $u(\mathbf{x})$ , the corresponding streamfunction  $\psi(\mathbf{x})$  and eddy streamfunction field  $\psi'(\mathbf{x})$ , the time-averaged jet velocity profile  $U(y)$  and the time-averaged eddy momentum flux convergence  $\overline{v'\zeta'}$ . (a) Two migrating jets with parameters  $\beta = 6.0$ ,  $\mu = 0.0007$ ,  $\varepsilon = 10^{-4}$ ,  $k_f = 16$ ,  $N = 256$ ,  $R_\beta = 3.28$ ; (b) Three migrating jets with parameters  $\beta = 9.0$ ,  $\mu = 0.0007$ ,  $\varepsilon = 10^{-4}$ ,  $k_f = 32$ ,  $N = 256$ ,  $R_\beta = 3.42$ ; (c) Four migrating jets with parameters  $\beta = 8.5$ ,  $\mu = 0.0015$ ,  $\varepsilon = 10^{-4}$ ,  $k_f = 32$ ,  $N = 256$ ,  $R_\beta = 2.81$ .

Accordingly, slow jet migration only occurs in multiple-jet configurations, with example NL simulations presented in Figure 4.9 showing cases in which two, three and four jets migrate. The arrangements of the jets are not straightforward to describe, and we are not able to generalise the configurations in the same manner as we did for fast migration when multiple (two or three) jets were present in the domain.

A system in which two jets migrate, with an asymmetry in jet strengths, is shown in Figure 4.9(a). This is the migrating analogue of Figure 4.6(c), with virtually indistinguishable snapshots of the flow field revealing an eddy field that is dominated by a large-scale coherent wave given by  $\mathbf{k} = (1, 2)$ . Systems in which three jets slowly migrate tend to involve asymmetries in both the jet strengths and spacings, often with two weaker jets accompanied by a stronger jet, as illustrated in Figure 4.9(b). In this arrangement, the weaker jets meander with opposite phases while the stronger jet meanders with a phase that is aligned with the closest weaker jet. The eddy streamfunction is dominated by a coherent wave with latitudinal wavenumber that appears to be somewhere between two and three, i.e.  $\mathbf{k} = (1, 2.5)$ . Figure 4.9(c) shows an example of four migrating jets in which the jets are alternately strong and weak. Each pair of jets meanders with opposite phase giving rise to an associated eddy field with dominant structure  $\mathbf{k} = (1, 3)$ . In each of these examples, the latitudinal wavenumber of the dominant eddy field structure does not necessarily equal the number of jets; in fact, there is no discernible relationship between the two. In addition, there is a strong correlation between the velocity profiles and eddy momentum flux convergences, with their degrees of asymmetry about the jet cores being very weak, in contrast to the stronger asymmetries associated with the profiles in Figure 4.8.

Unlike fast migration, we do in fact observe examples of slow migration in the QL model. Arrangements in which three and six jets slowly migrate, albeit with some unsteadiness, are shown in Figure 4.10, and

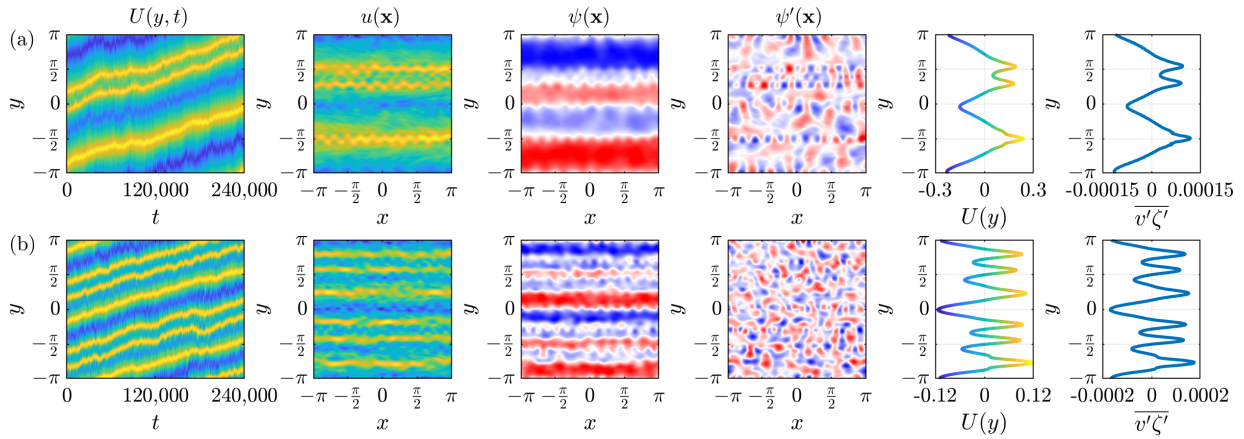


**Figure 4.10** Slow zonal jet migration in the QL model. From left to right we show a latitude-time plot of the zonal mean zonal velocity field  $U(y, t)$ , a single snapshot of the zonal velocity field  $u(\mathbf{x})$ , the corresponding streamfunction  $\psi(\mathbf{x})$  and eddy streamfunction field  $\psi'(\mathbf{x})$ , the time-averaged jet velocity profile  $U(y)$  and the time-averaged eddy momentum flux convergence  $\overline{v'\zeta'}$ . (a) Three migrating jets with parameters  $\beta = 6.5$ ,  $\mu = 0.0005$ ,  $\varepsilon = 10^{-5}$ ,  $k_f = 16$ ,  $N = 256$ ,  $R_\beta = 3.21$ ; (b) Six migrating jets with parameters  $\beta = 7.5$ ,  $\mu = 0.0015$ ,  $\varepsilon = 10^{-5}$ ,  $k_f = 16$ ,  $N = 256$ ,  $R_\beta = 2.47$ .

there are hints of two jets migrating slowly in Figure 4.3(c) in the interval  $180,000 < t < 190,000$ . Beyond the latitude-time plots, however, the similarities with the NL jets are virtually non-existent. We also note that the persistence of slow migration in the QL model is observed to be weaker than that in the NL model. In addition, there is evidently no coherent structure dominating the organisation of the eddy field that coexists with the jets and there is no meandering behaviour. Nevertheless, the lack of a coherent wave structure implies that this is not an essential ingredient for slow migration, leaving open the question regarding what is responsible for the long-time persistence of this behaviour in the NL and QL systems.

Slow migration is much less prevalent, and persistent, than fast migration, and we wouldn't like to rule out the possibility of other configurations (with the same numbers of jets) beyond those already discussed. While in Chapter 5 we propose a mechanism for fast jet migration, we are not able to offer an equivalent explanation for the slow migration behaviour. The fact that this latter regime occurs less frequently suggests that the mechanism may be weaker and less easily identifiable. What is clear, however, is that nonlinear eddy-eddy interactions do not play a role; this is a point that we shall return to in Chapter 6.

### 4.3 The dependence of variability on system parameters

The classification of beta-plane zonal jet dynamics was constructed after analysing a large number of NL and QL numerical simulations across a broad range of parameters. Our discussions have thus far been independent of the role of these parameters, focussing instead on a description of the fundamental constituents of variability. However, some types of variability are found to be parameter-dependent, such as the spacings, strengths and structures of zonal jet solutions. It is therefore our goal in this section to document how certain aspects of variability are influenced by these parameters, in particular, the importance of the Rhines scale, the zonostrophy parameter and the forcing wavenumber.

#### 4.3.1 Parameter space and zonostrophic flow regimes

We begin by defining a parameter space in order to visualise our simulations. The key parameters of interest in this study are the Rhines wavenumber,  $k_{Rh}$ , which is believed to be linked to the latitudinal spacing

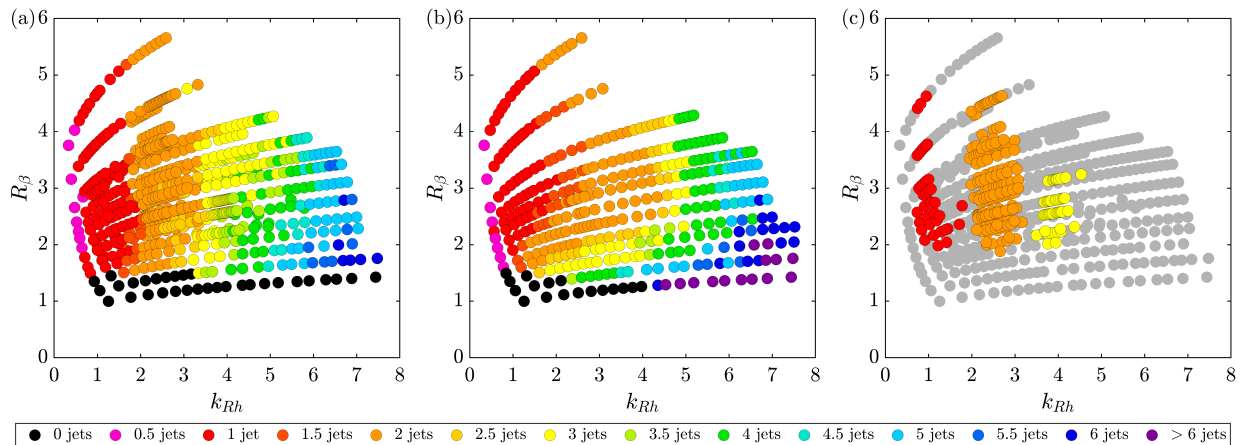


**Figure 4.11** The parameter space defined in terms of the ideal Rhines wavenumber,  $k_{Rh}$ , along the horizontal axis and the ideal zonostrophy parameter,  $R_\beta$ , along the vertical axis. The data includes 839 NL and 547 QL simulations with resolution  $N = 256$  across a range of forcing wavenumbers  $k_f \leq 32$ . Each point represents a single simulation that is coloured according to the average number of jets within the domain over long-time averages, with non-integral numbers allowed for merging and nucleating behaviours. (a) All NL simulations; (b) all QL simulations; (c) same as (a) except only those simulations in which the jets migrate (fast-type) are coloured.

between the jets, the zonostrophy parameter,  $R_\beta$ , which is considered to be a measure of the strength of the jets, and the wavenumber,  $k_f$ , associated with the stochastic forcing. Strictly speaking, our parameter space should be three-dimensional, however, we note that for clarity we choose to represent it in two-dimensions in terms of  $k_{Rh}$  and  $R_\beta$  and reserve our discussion of the dependence on  $k_f$  to Section 4.3.4.

Figures 4.11(a) and 4.11(b) show the broad range of numerical simulations that we have run, plotted on the respective NL and QL parameter spaces. Each point corresponds to an individual simulation, positioned according to its ideal Rhines wavenumber and zonostrophy parameter, and defined with a colour that represents the average number of jets within the domain, computed over long-time averages. Due to the common occurrence of simulations in which the number of jets is not well-defined due to oscillations as a result of jet mergers and nucleations, we include fractional numbers where necessary. In addition, those simulations in which the zonal mean zonal flow did not reveal the formation of jets are shown in black.

The NL model shows a clear transition at  $R_\beta = 1.5$ , below which the turbulence remains isotropic and is dominated by vortices rather than the formation of zonal flows. This is consistent with the findings of Galperin et al. (2010) for the transition between their friction-dominated regime (in which jets do not form) and the transitional regime (in which jets are visible after averaging the flow field). In addition, the number of jets clearly increases with  $k_{Rh}$ , however, there are no sharp boundaries as the system transitions between  $n$  and  $n + 1$  jets. On the other hand, the QL model reveals evidence of zonostrophy and jet formation when  $R_\beta < 1.5$ , particularly as  $k_{Rh}$  increases. In addition, the relationship between the number of jets and the Rhines wavenumber in the QL model shows evidence of a dependence on zonostrophy for  $R_\beta \lesssim 2$ , i.e. in the transitional regime, where the number of jets increases as the zonostrophy decreases. This is visible to some extent in Figures 4.3(c,d), suggesting that the QL model systematically differs from the NL model when the zonostrophy parameter is too small. We believe that this is related to the linear stability results of Farrell and Ioannou (2007), in which the latitudinal scale of the jets was determined by the most unstable linear mode for weak forcing.

In addition to providing the reader with a visualisation of the range of numerical simulations that are included in this study, the parameter space is also useful for highlighting those parameters for which the

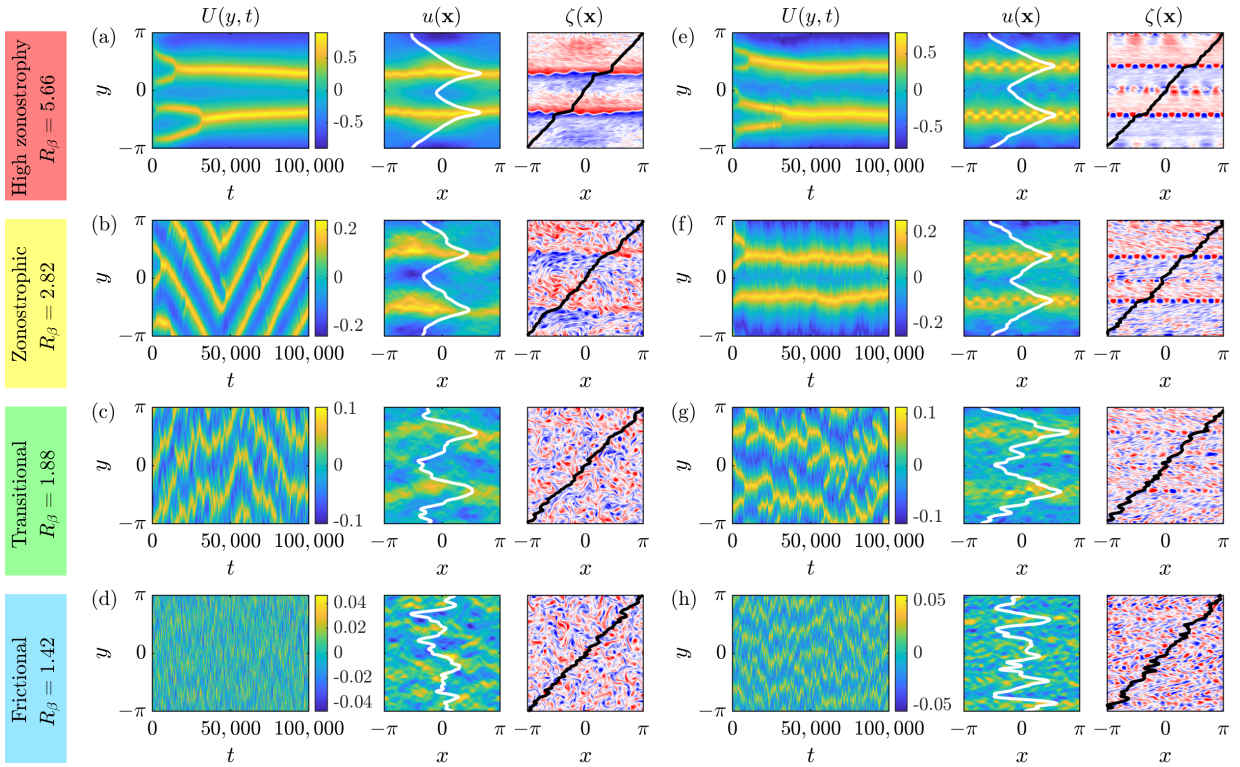


**Figure 4.12** Zonostrophic flow regimes in the NL and QL models in which  $k_{Rh} = 2.6$ ,  $k_f = 16$  and  $N = 256$ . Figures (a-d) correspond to the NL model and figures (e-h) correspond to the QL model. Plotted from left to right are: a latitude-time plot of the zonal mean zonal velocity, a snapshot of the zonal velocity field  $u(\mathbf{x})$ , and the corresponding vorticity field  $\zeta(\mathbf{x})$ . White lines show the instantaneous jet velocity profile  $U(y)$  and black lines show the corresponding zonal mean potential vorticity  $\zeta + \beta y$ . Top row: *high zonostrophy* (parameters  $\beta = 6.0$ ,  $\mu = 0.00005$ ,  $\varepsilon = 10^{-5}$ ,  $R_\beta = 5.66$ ); Second row: *zonostrophic regime* (parameters  $\beta = 1.8$ ,  $\mu = 0.0005$ ,  $\varepsilon = 10^{-5}$ ,  $R_\beta = 2.82$ ); Third row: *transitional regime* (parameters  $\beta = 1.0$ ,  $\mu = 0.002$ ,  $\varepsilon = 10^{-5}$ ,  $R_\beta = 1.88$ ); Bottom row: *friction-dominated regime* (parameters  $\beta = 0.6$ ,  $\mu = 0.005$ ,  $\varepsilon = 10^{-5}$ ,  $R_\beta = 1.42$ ).

fast type of jet migration occurs. These regions are clearly-defined and are shown in Figure 4.11(c) by those simulations which have been denoted colours. With a few exceptions, there is a clear dependence on  $k_{Rh}$ , with jets being observed to migrate over certain discrete intervals of this continuous range. In addition, migration only occurs for  $R_\beta \geq 2$ , i.e. the zonostrophic regime identified by Galperin et al. (2010), which excludes most of the terrestrial zonal jet systems. In addition, our relatively small number of high-zonostrophy simulations suggest that it may not persist for very large zonostrophy in which  $R_\beta \geq 5$ , which would also exclude the strong jets in the atmospheres of the gas giant planets in which  $R_\beta > 5$ . It would appear, therefore, that migration behaviour is a phenomenon that requires well-defined, but moderately-strong, zonal jets, and that the relationship between the preferred jet spacing and the Rhines scale is crucial for its existence.

In order to visualise the data in Figure 4.11 and get a feel for the role of the zonostrophy parameter along the vertical axis, we have chosen a single Rhines wavenumber,  $k_{Rh} = 2.6$ , and selected four example simulations representing the friction-dominated regime ( $R_\beta < 1.5$ ), the transitional regime ( $1.5 < R_\beta < 2$ ), the zonostrophic regime ( $R_\beta > 2$ ), and a simulation which we consider to have high zonostrophy ( $R_\beta > 5$ ). Figure 4.12 shows latitude-time plots of the zonal mean zonal velocity evolution for each of these examples in both the NL (left) and QL (right) models. In addition, we show snapshots of the zonal velocity field and the vorticity field, along with the instantaneous jet velocity profile (white lines) and the zonal mean

potential vorticity distribution (black lines) in order to visualise how the strength of the jets and the degree of anisotropy vary with the zonostrophy parameter.

The NL model shows little evidence of zonal jet formation in the frictional regime, in either the latitude-time data or the individual flow snapshots. In the transitional regime, we observe two zonal jets displaying hints of migration, however, rapid fluctuations prevent the system from persisting in a stable state. Whilst weak jets are almost visible in the corresponding zonal velocity field, very little anisotropy can be seen in the vorticity field without applying a spatial average. The zonostrophic regime, nevertheless, exhibits increasing anisotropy in the vorticity field, where we begin to see some layering in the distribution. This is also associated with two strong jets in the zonal velocity field, visible in both the two-dimensional flow field and the zonally-averaged profile, along with persistent fast migration (due to the choice of  $k_{Rh}$ ) in the latitude-time data. At high-zonostrophy, the migration behaviour disappears, leaving two robust jets that dominate the organisation of the flow field, leading to a stronger layering of the vorticity field.

There are some notable differences in the QL model, as predicted by the parameter space. Firstly, the friction-dominated regime shows approximately four weak jets in the latitude-time plot that fluctuate significantly, even though the flow snapshots barely show any degree of anisotropy. Between two and three zonal jets are visible in the transitional regime in the latitude-time data, undergoing continuous mergers and nucleations. Here, the jets can be distinguished in the snapshot of the zonal velocity field, and perhaps to a small extent in the vorticity field. The zonostrophic regime, while capturing the correct number of jets, instead fails to capture the same behaviour as the NL model. Here, the jets are not migrating; rather, we observe two equally-strong but unequally-spaced jets which also show a distinct signature in the flow field snapshots. Finally, as we reach high-zonostrophy, the QL jets begin to resemble the NL jets, in terms of their strengths, spacings and the stronger anisotropy and layering present in their flow fields. It is interesting that this same tendency towards layering in the potential vorticity field is observed in the QL model, despite the fact that potential vorticity is not materially conserved here.

### 4.3.2 Relationship between the Rhines scale and jet spacings

We now turn our attention to examine the dependence of aspects of variability on individual parameters in more detail, starting with the Rhines wavenumber and its association with the number of jets in the domain. In Figure 4.13 we plot the observed number of jets, which we shall denote  $k_{jet}$ , against the Rhines wavenumber,  $k_{Rh}$ , for all NL and QL numerical simulations. Each data point represents a single simulation and the colours denote the zonostrophy parameter. We include a range of forcing wavenumbers since no systematic dependence on  $k_f$  was observed. Results highlight a linear trend for each model, with less variability associated with jet spacings in the NL simulations. The larger spread of data from the QL model appears to be accounted for by the over-estimation of  $k_{jet}$  by those simulations with low zonostrophy.

Lines of best fit, computed using all data points, suggest that the linear relationship in each case has an identical prefactor, such that  $k_{jet} = 0.77k_{Rh}$ . However, given our concerns regarding the applicability of the QL model for  $R_\beta \lesssim 2$ , we choose instead to include only those simulations that lie within the zonostrophic regime. This includes 740 NL and 441 QL simulations, where the respective relationships are given by

$$\text{NL model: } k_{jet} = 0.80k_{Rh}; \quad \text{QL model: } k_{jet} = 0.72k_{Rh}. \quad (4.1)$$

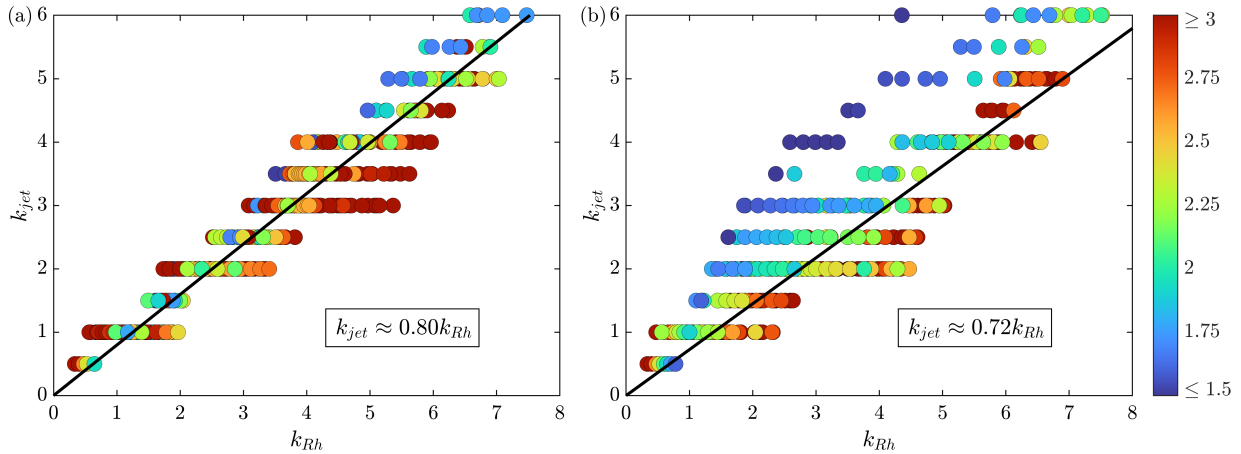


**Figure 4.13** The relationship between the number of jets,  $k_{jet}$ , and the Rhines wavenumber,  $k_{Rh}$ , in the (a) NL model and (b) QL model. Each point represents a single simulation that is coloured according to zonostrophy parameter,  $R_\beta$ . The data includes 839 NL and 485 QL simulations across a range of forcing wavenumbers  $k_f \leq 32$ . Lines of best fit denote the average relationship when all simulations such that  $R_\beta \geq 2$  are included.

There is now a small bias in favour of fewer jets in the QL model, indicating on average a 10% reduction. This difference between systems could be attributed to the tendency of the QL model to be associated with higher zmf indices (to be discussed in Section 4.3.3), in which a larger fraction of the energy is contained in the zonal mean zonal flow. Faster flowing jets are associated with larger spacings, as is evident from the definition of the Rhines scale,  $L_{Rh} = (2U/\beta)^{1/2}$ . Another possible explanation would be more complete mixing taking place in the NL model, leading to a greater propensity of the potential vorticity field to form layers, which in turn would support more jets for a given total energy. It is noted, however, that there is limited evidence for this in Figure 4.12.

Our findings are broadly in agreement with other studies which have also sought to establish a relationship for jet spacings. For example, theoretical studies by Dunkerton and Scott (2008) and Dritschel and McIntyre (2008) deduced that the exact relationship that is valid in the limit of zonally symmetric perfect potential vorticity staircases is  $k_{jet} = k_{Rh}/\sqrt{6}$ . In terms of numerical studies, Farrell and Ioannou (2007) noted an approximate agreement between jet spacings and the Rhines scale within their barotropic SSST system, provided that the turbulence is sufficiently strong. Panetta (1993) instead used a two-layer (baroclinic) beta-plane model and also found that the number of jets is given by the Rhines scale, such that  $k_{jet} = k_{Rh}$ , while a smaller prefactor, close to 0.4, was deduced by Williams and Kelsall (2015) in their baroclinic system. We note, however, that each of these numerical studies used a relatively small number of simulations covering a narrower range of parameters to those which have been simulated here. Nevertheless, there is consistency with the prefactor being of  $O(1)$  in each case, and we attribute the relatively small discrepancies to modelling differences.

### 4.3.3 Influence of the zonostrophy parameter on jet strengths

The zonostrophy parameter is also closely linked to aspects of zonal jet variability, including the strength of the jets relative to the eddies (defined, for instance, by the zmf index). By modifying ideas presented in Galperin et al. (2014), we propose a relationship between the zonostrophy parameter and the zmf index using theoretical scaling arguments. Explicitly, we consider a simple model in which the zonal,  $\mathcal{E}_Z(k)$ , and eddy,  $\mathcal{E}_R(k)$ , kinetic energy spectra are composed, respectively, of the zonostrophic and isotropic

inertial energy cascades (given by equations (2.21) and (2.25)) for wavenumbers larger than the Rhines wavenumber,  $k_{Rh}$ , and zero for smaller wavenumbers. This gives

$$\mathcal{E}_Z(k) = 0, \quad k < k_{Rh}, \quad (4.2)$$

$$\mathcal{E}_Z(k) = C_\beta \beta^2 k^{-5}, \quad k > k_{Rh}, \quad (4.3)$$

for the zonal kinetic energy spectra, and

$$\mathcal{E}_R(k) = 0, \quad k < k_{Rh}, \quad (4.4)$$

$$\mathcal{E}_R(k) = C_\varepsilon \varepsilon^{2/3} k^{-5/3}, \quad k > k_{Rh}, \quad (4.5)$$

for the eddy kinetic energy spectra. Analytic expressions for the zonal kinetic energy density,  $E_Z$ , and the eddy kinetic energy density,  $E_R$ , can then be found by integrating these expressions over all wavenumbers:

$$E_Z = \int_0^\infty \mathcal{E}_Z(k) dk = \int_{k_{Rh}}^\infty C_\beta \beta^2 k^{-5} dk = \frac{1}{4} C_\beta \beta^2 k_{Rh}^{-4}, \quad (4.6)$$

$$E_R = \int_0^\infty \mathcal{E}_R(k) dk = \int_{k_{Rh}}^\infty C_\varepsilon \varepsilon^{2/3} k^{-5/3} dk = \frac{3}{2} C_\varepsilon \varepsilon^{2/3} k_{Rh}^{-2/3}. \quad (4.7)$$

Arguing that the ratio of constants is approximately  $(C_\beta/C_\varepsilon)^{3/10} \simeq 0.5$ , and using expression (2.24) for the transitional scale,  $k_\varepsilon$ , we can derive an anisotropy index,  $\Gamma$ , giving the ratio of zonal to eddy kinetic energy:

$$\Gamma \equiv \frac{E_Z}{E_R} = \frac{\frac{1}{4} C_\beta \beta^2 k_{Rh}^{-4}}{\frac{3}{2} C_\varepsilon \varepsilon^{2/3} k_{Rh}^{-2/3}} = \frac{1}{6} \left( \frac{C_\beta}{C_\varepsilon} \right) \left( \frac{\beta^3}{\varepsilon} \right)^{2/3} k_{Rh}^{-10/3} = \frac{1}{6} \frac{k_\varepsilon^{10/3}}{k_{Rh}^{10/3}} = \frac{1}{6} R_\beta^{10/3}. \quad (4.8)$$

A simple calculation then gives an analytical expression for the dependence of the zmf index, defined in expression (3.11), on the zonostrophy parameter, which can be formulated as

$$\text{zmf} = \frac{E_Z}{E_Z + E_R} = \frac{\Gamma}{1 + \Gamma}. \quad (4.9)$$

Seeking to verify this expression using our simulation data and investigate its applicability to the QL model, we compare this analytical result to data from a large number of simulations. The results are shown in Figure 4.14, in which the points represent individual simulations (plotted using ideal values of  $R_\beta$  and time-averages of  $\text{zmf}(t)$ ) and the black curve shows the analytical relationship (4.9) for comparison.

Figures 4.14(a) and 4.14(b) correspond to the NL and QL models respectively, where we observe that all simulations lie below this analytical curve, with values of zmf emerging below the predicted values. This is especially true in the NL model, which in general is associated with lower zmf indices than the QL model, and could either be due to damping effects as a result of the hyperviscosity, or else the model for wavenumbers  $k < k_{Rh}$  requires an adjustment. Nevertheless, there are qualitative similarities in the distributions of data and the shape of relationship (4.9), albeit with some variability. This is particularly apparent for the NL model, which closely follows the theoretical trend for low and high zonostrophy, however, there is a large degree of variability in the zonostrophic regime when  $R_\beta > 2$ . On the other hand, there is a tighter relationship between the zmf index and the zonostrophy parameter in the QL model (provided  $R_\beta > 2$ ), however, there is evidence that the zmf index for QL simulations asymptotes to a value

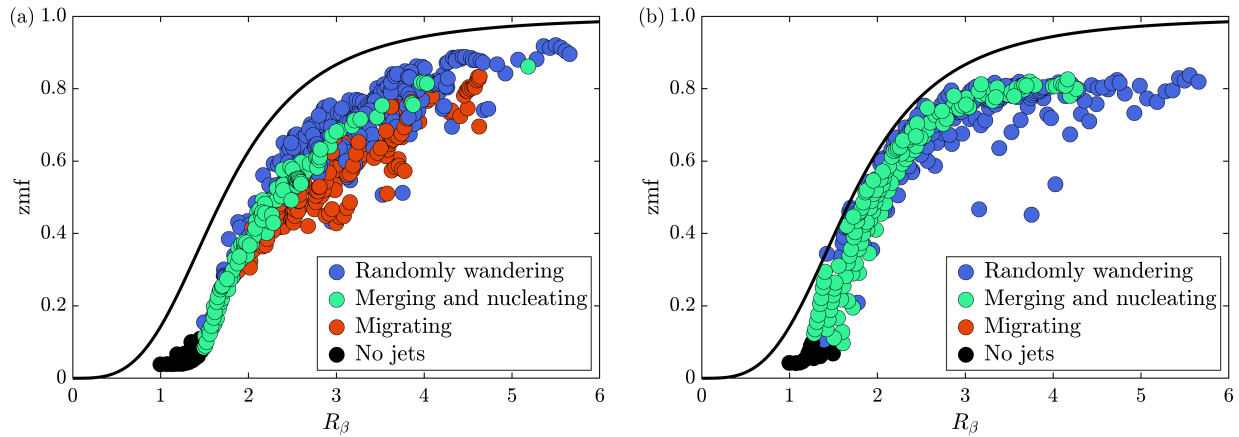


**Figure 4.14** The relationship between the zonestrophy parameter,  $R_\beta$ , and the zmf index for a large collection of 629 NL simulations and 366 QL simulations in which  $k_f = 16$ . Figure (a) corresponds to the NL model while figure (b) corresponds to the QL model. Each point represents a single simulation in which an average of the zmf index has been computed over a time period during which the fundamental type of variability, denoted by the colour, remains unchanged. The black curves plot the theoretical relationship in expression (4.9) using  $C_\beta = 0.5$ .

that is less than one as  $R_\beta \rightarrow \infty$ . Further simulations would need to confirm this potentially significant result, nevertheless, this suggests that the modelling assumptions used to derive (4.9) may not be valid for the QL model, unlike the NL model which shows stronger evidence of conforming to the pattern.

Proceeding to investigate the relatively large spread of zmf values for any given zonestrophy parameter in the zonestrophic regime, and the potential dependency on aspects of variability, each point in Figures 4.14(a) and 4.14(b) has been assigned a colour according to the main type of dynamical behaviour observed. Those simulations in which more than one type of variability persisted were categorised according to the type which persisted over the longest time period. In these cases, the zmf index was averaged only over the time period in which the selected behaviour was observed. There are clear patterns associated with the relationship between the zonestrophy parameter and the zmf index with regards to dynamical regimes in the NL model. Here, migrating jets have a preference for lower zmf values, while randomly wandering jets are most likely to be associated with the highest values, lying closest to the analytical curve. On the other hand, merging and nucleating systems would appear to have a well-defined relationship in the NL model, occurring at the interface between the randomly wandering and migrating behaviours.

Similar dependencies of the QL simulations on their dynamical regimes are less clear, however, we note that the spread of data this time is attributed solely to randomly wandering jets. A closer investigation (not plotted), shows that the outliers with significantly smaller zmf indices all correspond to single-jet regimes in which there may be a domain size limitation constraining the width of the jet. Thus, we believe that in general, the zonestrophy parameter and the zmf index are closely related in the QL model, with no dependency on aspects of variability, in contrast to the NL model which does depend on the behaviour of the jets. These findings agree with and generalise the observations in Figure 4.3, in which the zmf index in the NL model depended on the type of dynamical behaviour, whereas in the QL model it varied continuously with the Rhines scale, or equivalently, the zonestrophy parameter.

#### 4.3.4 Influence of the forcing wavenumber on jet widths

In addition to the Rhines scale and the zonestrophy parameter, we have also investigated the effect that the scale of the forcing has on the large-scale properties of solutions. Whilst we do not observe any significant

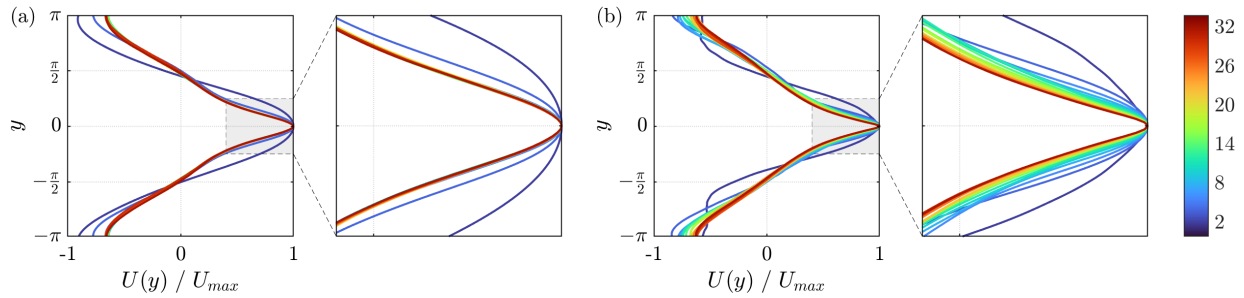


**Figure 4.15** The effect of the forcing wavenumber  $k_f \in [2, 4, 6, \dots, 32]$ , denoted by colour, on the jet velocity profile  $U(y)$  normalised by its maximum value  $U_{max}$  for the (a) NL model and (b) QL model. Time averages were computed over intervals during which the positions of the jets were quasi-stationary. Insets show enlarged versions of the grey regions around the jet cores. The parameters used are:  $\beta = 0.8$ ,  $\mu = 0.0002$ ,  $\varepsilon = 10^{-5}$ ,  $N = 256$ ,  $R_\beta = 3.27$ .

dependency on jet strengths or jet spacings, there are interesting differences between the NL and the QL models with regards to how the latitudinal widths of the emergent zonal jets vary with  $k_f$ .

In Figures 4.15(a,b) we plot the jet velocity profile  $U(y)$  normalised by its maximum value  $U_{max}$  for a set of simulations in which  $k_f \in [2, 32]$ , keeping all other parameters constant. In each case, a single jet equilibrates with a well-defined velocity profile except for the gravest forcing wavenumber  $k_f = 2$ . Figure 4.15(a) shows that the NL jet profile is almost identical in each case except for the largest wavenumbers  $k_f \leq 4$ , indicating that  $k_f$  plays no role in the structure of the emergent solutions. However, there is evidence of a  $k_f$ -dependence in the QL model, shown in Figure 4.15(b). Here we see that the jets have a tendency to become narrower around their core as the scale of the forcing decreases, however, we remark that this does not affect the spacing between the jets, or equivalently the number of jets that emerge in the domain. The fact that the QL model does not admit universal jet profiles, independent of  $k_f$ , presumably relates to the fact that its eddy wavenumber spectrum (not plotted) is marginally less universal than in the NL model.

## 4.4 Hysteresis, non-uniqueness and spontaneous regime transitions

Zonal jet variability is a rich, but complex, topic, with complexities reaching beyond our simple classification. Indeed, the precise behaviours of jets and their configurations within the domain are not fully predictable based upon the system parameters. In some instances, we observe dependencies on previous states of the system as parameters are varied; in others, we observe the existence of multiple stable solutions (keeping parameters fixed). In addition, the system has the capacity to rapidly transition between different stable configurations, giving rise to spectacular behaviours. In this final section, we seek to uncover some of these complexities in order to complete our categorisation of variability.

### 4.4.1 Hysteresis as $\beta$ varies

The dependence of the state of a system on its history is known as *hysteresis*. Such tendencies are often investigated by varying a single parameter during the course of a simulation, such as the Rhines wavenumber in Figure 4.3. By systematically increasing and decreasing the chosen parameter, it is possible to investigate how the state of the system depends on its previous values. We investigate hysteresis behaviour in the both the NL model and the QL model by linearly increasing or decreasing the value of  $\beta$  in time over the range  $0 \leq \beta \leq 8$ , ensuring that the rate of change of  $\beta$  is significantly slower than other time scales of motion within the system, whilst keeping all other parameters fixed. The simulations are spun-up prior to the

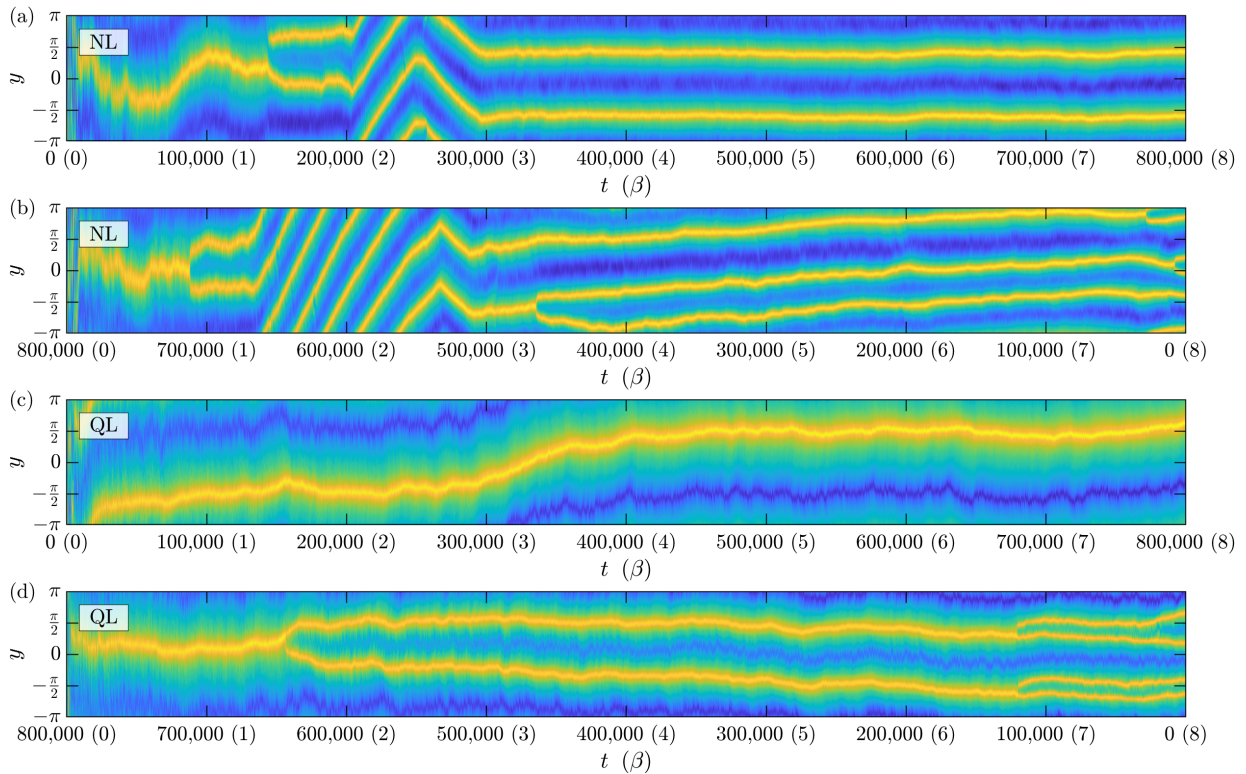


**Figure 4.16** Hysteresis observed as the parameter  $\beta$  is linearly varied in time over the range  $0 \leq \beta \leq 8$ . Figures (a) and (b) used the NL model while figures (c) and (d) used the QL model.  $\beta$  is linearly increased in figures (a) and (c) while in figures (b) and (d)  $\beta$  is linearly decreased and the direction of time is reversed. The parameters used in all plots were:  $\mu = 0.0004$ ,  $\varepsilon = 10^{-5}$ ,  $k_f = 16$ ,  $N = 256$ ,  $0 \leq R_\beta \leq 3.46$ .

commencement of changes of  $\beta$ . Latitude-time plots of the zonal mean zonal velocity field are shown in Figure 4.16 for each of these cases, with  $t = 0$  denoting the time when  $\beta$  begins to change, not the initial spin-up time. The direction of time has been reversed in Figures 4.16(b,d) for ease of comparison.

As  $\beta$  increases, the NL model shows the initial formation of a single jet, followed by a second jet when  $\beta \approx 1.5$ . No further jets form, resulting in a configuration in which two strong zonal jets are present when  $\beta = 8$ . In the reverse experiment, we observe the initial formation of between three and four jets when  $\beta = 8$ , followed by a series of mergers as  $\beta$  decreases towards zero. This difference in jet numbers is even more pronounced in the QL model, where we see that the system fails to allow jet nucleations as  $\beta$  increases. Consequently, the domain contains a single strong jet when  $\beta = 8$  compared with four jets when the reverse experiment is performed. Thus, hysteresis is present in both systems, however, it does seem to be dependent on parameter values since it was not detectable in Figure 4.3 in which a similar type of experiment was performed. We speculate that hysteresis arises due to the propensity with which jets can merge (as  $\beta$  decreases) rather than nucleate (as  $\beta$  increases) - a point that we shall return to in Chapter 6.

#### 4.4.2 Existence of multiple stable attractors

The existence of multiple stable configurations may or may not be manifested through hysteresis. Indeed, different ensemble members or very long integrations (keeping all parameters fixed) highlight the presence of multiple attractors, along with spontaneous transitions between these attractors. At the most basic level, this could represent, for example, the non-uniqueness of jet numbers that occur via merging and nucleating behaviours, as predicted using statistical approaches (Farrell and Ioannou, 2007) or by analogy with pattern

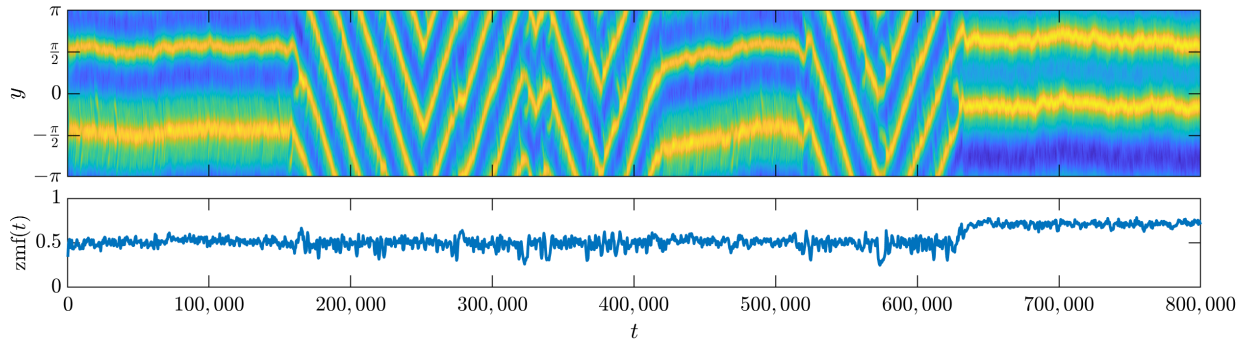


**Figure 4.17** The existence of multiple stable attractors in the NL model, illustrated using a numerical simulation that is run over a long time period. The top figure shows a latitude-time plot of the zonal mean zonal velocity field, and the bottom figure shows the corresponding evolution of the zmf index. The parameters used were:  $\beta = 1.5$ ,  $\mu = 0.0005$ ,  $\varepsilon = 10^{-5}$ ,  $k_f = 16$ ,  $N = 256$ ,  $R_\beta = 2.77$ .

formation (Parker and Krommes, 2013). It also includes the possibility of multiple stable attractors in configurations where the number of jets is fixed.

A particularly striking example is illustrated in Figure 4.17 in which the long-time evolution of a simulation with fixed parameters spontaneously transitions between at least four different stable attractors, each involving a pair of jets. These include two equally spaced but unequally strong jets, two unequally spaced but equally strong jets, and fast migration in both the northward and southward directions. Each regime is associated with its own average zmf index such that regime transitions in some cases involve increased rates of energy transfer between the zonal mean flow and the eddy field. We note that bistability in the QL model appears to be restricted to jet numbers rather than specific dynamical regimes, with the QL simulations showing more predictability for a given set of parameters. Consequently, the nonlinear eddy-eddy interactions play an important role in the complex behaviour that we observe in the fully nonlinear system, as we discuss further in Chapter 5.

#### 4.4.3 The dynamics of spontaneous regime transitions

We complete our categorisation of zonal jet variability with a discussion of spontaneous transitions between stable attractors, noting that we aim to lay the foundations rather than provide an exhaustive list of possibilities. The first case that we wish to discuss is merging behaviour, involving a reduction in the number of jets. Choosing to focus on the simplest case, we investigate the dynamical behaviour when a pair of jets merge to form a single jet in a domain. Examples of this transition in both the NL model and the QL model are shown in Figure 4.18, chosen such that the zonostrophy parameter is similar in each case.

Jet merging behaviour in the NL model is, in general, a latitudinally-symmetric phenomenon, as illustrated in Figure 4.18(a). Prior to a merger, the jets organise themselves such that they are equally strong but unequally spaced, meandering with opposite phases to one another in a similar fashion to that previously shown in Figure 4.6(b). Gradually, the separation distance between the jets reduces until a connection is established, as shown at time  $t_2$ . Maintaining their latitudinal symmetry, they ultimately merge and, in doing so, the new single jet pulsates, as shown at time  $t_3$ . In general, the zmf index of the merged jet is larger than that for the two separate jets, reaching its peak at the point of transition before settling into a new stable state. Generalisations of this rule to larger systems of jets are non-trivial because the behaviour of each jet contributes to the fraction of energy in the zonal mean flow, and jet mergers are often accompanied by changes of behaviour of the remaining jets. In addition, we note that our statement is

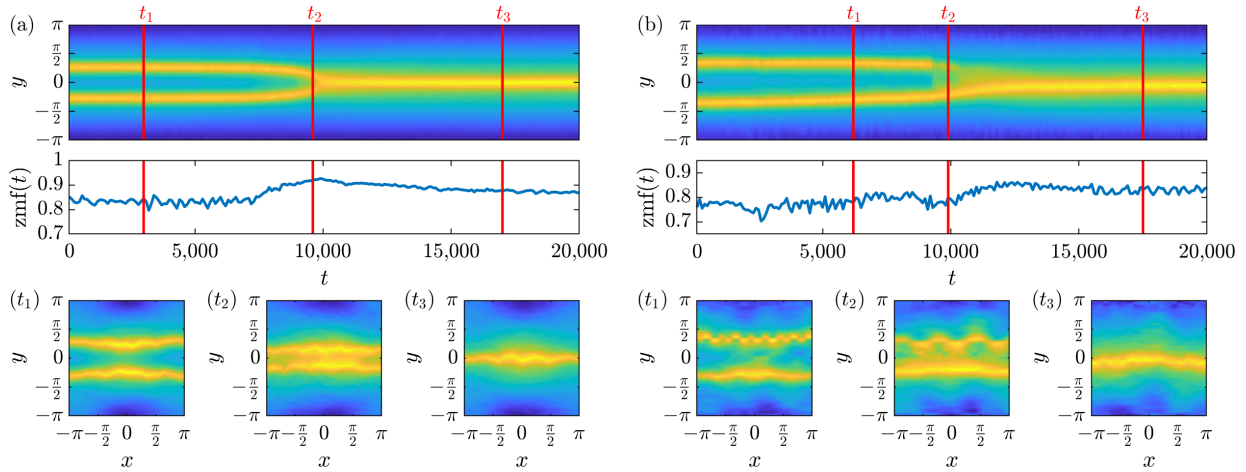


**Figure 4.18** The dynamics of merging behaviour in the (a) NL model with parameters  $\beta = 2.5$ ,  $\mu = 0.00005$ ,  $\varepsilon = 10^{-5}$ ,  $k_f = 16$ ,  $N = 256$ ,  $R_\beta = 5.18$ , and (b) QL model with parameters  $\beta = 2.0$ ,  $\mu = 0.00005$ ,  $\varepsilon = 10^{-5}$ ,  $k_f = 16$ ,  $N = 256$ ,  $R_\beta = 5.07$ . Plotted are latitude-time plots of the zonal mean zonal velocity, the evolution of the zmf index, and three snapshots in time of the zonal velocity  $u(\mathbf{x})$  showing the flow field before, during, and after the transition.

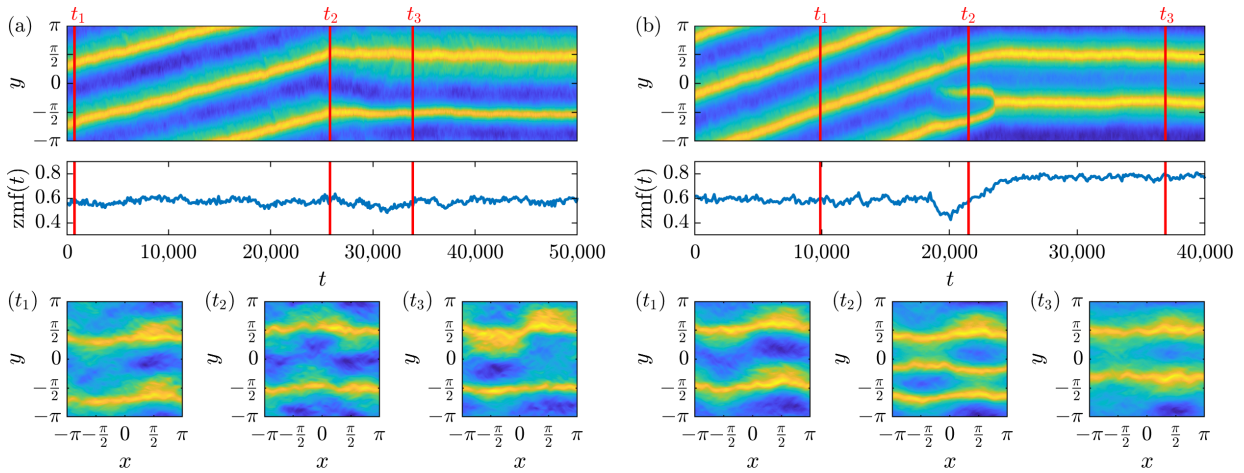


**Figure 4.19** The dynamics of regime transitions in the NL model in which (a) a pair of migrating jets transition to a pair of equally spaced but unequally strong non-migrating jets (parameters:  $\beta = 2.0$ ,  $\mu = 0.0005$ ,  $\varepsilon = 10^{-5}$ ,  $k_f = 16$ ,  $N = 256$ ,  $R_\beta = 2.85$ ), and (b) a pair of migrating jets transition to a pair of unequally spaced but equally strong non-migrating jets (parameters:  $\beta = 4.5$ ,  $\mu = 0.0007$ ,  $\varepsilon = 10^{-4}$ ,  $k_f = 16$ ,  $N = 256$ ,  $R_\beta = 3.19$ ). Plotted are latitude-time plots of the zonal mean zonal velocity, the evolution of the zmf index, and three snapshots in time of the zonal velocity  $u(\mathbf{x})$  showing the flow field before, during, and after the transition.

not consistent with Lee (1997), who reported that two-jet states were characterised by smaller values of eddy energy than one-jet states. This discrepancy is likely due to significant modelling differences between our barotropic system with statistically homogeneous forcing and their baroclinic system with a finite width of baroclinic instability in the domain.

The dynamical behaviours associated with merging behaviour in the QL model are different, as shown in Figure 4.18(b) (and also visible in Figure 4.16(d) at about  $t \approx 640,000$ ). Rather than being a symmetric transition, it is asymmetric with the jets developing different strengths prior to a merger. Immediately prior to the transition, the weaker jet loses a significant fraction of its kinetic energy before shifting towards the stronger jet, leaving a merged jet that has a larger associated zonal mean flow index than the original two jets. This demonstrates that nonlinear eddy-eddy interactions are not necessary for merging behaviour, although they do play a role in the way in which the mergers take place.

Spontaneous transitions also occur in the NL model in configurations in which the number of jets remains constant, such as those illustrated in Figure 4.17. This is best demonstrated for the case of two jets, which is the simplest system in which we have observed such behaviour. Analysis of a large number of simulations suggests that there exist at least two different mechanisms for these transitions, which are shown in Figure 4.19. In the first example (see Figure 4.19(a)), the initially meandering jets transition to pulsing behaviour, before reconfiguring themselves into a new state. No significant changes in the zmf index occur at the point of transition. A different type of transition involves a small jet nucleation followed by a rapid merger, as illustrated in Figure 4.19(b). Here, the nucleation and merger lead to a temporary reduction in the zmf index and enable the system to reconfigure itself into a new stable state. In both cases, any longer-term changes in the zmf index after the transition depend on the particular stable attractors that the system transitions between.

#### 4.4.4 Analogy of multiple stochastic potential wells

The existence of spontaneous transitions gives rise to some interesting questions relating to the factors which influence these transitions and their associated probabilities of occurrence. Whilst an in-depth investigation is beyond the scope of this thesis, we take some preliminary steps towards addressing these questions, focussing on regime transitions in the NL model. Zonostrophy is an important factor, with larger zonostrophy parameters leading to stronger jets relative to the coexistent eddy field, and less frequent transitions. This is demonstrated in Figure 4.20 in which we consider the example of transitions between northward and southward (fast) migration. Four simulations have been selected showing a pair of migrating jets associated with zonostrophy parameters in the range (2.49 – 3.66). For smaller zonostrophy, the jets behave more stochastically, changing direction relatively frequently. As the zonostrophy increases, the changes become less frequent and the jets behave almost deterministically. We might conjecture, therefore, that the probability of spontaneous transitions is negatively correlated with  $R_\beta$ .

An increase in zonostrophy is associated with a reduced fraction of kinetic energy in the eddy field, as discussed in Section 4.3.3. The fact that this reduction in the strength of the eddies relative to the jets leads to reduced frequencies of transitions suggests that the eddies contribute significantly towards facilitating

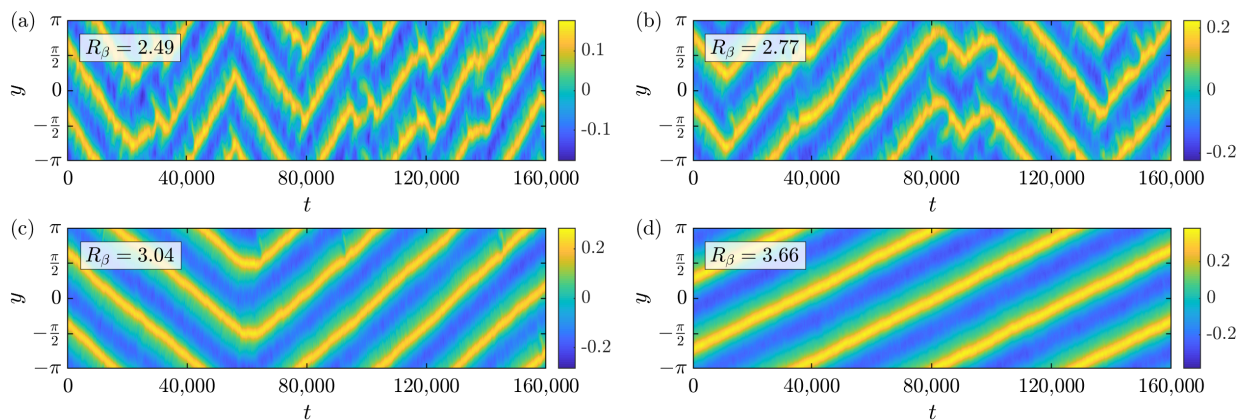


**Figure 4.20** The influence of the zonostrophy parameter on the frequency of regime transitions. Latitude-time plots showing the zonal mean zonal velocity field are selected for four simulations in which fast jet migration behaviour is observed. In order of increasing zonostrophy, the parameters used are (a)  $\beta = 1.2$ ,  $\mu = 0.0007$ ,  $\varepsilon = 10^{-5}$ ,  $k_f = 16$ ,  $N = 256$ ,  $R_\beta = 2.49$ ; (b)  $\beta = 1.5$ ,  $\mu = 0.0005$ ,  $\varepsilon = 10^{-5}$ ,  $k_f = 16$ ,  $N = 256$ ,  $R_\beta = 2.77$ ; (c)  $\beta = 2.2$ ,  $\mu = 0.0004$ ,  $\varepsilon = 10^{-5}$ ,  $k_f = 16$ ,  $N = 256$ ,  $R_\beta = 3.04$ ; (d)  $\beta = 2.5$ ,  $\mu = 0.0002$ ,  $\varepsilon = 10^{-5}$ ,  $k_f = 16$ ,  $N = 256$ ,  $R_\beta = 3.66$ .

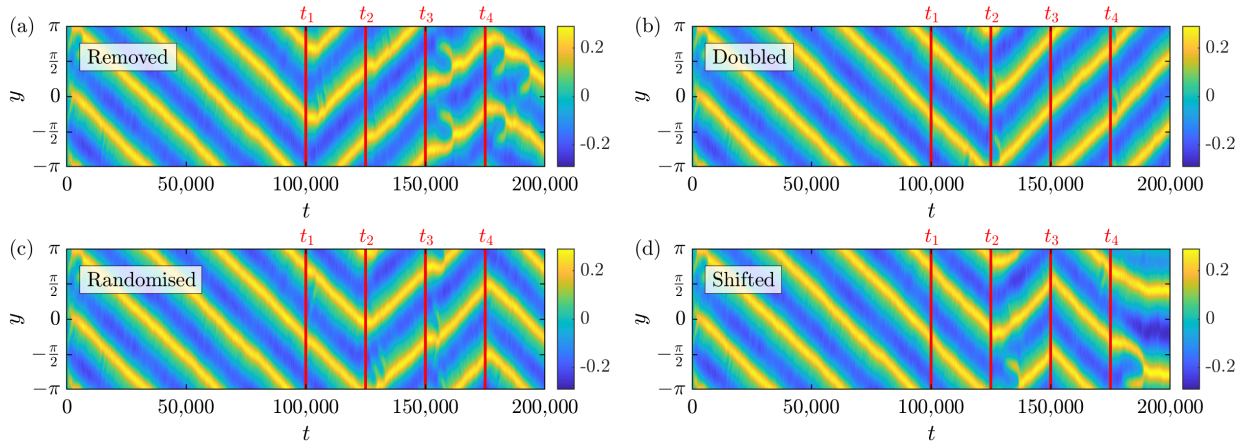


**Figure 4.21** The influence of abrupt eddy field changes on regime transitions, illustrated using four different approaches. Latitude-time plots of the zonal mean zonal velocity field are shown and red vertical lines indicate the individual time steps  $t_1 - t_4$  at which abrupt changes are made. These include (a) the removal of the eddy field, (b) the doubling of the eddy field energy, (c) the randomisation of the eddy field and (d) the latitudinal shifting of the eddy field. The same parameters were used in each case:  $\beta = 2.0$ ,  $\mu = 0.0003$ ,  $\varepsilon = 10^{-5}$ ,  $k_f = 16$ ,  $N = 256$ ,  $R_\beta = 3.24$ .

these changes. In order to emphasise this point further, we conducted a series of numerical experiments in which abrupt changes are made to the eddy field,  $\zeta'(\mathbf{x}, t) = \zeta(\mathbf{x}, t) - \bar{\zeta}(y, t)$ , at single timesteps  $t_i \in (t_1, t_2, t_3, t_4)$ , with the flow allowed to evolve as normal for  $t_i < t < t_{i+1}$ . There is a sufficient time separation between each  $t_i$ , of length  $\mu t = 7.5$ , in order to ensure that the system re-equilibrates before the change occurs again. The nature of the flow is recovered very soon after the perturbation and the system does remember some information about the previous flow state through the zonal mean flow. The specific changes that we have made fall under four types, each repeated four times within a given simulation:

- (a) The eddy field is *removed*:  $\zeta'(x, y, t_i) \rightarrow 0$ ,
- (b) The eddy kinetic energy is *doubled*:  $\zeta'(x, y, t_i) \rightarrow \sqrt{2}\zeta'(x, y, t_i)$ ,
- (c) The eddy field is *randomised*:  $\zeta'(x, y, t_i) \rightarrow \Theta(x, y, t_i)$ ,
- (d) The eddy field is latitudinally *shifted*:  $\zeta'(x, y, t_i) \rightarrow \zeta'(x, y + \frac{1}{3}\pi, t_i)$ .

Here,  $\Theta(\mathbf{x}, t)$  represents a randomised field, constructed such that each Fourier mode with  $k \leq k_{max}$  is assigned a value  $e^{i\theta_k}$ , where  $\theta_k \in [0, 2\pi)$  is a randomly selected number, and then normalised such that the domain-averaged eddy kinetic energy remains constant. Since no changes are made to the zonal mean flow in any of these experiments, the total kinetic energy density,  $E$ , is temporarily reduced in case (a), temporarily increased in case (b), but remains constant in cases (c) and (d).

Choosing a simulation in which a pair of jets with relatively high zonestrophy exhibit robust southward migration, we numerically impose these changes with a view towards investigating whether transitions are initiated. The results, presented in Figure 4.21, demonstrate that transitions do take place following each type of disruption, however, not on every single occasion. This simple experiment highlights the role of the eddies, and suggests that large fluctuations in the system permit a restructuring of the flow field which may, or may not, allow the system to transition into a different stable attractor.

Having discussed a variety of concrete results along with the notion of stable attractors and spontaneous eddy-driven transitions, it seems apt to conclude this chapter by tying these ideas together with a commonly

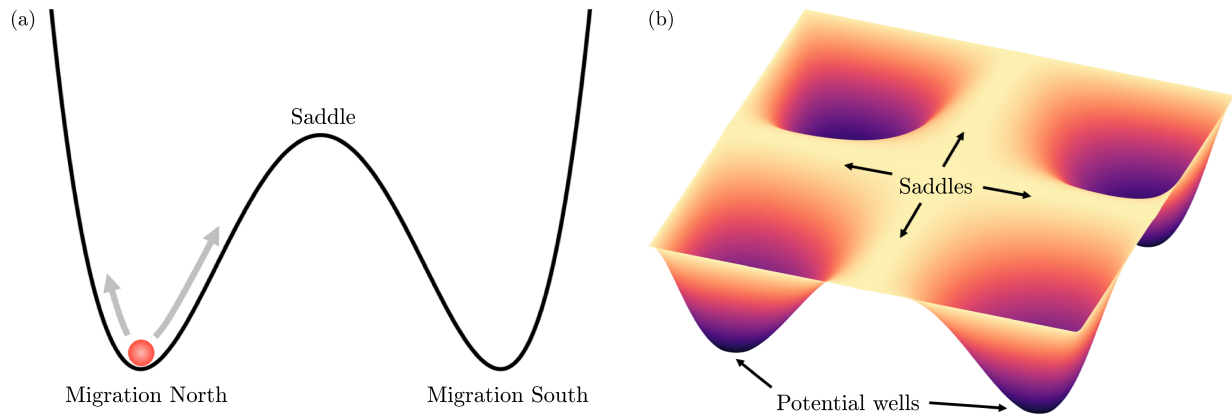


**Figure 4.22** (a) A simple analogy between two stable attractors, such as northward and southward jet migration, and a double potential well; (b) a more realistic analogy between multiple stable attractors and multiple potential wells.

used analogy: potential wells. At the most basic level, we might conceive a system in which there are two stable attractors, for example  $n$  and  $n + 1$  jets, or northward and southward migration. The system will naturally gravitate towards either of these attractors, or *potential wells* (illustrated in Figure 4.22(a)), however, fluctuations due to the stochasticity will lead to continuous perturbations. A sufficiently large fluctuation may enable the system to overcome the barrier, or the *saddle*, between the two states, with the height of these saddles, or equivalently the relative depths of the wells, varying according to the system parameters. In the case of Figure 4.20, we would then infer that higher zonostrophy is associated with deeper wells, meaning that larger fluctuations would be required to escape from a particular stable attractor corresponding to a given direction of migration. Applying the same analogy to configurations such as randomly wandering jets suggests that these systems may be rapidly fluctuating between very weak attractors, connected by low saddles that are associated with high probabilities of transitions.

There are, however, often more than two stable attractors. This is demonstrated in Figure 4.17 in which at least four distinct regimes are visible. Consequently, the picture will often be more complex, requiring at least two-dimensions to capture the multitude of wells and saddles, such as the surface illustrated in Figure 4.22(b). Whilst a more rigorous treatment of this topic will remain the subject of future work, these ideas rely on the assumption that all types of transitions are eddy-driven - a point that we shall return to in Chapter 6 using a statistical treatment in which random fluctuations are excluded.

## 4.5 Discussion

In this chapter, we have studied zonal jet variability within a barotropic beta-plane system, damped by linear friction, in which stochastic forcing generates a kind of turbulence that in more complicated systems would be generated by internal dynamical instabilities such as baroclinic instability. Treating the term *variability* in the broadest sense, we have sought to establish a categorisation of the zoology of dynamical behaviours, flow regimes and transitions, focussing on the fundamental building blocks that characterise more complex configurations. By comparing a large number of numerical simulations that have been run across a broad range of parameters using both a fully nonlinear model and a quasilinear version, we have sought to establish the necessity of nonlinear eddy-eddy interactions in aspects of variability.

We have focussed on the zonostrophic regime, defined by Galperin et al. (2010) to occur when sufficiently strong jets equilibrate that are visible in the flow field, requiring  $R_\beta \geq 2$ . Each system reveals a

rich variety of configurations and dynamical regimes which we have classified using three fundamental types. These include randomly wandering behaviour and merging and nucleating behaviour, both of which are present in the NL and the QL models, along with a new type of variability, notably migrating behaviour, aspects of which only occur in the NL model. A more detailed categorisation of the zoology of the sub-range of stable attractors reveals that the jets in the NL system coexist with eddy fields that are dominated by coherent wave structures, each with zonal wavenumber  $k_x = 1$  and varying latitudinal wavenumber. In general, no such structures are present in multiple-jet QL systems where we also note a reduced set of possible flow configurations.

Zonal jet migration behaviour is a phenomenon whereby jets are observed to systematically migrate north or south with equal probability, occasionally changing their direction of migration. Sub-categories reveal two types: a fast and symmetric type, in which the jet spacings and strengths are symmetric, and a slow and asymmetric type, in which these properties are asymmetric. Whilst slow jet migration is observed to some degree in both models, fast jet migration is only observed in the NL model, being a robust type of variability in subsets of parameter space. Its absence in the QL model therefore provides a concrete example of the types of dynamics that the quasilinear approximation cannot capture.

As reported by Bouchet et al. (2018), the QL model is associated with greater variance in the probability density function of its eddy momentum flux convergence (see Figure 2.11). It could be argued, therefore, that fast migration *is* a solution in the QL system and that it is the greater probability of large fluctuations that prevents the jets from consistently migrating in a single direction in the manner observed in the NL model. However, given the fact that other stable regimes do exist in the QL model, we do not consider this to be the case. As we argue in Chapter 5, we believe that zonons (which are not captured in the QL model) play a role in organising the eddy field, acting as a persistent symmetry-breaking mechanism.

Simple relationships between aspects of variability and parameter values highlight, for example, that there is a linear relationship between the Rhines wavenumber and the number of jets within the domain, in agreement with the findings from previous studies. Whilst this is valid for both the NL model and the QL model, we acknowledge that the QL model has a tendency to underestimate the number of jets. In addition, a relationship between the zonostrophy parameter and the zmf index closely follows an analytical relationship in both models, however, the larger degree of associated variance observed in the NL model is found to depend on jet behaviour. Migrating jets are associated with the smallest zmf indices, whilst the strongest jets are those that fall under the randomly wandering category. Finally, the forcing wavenumber plays no role in the large-scale structure of solutions in the NL model, where the jets, within a particular regime, have a universal profile. The QL model, on the other hand, fails to reproduce this universality, highlighting another restriction imposed by a constrained eddy wavenumber spectrum.

We conclude by demonstrating that a complete picture of zonal jet variability is complicated by effects due to hysteresis and also the existence of multiple stable attractors. The occurrence of spontaneous transitions between these states leads to the analogy of multiple stochastic potential wells, an idea which may be applicable more widely, and may explain why certain configurations, such as randomly wandering behaviour, display no apparent organisation whilst other configurations reveal eye-catching pattern formation. Of course, this analogy relies on the assumption that random fluctuations are an essential component in regime transitions - a point that we shall address in Chapter 6. In addition, the physical mechanisms associated with the fundamental differences between the NL and QL are yet to be ascertained, therefore we strive to further understand the role of eddy-eddy interactions in Chapter 5.

## Chapter 5

# The dynamics of zonal jet migration

### 5.1 Introduction

The phenomenon of zonal jet migration, introduced in Chapter 4, has received considerable attention over the last few decades, being the subject of numerous observational and modelling studies. However, for the reasons outlined below, none of these studies are directly relevant to the types of migration introduced in Chapter 4. Discussions date back to the 1950s, when Riehl et al. (1950) observed the latitudinal propagation of zonal jet anomalies in the troposphere, sometimes equatorward, but usually in the poleward direction. Similar behaviours, albeit purely in the poleward direction, have since been observed in the troposphere on interannual timescales using observational or reanalysis data (Dickey et al., 1992; Feldstein, 1998), or simplified GCMs (Chemke and Kaspi, 2015b; James and Dodd, 1996; James et al., 1994), with examples of each shown in Figure 5.1. Migrating jets have also been observed in oceanic or Jovian modelling studies, however, their direction of propagation has instead been shown to be equatorward in these systems (Ashkenazy and Tziperman, 2016; Chan et al., 2007; Williams, 2003; Young et al., 2019).

The common ground between these studies and the migration behaviour identified in Chapter 4 is the role of anomalies in the eddy momentum flux convergence, which has been discussed in a number of studies that have attempted to determine the (possibly different) mechanisms responsible for jet migration

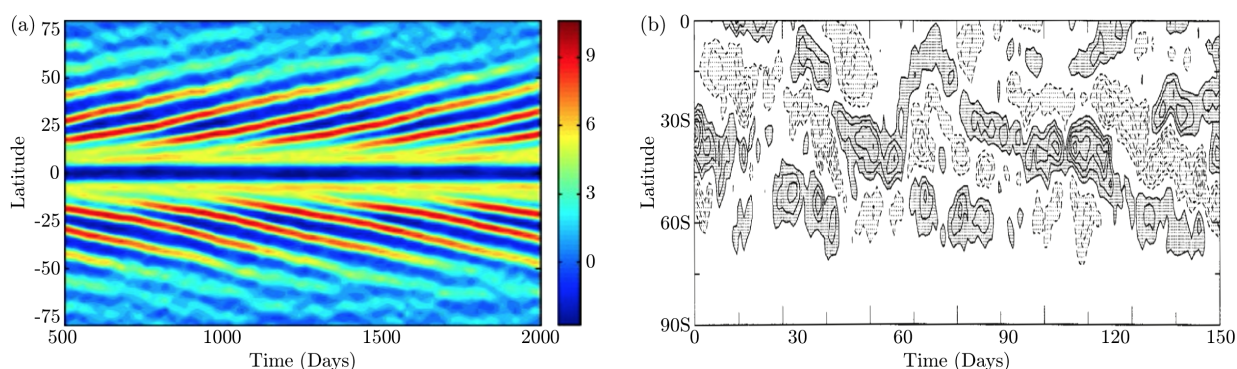


**Figure 5.1** Geophysical examples of jet stream migration. (a) A modelling study of migration: Hovmöller diagram of the zonal and vertically averaged zonal wind [ $m s^{-1}$ ] for an idealised GCM with rotation rate  $10\Omega_e$  (adapted from Chemke and Kaspi, 2015b). (b) An observational study of migration: Hovmöller diagram of the zonal mean relative angular momentum anomalies for the southern hemisphere summer of 1990/91, commencing 1<sup>st</sup> November. The contour interval is  $0.4 \times 10^{24} kg m^2 s^{-1}$ , in which solid contours are positive, dashed contours are negative and the zero contour is omitted. Shaded values exceed a magnitude of  $0.4 \times 10^{24} kg m^2 s^{-1}$  (adapted from Feldstein, 1998).

within each of these planetary systems. For example, Dickey et al. (1992) related the systematic poleward migration of atmospheric zonal jet anomalies to the occurrence of El Niño and La Niña events. Feldstein (1998) showed that they coincide with transient eddy momentum flux convergence feedbacks and James and Dodd (1996) showed that there exists a poleward bias in the eddy momentum flux convergence around the jet core, arising due to the equatorward propagation of Rossby waves. More recently, Chemke and Kaspi (2015b) argued that the poleward migration of eddy-driven jets occurs when they are clearly separated from the subtropical jets, with the migration being caused by a poleward bias in baroclinicity across the width of the jet. Meanwhile, equatorward migration has been attributed to a residual circulation generated by the relative patterns of convergent and divergent EP fluxes on the jet flanks (Chan et al., 2007) along with asymmetric eddy momentum flux convergences across the jets (Young et al., 2019).

The distinction, on the other hand, concerns the existence of a latitudinal symmetry breaking mechanism in each of these studies, such as that due to the sphericity of the planet or the localisation of baroclinicity as a mechanism for the generation of eddies, which gives rise to a preferred direction of translation. This is in contrast to the migration behaviour discussed in Chapter 4, where we demonstrated that zonal jet migration also occurs in systems which are latitudinally symmetric, suggesting that the fundamental mechanisms are related to internal dynamics rather than external asymmetries. In this chapter, we consider the phenomenon of zonal jet migration in more detail, focussing specifically on the fast type that was introduced in Section 4.2.3.1. We conduct a detailed analysis which utilises the findings from a generalisation of the quasilinear approximation in order to formulate a new theory for the dynamics of fast zonal jet migration.

## 5.2 Mathematical formulation

The fast type of zonal jet migration is a robust type of variability in the NL model, occurring over distinct regions of the parameter space. Nevertheless, the QL model does not reproduce the same behaviour, leading to the conclusion that certain eddy-eddy interactions are an essential ingredient. In order to investigate these interactions further, we choose to employ a generalisation of the quasilinear approximation, first mentioned in Section 2.4.1.2, which admits a continuum of reduced models that interpolate between the NL and QL systems and provides a systematic way of restoring eddy-eddy interactions to the QL model. We follow the methodology of Marston et al. (2016) in our mathematical formulation of these models in this section.

### 5.2.1 Generalised quasilinear (GQL) approximation

We begin by considering a state vector of variables,  $\mathbf{q}(\mathbf{x}, t)$ , satisfying the equation of motion

$$\frac{\partial \mathbf{q}}{\partial t} = \mathcal{L}[\mathbf{q}] + \mathcal{N}[\mathbf{q}, \mathbf{q}], \quad (5.1)$$

where  $\mathcal{L}$  is a linear operator and  $\mathcal{N}$  includes nonlinear terms of quadratic order. This time, rather than employing the quasilinear approximation, in which the state vector is decomposed using a standard Reynolds decomposition into a mean component and fluctuations away from the mean, we generalise the decomposition using a spectral filter. Known as the generalised quasilinear approximation (GQL), the state vector is separated into two parts: one that is associated with low wavenumber modes,  $\bar{\mathbf{q}}^L$ , and one that is associated with high wavenumber modes,  $\bar{\mathbf{q}}^H$ , where  $\mathbf{q} = \bar{\mathbf{q}}^L + \bar{\mathbf{q}}^H$ . There is flexibility regarding the method used to decompose the variables, which is usually motivated by the particular application. In our

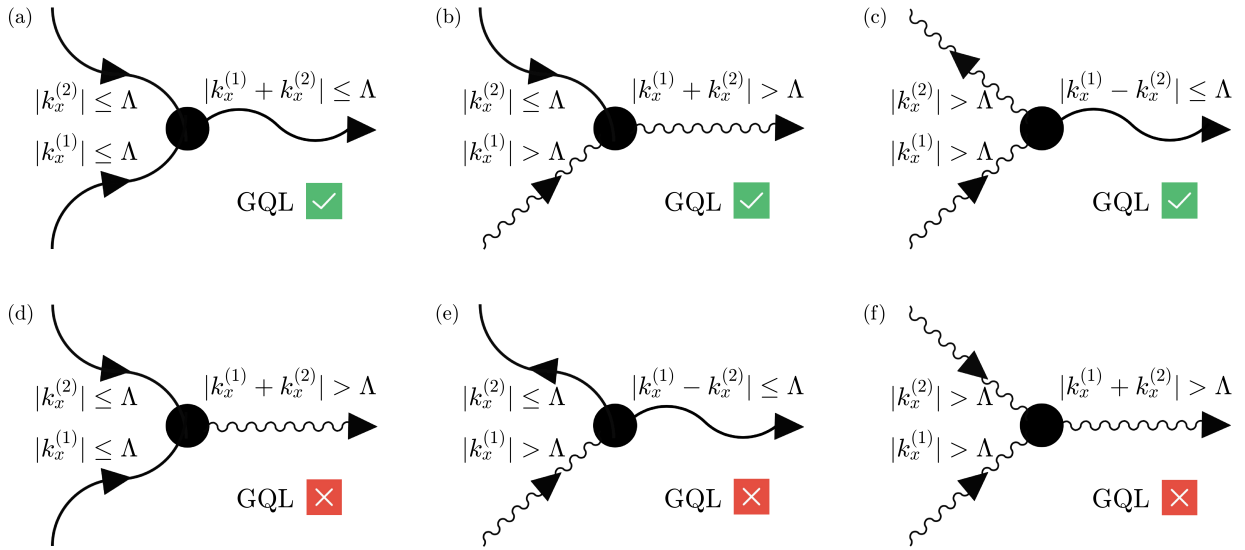


**Figure 5.2** Illustrations of the possible interactions between the high modes, denoted with short waves, and the low modes, denoted with long waves. Note that all interactions are present in the NL model while only (a), (b) and (c) are present in the generalised quasilinear system. Inspiration for the figures came from Marston et al. (2016).

case, we choose to consider a zonal decomposition in which the filter separates the *low modes*, with zonal wavenumbers  $|k_x| \leq \Lambda$ , from the *high modes*, in which  $|k_x| > \Lambda$ :

$$\bar{\mathbf{q}}^L(\mathbf{x}, t) = \frac{1}{N^2} \sum_{|k_x| \leq \Lambda} \sum_{k_y} \mathbf{q}(\mathbf{k}, t) e^{i\mathbf{k} \cdot \mathbf{x}}, \quad (5.2)$$

$$\bar{\mathbf{q}}^H(\mathbf{x}, t) = \frac{1}{N^2} \sum_{|k_x| > \Lambda} \sum_{k_y} \mathbf{q}(\mathbf{k}, t) e^{i\mathbf{k} \cdot \mathbf{x}}, \quad (5.3)$$

thereby introducing a new parameter,  $\Lambda$ , which is a partition wavenumber representing the largest zonal wavenumber retained in the low modes. These filters obey  $\overline{\bar{\mathbf{q}}^L} = \bar{\mathbf{q}}^L$  and  $\overline{\bar{\mathbf{q}}^H} = \bar{\mathbf{q}}^H = 0$ , but not  $\overline{\bar{\mathbf{q}}^H \bar{\mathbf{q}}^H} = \bar{\mathbf{q}}^H \bar{\mathbf{q}}^H$ , as is the case with a standard Reynolds decomposition.

In order to generalise the neglect of eddy-eddy interactions that occurs in the quasilinear approximation, a certain amount of care needs to be taken when selecting which nonlinear interactions to neglect in this new decomposition if the original conservation laws governing the conservation of energy and enstrophy are to be retained. Accordingly, we shall follow Marston et al. (2016) and use a GQL approximation that retains the interactions represented symbolically by Figures 5.2(a-c):

$$(a) \quad \overline{\mathcal{N}^L}[\bar{\mathbf{q}}^L, \bar{\mathbf{q}}^L], \quad (b) \quad \overline{\mathcal{N}^H}[\bar{\mathbf{q}}^L, \bar{\mathbf{q}}^H] + \overline{\mathcal{N}^H}[\bar{\mathbf{q}}^H, \bar{\mathbf{q}}^L], \quad (c) \quad \overline{\mathcal{N}^L}[\bar{\mathbf{q}}^H, \bar{\mathbf{q}}^H], \quad (5.4)$$

whilst neglecting those represented by Figures 5.2(d-f):

$$(d) \quad \overline{\mathcal{N}^H}[\bar{\mathbf{q}}^L, \bar{\mathbf{q}}^L], \quad (e) \quad \overline{\mathcal{N}^L}[\bar{\mathbf{q}}^L, \bar{\mathbf{q}}^H] + \overline{\mathcal{N}^L}[\bar{\mathbf{q}}^H, \bar{\mathbf{q}}^L], \quad (f) \quad \overline{\mathcal{N}^H}[\bar{\mathbf{q}}^H, \bar{\mathbf{q}}^H], \quad (5.5)$$

thereby treating the low modes as a fully nonlinear system. Marston et al. (2016) justify these choices using a multiple-scales asymptotic reduction of the underlying partial differential equations. Invoking these rules, the original equation given by (5.1) is then decomposed into two separate equations governing the

respective evolutions of the low and high modes:

$$\frac{\partial \bar{\mathbf{q}}^L}{\partial t} = \mathcal{L}[\bar{\mathbf{q}}^L] + \bar{\mathcal{N}}^L[\bar{\mathbf{q}}^H, \bar{\mathbf{q}}^H] + \bar{\mathcal{N}}^L[\bar{\mathbf{q}}^L, \bar{\mathbf{q}}^L], \quad (5.6)$$

$$\frac{\partial \bar{\mathbf{q}}^H}{\partial t} = \mathcal{L}[\bar{\mathbf{q}}^H] + \bar{\mathcal{N}}^H[\bar{\mathbf{q}}^L, \bar{\mathbf{q}}^H] + \bar{\mathcal{N}}^H[\bar{\mathbf{q}}^H, \bar{\mathbf{q}}^L]. \quad (5.7)$$

In the limit  $\Lambda \rightarrow \infty$ , the high modes disappear,  $\bar{\mathbf{q}}^H(\mathbf{x}, t) = 0$ , and we recover the NL model, whilst in the opposite limit,  $\Lambda = 0$  recovers the QL model. The intermediate range, when  $\Lambda$  is finite but non-zero, permits the neglect of the nonlinear interactions denoted by (5.5), thereby allowing a systematic investigation of the role of these interactions for different  $\Lambda$ .

The GQL system with  $\Lambda > 0$  offers two advantages over the original QL model. Firstly, it permits the formation of large-scale waves such as zonons, which are not directly forced, due to the fact that the low modes can be forced by the high modes, represented by the triad interaction in Figure 5.2(c). Secondly, the GQL model incorporates an energy scattering mechanism since the low modes can, in turn, affect the high modes via the triad interaction represented in Figure 5.2(b), provided that  $|k_x| \geq 1$ . It therefore serves as an ideal starting point from which to conduct a deeper investigation into those aspects of zonal jet dynamics in which significant differences exist between the NL and QL models, including the role of zonons.

## 5.2.2 Generalised quasilinear (GQL) model

Having laid the foundations of GQL theory, we now apply the approximation to our problem of interest, which is described by the beta-plane vorticity equation,

$$\frac{\partial \zeta}{\partial t} + J(\psi, \zeta) + \beta \frac{\partial \psi}{\partial x} = \xi - \mu \zeta + \nu_n \nabla^{2n} \zeta. \quad (5.8)$$

Following the procedure, the streamfunction is decomposed into its low modes and high modes,

$$\psi(\mathbf{x}, t) = \bar{\psi}^L(\mathbf{x}, t) + \bar{\psi}^H(\mathbf{x}, t), \quad (5.9)$$

with corresponding decompositions of the other variables. We proceed by applying the spectral filters given by expressions (5.2) and (5.3) to equation (5.8) in order to derive separate evolution equations for the low modes and the high modes. After expanding all terms, the equation for the low modes is given by

$$\begin{aligned} \frac{\partial \bar{\zeta}^L}{\partial t} + \frac{\overline{\psi_x \zeta_y}^L}{\psi_x \zeta_y} + \frac{\overline{\psi_x \zeta_y}^H}{\psi_x \zeta_y} - \frac{\overline{\psi_y \zeta_x}^L}{\psi_y \zeta_x} - \frac{\overline{\psi_y \zeta_x}^H}{\psi_y \zeta_x} + \left[ \frac{\overline{\psi_x \zeta_y}^L}{\psi_x \zeta_y} + \frac{\overline{\psi_x \zeta_y}^H}{\psi_x \zeta_y} - \frac{\overline{\psi_y \zeta_x}^L}{\psi_y \zeta_x} - \frac{\overline{\psi_y \zeta_x}^H}{\psi_y \zeta_x} \right] \\ + \beta \bar{\psi}_x^L = \bar{\xi}^L - \mu \bar{\zeta}^L + \nu_n \nabla^{2n} \bar{\zeta}^L, \end{aligned} \quad (5.10)$$

whilst the analogous equation for the high modes is found to be

$$\begin{aligned} \frac{\partial \bar{\zeta}^H}{\partial t} + \frac{\overline{\psi_x \zeta_y}^H}{\psi_x \zeta_y} + \frac{\overline{\psi_x \zeta_y}^L}{\psi_x \zeta_y} - \frac{\overline{\psi_y \zeta_x}^H}{\psi_y \zeta_x} - \frac{\overline{\psi_y \zeta_x}^L}{\psi_y \zeta_x} + \left[ \frac{\overline{\psi_x \zeta_y}^H}{\psi_x \zeta_y} + \frac{\overline{\psi_x \zeta_y}^L}{\psi_x \zeta_y} - \frac{\overline{\psi_y \zeta_x}^H}{\psi_y \zeta_x} - \frac{\overline{\psi_y \zeta_x}^L}{\psi_y \zeta_x} \right] \\ + \beta \bar{\psi}_x^H = \bar{\xi}^H - \mu \bar{\zeta}^H + \nu_n \nabla^{2n} \bar{\zeta}^H. \end{aligned} \quad (5.11)$$

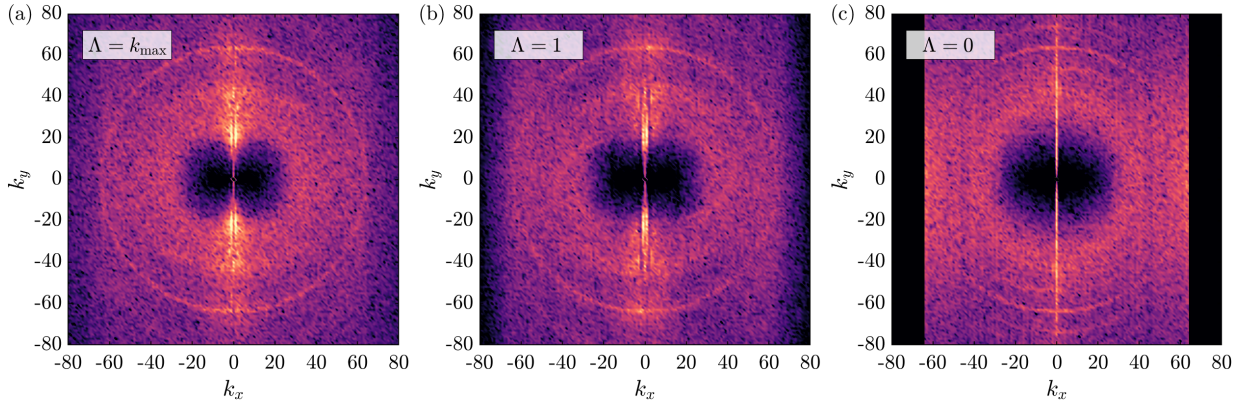


**Figure 5.3** The equilibrated kinetic energy spectrum in forced-dissipative beta-plane turbulence using (a) the NL model ( $\Lambda = k_{\max}$ ), (b) the GQL model ( $\Lambda = 1$ ), and (c) the QL model ( $\Lambda = 0$ ). A logarithmic colour scale is used in each case. The parameters are equivalent in each plot:  $\beta = 170$ ,  $\mu = 0.004$ ,  $\varepsilon = 10^{-5}$ ,  $k_f = 64$ ,  $N = 512$ ,  $R_\beta = 2.64$ .

We have identified using square brackets the nonlinear terms that correspond to the triad interactions that we wish to neglect, choosing to refer to these as the *high-high nonlinearity* (HHNL) terms:

$$\text{HHNL} = \overline{\psi_x^L \zeta_y^H} + \overline{\psi_x^H \zeta_y^L} - \overline{\psi_y^L \zeta_x^H} - \overline{\psi_y^H \zeta_x^L} + \overline{\psi_x^L \zeta_y^L} + \overline{\psi_x^H \zeta_y^H} - \overline{\psi_y^L \zeta_x^L} - \overline{\psi_y^H \zeta_x^H}. \quad (5.12)$$

The GQL approximation then defines  $\text{HHNL} = 0$ , which is mathematically equivalent to the subtraction of these terms from the original equation. Thus, the GQL beta-plane vorticity equation is given by

$$\frac{\partial \zeta}{\partial t} + J(\psi, \zeta) + \beta \frac{\partial \psi}{\partial x} - \text{HHNL} = \xi - \mu \zeta + \nu_n \nabla^{2n} \zeta, \quad (5.13)$$

which, as for the NL and QL models, is a single equation encapsulating the entire dynamics. This can be solved alongside the elliptic equation,  $\zeta = \nabla^2 \psi$ , using the numerical procedures and prescription of vorticity forcing,  $\xi$ , outlined in Chapter 3.

The influence of  $\Lambda$  on the distribution of eddy kinetic energy can be visualised by comparing the Fourier-transformed total kinetic energy spectra for simulations that have reached a state of statistical equilibrium. Example distributions are plotted in Figure 5.3 for the (a) NL model with  $\Lambda = k_{\max}$ , (b) GQL model with  $\Lambda = 1$ , and (c) QL model with  $\Lambda = 0$ . Whilst the NL system reveals an accumulation of energy in the wavevectors that lie close to the line  $k_x = 0$ , the QL model only permits an accumulation along the line  $k_x = 0$ , with no build-up in the surrounding zonal wavenumbers. This is rectified to some extent using the GQL model with only a single additional zonal wavenumber retained in the low modes, where we observe that the energy scattering mechanism reproduces the main features of the fully nonlinear spectrum, serving to exemplify the systematic manner in which GQL interpolates between the NL and QL systems.

### 5.3 Generalised quasilinear theory: the sufficiency of $\Lambda \geq 1$

Turning our attention to the study of zonal jet migration, we have investigated the effect of the partition wavenumber,  $\Lambda$ , on the existence of migration within our barotropic beta-plane system using a number of test cases in which the fully NL model is known to permit robust migration. One such example is shown in Figure 5.4, which considers a NL simulation (with  $\Lambda = k_{\max}$ ) in which migration does occur. Keeping all remaining parameters fixed, comparisons are made with GQL simulations with  $\Lambda \in \{1, 2, 3\}$ , and a QL

simulation with  $\Lambda = 0$ . The results are illustrative of a larger collection of examples, showing that jet migration is possible when  $\Lambda \geq 1$ , thereby demonstrating that the retention of just one additional zonal wavenumber in the low modes is sufficient to restore the capabilities of the fully nonlinear model.

The condition  $\Lambda \geq 1$  is also sufficient for the reproduction of the properties associated with migration. These include the translation speed that is inferred to be virtually independent of  $\Lambda$  in the latitude-time plots. In addition, the flow fields and zonally-averaged profiles in those simulations in which  $\Lambda \geq 1$  are almost indistinguishable, revealing a pair of equally-spaced and equally-strong jets that meander with equal phases. The corresponding eddy field is dominated by a coherent wave given by  $\mathbf{k} = (1, 2)$  in each case, in stark contrast to the QL eddy field which shows no discernible structure. These results would appear, at face value, to suggest that there is no advantage gained by considering a value of  $\Lambda > 1$ .

We note, however, that whilst  $\Lambda \geq 1$  is a sufficient condition for the existence of zonal jet migration, evidence from many simulations suggests that the likelihood and persistence of migration behaviour

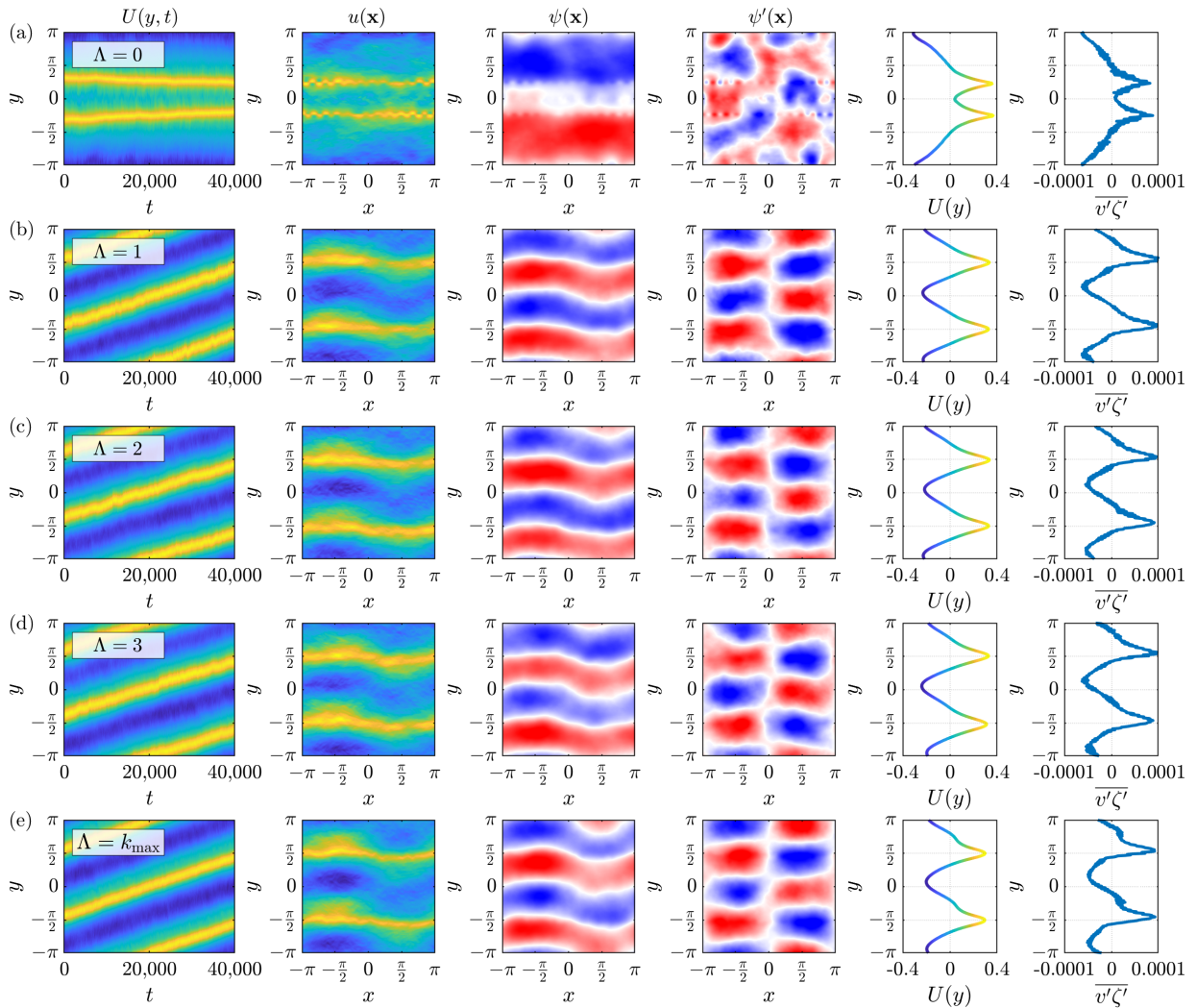


**Figure 5.4** The influence of the GQL partition wavenumber on zonal jet migration, keeping all remaining parameters fixed ( $\beta = 2.5$ ,  $\mu = 0.0002$ ,  $\varepsilon = 10^{-5}$ ,  $k_f = 32$ ,  $N = 256$ ,  $R_\beta = 3.66$ ). We have investigated (a)  $\Lambda = 0$  (QL model), (b)  $\Lambda = 1$  (GQL model), (c)  $\Lambda = 2$  (GQL model), (d)  $\Lambda = 3$  (GQL model), (e)  $\Lambda = k_{\max}$  (NL model). From left to right we show a latitude-time plot of the zonal mean zonal velocity field  $U(y, t)$ , a single snapshot of the zonal velocity field  $u(\mathbf{x})$ , the corresponding streamfunction  $\psi(\mathbf{x})$  and eddy streamfunction field  $\psi'(\mathbf{x})$ , the time-averaged jet velocity profile  $U(y)$  and the time-averaged eddy momentum flux convergence  $\overline{v'\zeta'}$ .

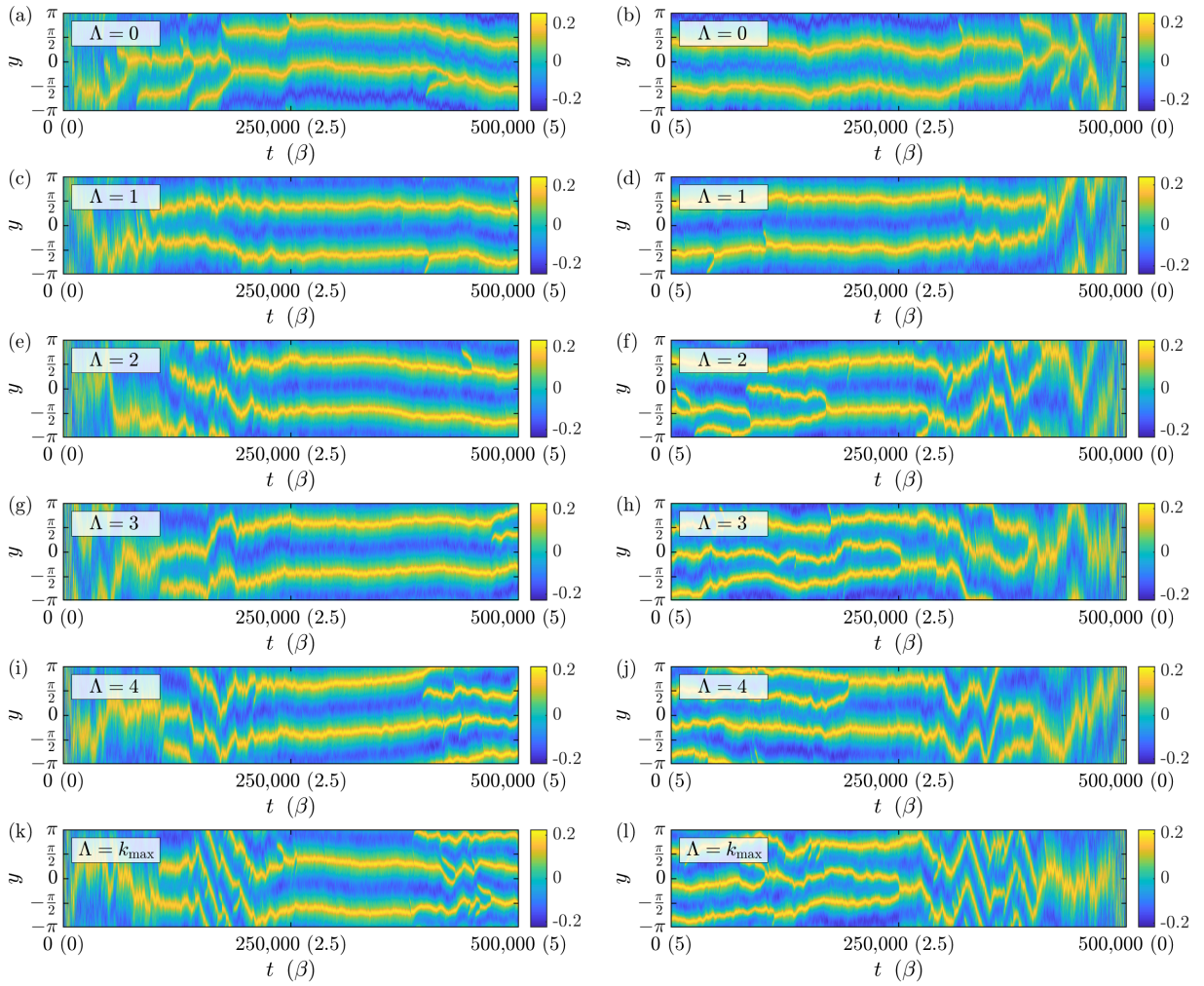


**Figure 5.5** The influence of the GQL partition wavenumber  $\Lambda$  as the parameter  $\beta$  is linearly varied in time over the range  $0 \leq \beta \leq 5$  in which (left)  $\beta$  is linearly increased and (right)  $\beta$  is linearly decreased. We investigate (a-b)  $\Lambda = 0$  (QL model), (c-d)  $\Lambda = 1$  (GQL model), (e-f)  $\Lambda = 2$  (GQL model), (g-h)  $\Lambda = 3$  (GQL model), (i-j)  $\Lambda = 4$  (GQL model), (k-l)  $\Lambda = k_{\max}$  (NL model). In each case, we show a latitude-time plot of the time evolution of the zonal mean zonal velocity field. The parameters used in all cases are  $0 \leq \beta \leq 5$ ,  $\mu = 0.0007$ ,  $\varepsilon = 10^{-5}$ ,  $k_f = 16$ ,  $N = 256$ ,  $0 \leq R_\beta \leq 2.87$ .

tends to increase as  $\Lambda$  increases. In an attempt to demonstrate this tendency, we conducted a series of numerical experiments using the methodology described in Chapter 4, in which the parameter  $\beta$  is linearly increased or decreased in time, keeping all other parameters constant. The results for a range of partition wavenumbers  $\Lambda \in \{0, 1, 2, 3, 4, k_{\max}\}$  are shown in Figure 5.5. In the fully nonlinear model, when  $\Lambda = k_{\max}$ , a pair of zonal jets exhibit migration behaviour over the approximate interval  $1 \lesssim \beta \lesssim 2$  as the Rhines wavenumber associated with  $\beta$  either increases or decreases. The GQL models, in which  $1 \leq \Lambda < k_{\max}$ , show an increasing tendency towards migration as  $\Lambda$  increases, with migration being barely detectable when  $\Lambda = 1$  but becoming increasingly prominent with each additional zonal wavenumber retained in the low modes. We also remark that the jet spacings becomes more closely aligned with the NL simulations as  $\Lambda$  increases, with a progressive reduction in the bias towards a smaller number of jets for any given Rhines wavenumber that was established in Chapter 4 for the QL model. For example, when  $\beta = 5$ , we observe two jets for  $\Lambda \leq 2$ , while  $\Lambda \geq 3$  reproduces the three jets that are visible in the NL model, suggesting that some aspects of variability are influenced by the choice of  $\Lambda$ . Nevertheless, significant improvements are gained by the restoration of some eddy-eddy interactions when  $\Lambda \geq 1$ , compared with the QL system.

## 5.4 A new theory for zonal jet migration

These results from the GQL models inspire us to develop a new theory for zonal jet migration in this section, focussing on the role of internal dynamical mechanisms rather than externally imposed symmetry-breaking mechanisms that have been emphasised in previous studies. For simplicity, we shall restrict attention to the NL model, both within this section and for the remainder of this chapter, noting that all ideas apply equally well to the GQL system, provided that  $\Lambda \geq 1$ .

### 5.4.1 Identification of zonons

The sufficiency of the condition  $\Lambda \geq 1$  for the existence of the fast type of zonal jet migration raises questions regarding the additional dynamics that are captured when the zonal mean flow is permitted to interact with the longest zonal waves. Flow structures with zonal wavenumber  $k_x = 1$  are natural candidates for further investigation, since we assume that the large-scale organisation of the eddy field that coexists with the jets is an important ingredient. Following our previous discussions of the streamfunction field, we now proceed to investigate the structure of the vorticity field in order to further analyse the flow features.

In Figure 5.6 we consider three NL simulations in which one, two and three jets are migrating north. Alongside the latitude-time plots, we show snapshots of the zonal velocity field and the vorticity field, both of which are tessellated in the zonal direction in order to allow the key features to be clearly seen. This time we observe additional non-zonal structures in the vorticity field that are observed to propagate alongside the jets on their northern flanks. A distinction in pattern arises between  $n = 1$  and  $n > 1$  jets, just

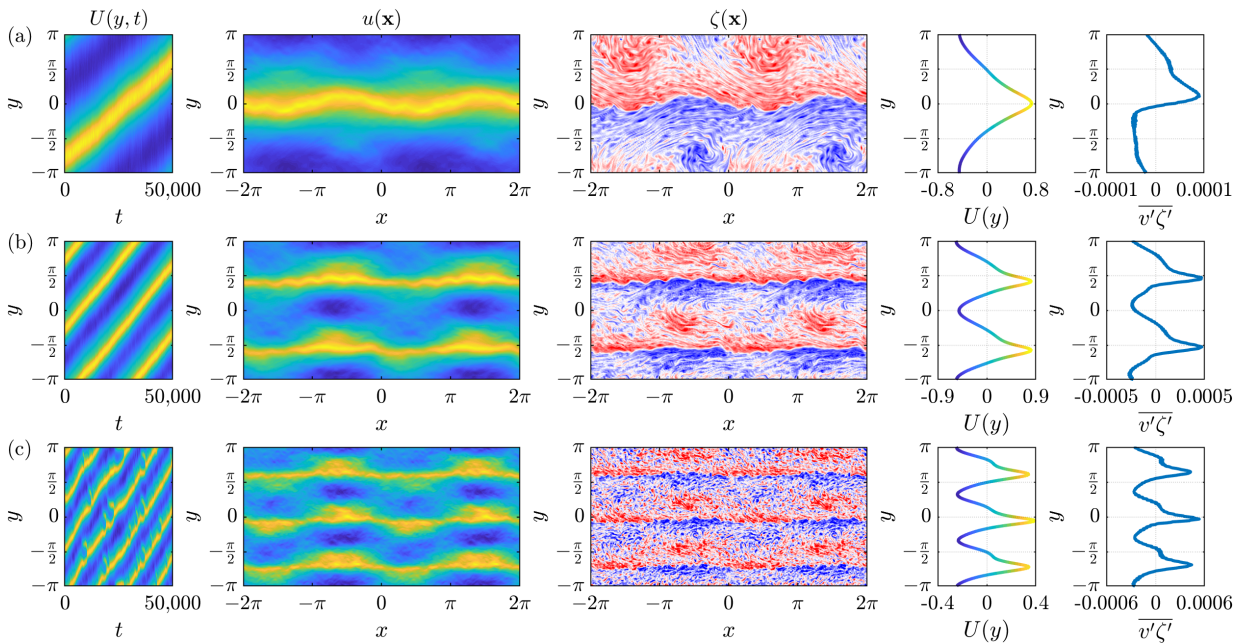


**Figure 5.6** The coexistence of jets and zonons during fast zonal jet migration in the NL model. From left to right we show a latitude-time plot of the zonal mean zonal velocity field  $U(y,t)$ , a single snapshot, duplicated in the zonal direction, of the zonal velocity field  $u(\mathbf{x})$ , the corresponding vorticity  $\zeta(\mathbf{x})$  (also duplicated in the zonal direction), the time-averaged jet velocity profile  $U(y)$  and the time-averaged eddy momentum flux convergence  $\overline{v'\zeta'}$ . (a) A single migrating jet with parameters  $\beta = 0.5$ ,  $\mu = 0.00005$ ,  $\varepsilon = 10^{-5}$ ,  $k_f = 16$ ,  $N = 256$ ,  $R_\beta = 4.41$ ; (b) Two migrating jets with parameters  $\beta = 6.0$ ,  $\mu = 0.0004$ ,  $\varepsilon = 10^{-4}$ ,  $k_f = 16$ ,  $N = 256$ ,  $R_\beta = 3.77$ ; (c) Three migrating jets with parameters  $\beta = 10.0$ ,  $\mu = 0.001$ ,  $\varepsilon = 10^{-4}$ ,  $k_f = 32$ ,  $N = 256$ ,  $R_\beta = 3.16$ .

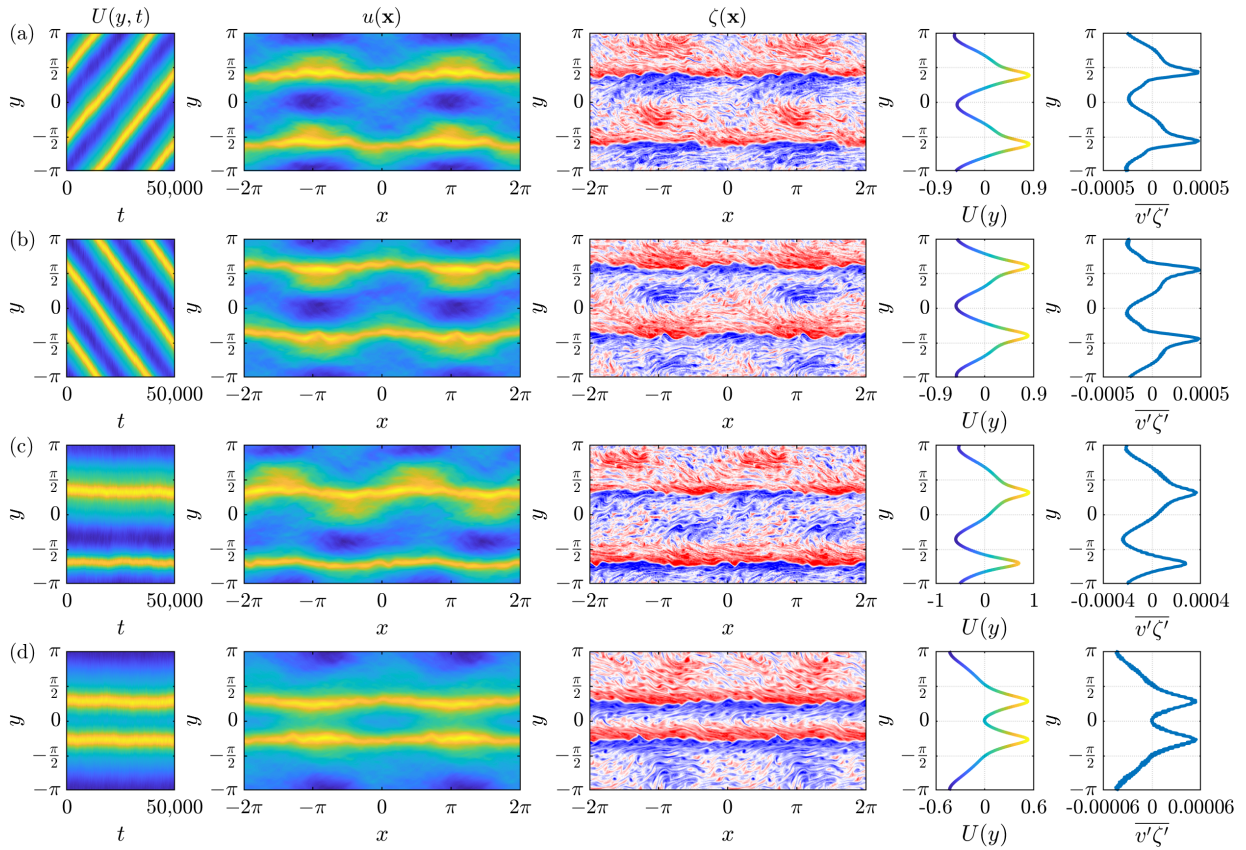


**Figure 5.7** The coexistence of jets and zonons in two-jet NL configurations. From left to right we show a latitude-time plot of the zonal mean zonal velocity field  $U(y,t)$ , a single snapshot, duplicated in the zonal direction, of the zonal velocity field  $u(\mathbf{x})$ , the corresponding vorticity  $\zeta(\mathbf{x})$  (also duplicated in the zonal direction), the time-averaged jet velocity profile  $U(y)$  and the time-averaged eddy momentum flux convergence  $\overline{v'\zeta'}$ . (a) Two jets migrating north with parameters  $\beta = 6$ ,  $\mu = 0.0004$ ,  $\varepsilon = 10^{-4}$ ,  $k_f = 16$ ,  $N = 256$ ,  $R_\beta = 3.77$ ; (b) Two jets migrating south with parameters  $\beta = 5.5$ ,  $\mu = 0.0004$ ,  $\varepsilon = 10^{-4}$ ,  $k_f = 16$ ,  $N = 256$ ,  $R_\beta = 3.74$ ; (c) Two equally-spaced but unequally-strong non-migrating jets with parameters  $\beta = 6.8$ ,  $\mu = 0.0004$ ,  $\varepsilon = 10^{-4}$ ,  $k_f = 16$ ,  $N = 256$ ,  $R_\beta = 3.82$ ; (d) Two unequally-spaced but equally-strong non-migrating jets with parameters  $\beta = 2.0$ ,  $\mu = 0.0001$ ,  $\varepsilon = 10^{-5}$ ,  $k_f = 16$ ,  $N = 256$ ,  $R_\beta = 4.26$ .

as we observed in the eddy streamfunction field in Figure 4.8. Multiple-jet configurations show strong positive (red) elliptical vorticity anomalies positioned on the northern side of the crests of the meandering jets. These are in phase with narrower negative (blue) anomalies associated with the jet meanders on the southern flanks. These features share the same wavevector,  $\mathbf{k} = (1, n)$ , as the underlying eddy field, and indeed the jet meanders, and they materialise in the zonal velocity field in the form of positive (yellow) zonal flow anomalies on the northern side of the jet meanders. Co-located features are also visible in the eddy momentum flux convergence profiles, and correspondingly, the jet velocity profiles in the form of anomalous *shoulders* protruding out from the northern side of the jet flanks. The single-jet regime in Figure 5.6(a) also shows the existence of these structures, however, this time the positive vorticity anomalies are in phase with the troughs of the jet meanders. Nevertheless, the associated eddy momentum flux convergence profile of this single-jet regime shares similarities with the profiles of the multiple-jet regimes.

These observations relate to a single stable attractor in which the jets migrate northwards. However, as discussed in Chapter 4, the system permits the existence of multiple stable attractors, such as the example shown in Figure 4.17 in which a pair of jets undergo spontaneous transitions between four different states, raising the question regarding how these flow structures reorganise themselves in each of these different

regimes. This is investigated in Figure 5.7 for these two-jet states, presented in a similar fashion to the plots in Figure 5.6. Unsurprisingly, southward migration is the opposite of northward migration, in which we see negative (blue) vorticity structures aligned on the southern side of the jets just below the troughs of the meanders. It is interesting, however, to see the existence of these features in the other two non-migrating regimes. Figure 5.7(c) shows two equally-spaced but unequally strong jets; here, the broader (top) jet is sandwiched between large-scale positive (negative) vorticity structures that are aligned above (below) the crests (troughs) of the jet meander, out of phase with one another. The final configuration in Figure 5.7(d) shows that these features are positioned on either side of the narrowly-spaced jets, however, in this case their phases do match. Thus, the arrangement of the jets and these structures is clearly important, not only for migrating regimes, but also for the large-scale dynamics of non-migrating regimes as well.

Collectively, these observations suggest that these features, which are associated with the large-scale organisation of the eddy field, play an important role in aspects of zonal jet variability, including migration behaviour. The fact that they do not form in the QL model but they are visible in the GQL models when  $\Lambda \geq 1$ , highlights that their source is via nonlinear interactions. As we proceed to argue, we believe that they constitute a single Rossby wave-like entity within the domain, known as a zonon, that has zonal wavenumber  $k_x = 1$  and which is associated with both the vorticity anomalies and the jet meanders. Before confirming this hypothesis, we must first clarify what exactly we mean by the term zonon, and how zonons relate to linear Rossby waves.

In Chapter 2 we derived the Rossby wave dispersion relation, given by (2.18), for a linear wave in the presence of a uniform background zonal flow,  $U$ . This dispersion relation, however, is not applicable in a system in which strong zonal jets have equilibrated, since the background flow,  $U(y)$ , is not constant but varies in latitude according to the structure of the jets. For a system with latitudinal shear, the derivation must be generalised to accommodate the fact that the coefficients in equation (2.15) are dependent on  $y$ . Accordingly, we seek solutions that are sinusoidal in  $x$ , however, the structure in  $y$  must remain arbitrary:

$$\psi' = \text{Re} \tilde{\psi}(y) e^{i(k_x x - \omega t)}, \quad (5.14)$$

where  $k_x$  is the zonal wavenumber,  $\omega$  is the frequency and  $\tilde{\psi}(y)$  is the (not necessarily monochromatic) amplitude, incorporating the details of the latitudinal structure. Substitution of (5.14) into (2.15) yields

$$\left( U - \frac{\omega}{k_x} \right) \left( \frac{\partial^2 \tilde{\psi}}{\partial y^2} - k_x^2 \tilde{\psi} \right) + \left( \beta - \frac{\partial^2 U}{\partial y^2} \right) \tilde{\psi} = 0, \quad (5.15)$$

which is known as the Rayleigh-Kuo equation. Both the mean flow,  $U(y)$ , given by the jet velocity profile, and the latitudinal wave structure,  $\tilde{\psi}(y)$ , can be decomposed into their individual Fourier components:

$$U(y) = \frac{1}{N} \sum_{|m| \leq k_{max}} U_m e^{imy}, \quad \tilde{\psi}(y) = \frac{1}{N} \sum_{|k_y| \leq k_{max}} \psi_{k_y} e^{ik_y y}. \quad (5.16)$$

Substituting these series into equation (5.15) and using the orthogonality property of complex exponentials, we obtain a  $(2k_{max} + 1)$  algebraic system of equations for the  $\psi_{k_y}$  for  $k_y \in (-k_{max}, k_{max})$ :

$$\frac{1}{N} \sum_{|m| \leq k_{max}} U_m \left( \frac{(k_y - m)^2 + k_x^2 - m^2}{k_x^2 + k_y^2} \right) \psi_{k_y - m} - \frac{\beta}{k_x^2 + k_y^2} \psi_{k_y} = \frac{\omega}{k_x} \psi_{k_y}. \quad (5.17)$$

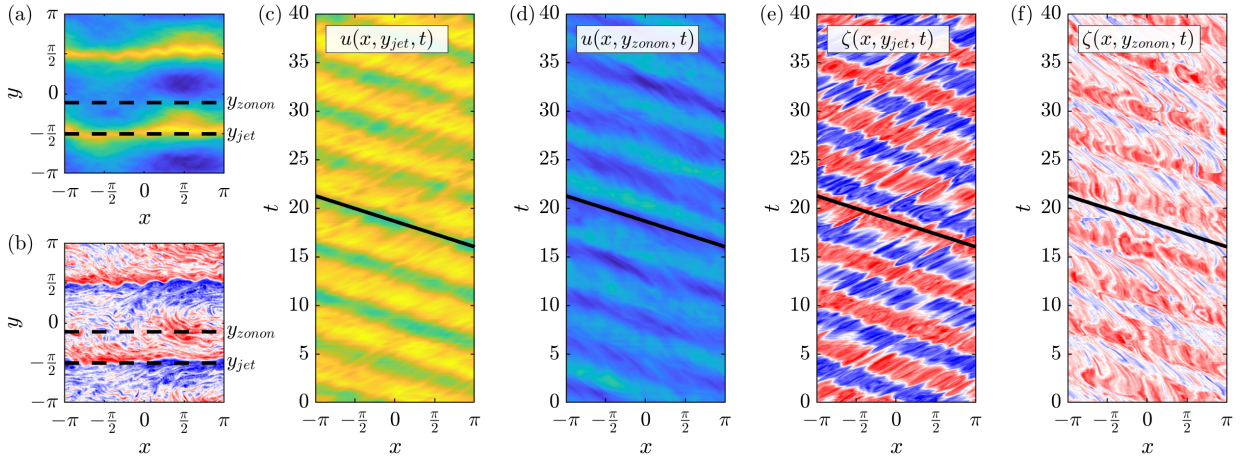


**Figure 5.8** Establishing the equivalence of the zonal phase speed,  $c_{p,x}$ , of jets and zonons in the NL model in a simulation in which a pair of jets migrate north. (a) A snapshot of the zonal velocity field; (b) the corresponding snapshot of the vorticity field; (c) a longitude-time plot of the zonal velocity at latitude  $y = y_{jet}$ ; (d) same as (c) except at latitude  $y = y_{zonon}$ ; (e) a longitude-time plot of the vorticity at latitude  $y = y_{jet}$ ; (f) same as (e) except at latitude  $y = y_{zonon}$ . Dashed lines in (a) and (b) show latitudes  $y = y_{jet}$  and  $y = y_{zonon}$  and solid lines in figures (c-f) show the theoretical zonal Rossby wave speed,  $c_{p,x} = -\frac{6}{5}$ , computed for wave  $\mathbf{k} = (1, 2)$ . The parameters used were  $\beta = 6.0$ ,  $\mu = 0.0004$ ,  $\varepsilon = 10^{-4}$ ,  $k_f = 16$ ,  $N = 256$ ,  $R_\beta = 3.77$ .

This system can be re-formulated as an eigenvalue problem for the zonal phase speeds,  $c_{p,x} = \frac{\omega}{k_x}$ , such that

$$\mathbf{A}(k_x, k_y, m, \beta) \mathbf{X} = c_{p,x} \mathbf{X}, \quad (5.18)$$

where  $\mathbf{X} = (\psi_{-k_{max}}, \dots, \psi_{k_{max}})$  and  $\mathbf{A}$  is a  $(2k_{max} + 1) \times (2k_{max} + 1)$  square matrix. Equation (5.18), which must be solved numerically, has  $2k_{max} + 1$  eigenvalues,  $c_{p,x}$ , which give the phase speeds of the associated eigenfunctions,  $\tilde{\psi}(y)$ , that correspond to the latitudinal structures of the waves. Those eigenfunctions for which  $c_{p,x} \in \mathbb{R}$  are real functions that are predominantly associated with a dominant latitudinal wavenumber,  $k_y = L$ , i.e. a single sinusoid, along with small perturbations (due to the presence of the mean flow) which project onto a set of latitudinal Fourier components. Numerical examination of a number of test cases suggests that the eigenfunctions are orthogonal and their corresponding phase speeds are well approximated by the linear Rossby wave dispersion relation (2.18), for a  $\mathbf{k} = (k_x, L)$  wave in the absence of a mean flow. Thus, the latitudinal shear associated with the jets modulates the structure of Rossby waves, generating a new class of waves which share the same zonal wavenumber and zonal phase speed, and which are associated with a range of latitudinal wavenumbers. These non-dispersive wave packets, known as zonons (Sukoriansky et al., 2008), are closely related to linear Rossby waves in the absence of a mean flow.

Returning to our hypothesis, it is necessary to verify two properties of the system in order to confirm that the flow structures observed in the vorticity field (and the corresponding large-scale organisation of the eddy field) do correspond to zonons, i.e. single entities that behave like waves. Firstly, we must check that the large-scale vorticity anomalies share the same zonal phase speeds as those associated with the jet meanders, which in turn should be well approximated by linear Rossby wave theory. Secondly, it is necessary to confirm that these vorticity structures correspond to propagating waves rather than coherent vortices. For simplicity, we restrict attention to the situation in which a pair of jets are migrating.

Focussing initially on the first property, we seek to verify that the previously identified features form a single structure that propagates with a zonal phase speed that is well defined by the linear Rossby wave

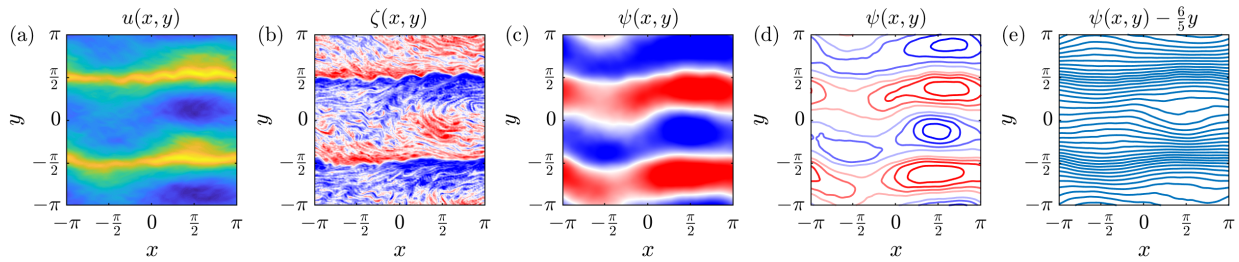


**Figure 5.9** An examination of the streamlines in a frame of reference moving with the zonons. (a) A snapshot of the zonal velocity field and the corresponding (b) vorticity field and (c) streamfunction field. (d) A contour plot showing a snapshot of the streamlines and (e) a contour plot showing the streamlines in the frame of reference moving with the jets and the zonons,  $\psi - \frac{6}{5}y$ . The parameters used were  $\beta = 6.0$ ,  $\mu = 0.0004$ ,  $\varepsilon = 10^{-4}$ ,  $k_f = 16$ ,  $N = 256$ ,  $R_\beta = 3.77$ .

dispersion relation (2.18). Accordingly, in Figure 5.8 we have selected a NL simulation in which a pair of jets are migrating north, and we investigate the evolution of the flow at two different latitudes which are fixed relative to one of the jets. These include the jet latitude,  $y = y_{\text{jet}}$ , located at the extremum of the zonal velocity profile, and the zonon latitude,  $y = y_{\text{zonon}}$ , chosen to be a fixed distance north of the jet core such that it is positioned through the centre of the structure that we associate with the zonons. These choices are shown in Figures 5.8(a,b) using dashed lines which overlay snapshots of the zonal velocity field and the vorticity field. The time evolution of the flow through these translating latitudinal slices is presented in Figures 5.8(c-f) in the form of longitude-time plots. Here, we have indicated using black lines the zonal Rossby wave speed using expression (2.19) for a dominant  $\mathbf{k} = (1, 2)$  wave, as deduced from the large-scale organisation of the eddy field. Computed to be

$$c_{p,x} \approx -\frac{\beta}{k_x^2 + k_y^2} = -\frac{6}{5}, \quad (5.19)$$

this aligns perfectly with the observed westward propagation speed of the jet meanders in Figures 5.8(c,e) and, crucially, the vorticity anomalies that we associate with the zonons in Figures 5.8(d,f), confirming that these features do form a single structure.

In order to verify the second property, notably that these features in the vorticity field correspond to waves and not coherent vortices, it is necessary to consider the organisation of the streamlines in a frame of reference that propagates with these features. This is shown in Figure 5.9, using the same example as that used in Figure 5.8. Alongside various flow field snapshots for comparison, Figure 5.9(d) plots the streamlines that correspond to the full streamfunction,  $\psi(x, y)$ , while Figure 5.9(e) shows the equivalent streamlines in a frame of reference that propagates with the zonons, given by  $\psi(x, y) - \frac{6}{5}y$ . The fact that all of these streamlines in Figure 5.9(e) are open and meandering rather than closed and circular implies that these structures are waves rather than vortices since fluid parcels move through the wave pattern. This completes our verification, thereby demonstrating the existence of zonons in our system.

#### 5.4.2 Partition of energy between jets and zonons

In our domain, zonons always have zonal wavenumber  $k_x = 1$ , equal to that of the large-scale master Rossby waves. The emergence of both zonal jets and zonons via nonlinear interactions, the ultimate source of which comes from the forcing, implies that significant fractions of the total kinetic energy are contained within both the zeroth and the first zonal wavenumber modes. In Chapter 4 we found that the zmf index in

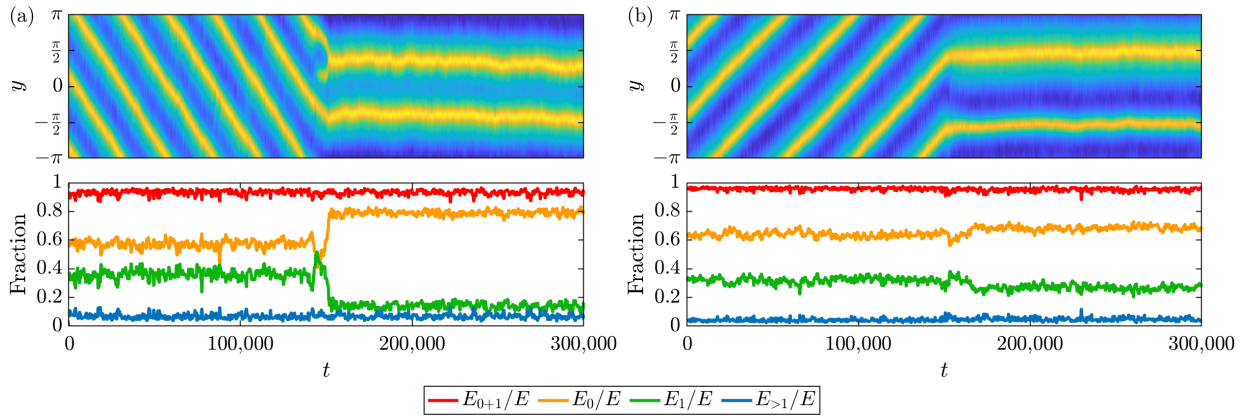


**Figure 5.10** The partition of energy between jets and zonons. (Top) Latitude-time plots showing the time evolution of the zonal mean zonal flow. (Bottom) The corresponding evolution of the fraction of energy in various zonal mode decompositions defined by expression 5.20. (a) Two jets migrating southward spontaneously reconfigure into two equally strong but unequally spaced non-migrating jets (parameters:  $\beta = 1.7$ ,  $\mu = 0.0003$ ,  $\varepsilon = 10^{-5}$ ,  $k_f = 16$ ,  $N = 256$ ,  $R_\beta = 3.19$ ). (b) Two jets migrating northward spontaneously reconfigure into two equally spaced but unequally strong non-migrating jets (parameters:  $\beta = 2.0$ ,  $\mu = 0.0002$ ,  $\varepsilon = 10^{-5}$ ,  $k_f = 16$ ,  $N = 256$ ,  $R_\beta = 3.58$ ).

the NL model varied widely between different dynamical regimes for any given zonostrophy parameter, with migration behaviour being associated with the smallest indices. In light of the identification of zonons, we hypothesize that this variability is due to the redistribution of kinetic energy between the jets and the zonons, with changes in the zmf index, associated with the jets, being compensated for by corresponding changes in the energy associated with the zonons.

This is tested in Figure 5.10, where we consider the two canonical NL regime changes from Chapter 4 in which a pair of migrating jets spontaneously transition to two different non-migrating regimes. The total energy density,  $E$ , is decomposed into components from the zonal mean flow associated with the jets, which we shall denote  $E_0$ , the first zonal wavenumber associated with the zonons,  $E_1$ , and all remaining wavenumbers,  $E_{>1}$ . Thus,  $E = E_0 + E_1 + E_{>1}$ , where each individual component is given by

$$E_j = \sum_{|k_x|=j} \sum_{k_y} \left\langle \left| \frac{k^2}{2N^2} \tilde{\psi}(\mathbf{k}, t) e^{i\mathbf{k}\cdot\mathbf{x}} \right|^2 \right\rangle. \quad (5.20)$$

If our hypothesis is true then we would expect that the combined proportion of energy in the jets and the zonons, which we shall denote  $E_{0+1}/E$ , would remain approximately constant, regardless of the dynamical behaviour in the system. This quantity is illustrated using the red lines in the lower plots in Figure 5.10, showing that this is indeed the case. The transition shown in Figure 5.10(a) involves a significant increase in the zmf index, shown using the orange line ( $E_0/E$ ), as the jets reconfigure themselves into their new, non-migrating, state. This implies that energy is dissipated substantially by the zonons during the transition, shown using the green line ( $E_1/E$ ). No significant changes in the zmf index take place in the second transition shown in Figure 5.10(b), where we observe a large fraction of the energy remaining in the zonons.

These results highlight that transitions between states may or may not be associated with a redistribution of energy between the  $k_x = 0$  and  $k_x = 1$  modes, however, regardless of the dynamical behaviour, there is always a significant amount of energy associated with the zonons, implying their significance in non-migrating states as well. Given the observed variance associated with the zmf index, we propose an alternative, behaviour-independent diagnostic that quantifies the degree of zonostrophy, or the strength of the jets, to be the combined fraction of energy in the jets and the zonons,  $E_{0+1}/E$ . Further investigation is

required to investigate the relationship between this quantity, which we shall term the generalised zonal mean flow (gzmf) index, and the zonostrophy parameter,  $R_\beta$ .

### 5.4.3 Organisational role of zonons

Zonons are evidently an important component within our simulations, leaving a strong visual footprint in the vorticity field and accounting for substantial fractions of the total kinetic energy. However, to what extent are they directly responsible for behaviours such as zonal jet migration? To answer this question, we seek to understand the degree to which the eddy momentum flux convergence profiles, such as those presented in Figures 5.7(a,b), can be accounted for by the presence of the zonons themselves. Consequently, we are interested in the contributions to these profiles from modes with zonal wavenumber  $k_x = 1$ . The eddy perturbation fields, denoted by state vector  $\mathbf{q}'$ , can be decomposed into contributions from zonal wavenumber  $k_x = 1$  modes,  $\mathbf{q}'_1$ , and contributions from modes with zonal wavenumbers  $k_x > 1$ , given by  $\mathbf{q}'_R$ :

$$\mathbf{q}'_1(\mathbf{x}, t) = \frac{1}{N^2} \sum_{|k_x|=1} \sum_{k_y} \mathbf{q}'(\mathbf{k}, t) e^{i\mathbf{k}\cdot\mathbf{x}}, \quad \mathbf{q}'_R(\mathbf{x}, t) = \frac{1}{N^2} \sum_{|k_x|>1} \sum_{k_y} \mathbf{q}'(\mathbf{k}, t) e^{i\mathbf{k}\cdot\mathbf{x}}. \quad (5.21)$$

These are then substituted into the eddy momentum flux convergence to give a component that depends on modes with  $k_x = 1$ , denoted  $\overline{v'_1 \zeta'_1}$ , and a component that depends on modes with  $k_x > 1$ , denoted  $\overline{v'_R \zeta'_R}$ :

$$\overline{v' \zeta'} = \overline{v'_1 \zeta'_1} + \overline{v'_R \zeta'_R}. \quad (5.22)$$

We plot time averages of both of these contributions, in frames of reference that move with the jets, alongside the full profile in Figure 5.11 for a simulation in which a pair of jets are migrating north. The  $\overline{v'_1 \zeta'_1}$  profile in Figure 5.11(d) displays random fluctuations about zero and bears no resemblance to the full profile in Figure 5.11(c). Instead, it is the  $\overline{v'_R \zeta'_R}$  profile which is the important contribution, showing the strongest agreement with the full profile and providing the small but essential latitudinal offset from the jet core of the corresponding velocity profile. At first, this result seems somewhat surprising; nevertheless, we are left to deduce that it is predominantly the smaller scales, or the larger wavenumbers, which maintain the jets and break the latitudinal symmetry. On the other hand, we have deduced that the zonons are an essential component of jet migration, therefore we conclude that they play an organisational role, facilitating the coherent and persistent clustering of smaller scale eddies which ultimately permit zonal jet migration regimes to persist over long time periods.

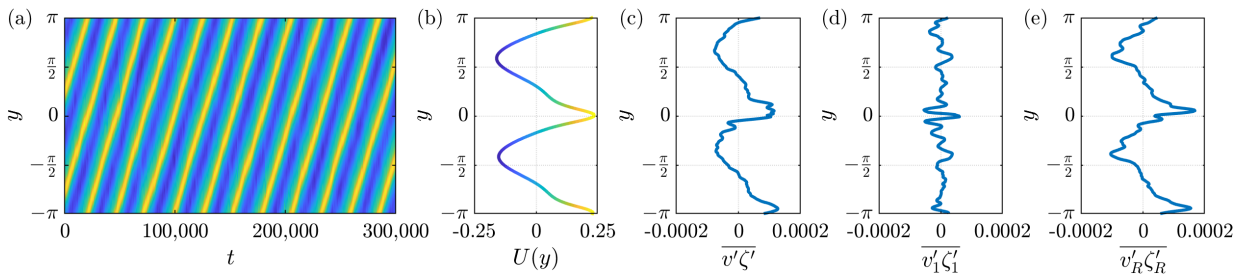


**Figure 5.11** Decomposition of the eddy momentum flux convergence. (a) Latitude-time plot of the zonal mean zonal velocity field; (b) zonal jet velocity profile,  $U(y)$ ; (c) total eddy momentum flux convergence,  $\overline{v' \zeta'}$ , and its contributions from (d) modes with zonal wavenumber  $k_x = 1$ , denoted  $\overline{v'_1 \zeta'_1}$ , and (e) all remaining modes  $k_x > 1$ , denoted  $\overline{v'_R \zeta'_R}$ . The parameters used were  $\beta = 2.2$ ,  $\mu = 0.0004$ ,  $\varepsilon = 10^{-5}$ ,  $k_f = 16$ ,  $N = 256$ ,  $R_\beta = 3.04$ .

#### 5.4.4 Necessity of small-scale eddies

As we have seen, the large-scale organisation of small-scale eddies is an essential component in the mechanism for fast jet migration. Eddies of varying sizes are formed as a consequence of nonlinear interactions, with energy predominantly flowing from small scales (associated with, for example, the forcing) to larger scales via the inverse cascade. This leads to speculation about whether the existence or the properties of the stochastic forcing that generate these eddies influence the likelihood or the robustness of migration behaviour. To answer this question, we begin by demonstrating a basic, but fundamental, point, notably that the generation of eddies by the stochastic forcing of the vorticity field is an essential requirement for zonal jet migration, and indeed aspects of variability in more general.

This is illustrated in Figure 5.12, where we show an example of a simulation in which two stochastically-forced jets migrate north with constant translation speed. At  $t = 100,000$ , indicated by the red line, we abruptly switch off both the stochastic forcing and the linear friction, leaving the hyperviscosity term for numerical stability. This leaves the unforced, undamped beta-plane vorticity equation,

$$\frac{\partial \zeta}{\partial t} + J(\psi, \zeta) + \beta \frac{\partial \psi}{\partial x} = \nu_n \nabla^{2n} \zeta, \quad (5.23)$$

which we continue to solve for the remainder of the simulation. The evolution of the zonal mean zonal flow in the latitude-time plot in Figure 5.12(a) shows that, once the forcing is turned off, the pair of jets stop migrating and their latitudinal positions become steady in space and time. There are no significant changes to their relative strengths or spacings, or indeed the fraction of energy in the zonal mean flow. Interestingly, once the forcing is turned off, the jet velocity profiles maintain the latitudinal asymmetries from the migration regime, however, the associated eddy momentum flux convergence profiles lose their offset from

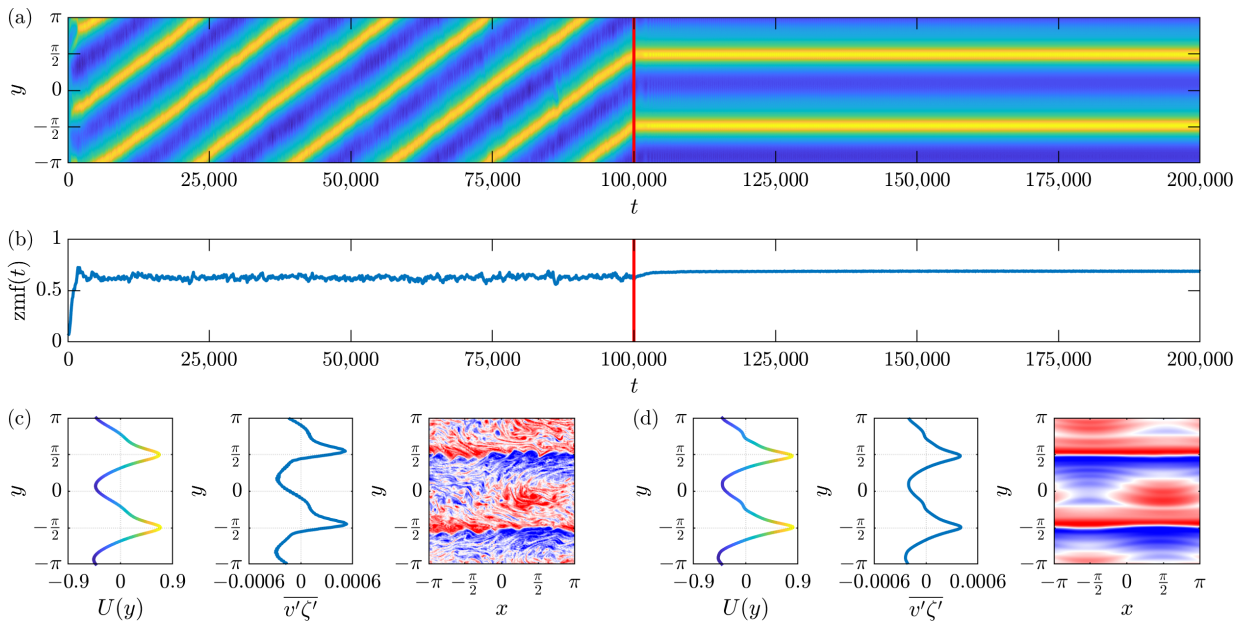


**Figure 5.12** The necessity of external forcing for jet migration behaviour in the NL model. (a) Latitude time plot of the zonal mean zonal velocity in which we abruptly turn off the stochastic forcing and linear friction at  $t = 100,000$  and solve the deterministic equation thereafter; (b) the evolution of the zmf index; (c) time averages of the jet velocity profile and the eddy momentum flux convergence for  $t < 100,000$  and a snapshot of the vorticity field  $\zeta(\mathbf{x})$ ; (d) same as (c) except for  $t > 100,000$ . Parameters used are  $\beta = 4.5$ ,  $\mu = 0.0005$ ,  $\varepsilon = 10^{-4}$ ,  $k_f = 16$ ,  $N = 256$ ,  $R_\beta = 3.47$ .

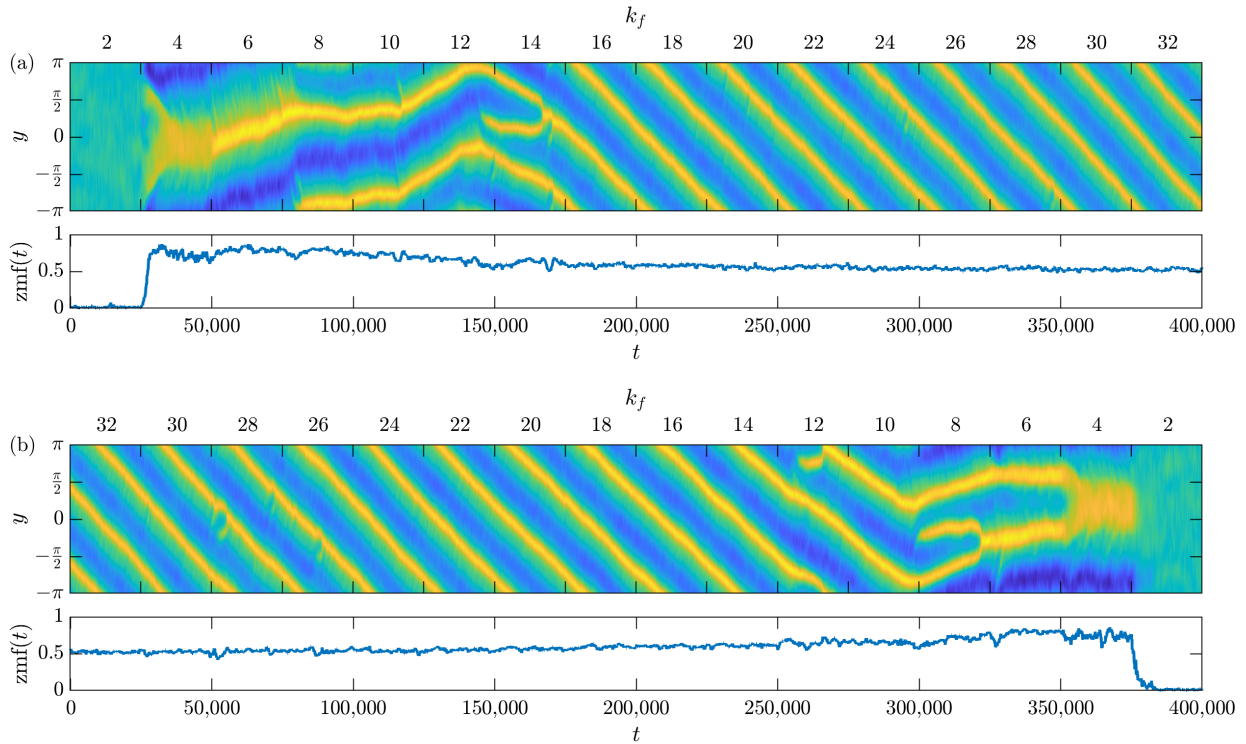


**Figure 5.13** The dependence of jet migration behaviour on the forcing wavenumber,  $k_f$ , in the NL model. Plotted are latitude-time plots of the zonal mean zonal velocity field and the corresponding evolution of the zmf index. All parameters are held constant except for the value of  $k_f$  which is piecewise constant over time periods of duration  $t = 25,000$  and changed in multiples of two over the range  $2 \leq k_f \leq 32$  via (a) increases in  $k_f$  and (b) decreases in  $k_f$ . The parameters used are  $\beta = 2.2$ ,  $\mu = 0.0004$ ,  $\varepsilon = 10^{-5}$ ,  $N = 256$ ,  $R_\beta = 3.04$ .

the jet cores. In addition, snapshots of the vorticity field in Figures 5.12(c) and 5.12(d) highlight that the zonons persist after the forcing has been turned off, further demonstrating that the zonons themselves do not drive the migration. Despite imposing jet migration as an initial condition in this deterministic system, we see that the eddies are an essential component.

It is also useful to investigate the effects of the forcing wavenumber,  $k_f$ , on the propensity of jets to migrate, since this in turn will influence the spectrum of eddy wavenumbers. Our findings indicate that smaller forcing scales (i.e. larger  $k_f$ ) lead to more robust migration tendencies, and vice-versa, with no migration at all when the scale of the forcing is sufficiently large. This is demonstrated in Figure 5.13, which shows a couple of long numerical simulations in which all parameters are held constant except for the value of the forcing wavenumber, which is held piecewise constant over time intervals of duration  $t = 25,000$  ( $\mu t = 10$ ) and is either increased or decreased in multiples of two over the range  $2 \leq k_f \leq 32$  at discrete time steps. The parameters were chosen such that we would expect to see two migrating jets within the domain. Latitude-time plots show that at the smallest wavenumbers, jets either do not form ( $k_f = 2$ ), the number of jets is underestimated ( $4 \lesssim k_f \lesssim 6$ ) or else two jets form which do not migrate ( $6 \lesssim k_f \lesssim 8$ ). However, as  $k_f$  increases, we see robust jet migration behaviour that is associated with a seemingly constant speed of latitudinal translation. The associated zmf index is higher for the smaller forcing wavenumbers in which jets exist but migration behaviour does not occur, in line with previous observations.

Combining these findings, we are thus left to conclude that small-scale eddies, the ultimate source of which comes from the stochastic forcing within our models, are essential for this organised behaviour.

### 5.4.5 Summary of the zonal jet migration mechanism

To summarise this new theory for zonal jet migration, we have identified the existence of zonons, which are not captured in the QL model, and have determined their importance for migration behaviour. Zonons, which are forced by nonlinear interactions, are the generalisation of linear Rossby waves to flows with latitudinal shear. Whilst they share the same zonal wavenumber,  $k_x$ , as equivalent Rossby waves in a system at rest, their latitudinal structure exhibits perturbations about a dominant sinusoid (with latitudinal wavenumber  $L$ ) such that it projects onto a range of latitudinal Fourier components. To the first approximation, this wavepacket behaves like a  $\mathbf{k} = (k_x, L)$  Rossby wave in a system with no background flow, sharing the same zonal phase speed. In the context of zonal jet migration, we observe a single dominant zonon with zonal wavenumber  $k_x = 1$  that is associated with both the jet meanders and the wave-like pattern of vorticity anomalies that can be seen quite clearly in the flow snapshots.

This geometrical organisation can be visualised in snapshots of the vorticity field, for example in Figures 5.7(a,b), showing the relative pattern of large-scale vorticity anomalies and the meanders associated with the zonal jets. As can be seen, strong vorticity anomalies, which we associate with the zonons, are positioned on the side of the jets towards which they are migrating, causing coherent patterns of positive (north) or negative (south) vorticity. These are in phase with anomalies of the opposite sign that are associated with the jet meanders. The zonons play an organisational role of the smaller scale eddy field which allows for the persistent breaking of the north-south symmetry in the eddy momentum flux convergence, causing positive zonal flow anomalies on the jet crests (north) or troughs (south), and thus a tendency towards migration in the direction of these anomalies. The generation of small-scale eddies by stochastic forcing is essential for this mechanism, however, the precise nature in which these eddies are organised by the zonons is not clear.

Of course, we would like to emphasize that any randomly occurring flow structures that break the north-south symmetry will result in a net northward or southward force on the jet, causing, for example, randomly wandering behaviour. The zonons, however, are sufficiently robust in space and time that migration behaviour becomes a stable attractor of the system for certain sets of parameters. No equivalent mechanism exists in the QL model, which is why we do not observe this type of robust migration there. These ideas support and go beyond previously discussed hypotheses which revolve around the idea that jet migration requires a latitudinal bias in the eddy momentum flux convergence about the jet core, providing a new explanation for the persistence of this symmetry breaking mechanism. We believe that this is the first study to demonstrate one of the roles that zonons play in the dynamics of geophysical turbulence.

## 5.5 The translation speed of migrating zonal jets

The final property of zonal jet migration that we wish to investigate concerns the factors which affect the translation speed of the jets. As we have mentioned, we observe a unique translation speed in the latitude-time plots for any given set of external parameters for which fast migration occurs, suggesting that the translation speed is a predictable property of the system. The measurement of these speeds is not trivial due to the fluctuating nature of the jets, leading to a small-degree of variability present in each simulation, visible for example in Figure 4.1(c). Nevertheless, we use the procedure outlined in Section 3.4.3 and take the approach of measuring the speed over the longest possible time period in each simulation, to obtain an average value. These results are analysed using two complementary approaches. Firstly, we consider the relationship between translation speeds and the resultant force balance acting on the jets due to latitudinal

asymmetries in the eddy momentum flux convergence. This is followed by a second approach where we conduct an empirical investigation of the dependence of the speeds on external parameters.

### 5.5.1 Self-similarity of velocity profiles and eddy momentum flux convergences

It is helpful to begin with a discussion of the properties of the zonally-averaged profiles of migrating jet systems, and their relative dependencies on translation speeds. For example, we demonstrate in Figures 5.14(a,b) that the shapes of these profiles are universal. This is confirmed using nine simulations, selected such that the system equilibrated with a pair of jets that migrated north with a broad range of translation speeds (associated with different external parameters). Figure 5.14(a) plots each jet velocity profile, normalised by its maximum value,  $U_{\max}$ , while Figure 5.14(b) shows the corresponding eddy momentum flux convergence profiles, normalised by their maximum values,  $\overline{v'\zeta'}_{\max}$ . In each case all curves are close to a single profile, regardless of the translation speeds, suggesting that the relative organisation of the jets and zonons (and the associated eddy momentum flux convergence profiles) conforms to a particular pattern.

With this in mind, there must be a well-defined relationship between the relative magnitudes of these profiles and the translation speed,  $\mathcal{V}$ , of the jets. This can be seen by inspection of the transformed equation for the maintenance of the jets (3.31), given in Chapter 3, which introduced the coordinate  $\varphi = y - \mathcal{V}t$  in order to work in a frame of reference that moves with the jets. Within this reference frame, we consider a solution with zonal velocity and eddy momentum flux convergence profiles given respectively by

$$U(\varphi) = aU_{\text{profile}}(\varphi), \quad \overline{v'\zeta'}(\varphi) = b\overline{v'\zeta'}_{\text{profile}}(\varphi), \quad (5.24)$$

where  $U_{\text{profile}}$  is a universal velocity profile,  $\overline{v'\zeta'}_{\text{profile}}$  is a universal eddy momentum flux convergence profile, and the prefactors  $a$  and  $b$  control their relative magnitudes. Substituting these into (3.31) and dividing by  $a$ , noting that hyperviscosity is negligible (see Chapter 3) and therefore can be discarded, the transformed zonal mean momentum equation becomes

$$-\mathcal{V} \frac{d}{d\varphi} U_{\text{profile}}(\varphi) = \frac{b}{a} \overline{v'\zeta'}_{\text{profile}}(\varphi) - \mu U_{\text{profile}}(\varphi). \quad (5.25)$$

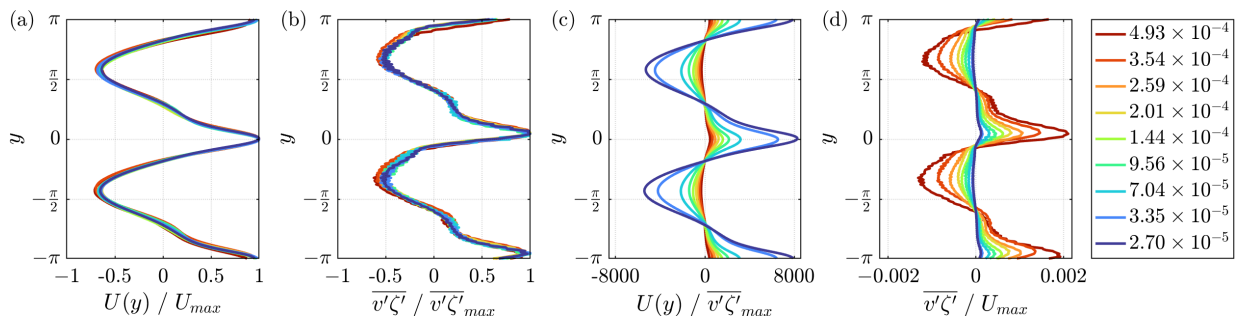


**Figure 5.14** The velocity profiles and eddy momentum flux convergences for nine different configurations in which a pair of zonal jets migrate northwards, selected in order to include a wide spectrum of translation speeds which are indicated by the line colours. (a) The velocity profiles normalised by their maximum values,  $U(y)/U_{\max}$ . (b) The eddy momentum flux convergences normalised by their maximum values,  $\overline{v'\zeta'}/\overline{v'\zeta'}_{\max}$ . (c) The velocity profiles normalised by the maximum eddy momentum flux convergence values,  $U(y)/\overline{v'\zeta'}_{\max}$ . (d) The eddy momentum flux convergences normalised by the maximum velocity profile values,  $\overline{v'\zeta'}/U_{\max}$ .

Whilst the explicit profiles are not determinable from this equation, it does predict that the magnitude of the translation speed,  $\mathcal{V}$ , must be balanced by changes in both the ratio,  $b/a$ , corresponding to the relative magnitude of the eddy momentum flux convergence profile, in addition to the frictional damping rate,  $\mu$ .

This former balance is demonstrated to some extent in Figures 5.14(c,d), which plot the same profiles as those presented in Figures 5.14(a,b), however, this time we normalise each profile by the maximum value of its corresponding profile. For example, the velocity profiles are plotted by assuming a constant magnitude eddy momentum flux convergence profile, and vice versa. Clear trends emerge in relation to the translation speed, denoted using colours, where faster translation speeds are associated with larger magnitude eddy momentum flux convergence profiles for any given velocity profile, and vice versa, supporting the theoretical predictions.

### 5.5.2 Dependence of translation speeds on eddy momentum flux convergences

This brings us to our first analysis of jet translation speeds, where we seek to verify in a more rigorous fashion the role of the eddy momentum flux convergence using data that has been analysed from 130 different numerical simulations exhibiting jet migration. The jet migration mechanism summarised in Section 5.4.5 suggests that the translation speed,  $\mathcal{V}$ , should be related to the eddy momentum flux convergence asymmetry across the jet core (the resultant force), which in turn is related to the relative amplitudes of the profiles, defined as  $b/a$ , due to their universal shape. Chemke and Kaspi (2015b) demonstrated this to be the case for the poleward translation speed of migrating jets in their idealised GCM with spherical geometry. They defined a quantity which they termed the net eddy momentum flux convergence, equal to the sum of the eddy momentum flux convergence on the poleward flank (i.e. the direction of migration) minus the sum on the equatorward flank. The meridional width of each flank was defined as the distance between the latitude,  $y_{\text{jet}}$ , at which the maximum zonal mean zonal velocity,  $U_{\text{max}}$ , occurs, and the latitude,  $y_0$ , at which  $U(y)$  first becomes zero. Defining the northern boundary by  $y_0^{(+)}$  and the southern boundary by  $y_0^{(-)}$ , the net eddy momentum flux convergence,  $\overline{v'\zeta'}_{\text{net}}$ , can be computed as

$$\begin{aligned}\overline{v'\zeta'}_{\text{net}} &= \int_{y_{\text{jet}}}^{y_0^{(+)}} \overline{v'\zeta'} dy - \int_{y_0^{(-)}}^{y_{\text{jet}}} \overline{v'\zeta'} dy \\ &= \overline{v'\zeta'}^{(+)} - \overline{v'\zeta'}^{(-)}.\end{aligned}\tag{5.26}$$

This calculation is illustrated in Figure 5.15(a), where  $\overline{v'\zeta'}_{\text{net}}$  is computed by subtracting the light blue area, corresponding to  $\overline{v'\zeta'}^{(-)}$ , from the dark blue area, corresponding to  $\overline{v'\zeta'}^{(+)}$ .

Chemke and Kaspi (2015b) determined that the translation speed of their jets was proportional to  $\overline{v'\zeta'}_{\text{net}}$ , however, it should be noted that their conclusions were based on a restricted collection of numerical simulations in which the only parameter to be varied was the rotation speed of the planet, ensuring that the total energy remained constant. This is certainly not the case in our simulations due to the fact that all parameters are explored systematically. Wishing to check the applicability of these findings to our own simulations, we therefore choose to include a normalisation factor in the definition of  $\overline{v'\zeta'}_{\text{net}}$ , thereby ensuring that it remains dimensionally consistent with the translation speeds. As demonstrated in Figure 5.14 and hinted at by equation (5.25), a suitable choice is to normalise by  $U_{\text{max}}$  such that the amplitudes of the jet profiles are held constant.

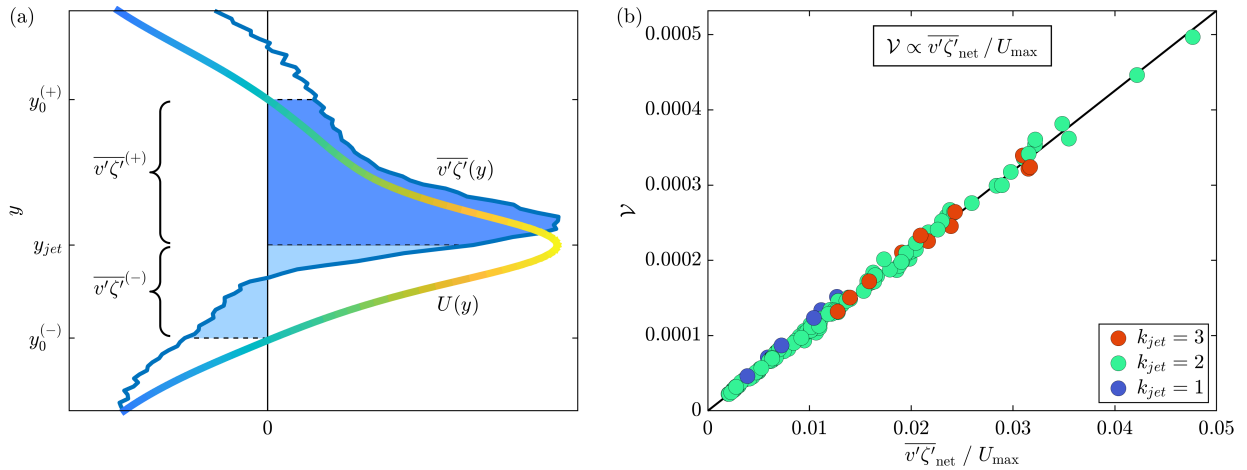


**Figure 5.15** (a) An illustration depicting the procedure for computing the eddy momentum flux convergence bias across the jet core for the case of a jet migrating northwards. The contributions to  $\overline{v'\zeta'}$  (blue curve) on the jet flanks (coloured curve) are integrated between the jet core at  $y_{jet}$  and the latitudes at which the jet attains zero velocity, denoted by  $y_0^{(+)}$  and  $y_0^{(-)}$ . The southward (light blue) contribution,  $\overline{v'\zeta'^{-}}$ , is subtracted from the northward (dark blue) contribution,  $\overline{v'\zeta'^{+}}$  to give  $\overline{v'\zeta'_{net}}$ . The situation is flipped for southward migration. (b) The dependence of jet translation speeds,  $\mathcal{V}$ , on the normalised eddy momentum flux convergence bias,  $\overline{v'\zeta'_{net}}/U_{max}$ , for a range of simulations showing different numbers of jets migrating (colours).

In Figure 5.15(b) we plot  $\overline{v'\zeta'_{net}}/U_{max}$  against the translation speed,  $\mathcal{V}$ , for a range of simulations in which varying numbers of jets (denoted by colour) migrate. A clear linear relationship is visible, confirming that  $\mathcal{V} \propto \overline{v'\zeta'_{net}}/U_{max}$ , or equivalently,  $\mathcal{V} \propto \frac{b}{a}\overline{v'\zeta'}$ , due to the universality of the profiles. These results, which we find to be independent of the manner in which the meridional widths of the integrated areas associated with  $y_0^{(-)}$  and  $y_0^{(+)}$  are defined, confirm the necessity of the shape and offset of the eddy momentum flux convergence profile in the migration mechanism. Nevertheless, this approach does not reveal a relationship between the translation speed and the system parameters, as implied by the uniqueness of the speed for any given set of parameters. Consequently, we now seek to investigate the dependence on individual parameters in more detail.

### 5.5.3 Dependence of translation speeds on system parameters

In our quest for an explicit parameter-dependent relationship governing the translation speed of migrating zonal jets, it is necessary to identify the key parameters. Ideally, we would hope that the translation speed depends on the set of input parameters,  $\{\beta, \mu, \varepsilon, k_f, L_D\}$ , since in theory the emergent quantities are functions of these parameters, however, there may also be a dependence on quantities such as  $k_{jet}$  which do not vary continuously (noting that  $k_{jet}$  may or may not be dimensional depending on the role that  $L_D$  plays). We choose to neglect the consideration of  $L_D$  since it has not been varied explicitly in our simulations, however, implicit variation has been simulated via different combinations of parameters due to the fact that there are more input parameters than dimensions. Consequently, we shall assume that

$$\mathcal{V} \sim \mathcal{F}(\beta, \mu, \varepsilon, k_f, k_{jet}), \quad (5.27)$$

i.e. an explicit relationship exists where our goal is the determination of the function  $\mathcal{F}$ .

A sensible starting point is the hypothesis that  $\mathcal{V}$  is related to the velocity  $U_{rms} = \sqrt{2E} = \sqrt{\varepsilon/\mu}$ , chosen on the basis that it is a naturally occurring velocity scale and also due to the ease with which it can be written in terms of external parameters. This theory is tested using the same data set that was analysed in the previous section, which considered a broad spectrum of parameters. In Figures 5.16(a-e) we plot  $\mathcal{V}/\sqrt{\varepsilon/\mu}$  against  $R_\beta$ , both of which are dimensionless, where each simulation is represented with a single circle. Each row corresponds to the investigation of the dependence on individual parameters, listed on the left-hand side and denoted using colours.

The results, in general, support the hypothesis that  $\mathcal{V}$  is related to  $\sqrt{\varepsilon/\mu}$  by highlighting a striking  $R_\beta^{-5}$  scaling, shown using the black lines, giving  $\mathcal{V} \sim \sqrt{\varepsilon/\mu} R_\beta^{-5}$ . This can be re-written using expressions (3.9) and (3.10) to give a simple relationship in terms of the frictional damping rate and the Rhines scale:

$$\mathcal{V} \sim \frac{\mu^{3/4} \varepsilon^{1/4}}{\beta^{1/2}} \sim \mu L_{Rh}. \quad (5.28)$$

Figures 5.16(f-j) check this empirical relationship by plotting  $\mathcal{V}$  against  $\mu L_{Rh}$ , once again investigating the dependence on individual parameters. Whilst no additional dependence on the set of input parameters  $\{\beta, \mu, \varepsilon, k_f\}$  is detectable, there are hints that  $k_{jet}$  may play a role in the scaling, where we notice some deviations away from the trend, particularly when  $k_{jet} = 1$ . Moreover, the data show a certain amount of variability around the scaling, which may or may not be linked to the issues surrounding the measurements of the translation speeds. Figures 5.16(k-o) provide additional justification to these observations by plotting  $\mathcal{V}/(\mu L_{Rh})$  against  $R_\beta$ , where we deduce that the prefactor for the relationship is close to 0.8, giving

$$\mathcal{V} \approx 0.8 \mu L_{Rh}. \quad (5.29)$$

In a perfect fit, all data points would lie along this horizontal line, therefore the vertical spread over the range of prefactors  $\in (0.5, 1.4)$  quantifies the associated variability, and also further highlights the potential dependency of the relation on  $k_{jet}$ .

Rather than applying an iterative series of ad hoc adjustments to expression (5.29) to incorporate this additional contribution, we take a step back and apply a more systematic approach by assessing the individual contributions to the relation on a parameter-by-parameter basis, as shown in Figures 5.17(a-e). We begin by keeping all parameters fixed except for the value of  $\beta$  which we vary over a series of six simulations shown in Figure 5.17(a). A scaling of  $\mathcal{V} \sim \beta^{-1}$  emerges, which differs from expression (5.28). Incorporating this contribution into  $\mathcal{V}$ , we next investigate the dependence on  $\mu$  in Figure 5.17(b) by keeping the remaining parameters constant (excluding  $\mu$  and  $\beta$ ). This scaling, given by  $\mathcal{V}/\beta^{-1} \sim \mu^{1/2}$ , also differs from expression (5.28), where we deduce that  $\mathcal{V} \sim \beta^{-1} \mu^{1/2}$ . Continuing in this fashion, we subsequently investigate the dependence on  $\varepsilon$ , followed by  $k_f$ , and finally  $k_{jet}$ . The results are found to be independent of the order in which the parameters are investigated, with the empirical relationship being

$$\mathcal{V} \sim \frac{\varepsilon^{1/2} \mu^{1/2} k_{jet}}{\beta} \sim \mu \left( \frac{\varepsilon^{1/4}}{\beta^{1/2} \mu^{1/4}} \right)^2 k_{jet} \sim (\mu L_{Rh}) (L_{Rh} k_{jet}), \quad (5.30)$$

after a small rearrangement, which is dimensionally consistent provided that  $k_{jet}$  has dimension  $L^{-1}$ .

As before, we verify this expression using data from our simulations, with the results presented in Figures 5.17(f-j) and 5.17(k-o), analogously to those in Figure 5.16. There is arguably less variability, and

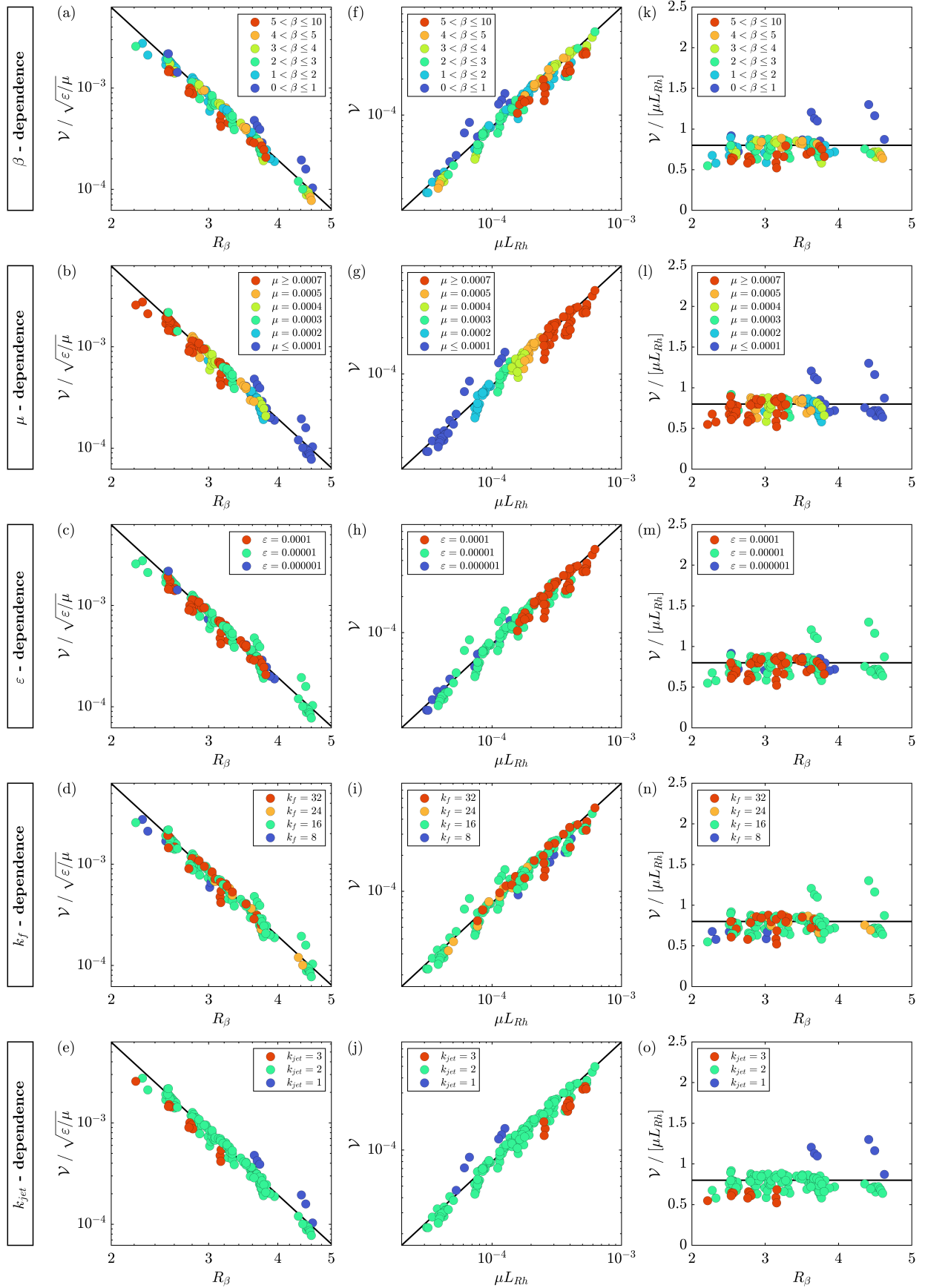


**Figure 5.16** The dependence of the translation speed,  $\mathcal{V}$ , on the characteristic flow speed  $\sqrt{\varepsilon/\mu}$ , broken down by the parameters indicated on the left hand side. (Left)  $\mathcal{V} / \sqrt{\varepsilon/\mu}$  plotted against  $R_\beta$ , revealing the scaling  $\mathcal{V} / \sqrt{\varepsilon/\mu} \sim R_\beta^{-5}$ . (Middle) Verification of the scaling  $\mathcal{V} \sim \mu L_{Rh}$ . (Right) The dependence of the scaling  $\mathcal{V} \sim \mu L_{Rh}$  on  $R_\beta$ .

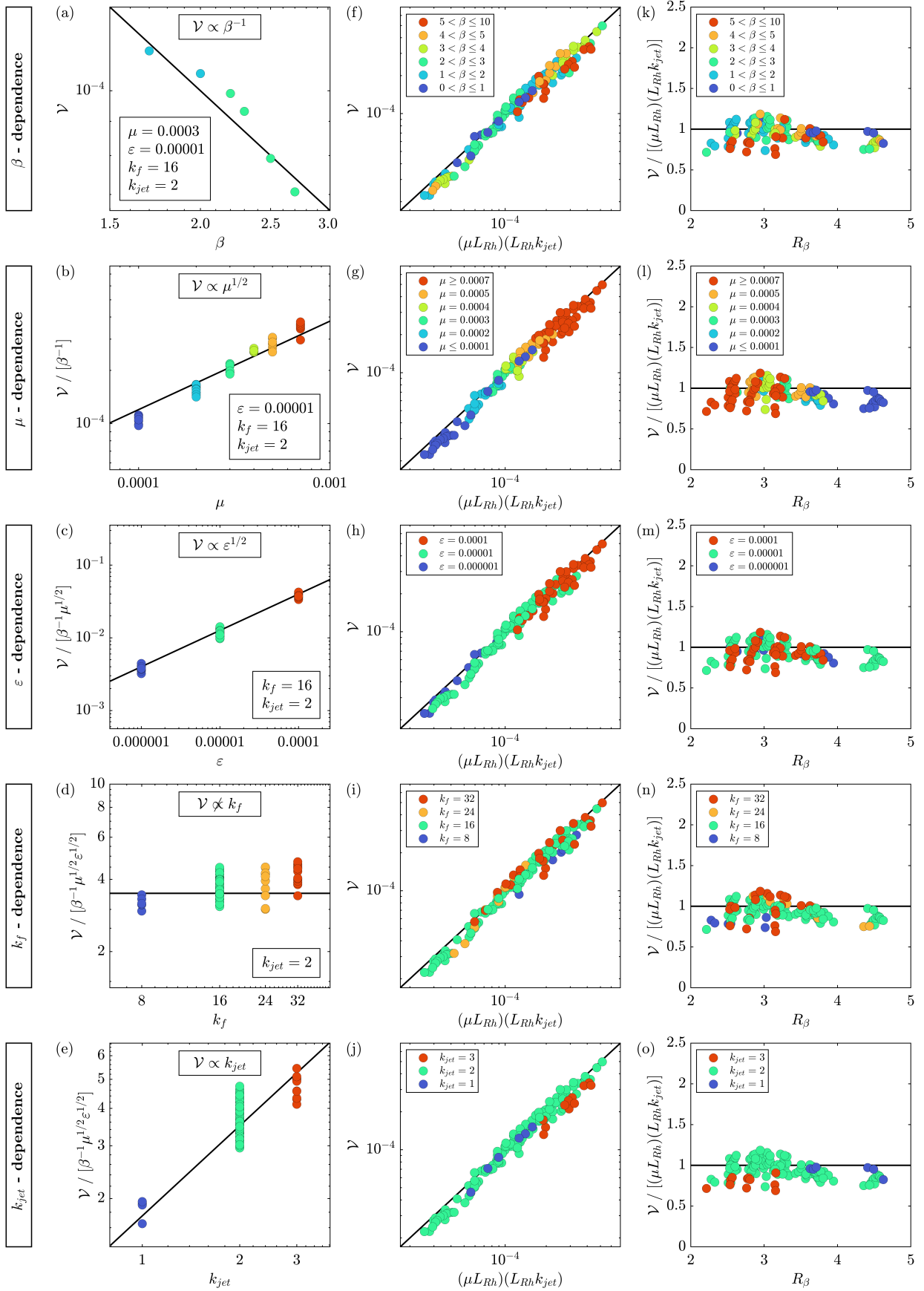


**Figure 5.17** An empirical deduction of the dependence of the translation speed,  $\mathcal{V}$ , on the external parameters  $\{\beta, \mu, \epsilon, k_f\}$  in addition to  $k_{jet}$ . (Left) The determination of parameter-dependent scalings. (Middle) Verification of the empirical scaling  $\mathcal{V} \sim (\mu L_{Rh})(L_{Rh} k_{jet})$ . (Right) The dependence of the empirical scaling  $\mathcal{V} \sim (\mu L_{Rh})(L_{Rh} k_{jet})$  on  $R_\beta$ .

no obvious additional dependency on any of the parameters, suggesting that this new relationship is an improvement on our initial estimate. In addition, we find that the prefactor is approximately unity, giving

$$\mathcal{V} \approx (\mu L_{Rh}) (L_{Rh} k_{jet}). \quad (5.31)$$

This expression bears strong resemblance to our earlier estimate given by (5.29), retaining the dependence on  $\mu L_{Rh}$  while combining this with an additional dimensionless contribution given by  $L_{Rh} k_{jet}$ .

It is interesting, and perhaps of significance, that in Chapter 4 we deduced that the linear relationship between the number of jets and the Rhines scale is  $k_{jet} = 0.80 k_{Rh}$  in our NL simulations. Upon rearranging, this gives  $L_{Rh} k_{jet} = 0.80$ , which is precisely the prefactor determined in our original expression for the translation speeds (5.29). It seems plausible, therefore, that the additional factor of  $L_{Rh} k_{jet}$  represents a *quantisation* factor, i.e. the degree to which the configuration of jets conforms to the theoretical number predicted by the Rhines scale. Indeed, the number of jets is not a continuous quantity, and a system possesses an integral number at any one time.

We explore this idea in Figure 5.18(a), where we plot the quantity  $L_{Rh} k_{jet}$  against  $R_\beta$  for each of our 130 simulations in which the jets migrate. As can be seen, the degree of variability decreases as  $k_{jet}$  increases, with the greatest variance associated with those simulations in which  $k_{jet} = 1$ , in agreement with the previous observations in Figure 5.16. Extrapolating this investigation in Figure 5.18(b) to all simulations from the NL model where  $k_{jet} \in \{1, 2, 3\}$ , which includes those where the jets do not migrate, we see similar patterns emerging. This demonstrates that the additional factor,  $L_{Rh} k_{jet}$ , represents the uncertainty in  $k_{jet}$ , which is a simple consequence of the fact that it must be an integer and cannot vary continuously with  $k_{Rh}$ .

In summary, both relationships given by (5.29) and (5.31) offer a skilful prediction of zonal jet translation speeds based on data covering more than one order of magnitude. In addition, both relationships are independent of the forcing wavenumber,  $k_f$ , in agreement with Figure 5.13. Nevertheless, it seems sensible to restrict our attention to the simpler expression given by  $\mathcal{V} \sim \sqrt{\varepsilon/\mu} R_\beta^{-5} \sim \mu L_{Rh}$ , keeping in mind that the factor  $L_{Rh} k_{jet} \sim O(1)$  results from quantisation restrictions on  $k_{jet}$ .

Wishing to relate these findings to our earlier discussions in Chapter 4, we seek parameter-related conditions for the existence of zonal jet migration. An important observation that is apparent in Figures

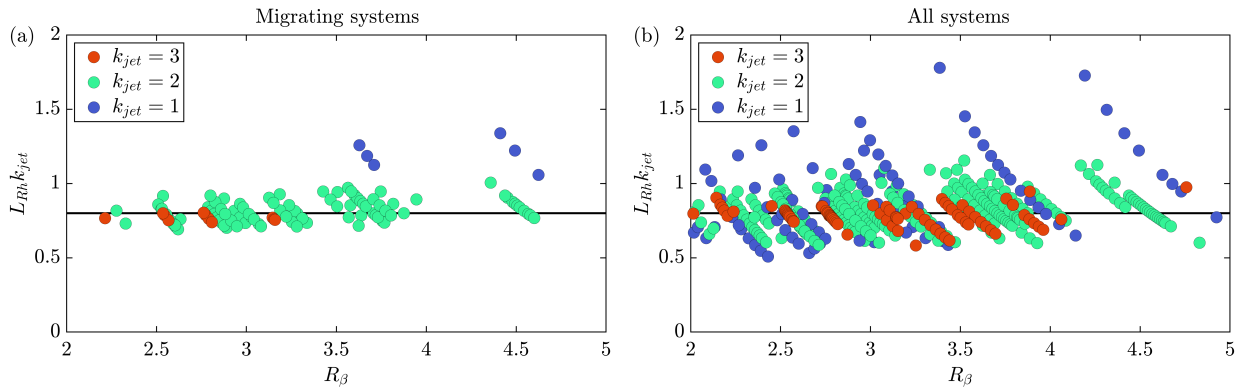


**Figure 5.18** The relationship between the Rhines scale and the number of jets, defined as  $L_{Rh} k_{jet}$ , plotted as a function of the zonostrophy parameter,  $R_\beta$ , for (a) 130 numerical simulations selected in which the jets migrate and (b) all numerical simulations in which one, two or three jets emerged (including those that did not migrate). Each circle represents a single simulation, colour coded according to the number of the jets within the domain. The black lines indicate  $L_{Rh} k_{jet} = 0.8$ , i.e. the linear relationship identified in Chapter 4 for NL simulations.

5.16(a-e) reveals that  $\mathcal{V} \ll \sqrt{\varepsilon/\mu}$ , i.e. translation speeds are significantly smaller than characteristic flow velocities. This implies that  $\mu L_{Rh} \ll \sqrt{\varepsilon/\mu}$ , which, upon rearranging, and using expression (3.10) for the zonostrophy parameter, shows that a necessary condition for migration is  $R_\beta^5 \gg 1$ . This is consistent with our earlier findings that jet migration is visible in our simulations when  $R_\beta > 2$ . In addition, we see that the ratio  $\mathcal{V}/\sqrt{\varepsilon/\mu} \rightarrow 0$  as  $R_\beta \rightarrow \infty$ , suggesting that there may be an upper bound on the zonostrophy parameter for the existence of zonal jet migration. Indeed, this was suggested by the parameter space in Figure 4.11(c) in which no migration was observed in those simulations for which  $R_\beta \gtrsim 5$ .

It is worth noting that our findings are in line with those deduced by Chemke and Kaspi (2015b), who related the translation speed of migrating jets in their idealised GCM to both the rotation speed,  $\Omega$ , of the planet and the number of jets in the domain. They found that  $\mathcal{V} \propto \Omega^{-0.44}$ , which is fairly consistent with the dependency on  $\beta$  in expression (5.28). In addition, they noted that  $\mathcal{V} \propto k_{jet}^{-1}$  which agrees with our findings, where we argue that translation speeds decrease as the jet widths decrease. This is likely to be due to our earlier results, in which we related the migration speeds to the eddy momentum flux convergence asymmetries. Narrower jets will be associated with smaller asymmetries, and consequently, smaller net forces, leading to slower migration speeds. Finally, these results also confirm the dependency of translation speeds on the frictional damping rate,  $\mu$ , predicted in expression (5.25), thereby confirming that  $\mathcal{V}$  scales with  $\mu$ , as required.

## 5.6 Discussion

The objective of this chapter was the study of the fast type of zonal jet migration behaviour that was identified in our NL simulations in Chapter 4. Previous studies have identified jet migration, albeit in more complex systems in which there is a tendency for jets to migrate purely in one direction due to a naturally occurring symmetry-breaking mechanism associated with the geometry of the domain or the details of the forcing. In this study, we have established that these external conditions are not essential, and that persistent jet migration can also occur as a result of internal dynamical mechanisms.

The fact that zonal jet migration does not occur in the QL model, in which eddy-eddy interactions are neglected, motivated an understanding regarding which nonlinear interactions are essential for this behaviour. Consequently, we employed a hybrid model, involving a generalisation of the quasilinear approximation, which provided a systematic way of restoring eddy-eddy interactions to the QL model. This GQL system separates the *low* modes with zonal wavenumbers  $k_x \leq \Lambda$  from the *high* modes with  $k_x > \Lambda$ , where the low modes are permitted to interact fully nonlinearly while restrictions are placed on the high modes such that the conservation properties of the system are retained. Jet migration behaviour, along with its associated properties such as the translation speed of the jets, was reproduced provided that  $\Lambda \geq 1$ , thereby demonstrating that the GQL model offers a useful step towards the reproduction of NL behaviour.

These results led to the formulation of a new theory for zonal jet migration by revealing the importance of the large-scale organisation of the eddy field, which we subsequently associated with the existence of zonons. Materialising as long waves, zonons are defined as the generalisation of Rossby waves to systems with latitudinal shear, and as such, their latitudinal structure exhibits perturbations about a sinusoidal profile that projects onto a series of latitudinal Fourier components. In our domain, we always observed zonons with zonal wavenumber  $k_x = 1$ , which were naturally associated with the jet meanders and which resulted in a wave-like pattern of vorticity anomalies that propagated alongside the jets. However, rather than being

directly responsible for zonal jet migration, the zonons were deduced to play an organisational role of the smaller scale eddy field, which in turn allows for a persistent state of asymmetry in the eddy momentum flux convergence, and a corresponding net latitudinal force on the jets. The persistence of the zonons, which were found to account for a significant fraction of the total kinetic energy, leads to robust migration behaviour that exists over extended periods of time. Whilst both northward and southward directions of translation were equally probable, we presume that the addition of weak asymmetry to the system would give rise to a preferred direction of translation, in line with previous studies.

Translation speeds were found to be significantly smaller than characteristic flow velocities, in agreement with atmospheric observations (James and Dodd, 1996; James et al., 1994). Furthermore, numerical simulations suggested that jets migrate with a unique translation speed for any given set of parameters, prompting an investigation into the relationship between translation speeds and various properties of the system. The identification of universal velocity and eddy momentum flux convergence profiles associated with jet migration states led to a simple momentum balance that allowed for the prediction of scalings associated with the translation speeds of jets. These scalings were subsequently confirmed using a large number of numerical simulations across a broad range of parameters. For example, translation speeds were found to be directly proportional to the net eddy momentum flux convergences across the jet cores (in agreement with Chemke and Kaspi (2015b)), thereby demonstrating the importance of these momentum fluxes for migration behaviour. Further investigations, in which we systematically deduced the dependence on individual parameters, revealed a striking relationship, such that  $\mathcal{V} \sim \mu L_{Rh}$ , showing that the speed of translation is proportional to both the frictional damping rate and the Rhines scale, or equivalently, the jet widths. This is a significant result that should be verified in more complex systems.

Whilst these results relate specifically to the fast type of zonal jet migration, the idea that zonons play an essential role in organising the small-scale eddies may be relevant to other types of phenomena as well. Indeed, the observation of zonons in various non-migrating NL regimes may or may not be associated with the reduced set of variability regimes observed in the QL model. On the other hand, the existence of the slow type of migration in both the NL and QL models suggests that there is more to the story than the simple ‘zonon-organising’ mechanism proposed in this chapter. These are some of the questions that we will consider in Chapter 6, where we consider a statistical modelling approach with the combined aims of further investigating the role of eddy-eddy interactions, in addition to evaluating the necessity of random fluctuations, in order to deepen our understanding of zonal jet dynamics observed within the NL system.

## Chapter 6

# Direct statistical simulation of zonal jet dynamics

### 6.1 Introduction

The study of turbulent phenomena, such as zonal jet dynamics, using the DNS of single-realisation models often involves very long integrations in order to capture the long-time dynamics of the system, or indeed for the convergence of the statistical properties. Moreover, the regions of parameter space that are relevant for the physical problem of interest are often computationally prohibitive using DNS due to the large range of spatial and temporal scales. With a vision towards overcoming these obstacles, there has been a recent surge of interest in the development of statistical approaches which, as proposed by Lorenz (1967), offer an alternative method that ‘consists of deriving a new system of equations whose unknowns are the statistics themselves’. Their aim is to capture the macroscopic features of turbulent flows using low-order statistics, such as the mean and covariance, which may be associated with fixed points that can be easily computed.

In this chapter we continue our exploration of zonal jet dynamics using a form of direct statistical simulation (DSS) that has become popularly known as CE2. This reduced model offers certain advantages over the DNS systems, including the potential for analytical exploration, which motivates an understanding of the behaviour that it can reproduce. After formulating the model mathematically, we begin by categorising the zoology of the fundamental types of solutions that can be captured using such an approach. This is followed by an investigation into the properties of these solutions, and finally a discussion of further insights that can be obtained regarding zonal jet migration behaviour. In addition to further understanding the role of eddy-eddy interactions, our goal is to investigate the neglect of random fluctuations as we examine some of the limitations of this form of DSS, and, crucially, when it can adequately approximate DNS models.

### 6.2 Mathematical formulation

A brief introduction to DSS was provided in Chapter 2, in which we outlined the concept of statistical models and the corresponding closure problem. In this chapter we choose to investigate the properties and insights from a second order closure scheme which incorporates the quasilinear approximation. Termed CE2 by Tobias et al. (2011), this type of model is known to reproduce the spontaneous formation of zonal jets and is therefore a suitable candidate for further investigation of zonal jet dynamics.

### 6.2.1 Cumulant expansion truncated at second order (CE2) methodology

Elaborating on the ideas introduced in Chapter 2, it is helpful to begin with a generic formulation of the CE2 framework to lay the groundwork. As before, we consider a canonical system that can be described by the evolution of a state vector of variables,  $\mathbf{q}(\mathbf{x}, t)$ , satisfying the equation of motion

$$\frac{\partial \mathbf{q}}{\partial t} = \mathcal{L}[\mathbf{q}] + \mathcal{N}[\mathbf{q}, \mathbf{q}], \quad (6.1)$$

where  $\mathcal{L}$  is a linear operator and  $\mathcal{N}$  includes nonlinear terms of quadratic order. Our goal is the construction of the equations of motion for the cumulants, the first two of which are described by the mean,  $\overline{\mathbf{q}}$ , and the covariance (or two-point correlation function),  $\overline{\mathbf{q}'\mathbf{q}'}$ . Consequently, we apply a Reynolds decomposition of  $\mathbf{q}(\mathbf{x}, t)$  into the sum of its mean and fluctuating parts, denoted by an overbar and a prime respectively,

$$\mathbf{q} = \overline{\mathbf{q}} + \mathbf{q}', \quad (6.2)$$

where the type of averaging operator must be chosen such that it satisfies the Reynolds-averaging rules  $\overline{\mathbf{q}'} = 0$ ,  $\overline{\overline{\mathbf{q}}} = \overline{\mathbf{q}}$  and  $\overline{\overline{\mathbf{q}}\mathbf{q}} = \overline{\mathbf{q}}\overline{\mathbf{q}}$ . This includes spatial, temporal and ensemble averages, and the particular selection is chosen in order to best suit the given application. Postponing the choice of operator until later, we apply this generic operator to equation (6.1) to give the evolution equation for the first cumulant:

$$\frac{\partial \overline{\mathbf{q}}}{\partial t} = \mathcal{L}[\overline{\mathbf{q}}] + \overline{\mathcal{N}[\mathbf{q}, \mathbf{q}]}, \quad (6.3)$$

assuming that the averaging and linear operators commute. As mentioned previously, we now wish to determine the evolution equation for the second cumulants associated with the  $\overline{\mathcal{N}[\mathbf{q}, \mathbf{q}]}$  term, which concern the average of the fluctuation–fluctuation interactions. Making no assumptions about the homogeneity or isotropy of the nonlinear interactions, we therefore consider nonlocal correlations of the form  $\overline{\mathbf{q}'(\mathbf{x}_1)\mathbf{q}'(\mathbf{x}_2)}$ , where  $\mathbf{x}_1$  and  $\mathbf{x}_2$  are the positions of two points within the domain. To obtain the equation governing the evolution of this quantity, we proceed by multiplying equation (6.1), evaluated at point  $\mathbf{x}_1$ , by  $\mathbf{q}(\mathbf{x}_2)$ , and then add its symmetric variant with the points  $\mathbf{x}_1$  and  $\mathbf{x}_2$  reversed. After expanding all variables using (6.2) and subtracting off equation (6.3) for the mean, we obtain

$$\frac{\partial}{\partial t} \overline{\mathbf{q}'(\mathbf{x}_1)\mathbf{q}'(\mathbf{x}_2)} = \overline{\mathbf{q}(\mathbf{x}_1)\mathcal{L}[\mathbf{q}(\mathbf{x}_2)]} + \overline{\mathbf{q}(\mathbf{x}_2)\mathcal{L}[\mathbf{q}(\mathbf{x}_1)]} + \left[ \overline{\mathbf{q}(\mathbf{x}_1)\mathcal{N}[\mathbf{q}(\mathbf{x}_2), \mathbf{q}(\mathbf{x}_2)]} + \overline{\mathbf{q}(\mathbf{x}_2)\mathcal{N}[\mathbf{q}(\mathbf{x}_1), \mathbf{q}(\mathbf{x}_1)]} \right]. \quad (6.4)$$

Here, the first two (quadratic) terms on the right-hand side include second cumulants, however, we have also introduced nonlocal cubic terms, i.e. third cumulants, defined in square brackets, which are unknown quantities. In order to close the system of equations, it is customary to either parameterise these terms as functions of the first two cumulants, or else to remove them from the system. This latter approach, typically referred to as the cumulant expansion truncated at second order (CE2), is frequently adopted due to its mathematical simplicity, leaving a pair of coupled equations for the first two cumulants.

Popular choices for the averaging operator include zonal and ensemble averages, with each leading to distinct systems. An ensemble average permits the retention of non-zonal coherent structures, such as zonons, which certainly has advantages in the study of zonal jet migration. The triad interactions that are retained in this *ensemble* CE2 are analogous to those shown in Figures 3.1(a,b), along with the addition of an extra type involving the interaction of two mean fields to produce another mean field, since the mean

may contain non-zonal structures. Nevertheless, this system has four spatial dimensions (two dimensions associated with each point in the second cumulants), which poses computational challenges (for further details, see Allawala et al., 2020). On the other hand, *zonal* CE2, in which the averaging operator is a zonal mean, alleviates this issue to a certain extent by reducing the dimension of the system in the zonal direction by one. In this formulation, the second cumulant depends on the latitudes,  $y_1$  and  $y_2$ , of the two points in addition to the difference between their longitudes,  $x = x_2 - x_1$ , giving  $\overline{\mathbf{q}'(\mathbf{x}_1)\mathbf{q}'(\mathbf{x}_2)} = Q(x, y_1, y_2)$ , where  $Q$  is the second cumulant. This approach utilises a quasilinear approximation in the sense that it permits the eddy-mean flow interactions denoted by Figures 3.1(a,b) but neglects the eddy-eddy scattering interactions associated with Figure 3.1(c) since the second order terms in equation (6.4) appear only in the zonal mean. Wishing to maintain computational efficiency along with our continued investigation of the insights that can be obtained from the quasilinear approximation, we proceed with the choice of a zonal averaging operator.

### 6.2.2 Cumulant expansion truncated at second order (CE2) model

Following the methodology of Srinivasan and Young (2012), we now apply this CE2 framework to our study of zonal jet dynamics, described by the NL beta-plane vorticity equation,

$$\frac{\partial \zeta}{\partial t} + J(\psi, \zeta) + \beta \frac{\partial \psi}{\partial x} = \xi - \mu \zeta + \nu_n \nabla^{2n} \zeta. \quad (6.5)$$

The streamfunction is decomposed using a standard Reynolds decomposition into its zonal mean component, denoted by an overbar, and the fluctuations, or eddies, about the mean:

$$\psi(x, y, t) = \overline{\psi}(y, t) + \psi'(x, y, t), \quad (6.6)$$

with corresponding decompositions of the other variables. Applying this decomposition to equation (6.5), we derive respectively the evolution equations for the zonal mean flow and the eddy vorticity, given by:

$$\frac{\partial U}{\partial t} = \overline{v' \zeta'} - \mu U + \nu_n \frac{\partial^{2n} U}{\partial y^{2n}}, \quad (6.7)$$

$$\frac{\partial \zeta'}{\partial t} + U \frac{\partial \zeta'}{\partial x} + \left( \beta - \frac{\partial^2 U}{\partial y^2} \right) \frac{\partial \psi'}{\partial x} + \left[ \frac{\partial \psi'}{\partial x} \frac{\partial \zeta'}{\partial y} - \frac{\partial \psi'}{\partial y} \frac{\partial \zeta'}{\partial x} - \frac{\partial}{\partial y} \left( \frac{\partial \psi'}{\partial x} \zeta' \right) \right] = \xi - \mu \zeta' + \nu_n \nabla^{2n} \zeta', \quad (6.8)$$

using the fact that  $\overline{\zeta} = -\partial_y U$ . It is helpful to apply the quasilinear approximation at this stage in order to simplify the equations and the algebra. Consequently, we define the quantities inside the square brackets to be zero, consistent with the removal of eddy-eddy interactions, leaving a quasilinear PDE given by

$$\frac{\partial \zeta'}{\partial t} + \mathcal{L} \frac{\partial \psi'}{\partial x} = \xi - \mu \zeta' + \nu_n \nabla^{2n} \zeta', \quad (6.9)$$

where, for ease of notation, the Rayleigh-Kuo linear operator  $\mathcal{L}$  has been introduced:

$$\mathcal{L} = U \nabla^2 + \beta - \frac{\partial^2 U}{\partial y^2}. \quad (6.10)$$

Since our goal is the derivation of a set of coupled equations governing the low-order statistics of the flow, we introduce some new notation in order to simplify our expressions and accommodate the evaluation

of variables at different points within the domain. For shorthand, numerical subscripts shall denote the particular point at which a variable is evaluated, i.e.  $\zeta'_n = \zeta'(\mathbf{x}_n, t)$  and  $U_n = U(y_n, t)$ , or the particular point on which an operator acts, i.e.  $\nabla_n = (\partial_{x_n}, \partial_{y_n})$ . In addition, the difference coordinates  $x$  and  $y$  shall refer to the respective zonal and latitudinal differences between points:

$$x = x_2 - x_1, \quad y = y_2 - y_1. \quad (6.11)$$

Within our system, the first cumulant is equal to the zonal mean flow, i.e.  $U(y, t)$ , while the second cumulants are given by the two-point, equal-time eddy vorticity or eddy streamfunction correlation functions

$$\mathcal{Z}(x, y_1, y_2, t) = \overline{\zeta'_1 \zeta'_2}, \quad \Psi(x, y_1, y_2, t) = \overline{\psi'_1 \psi'_2}, \quad (6.12)$$

where these in turn are related via the expression  $\mathcal{Z} = \nabla_1^2 \nabla_2^2 \Psi$ . Zonal averaging dictates that these second cumulants are zonally homogeneous, ensuring, for example, that  $\partial_{x_2} = -\partial_{x_1} = \partial_x$ . Meanwhile, the two-point, two-time correlation function of the stochastic force,  $\xi(\mathbf{x}, t)$ , is specified to be isotropic and homogeneous,

$$\overline{\xi(\mathbf{x}_1, t_1) \xi(\mathbf{x}_2, t_2)} = \Xi(r) \delta(t_2 - t_1), \quad (6.13)$$

where  $r = \sqrt{x^2 + y^2}$ . Provided we assume that the forcing is ergodic such that an ensemble average,  $\langle \bullet \rangle$ , over multiple realisations is equivalent to an instantaneous zonal average,  $\overline{\bullet}$ , of a single realisation, then (6.13) is equivalent to expression (3.18) in Chapter 3.

Using this notation, equation (6.7) for the mean flow contains an eddy momentum flux convergence term which can be re-written in terms of the second cumulant as follows:

$$\overline{v' \zeta'}(y, t) = \frac{1}{2} \left( \overline{v'_1 \zeta'_2} + \overline{v'_2 \zeta'_1} \right) \Big|_{x=0, y_1=y_2=y} \quad (6.14)$$

$$= \frac{1}{2} \left( \partial_{x_1} \nabla_1^{-2} \mathcal{Z} + \partial_{x_2} \nabla_2^{-2} \mathcal{Z} \right) \Big|_{x=0, y_1=y_2=y} \quad (6.15)$$

$$= \frac{1}{2} \left( \nabla_2^{-2} - \nabla_1^{-2} \right) \partial_x \mathcal{Z}(0, y, y, t). \quad (6.16)$$

Consequently, the evolution equation for the first cumulant becomes

$$\frac{\partial U}{\partial t} = \frac{1}{2} \left( \nabla_2^{-2} - \nabla_1^{-2} \right) \frac{\partial \mathcal{Z}}{\partial x}(0, y, y, t) - \mu U + \nu_n \frac{\partial^{2n}}{\partial y^{2n}} U. \quad (6.17)$$

In order to derive an equation for the second cumulant, we multiply equation (6.8), evaluated at point  $\mathbf{x}_1$ , by  $\zeta'_2$  and symmetrise by adding this to the expression obtained when the points are reversed. The previous removal of quadratic terms ensures that the resultant equation contains no cubic terms, or third cumulants. After some algebra, and noting that  $\mathcal{L}_n = U_n \nabla_n^2 + (\beta - \partial_{y_n}^2) U_n$ , this becomes

$$\frac{\partial \mathcal{Z}}{\partial t} + \left( \nabla_1^{-2} \mathcal{L}_1 - \nabla_2^{-2} \mathcal{L}_2 \right) \frac{\partial \mathcal{Z}}{\partial x} = \left[ \overline{\zeta'_1 \xi_2} + \overline{\zeta'_2 \xi_1} \right] - 2\mu \mathcal{Z} + \nu_n \left( \nabla_1^{2n} + \nabla_2^{2n} \right) \mathcal{Z}. \quad (6.18)$$

Here, we can make use of a property that arises due to the fact that the forcing is delta-correlated in time. As shown in Appendix B.4, this permits the terms highlighted in square brackets to be simplified using

$$\overline{\zeta'_1 \xi_2} + \overline{\zeta'_2 \xi_1} = \Xi, \quad (6.19)$$

in which case the evolution equation for the second cumulant becomes

$$\frac{\partial \mathcal{Z}}{\partial t} + (\nabla_1^{-2} \mathcal{L}_1 - \nabla_2^{-2} \mathcal{L}_2) \frac{\partial \mathcal{Z}}{\partial x} = \Xi - 2\mu \mathcal{Z} + \nu_n (\nabla_1^{2n} + \nabla_2^{2n}) \mathcal{Z}. \quad (6.20)$$

Equations (6.17) and (6.20) form a closed set of coupled equations governing the time evolution of the mean flow and the two-point correlation function of the eddy field. This system is mathematically equivalent to the QL model, provided that the ergodic assumption in expression (6.13) holds along with property (6.19) which replaces the fluctuations in a single realisation of the eddy field with the statistical properties of an infinite ensemble of eddy fields. In this sense, the CE2 system, which is deterministic since  $\Xi$  is independent of time, governs the fluctuation-free dynamics of the statistical mean state, converting the QL model from a single simulation into a predictive theory of turbulent dynamics.

We conclude this section with a couple of important properties of this system of equations. Firstly, it is useful to observe that when  $\Xi$  is defined to be statistically isotropic and homogeneous, a fixed point of the CE2 equations is an isotropic and homogeneous solution with no zonal flow, satisfying the equations

$$U_H(y) = 0, \quad (2\mu - \nu_n (\nabla_1^{2n} + \nabla_2^{2n})) \mathcal{Z}_H(x, y_1, y_2) = \Xi(x, y_1, y_2). \quad (6.21)$$

This can be seen by virtue of the fact that a system that is symmetric with respect to  $\mathbf{x}_1 \leftrightarrow \mathbf{x}_2$  and in which  $U(y) = 0$  will remain so. The equation for the correlation function,  $\mathcal{Z}_H$ , corresponding to this solution can easily be inverted, where we deduce that the Fourier coefficients are given by

$$\tilde{\mathcal{Z}}_H(k_x, k_{y_1}, k_{y_2}) = \frac{\tilde{\Xi}(k_x, k_{y_1}, k_{y_2})}{2\mu + \nu_n \left( (k_x^2 + k_{y_1}^2)^n + (k_x^2 + k_{y_2}^2)^n \right)}. \quad (6.22)$$

We note, therefore, that the notion of zonostrophic instability relates to the stability of this fixed point to small inhomogeneous perturbations, leading to solutions in which  $U(y, t) \neq 0$ .

The second remark concerns the fact that the CE2 equations conserve quadratic quantities, including the total kinetic energy per unit mass,  $E = \frac{1}{2} \langle |\nabla \psi|^2 \rangle$ . Motivated by our subsequent numerical solution of this system, it is useful to derive an expression for the energy in terms of known quantities, i.e. the cumulants. This can be achieved by decomposing the streamfunction into its zonal mean and fluctuating parts,  $\psi = \bar{\psi} + \psi'$ , and using the property that  $\langle \bar{\psi} \psi' \rangle = 0$ , where  $\langle \bullet \rangle$  denotes a domain average:

$$\begin{aligned} E &= \frac{1}{2} \left\langle \left( \frac{\partial \psi}{\partial x} \right)^2 + \left( \frac{\partial \psi}{\partial y} \right)^2 \right\rangle \\ &= \frac{1}{2} \left\langle \left( \frac{\partial \bar{\psi}}{\partial y} \right)^2 + \left( \frac{\partial \psi'}{\partial x} \right)^2 + \left( \frac{\partial \psi'}{\partial y} \right)^2 \right\rangle \\ &= \frac{1}{2} \langle U^2 \rangle + \frac{1}{2} \left\langle \partial_{y_1} \partial_{y_2} \overline{\psi'_1 \psi'_2} \Big|_{y_1=y_2=y} \Big|_{x=0} \right\rangle - \frac{1}{2} \left\langle \partial_x^2 \overline{\psi'_1 \psi'_2} \Big|_{y_1=y_2=y} \Big|_{x=0} \right\rangle \\ &= \frac{1}{2} \langle U^2 \rangle + \frac{1}{2} \langle \partial_{y_1} \partial_{y_2} \Psi(0, y, y, t) \rangle - \frac{1}{2} \langle \partial_x^2 \Psi(0, y, y, t) \rangle. \end{aligned} \quad (6.23)$$

It is also possible to deduce the corresponding contributions to  $E$  from the mean flow,  $E_Z$ , and the eddy field,  $E_R$ , (and hence the zmf index,  $E_Z/E$ ), which are given respectively by

$$E_Z = \frac{1}{2} \langle U^2 \rangle, \quad E_R = \frac{1}{2} \langle \partial_{y_1} \partial_{y_2} \Psi(0, y, y, t) \rangle - \frac{1}{2} \langle \partial_x^2 \Psi(0, y, y, t) \rangle. \quad (6.24)$$

### 6.3 Direct statistical simulations (DSS)

The CE2 system, comprising the pair of equations (6.17) and (6.20), is a form of direct statistical simulation (DSS) that must be solved numerically. We begin with a discussion of the numerical algorithm and the implementation of the forcing. This is followed by a comparison of the emergent properties of solutions from the DNS (NL and QL models) and DSS systems as a numerical verification exercise.

#### 6.3.1 Numerical formulation

The numerical solution of the CE2 equations is implemented analogously to that described for the DNS models in Chapter 3. Specifically, we use a pseudo-spectral algorithm in which time integration is performed in Fourier space using a second-order Runge-Kutta scheme whilst nonlinear terms are evaluated in physical space. There is an important caveat, however, that is worth mentioning. DSS models are usually more expensive computationally than equivalent DNS systems due to the fact that the cumulants may have higher dimension than the original system. Sometimes referred to as the ‘curse of dimensionality’ (Bellman, 1957, 1961), this is certainly the case with our CE2 model, which has increased the original number of spatial coordinates from two to three. Nevertheless, linearity in the zonal separation coordinate,  $x$ , permits the zonal wavenumbers,  $k_x$ , to be decoupled, whilst symmetry properties associated with the construction of the cumulants ensure that we only need to solve for those zonal wavenumbers which are explicitly forced:

$$k_x \in \{1, 2, 3, \dots, k_f + \delta k\}. \quad (6.25)$$

This reduces the system to a set of  $k_f + \delta k$  pairs of equations governing the evolution of two latitudinal coordinates, which is an enormous reduction in size, particularly when  $k_f + \delta k$  is not large. Further details of the implementation of the numerical algorithm are presented in Appendix C.2.

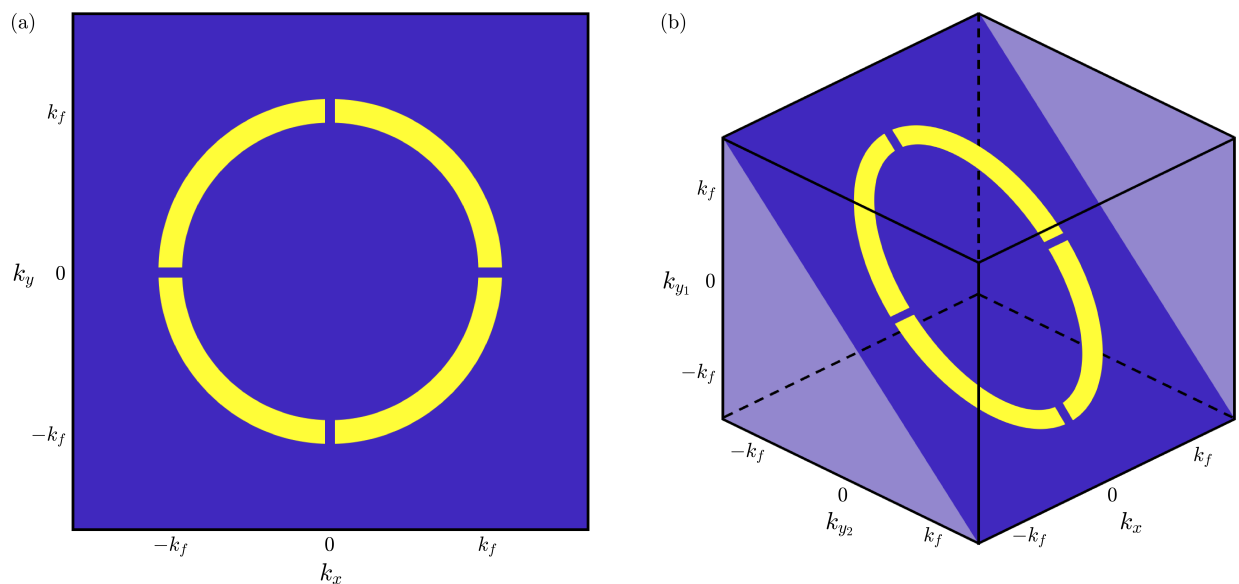


**Figure 6.1** Schematics showing (a) the DNS forcing distribution,  $\xi(\mathbf{x}, t)$ , and (b) the DSS forcing distribution,  $\Xi(x, y_1, y_2)$ , both in Fourier space. The distribution in (a) is mapped onto the (highlighted) surface  $k_{y1} + k_{y2} = 0$  in (b) with all other values (pale shading) equal to zero. In both cases, only the yellow wavevectors are forced.

The CE2 equations are forced using the statistical properties of an infinite ensemble of forcing fields given by the isotropic and homogeneous two-point correlation function,  $\Xi$ , in expression (3.18). For ease of comparison with our results in Chapters 4 and 5, we specify  $\Xi$  based upon the definition of  $\xi$  used in our DNS models. As discussed in Chapter 3, this equates to forcing only those wavevectors  $k = \sqrt{k_x^2 + k_y^2}$  such that  $|k - k_f| < \delta k$ , with the exception of wavevectors of the form  $\mathbf{k} = (0, k)$  and  $\mathbf{k} = (k, 0)$ . In Fourier space, this corresponds to a narrow annulus of wavevectors with thickness  $2\delta k$ , as illustrated using the schematic in Figure 6.1(a). The corresponding correlation function,  $\Xi(x, y_1, y_2)$ , in the CE2 equations and its Fourier transform,  $\tilde{\Xi}(k_x, k_{y_1}, k_{y_2})$ , are derived in Appendix B.3 and comprise a discretisation of (3.20). Given by

$$\Xi(x, y_1, y_2) = \frac{2\epsilon k_f^2}{N} \sum_{|k - k_f| < \delta k} e^{i(k_x x + k_{y_1} y_1 + k_{y_2} y_2)}, \quad \tilde{\Xi}(k_x, k_{y_1}, k_{y_2}) = \frac{2\epsilon k_f^2 N^3}{N}, \quad (6.26)$$

where  $k_{y_1} + k_{y_2} = 0$  and  $k = \sqrt{k_x^2 + k_{y_i}^2}$  for  $i \in \{1, 2\}$ , this amounts to a projection of the two-dimensional distribution in Figure 6.1(a) onto the surface  $k_{y_1} + k_{y_2} = 0$  in three-dimensional Fourier space, as illustrated in Figure 6.1(b), noting that the amplitudes of the forced (yellow) wavevectors are of course different.

We integrate the CE2 equations over a two-dimensional, doubly-periodic, square domain of size  $L_D$  with correlation function variables given by  $(x, y_1, y_2) \in [0, 2\pi L_D) \times [0, 2\pi L_D) \times [0, 2\pi L_D)$ . Compared with the solution of the DNS systems, it is necessary to use a coarser resolution for the CE2 model for reasons of practicality. Consequently, we opt for a grid resolution of  $N = 128$ , which, due to a  $2/3$  dealiasing rule, equates to a maximum allowed wavenumber of  $k_{max} = 42$ . The time-step,  $\Delta t$ , is held fixed within each simulation but varies between the simulations according to the parameters used. Values are up to five times larger than DNS equivalents, typically lying in the range  $0.01 \leq \Delta t \leq 0.05$ . As a verification, some numerical integrations were repeated using smaller time-steps in order to check for convergence since numerical stability was occasionally found to exist even when the solutions had not converged. This is demonstrated in Figure 6.2, where the integration with the larger time step,  $\Delta t = 0.02$ , does not reproduce the converged solution that was found when  $\Delta t = 0.01$  (shown) and  $\Delta t = 0.005$  (not shown).

Hyperviscosity parameters were selected using a similar procedure to that outlined in Chapter 3, where we chose the same parameters ( $\nu_n = 1$  and  $n = 4$ ) as those selected for the DNS models. Nevertheless, it is important to stress that the effect of hyperviscosity is stronger at lower grid resolution than the values reported in Chapter 3 when  $N = 256$ . Table 6.1 quantifies this effect when  $k_f = 16$  by computing average values over a large number of NL, QL and CE2 simulations of the measured total kinetic energy as a fraction of its ideal value,  $E^{(r)}/E^{(i)}$ , and equivalently for the Rhines scale,  $L_{Rh}^{(r)}/L_{Rh}^{(i)}$ . When  $N = 128$ , we

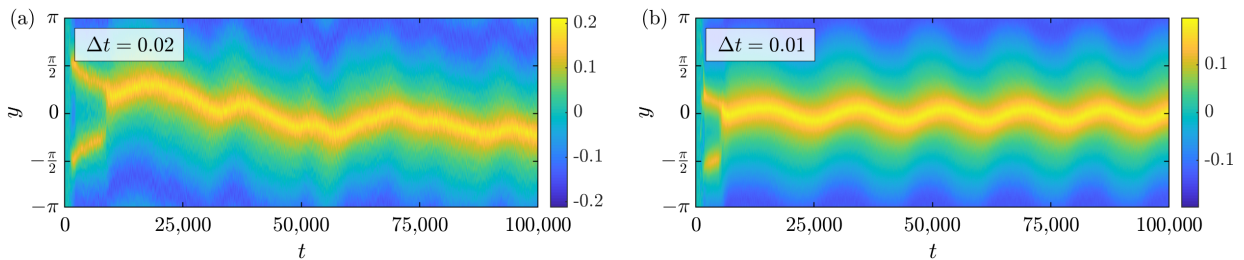


**Figure 6.2** Time step dependence within the CE2 model. Latitude-time plots showing the time evolution of the zonal mean zonal velocity,  $U(y, t)$ , for parameters  $\beta = 0.3$ ,  $\mu = 0.0005$ ,  $\epsilon = 10^{-5}$ ,  $k_f = 16$ ,  $N = 128$ ,  $R_\beta = 2.36$ . The time steps used in the numerical integration are indicated in the top-left corners, decreasing from left to right.

	NL model ( $N = 256$ )	QL model ( $N = 256$ )	NL model ( $N = 128$ )	QL model ( $N = 128$ )	CE2 model ( $N = 128$ )
$E^{(r)}/E^{(i)}$	$0.96 \pm 0.04$	$0.96 \pm 0.02$	$0.80 \pm 0.03$	$0.79 \pm 0.06$	$0.77 \pm 0.05$
$L_{Rh}^{(r)}/L_{Rh}^{(i)}$	$0.99 \pm 0.03$	$0.99 \pm 0.004$	$0.94 \pm 0.01$	$0.94 \pm 0.02$	$0.94 \pm 0.01$

**Table 6.1** The effect of hyperviscosity on the measured total kinetic energy as a fraction of its ideal value,  $E^{(r)}/E^{(i)}$ , and the measured Rhines scale as a fraction of its ideal value,  $L_{Rh}^{(r)}/L_{Rh}^{(i)}$ . Average values are computed for a large number of simulations using the NL and QL models when  $N = 256$  and  $N = 128$  and the CE2 model when  $N = 128$ . Values represent the mean and standard deviations, computing using all numerical simulations in which  $k_f = 16$ .

observe that just over 20% of the total energy that is injected into the system is lost to hyperviscosity, equating to a 6% reduction in the corresponding Rhines scales. This can be compared with values of approximately 4% and 1% respectively when  $N = 256$ , which is a noticeable difference.

In order to simulate an assortment of dynamical behaviours, we explore a broad range of parameters covering a spectrum of Rhines wavenumbers in the range  $0 < k_{Rh} < 8$  and zonostrophy parameters lying in the interval  $1 < R_\beta < 4$ . These regimes are achieved using many values of the background potential vorticity gradient that lie in the range  $\beta \in [0.1, 5]$ , while the linear damping rate covers two orders of magnitude,  $\mu \in [0.0001, 0.01]$ . For simplicity, all remaining parameters are fixed. These include an energy injection rate given by  $\varepsilon = 10^{-5}$ , and a domain size,  $L_D$ , which is chosen to be unity in all simulations. In addition, the forcing distribution, the choice of which is partially limited by the numerical resolution, is centred around a mean radial wavenumber  $k_f = 16$  with annulus thickness  $2\delta k = 2$ .

All simulations were initialised with small-amplitude inhomogeneous perturbations to the mean flow,  $U(y, 0)$ , to initiate zonostrophic instability while the second cumulant was initialised with  $\mathcal{Z}(x, y_1, y_2, 0) = 0$ , thereby ensuring that the initial kinetic energy is negligible. An example numerical integration showing the spin-up of a simulation from the CE2 model is shown in Figure 6.3(a) in which the system equilibrates

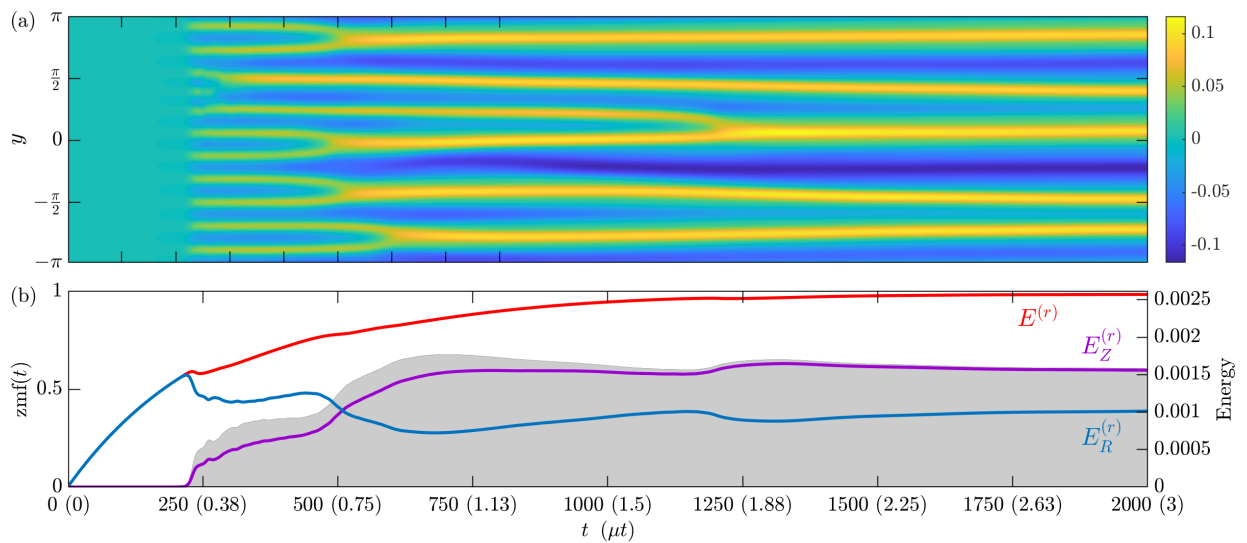


**Figure 6.3** (a) Latitude-time plot showing the time evolution of the zonal mean zonal velocity field. The system reaches a statistically steady state after about  $t = 1,750$ . (b) The corresponding evolution of the total kinetic energy  $E^{(r)}$  (red), zonal mean kinetic energy  $E_Z^{(r)}$  (purple) and eddy kinetic energy  $E_R^{(r)}$  (blue) plotted alongside  $zmf(t)$  (grey shading). The parameters used are:  $\beta = 3.4$ ,  $\mu = 0.0015$ ,  $\varepsilon = 10^{-5}$ ,  $k_f = 16$ ,  $N = 128$ ,  $R_\beta = 2.28$ .

after about  $t = 1,750$  ( $\mu t = 2.63$ ) with 5 jets. It was found that the time taken for the domain-averaged total kinetic energy, represented by the red curve in Figure 6.3(b), to reach a steady state during the initial spin-up period depends on the linear damping rate,  $\mu$ . Just as for the DNS models, this is usually achieved by time  $\mu t = 2 - 3$ , after which the simulations were integrated for a long time (typically between  $10 - 1000\mu t$  depending on parameters) in order to capture the long-time behaviour of the solutions.

The decomposition of the kinetic energy into contributions from the mean flow,  $E_Z$ , and the eddy field,  $E_R$ , computed using (6.24), are plotted in Figure 6.3(b) alongside the zmf index (grey shading). Initially, the solution remains linearly stable, and therefore homogeneous, with all energy building up in the eddy field, proportional to (6.22). After a critical threshold in  $E_R$  has been reached, zonostrophic instability occurs, where we suddenly observe the formation of 11 weak jets and a corresponding rise in  $E_Z$ . Further increases in energy push the system away from the linear stability threshold, where nonlinear effects become increasingly dominant. This permit a series of jet mergers to take place, each of which is associated with a larger fraction of the total energy being temporarily redistributed into the mean flow, and which ultimately lead to the equilibration of a statistically steady state. Just as for the DNS models, we shall refer solely to the zmf index in future discussions of the partition of energy.

### 6.3.2 Numerical comparison between DNS and DSS models

Before we proceed to examine the nature of solutions that emerge from the CE2 model, we conclude this section with a comparison between the numerical properties of solutions from DNS and DSS models. A natural comparison that we wish to make lies between the QL and the CE2 models, both of which are quasilinear in the sense that they neglect eddy-eddy interactions, however, we also choose to draw comparisons with the NL model where appropriate. We have run a large number of 253 CE2 simulations across a broad range of parameters such that the Rhines wavenumber lies in the range  $0 < k_{Rh} < 8$  and the zonostrophy parameter is in the interval  $1 < R_\beta < 4$ . For direct comparison with the NL and QL models at the same grid resolution,  $N = 128$ , and forcing wavenumber,  $k_f = 16$ , we have also run a large number of 447 NL and 383 QL simulations across the same parameter ranges.

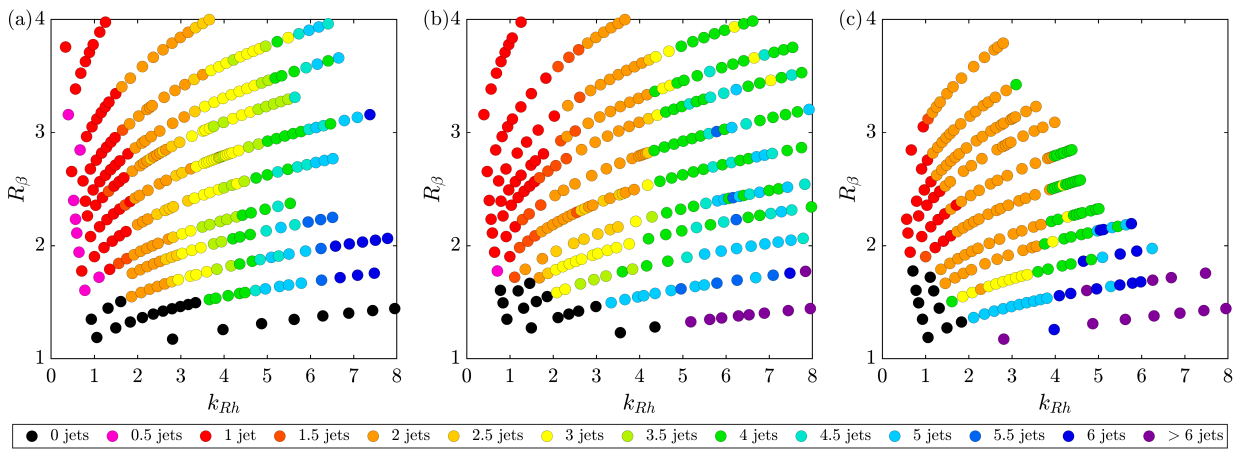


**Figure 6.4** The parameter space defined in terms of the ideal Rhines wavenumber,  $k_{Rh}$ , along the horizontal axis and the ideal zonostrophy parameter,  $R_\beta$ , along the vertical axis. The data includes (a) 447 NL simulations, (b) 383 QL simulations and (c) 253 CE2 simulations, each with resolution  $N = 128$  and forcing wavenumber  $k_f = 16$ . Each point represents a single simulation that is coloured according to the average number of jets within the domain over long-time averages, with non-integral numbers allowed for merging and nucleating behaviours.

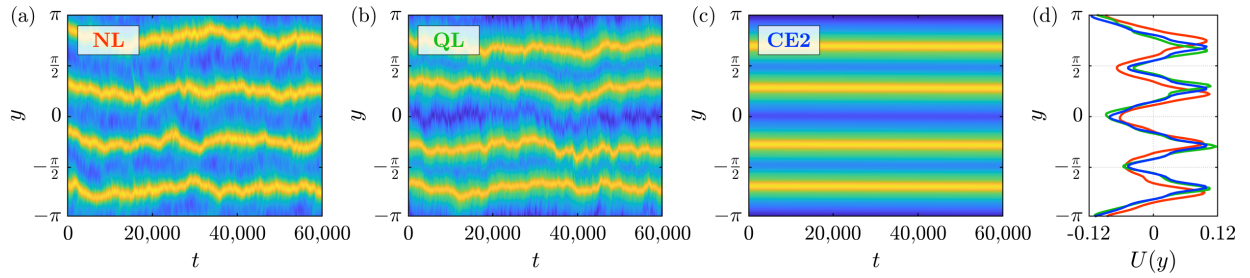


**Figure 6.5** A comparison of zonal jet solutions between the NL, QL and CE2 models, shifted in latitude to give the best agreement. Latitude-time plots of the time evolution of the zonal mean zonal velocity field for the (a) NL model, (b) QL model, and (c) CE2 model. (d) The time-averaged jet velocity profiles,  $U(y)$ , for the (red) NL model, (green) QL model, and (blue) CE2 model. The parameters used in all simulations were:  $\beta = 3.5$ ,  $\mu = 0.0015$ ,  $\varepsilon = 10^{-5}$ ,  $k_f = 16$ ,  $N = 128$ ,  $R_\beta = 2.29$ .

We begin by visualising our simulations within a two-dimensional parameter space, defined in a similar fashion to that in Chapter 4 using the Rhines wavenumber,  $k_{Rh}$ , and the zonostrophy parameter,  $R_\beta$ . Figures 6.4(a-c) show the broad range of simulations that we have run within the NL, QL and CE2 parameter spaces. Each point corresponds to an individual simulation, positioned according to its ideal Rhines wavenumber and zonostrophy parameter, and defined with a colour that represents the average number of jets within the domain, computed over long-time averages. Those simulations in which the zonal mean flow did not reveal the formation of jets are shown in black.

Reassuringly, our findings from the DNS models reproduce the results discussed in Section 4.3.1 at different grid resolution, whilst the CE2 model shows good agreement with the QL model. As mentioned previously, the NL model shows a clear transition at  $R_\beta = 1.5$ , above which the system shows evidence of zonostrophy. On the other hand, both the QL and the CE2 models show evidence of zonostrophy and zonostrophic instability when  $R_\beta < 1.5$ . In all three models the number of jets increases with  $k_{Rh}$ , however, it is interesting to observe that the CE2 model replicates the QL model's tendency to over-estimate the number of jets when  $R_\beta \lesssim 2$ . As mentioned previously, we believe that this is caused by the closer proximity in this transitional regime to the zonostrophic instability threshold where the number of jets has been shown to be determined by the most unstable linear mode (see Farrell and Ioannou, 2007).

In order to gain further insight into the data in Figure 6.4 and compare the nature of the solutions, we have selected a single set of parameters, given by  $k_{Rh} = 4.6$  and  $R_\beta = 2.29$ , and have plotted the time-evolution of the zonal mean zonal flow within each of the models in Figures 6.5(a-c). In all cases, four coherent jets equilibrate, however, the randomly wandering behaviour captured in the DNS models is not reproduced in the CE2 model, which instead captures the fluctuation-free dynamics of the statistical mean state. The CE2 model does, however, reproduce the preferred pattern of jet spacings within the QL model, which involves two pairs of closely spaced jets being separated by two broader westward flows. This can also be seen in Figure 6.5(d) which shows the time-averaged jet velocity profiles,  $U(y)$ , in each of the systems. The green (QL) and blue (CE2) profiles show remarkable agreement, virtually coinciding with one another. In addition, they are more strongly east-west symmetric than the red (NL) profile, in which the eastward jets are noticeably sharper than the westward flows.

These observations suggest that there are considerable similarities between the mean states of the QL and CE2 models. To quantify this degree of similarity, we consider all pairs of QL and CE2 simulations that have been run using identical parameters, and we compare their statistical attributes. Focussing initially on the average number of jets within the domain, we compute for each pair of simulations the difference

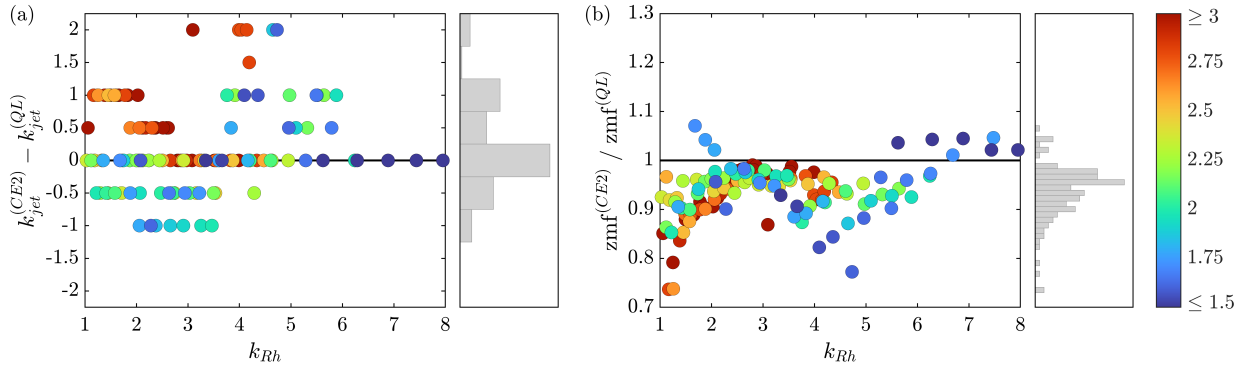


**Figure 6.6** A comparison between (a) the number of jets in the CE2 and QL models,  $k_{\text{jet}}^{(\text{CE2})} - k_{\text{jet}}^{(\text{QL})}$ , and (b) the zmf index in the CE2 and QL models,  $\text{zmf}^{(\text{CE2})} / \text{zmf}^{(\text{QL})}$ , as a function of the Rhines wavenumber (horizontal axes) and the zonostrophy parameter (colour). Histograms (grey) illustrate the frequencies. Comparisons are made between 131 QL and CE2 simulations with matching parameters. In each case,  $N = 128$  and  $k_f = 16$ .

between the number of jets within the CE2 domain and the QL domain, which we denote  $k_{\text{jet}}^{(\text{CE2})} - k_{\text{jet}}^{(\text{QL})}$ . The results are plotted in Figure 6.6(a), where each point represents a single pair, coloured according to their zonostrophy parameter. At first sight, there is a reasonable amount of spread either side of the line  $k_{\text{jet}}^{(\text{CE2})} - k_{\text{jet}}^{(\text{QL})} = 0$  (corresponding to a one-to-one correlation). This is not quite true, however, since further analysis reveals that, cumulatively, 41% of these pairs show identical numbers of jets in the domain, while 69% differ by at most 0.5 jets and 92% differ by at most one jet. We also find no strong evidence that the CE2 model systematically overestimates or underestimates the number of jets within the QL model.

Another useful measure of comparison between the QL and CE2 models concerns the ratio of their zmf indices, which we shall denote  $\text{zmf}^{(\text{CE2})} / \text{zmf}^{(\text{QL})}$ . This is computed for each pair of simulations, with the results plotted in Figure 6.6(b) using the same formatting as Figure 6.6(a). This time we do observe a small systematic bias towards smaller zmf indices in the CE2 model compared with the QL model, represented by the fact that most points lie below the line  $\text{zmf}^{(\text{CE2})} / \text{zmf}^{(\text{QL})} = 1$ . These differences are small, however, with the average value of  $\text{zmf}^{(\text{CE2})} / \text{zmf}^{(\text{QL})}$  being 0.94. In addition, the largest differences occur for either low zonostrophy, when the zmf index is typically small, or low Rhines wavenumber, when domain size limitations may play a role.

## 6.4 The zoology of CE2 beta-plane zonal jet dynamics

The solutions of the CE2 model exhibit a rich assortment of behaviours, despite the fact that the model does not account for fluctuations in the forcing, in addition to the fact that coherent zonal structures such as zonons are excluded. In this section we categorise and discuss the properties of the fundamental types of solutions that are observed on the basis of the evolution of the zonal mean zonal velocity. We focus our attention on the zonostrophic regime, given by  $R_\beta \gtrsim 2$ , where the system is sufficiently well separated from the zonostrophic instability threshold.

### 6.4.1 Fundamental types of solutions

We observe four distinct types of CE2 solutions in the latitude-time plots, illustrated in Figure 6.7. Firstly, the jets are sometimes observed to be steady in space and time, indicated by a jet velocity profile that at first glance is time independent. Upon closer inspection, these solutions are always associated with

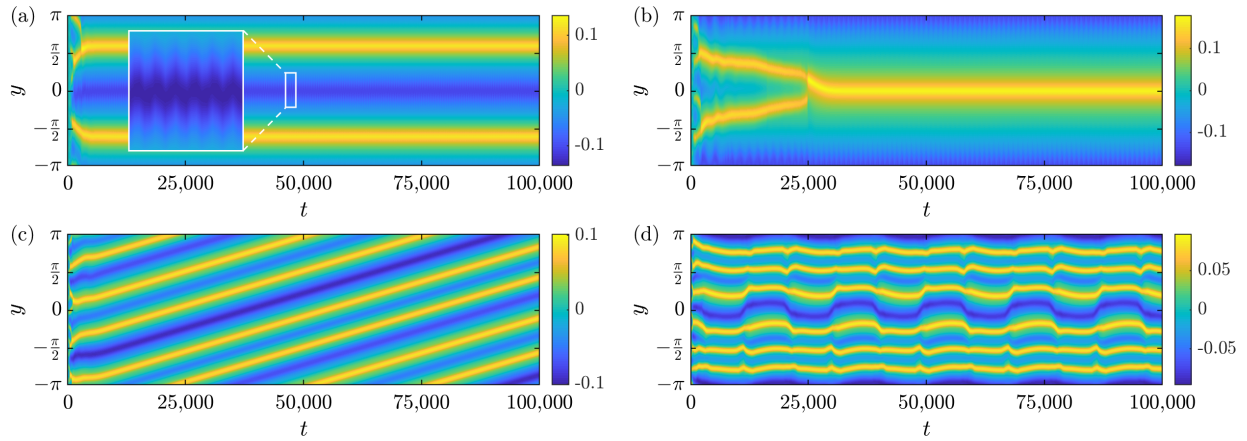


**Figure 6.7** The zoology of zonal jet variability in the CE2 model. (a) Quasi-steady behaviour (parameters used:  $\beta = 0.7$ ,  $\mu = 0.001$ ,  $\varepsilon = 10^{-5}$ ,  $k_f = 16$ ,  $N = 128$ ,  $R_\beta = 2.16$ ). (b) Merging behaviour (parameters used:  $\beta = 0.7$ ,  $\mu = 0.0007$ ,  $\varepsilon = 10^{-5}$ ,  $k_f = 16$ ,  $N = 128$ ,  $R_\beta = 2.36$ ). (c) Migrating behaviour (parameters used:  $\beta = 3.2$ ,  $\mu = 0.002$ ,  $\varepsilon = 10^{-5}$ ,  $k_f = 16$ ,  $N = 128$ ,  $R_\beta = 2.11$ ). (d) Periodic behaviour (parameters used:  $\beta = 3.7$ ,  $\mu = 0.002$ ,  $\varepsilon = 10^{-5}$ ,  $k_f = 16$ ,  $N = 128$ ,  $R_\beta = 2.14$ ).

time-periodic latitudinal fluctuations that are most prominent in the westward jets but are typically small in amplitude. An example simulation is shown in Figure 6.7(a), in which the inset shows an enlarged view of one of the westward jets undergoing regular latitudinal oscillations with a well-defined temporal frequency. We subsequently categorise these types of solutions as *quasi-steady* behaviour.

The second fundamental type of behaviour involves spontaneous transitions between integral numbers of jets, such that the total number of jets in the domain reduces from  $n + 1$  to  $n$  jets via the merging of two neighbouring jets. An example simulation illustrating this behaviour is shown in Figure 6.7(b) in which two jets merge to form a single jet. In contrast to the DNS models, the CE2 system does *not* permit new jets to be generated (nucleated) after the initial linear instability of the homogeneous state has occurred. These transitions, which we describe as *merging* behaviour, are the only mechanism by which the number of jets can change, since the splitting or vanishing of jets is also prohibited.

It is interesting that the CE2 model does permit *migrating* behaviour that was observed to varying degrees in the DNS systems, where the latitudinal symmetry is spontaneously broken and both northward and southward directions of translation are equally probable. Figure 6.7(c) shows an example of a simulation in which four jets are migrating north. Rather than being equally spaced and equally strong, a property of the fast type of migration that was identified in Chapter 4, CE2 simulations always exhibit asymmetries in their relative spacings. We shall discuss the phenomenon of zonal jet migration further in Section 6.6.

In addition to these three types of solutions, we also report the discovery of a new type of behaviour within the CE2 model that is fundamentally unsteady. The jets are sometimes observed to undergo periodic latitudinal displacements with low temporal frequency. An example is shown in Figure 6.7(d) in which the temporal evolution of the relative spacings and positions of six jets displays a striking pattern. The jets are not fixed in their positions relative to one another, but the pattern of displacements is cyclic in time, with a periodicity of duration  $\mu t \approx 40$  in this particular example that is found to be robust to changes in the length of the time steps. We therefore choose to categorise these types of solutions as *periodic* behaviour.

It should be pointed out that these four types of behaviour form the building blocks of the possible regimes within the CE2 model. Additional combinations also exist, for example, we observe the simultaneous occurrence of migrating and periodic behaviour. In addition, we wish to make the point that the

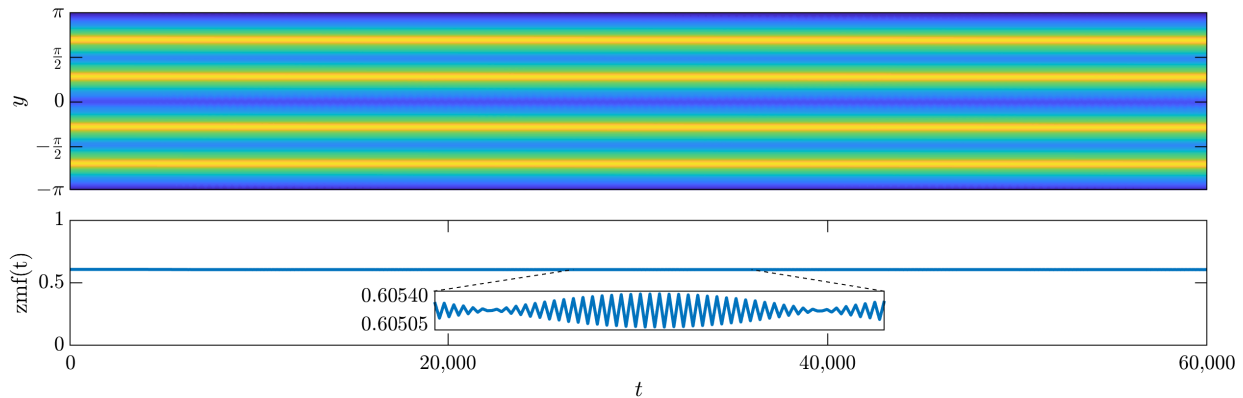


**Figure 6.8** (Top) A latitude-time plot of the time evolution of the zonal mean zonal velocity field and (Bottom) the corresponding evolution of the zmf index, enlarged in the inset to highlight the time-dependence. The CE2 model was used with parameters:  $\beta = 3.5$ ,  $\mu = 0.0015$ ,  $\varepsilon = 10^{-5}$ ,  $k_f = 16$ ,  $N = 128$ ,  $R_\beta = 2.29$ .

CE2 model reproduces the same types of jet spacings and strengths that are possible in the QL model. As discussed in Chapter 4, these solutions are never observed to be fully symmetric (with the exclusion of the single-jet state). In multiple-jet regimes, asymmetries are always present in jet strengths and/or jet spacings, with the exception of very low zonestrophy simulations.

#### 6.4.2 Time-dependency of CE2 solutions

An interesting property of CE2 solutions, partially alluded to in the descriptions of their fundamental types of behaviour, and also in agreement with Marston et al. (2019), is the fact that they *always* exhibit time dependency such that their numerical integration on a doubly-periodic domain never converges to a fixed point. The nature of this time-dependency is sometimes manifest in obvious ways, such as those examples illustrated in Figures 6.7(c,d), however, it is sometimes weak and much more subtle, as demonstrated by the quasi-steady behaviour in Figure 6.7(a). A further example of this is presented in Figure 6.8, showing four quasi-steady jets. The corresponding evolution of the zmf index reveals very small amplitude disturbances oscillating with two different frequencies: a ‘fast’ frequency with period  $\mu t \approx 1$  and a ‘slow’ frequency with period  $\mu t \approx 40$ . It is not possible to generalise the nature of the time dependency across simulations; rather, we comment that it is a fundamental property of solutions that can lead to some surprising transitions, as we discuss in the next section.

### 6.5 Hysteresis, non-uniqueness and spontaneous regime transitions

The CE2 equations permit a surprisingly rich and complex array of behaviours beyond the classification just outlined. In a similar fashion to that discussed in Chapter 4 in relation to the NL and QL models, the nature of the CE2 solutions and the configurations of jets are not fully predictable based upon the system parameters. In some instances, we observe dependencies on previous states of the system; in others, we observe the existence of multiple stable attractors that arise from different initial conditions. In addition, and quite surprisingly, the system also has the capacity to transition between these attractors. In this section, we explore some of these complexities in order to delve deeper into the assessment of the capabilities of the quasilinear approximation, in addition to investigating the impact that the removal of random fluctuations in statistical models has on their ability to reproduce aspects of fully nonlinear behaviour.

### 6.5.1 Hysteresis as $\beta$ varies

Hysteresis behaviour is investigated in the CE2 model by linearly increasing or decreasing the value of  $\beta$  in time over the range  $0 \leq \beta \leq 5$ , ensuring that the rate of change of  $\beta$  is significantly slower than other time scales of motion within the system, whilst keeping all other parameters fixed. In a similar fashion to the experiments conducted in Chapter 4, the simulations are spun-up prior to the commencement of changes in  $\beta$ . Latitude-time plots showing the evolution of the zonal mean zonal velocity are presented in Figure 6.9 for both of these cases, with  $t = 0$  denoting the time when  $\beta$  begins to change, not the initial spin-up time. We note that the direction of time has been reversed in Figure 6.9(b) for ease of comparison.

As  $\beta$  increases, we see the initial formation of three jets at approximately  $\beta \approx 0.35$ , once the system becomes zonostrophically unstable. No further jets form after this point, despite the decreasing Rhines scale, resulting in a configuration in which three strong zonal jets are present when  $\beta = 5$ . In the reverse experiment, we observe the initial formation of six jets, followed by a series of mergers as  $\beta$  decreases towards zero. The consequence of this is that, at the most extreme discrepancy when  $\beta = 5$ , we see a difference of three jets between the two domains for the same set of external parameters. These results arise due to the inability of the CE2 model to allow the generation, or nucleation, of jets after the initial zonostrophic instability. Indeed, we noted in Chapter 4 that zonal jets in the DNS models have a stronger propensity to merge (as  $\beta$  decreases) rather than nucleate (as  $\beta$  increases). It would seem that this property is captured to the extreme by the CE2 system.

Aside from the hysteresis behaviour which permits the existence of different numbers of jets at any particular value of  $\beta$ , these experiments also demonstrate that the system has the capacity to transition between migrating and non-migrating regimes as parameters are varied. This means that a symmetry between the jet velocity profile and the eddy momentum flux convergence profile can be spontaneously broken or restored. On a related note, the system also allows changes in the direction of migration, visible for example in Figure 6.9(b) at about  $t \approx 200,000$ , and also changes in the translation speed. These transitions can occur over a variety of different time scales, both as  $\beta$  increases and decreases, and they are not necessarily associated with merging events. We hypothesise that these properties arise due to the persistent time-dependency of the CE2 solutions, where even weak fluctuations can generate substantial time evolution in the configuration of the jets.

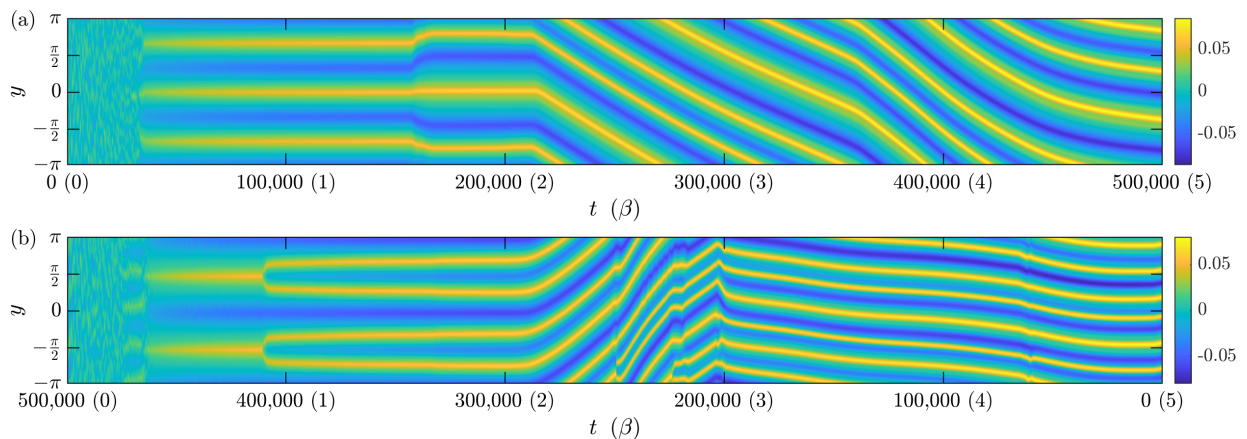


**Figure 6.9** Hysteresis observed as the parameter  $\beta$  is linearly varied in time over the range  $0 \leq \beta \leq 5$  in the CE2 model.  $\beta$  is linearly increased in figure (a) and linearly decreased, in figure (b), where the direction of time is reversed. The parameters used in both plots were:  $\mu = 0.003$ ,  $\varepsilon = 10^{-5}$ ,  $k_f = 16$ ,  $N = 128$ ,  $0 \leq R_\beta \leq 2$ .

### 6.5.2 Existence of multiple stable attractors

It was demonstrated by Farrell and Ioannou (2007), and later proven by Parker and Krommes (2013), that quasilinear statistical closure models exhibit non-unique solutions in terms of jet numbers, where the number of jets in the statistically steady state depends on the initial conditions. Our simulations confirm and go beyond this result, demonstrating that the type of behaviour associated with these jets is also non-unique. To some degree, this is evident by the existence of zonal jet migration in the CE2 model, where, by latitudinally reflecting the initial conditions about  $y = 0$ , we can obtain solutions exhibiting both northward and southward directions of translation. We can also deduce, therefore, that the sum of these initial conditions must give rise to a non-migrating state, which implies that the occurrence of jet migration for a particular set of parameters must be associated with at least three possible solutions.

In order to further explore the existence of multiple stable attractors, we have initialised the CE2 equations with different sets of initial conditions, corresponding to different sets of initial perturbations to the  $U(y)$  variable, for a given set of external parameters. Specifically, if these perturbations are given by

$$U(y, 0) = \sum_{|k_y| \leq k_{max}} \tilde{U}(k_y, 0) e^{ik_y y}, \quad (6.27)$$

with Fourier amplitudes  $\tilde{U}(k_y, 0)$  satisfying  $\tilde{U}(k_y, 0) = \tilde{U}^*(-k_y, 0)$ , then we have specified that  $\tilde{U}(k_y, 0) = A e^{in\theta_{k_y}}$ , where  $A \in \mathbb{R}$  is a small amplitude,  $\theta_{k_y}$  is a random number and  $n \in \mathbb{N}$  allows for variation between initial conditions, in addition to acting as an index. Thus, initial conditions with  $n = 0$  (i.e. real Fourier coefficients) give rise to a solution that is latitudinally-symmetric about  $y = 0$  (and will never migrate), while  $n = \pm 1$ ,  $n = \pm 2$ , etc, (i.e. complex Fourier coefficients) correspond to pairs of solutions that are latitudinally asymmetric about  $y = 0$ , where one solution is the mirror image of the other.

Figure 6.10 shows the results for  $n \in \{0, \pm 1, \pm 2\}$  for a particular set of external parameters which are held fixed. For initial conditions with  $n = 0$ , we observe a solution in which a configuration of six jets is latitudinally symmetric about  $y = 0$ ,  $n = \pm 1$  gives rise to solutions in which five jets migrate north or south, while  $n = \pm 2$  shows solutions in which four jets migrate north or south, albeit at a slower speed and with a different configuration of spacings and relative strengths. Whilst larger values of  $n$  did not reveal any new regimes, these solutions may not be an exhaustive set. Interestingly, the  $n = 0$  initial condition was highly unstable in the numerical integration, where exponentially small numerical truncation errors grew in size such that the system became asymmetric about  $y = 0$ . The only way to prevent this from occurring was to numerically impose the symmetry at each time step. Nevertheless, these results clearly demonstrate the existence of multiple stable attractors in the CE2 system, which may be related to the natural tendency of fluctuating zonal jets in more complex systems to undergo spontaneous transitions between states.

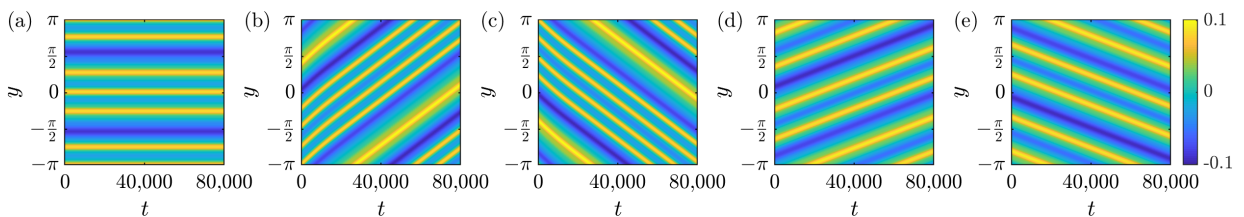


**Figure 6.10** The existence of multiple stable attractors in the CE2 model. Each simulation was integrated forwards in time with initial conditions satisfying (a)  $n = 0$ , (b)  $n = 1$ , (c)  $n = -1$ , (d)  $n = 2$ , (e)  $n = -2$ . The parameters used in all cases were:  $\beta = 3.7$ ,  $\mu = 0.002$ ,  $\varepsilon = 10^{-5}$ ,  $k_f = 16$ ,  $N = 128$ ,  $R_\beta = 2.14$ .

### 6.5.3 The dynamics of unforced regime transitions

A particularly intriguing property of the CE2 equations that we wish to discuss is their capacity to transition between different regimes in the absence of external influences, such as the variation in time of parameters. This is a property that we believe to be another consequence of the persistent time-dependency of the solutions. Rather than trying to establish an exhaustive list of transition types, we instead provide a couple of examples which overlap with our previous discussions from the DNS models and which also offer the potential for new insights into the properties of regime transitions.

One type of transition in the CE2 equations involves a reduction in the number of jets, i.e. merging behaviour. An example of this transition is shown in Figure 6.11(a), in which the merged state, in this particular case, involves a quasi-steady jet associated with small-amplitude fluctuations. The latitude-time plot of the zonal mean zonal flow reveals that the transition is latitudinally asymmetric about the two jets, just as we observed in the QL model in Chapter 4, providing further evidence that the quasilinear approximation does not have the facility of capturing the north-south symmetry property of jet mergers in the NL model. It does, however, reproduce the tendency of the merged state to be associated with a larger zmf index, and also more clearly highlights the manner in which the zmf index temporarily drops prior to the jets merging - a feature that was less easily distinguishable in the stochastic DNS systems. A second type of transition permits the system to shift from one stable attractor to another, as exemplified in Figure 6.11(b). Here, we observe four migrating jets that gradually transition to a new state that is associated with a slower speed of translation and a lower zmf index, thereby proving that the translation speed associated with the slow type of migration is not unique for a given set of parameters and a given number of jets.

Both of these examples reveal very interesting patterns of evolution prior to the transition. In the case of the merging behaviour, the jets gradually approach each other over a very long time scale of order  $10\mu t$ . The second transition, showing a change in translation speed, is preceded by an even longer time scale of evolution of order  $100\mu t$ , shown in the zmf index in the inset in Figure 6.11(b). This raises doubts about the universality of the analogy of stochastically-driven transitions between multiple potential wells. It could be argued, therefore, that regime transitions fall under two classes: *fast* transitions that are stochastically driven and which occur spontaneously on time scales that are commensurate with the damping time scale, and *slow* transitions that result from very long time scale evolutions of the system. Whilst the CE2 equations do not have the capacity to capture the former type of transition, they are able to reproduce the latter.

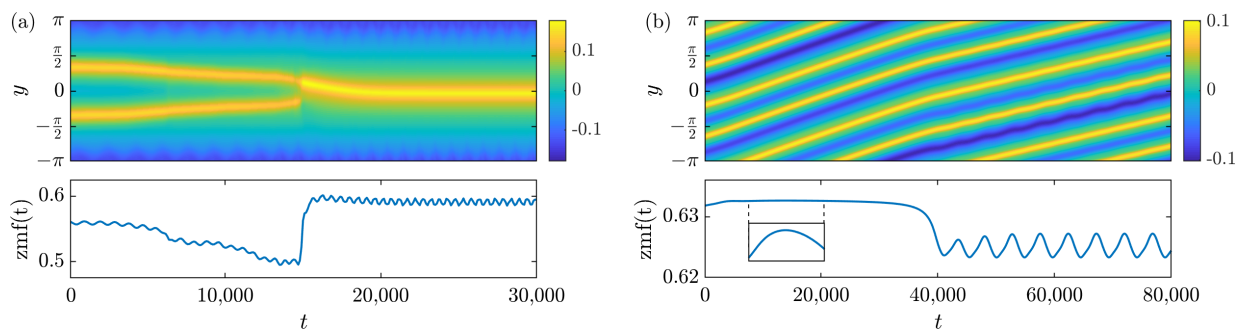


**Figure 6.11** Unforced regime transitions in the CE2 model. (a) A pair of migrating jets merge to form a single non-migrating jet (parameters:  $\beta = 0.7$ ,  $\mu = 0.0007$ ,  $\varepsilon = 10^{-5}$ ,  $k_f = 16$ ,  $N = 128$ ,  $R_\beta = 2.36$ ). (b) Four migrating jets transition to a new speed of translation (parameters:  $\beta = 4.2$ ,  $\mu = 0.002$ ,  $\varepsilon = 10^{-5}$ ,  $k_f = 16$ ,  $N = 128$ ,  $R_\beta = 2.17$ ). Plotted are (top) latitude-time plots of the zonal mean zonal velocity,  $U(y,t)$ , and (bottom) the evolution of the zmf index, where we note that the total energy,  $E$ , remains constant in each case.

## 6.6 A further look at zonal jet migration

In this final section, we take a closer look at the phenomenon of zonal jet migration which has been observed in a significant number of CE2 simulations. As mentioned in Chapter 4, we identified two types of migration in the NL model: fast migration, associated with symmetric jet configurations, and slow migration, in which the jets organised themselves asymmetrically in terms of their relative spacings and strengths. Both types existed in the NL model (and indeed the GQL models), where in Chapter 5 we associated the fast type with the coexistence of long waves, or zonons. However, the QL model only exhibited the slow type of migration, and very few robust examples were found. The CE2 system, therefore, provides an ideal opportunity to learn more about this phenomenon in the context of a quasilinear system.

Whilst we do not observe any particular patterns of occurrence in parameter space, just as we did for the fast type of migration in the NL model in Chapter 4, we do observe migration in many different configurations of jets. Examples in which between one and four jets migrate north are presented in Figure 6.12, showing the zonal mean zonal flow evolution in addition to the jet velocity profiles and corresponding eddy momentum flux convergence profiles. With the exception of the single jet regime, the multiple-jet regimes all involve asymmetries in the jet spacings and, where possible, the jet strengths. These examples are not exhaustive in terms of the possible jet configurations, but they do represent the generic properties.

In each of the multiple-jet regimes, there is a strong correlation between the velocity profiles and eddy momentum flux convergence profiles, with very little latitudinal asymmetry visible about the jet cores and no visible latitudinal offset between these profiles. This is in contrast to the stronger asymmetries associated with the profiles of the fast type of jet migration, discussed in detail in Chapter 5. The exception here is the single jet regime in Figure 6.12(a), where the eddy momentum flux convergence profile is slightly offset to the north of the velocity profile, and both are strongly north-south asymmetric, with stronger forcing on the northern flank. The reason for this difference is not clear.

These findings suggest, at least for the multiple-jet regimes, that the type of migration behaviour observed in the CE2 model is predominantly associated with slower translation speeds,  $\mathcal{V}$ , than the fast

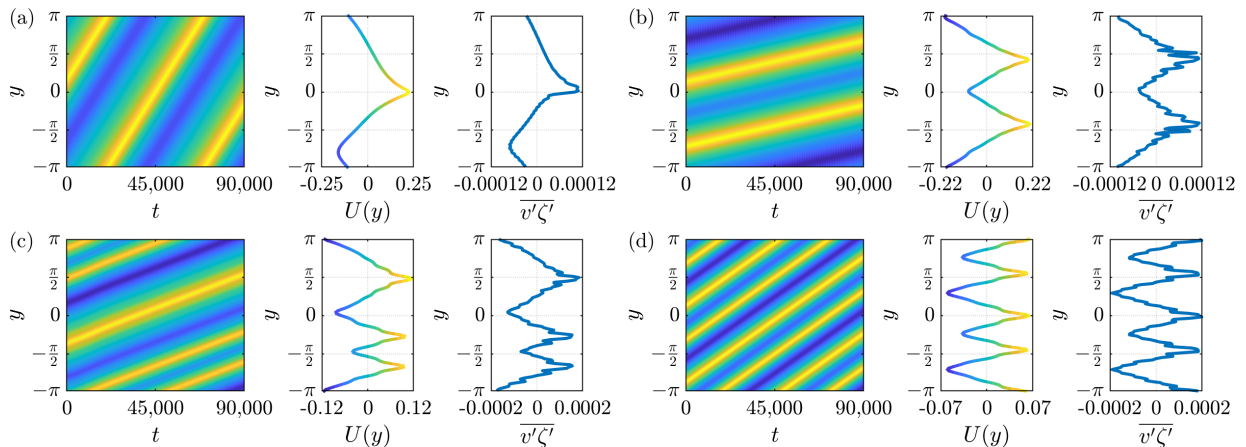


**Figure 6.12** Zonal jet migration in the CE2 model. From left to right we show a latitude-time plot of the zonal mean zonal velocity field  $\overline{U}(y,t)$ , the time-averaged jet velocity profile  $\overline{U}(y)$  and the time-averaged eddy momentum flux convergence  $\overline{v'\zeta'}$ . (a) A single migrating jet with parameters  $\beta = 0.4$ ,  $\mu = 0.0004$ ,  $\varepsilon = 10^{-5}$ ,  $k_f = 16$ ,  $N = 128$ ,  $R_\beta = 2.57$ ; (b) Two migrating jets with parameters  $\beta = 3.0$ ,  $\mu = 0.0015$ ,  $\varepsilon = 10^{-5}$ ,  $k_f = 16$ ,  $N = 128$ ,  $R_\beta = 2.26$ ; (c) Three migrating jets with parameters  $\beta = 2.3$ ,  $\mu = 0.0005$ ,  $\varepsilon = 10^{-5}$ ,  $k_f = 16$ ,  $N = 128$ ,  $R_\beta = 2.89$ ; (d) Four migrating jets with parameters  $\beta = 2.2$ ,  $\mu = 0.003$ ,  $\varepsilon = 10^{-5}$ ,  $k_f = 16$ ,  $N = 128$ ,  $R_\beta = 1.84$ .

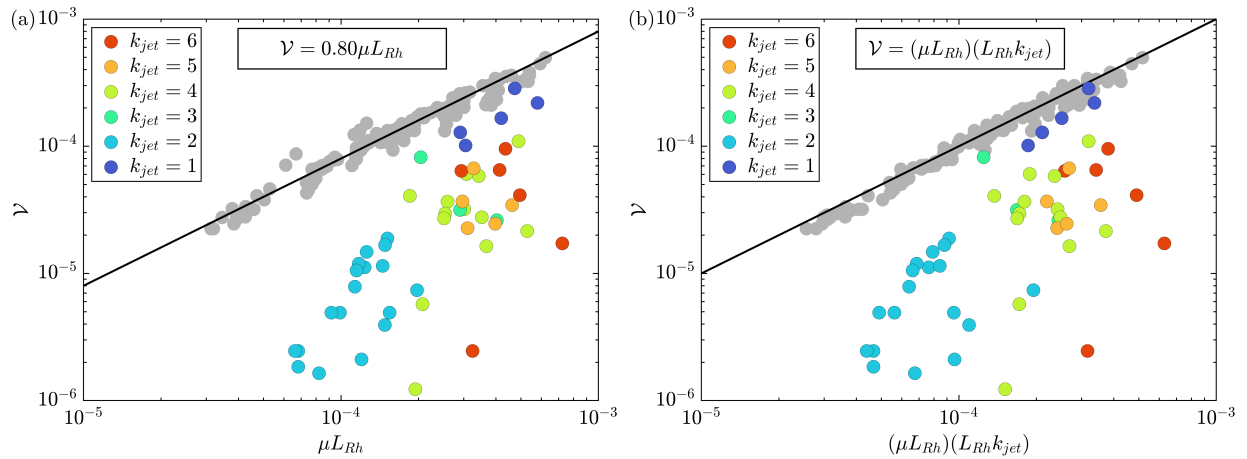


**Figure 6.13** A comparison between jet translation speeds,  $\mathcal{V}$ , for simulations run using the CE2 model (circles coloured by  $k_{jet}$ ) and the NL model (grey circles). (a) The translation speed plotted against  $\mu L_{Rh}$ , with the NL relationship  $\mathcal{V} = 0.80 \mu L_{Rh}$  shown using a black line. (b) The translation speed plotted against  $(\mu L_{Rh})(L_{Rh} k_{jet})$ , with the NL relationship  $\mathcal{V} = (\mu L_{Rh})(L_{Rh} k_{jet})$  shown using a black line.

type of migration in the NL model. The natural way to test this hypothesis is to compare the translation speed data from our CE2 simulations with the data that we analysed in Chapter 5 from the NL model. Consequently, we have computed  $\mathcal{V}$  for a selection of 53 CE2 simulations in which the solutions revealed between one and six migrating jets. These data points are compared in Figure 6.13 with the two expressions,

$$\mathcal{V} \approx 0.80 \mu L_{Rh} \quad \text{and} \quad \mathcal{V} \approx (\mu L_{Rh})(L_{Rh} k_{jet}), \quad (6.28)$$

which were empirically derived in Chapter 5, relating the unique translation speeds associated with the fast type of migration to the system parameters. Each point represents a single simulation, coloured according to the number of jets within the domain. Those simulations from the NL model (with  $N = 256$ ) are shown in grey, and the black lines denote the respective scalings, indicated at the top of each plot.

In both plots, it is immediately apparent that virtually all multiple-jet ( $k_{jet} \geq 2$ ) data points from the CE2 simulations lie significantly below those from the NL model, with migration speeds being up to two orders of magnitude slower than those predicted by expressions (6.28). In addition, the CE2 migration speeds are not necessarily unique for a given set of parameters, as we demonstrated in Section 6.5, implying that they are not linked to the external parameters. These findings indicate that the symmetry-breaking mechanism that permits jet migration in the CE2 model, which may be associated with the slow type of migration that was observed on a few occasions in the QL model, is different to that discussed in Chapter 5. Once again, the exception lies with the single jet regimes, which do show a tendency to adhere to the fast migration speeds, particularly when the second expression,  $\mathcal{V} \approx (\mu L_{Rh})(L_{Rh} k_{jet})$ , is used in Figure 6.13(b). This may be related to the fact that single-jet configurations cannot exhibit asymmetries in the relative spacings or strengths of jets - a property that was associated with the slow migration behaviour observed in the DNS models. At the present time, these differences between single and multiple-jet regimes remain a mystery.

Nevertheless, these results serve to highlight that, at the most basic level, the phenomenon of zonal jet migration does not require the co-existence of jets with long waves, or zonons, that arise in zonally asymmetric systems, at least in second-order closure models. Whether or not fast and slow types of zonal jet migration are distinct types of behaviour, or whether they lie on a spectrum, with the fast type of migration sitting firmly at one extremum, is yet to be determined. It is clear, however, that zonons do play a role

in organising the eddy field, along with the spatial distribution of the jets, in such a way that enhances modes of variability such as migration. On the other hand, the slow type of migration, which appears in quasilinear systems and therefore cannot depend on these zonons, is observed to be significantly less robust in the DNS models than the CE2 model, where it occurs with reasonably high probability. We attribute this to the fact that the organisational role played by the zonons is absent in the slow type (at least in the quasilinear systems), therefore the jets are more easily disturbed by naturally occurring fluctuations in the DNS systems. Whilst migrating states in the CE2 model do not require the additional organisational effect of the zonons to be robust to the effects of fluctuations, their associated translation speeds are compromised by the lack of this additional mechanism.

## 6.7 Discussion

Our focus in this chapter has been the continuation of our study of zonal jet variability using a form of DSS known as CE2 that uses a second order closure scheme. The CE2 model encompasses a pair of relatively simple deterministic equations governing the coupled evolution of the first two cumulants, notably the mean and the two-point correlation function. The fact that it offers potentially simple solutions along with the possibility for analytical exploration motivates the choice for going to this next order in model reduction. By studying the capabilities and limitations of the CE2 equations, along with the direct comparison of results from the DNS systems, we have sought new insights into the dynamical behaviours of zonal jets.

The CE2 equations, constructed using a zonal averaging operator in the definitions of the statistical quantities, are mathematically equivalent to the QL model, with the additional assumption of ergodicity and the replacement of a single realisation of the eddy field with its statistical properties. Thus, the CE2 model captures the fluctuation-free dynamics of the statistical mean state, leading to a predictive theory of the turbulent dynamics. Encouragingly, we found good agreement between the numerical properties of the QL and CE2 solutions, including the numbers of jets within the domain along with their various configurations of spacings and strengths, which were always asymmetric.

In some sense, the CE2 solutions can be interpreted as being equivalent to the QL solutions, except for the lack of random fluctuations that arise from the stochastic forcing. Indeed, they reproduce a rich assortment of behaviours in the zonostrophic regime, including quasi-steady, merging and (slow) migration behaviours, along with the existence of multiple stable attractors that arise from different initial conditions. A crucial difference, however, is the observation that the CE2 model does not permit the nucleation of new jets after the initial zonostrophic instability, which demonstrates that jet nucleations must arise from stochastically-driven fluctuations. This naturally leads to hysteresis behaviour as parameters are varied and bears some resemblance to the stronger propensity of jets to merge rather than nucleate in DNS systems.

An interesting property of the CE2 equations is the fact that they always exhibit time dependency, suggesting that the idea of using the solutions from the CE2 model as a guide to the QL model is perhaps misguided. This unsteadiness is manifest in different ways; sometimes it is very weak, whilst on other occasions it gives rise to very low frequency periodic oscillations of the entire system of jets - a behaviour that has no analogue in the DNS models. As a consequence, the CE2 equations have the capacity to permit transitions between different attractors, despite the lack of random fluctuations, however, it is not clear whether these transitions have any direct correspondence to those found in the DNS models. If they do, then the fact that they are preceded by very slow time scales of evolution leads us to argue that regime transitions

in general can be categorised according to two different types: *fast* transitions that are stochastically driven, and *slow* transitions that result from long time scale evolutions (and therefore do not conform to the analogy of stochastic potential wells). The CE2 model captures the latter type, which includes merging behaviour, but not the former, which includes nucleating behaviour.

We completed our study with a further investigation of the phenomenon of zonal jet migration in the CE2 model. Analysis of a large number of simulations determined that jet migration in the CE2 system (at least for multiple-jet regimes) corresponds to a slow and asymmetric type of migration that bears some resemblance to that observed in the DNS models, including the QL model, although direct correspondence is yet to be determined. Translation speeds were not found to be unique for a given set of parameters, and they bore no correspondence with the speeds of the fast and symmetric type of migration discussed in Chapter 5, being up to two orders of magnitude slower. Nevertheless, these results raise doubts about the necessity of zonons for the existence of zonal jet migration behaviour, since the mechanism of zonon generation is not accommodated in conventional second-order closure theories.

The source of the slow type of migration in the CE2 system, which requires that the velocity and eddy momentum flux convergence profiles be appropriately organised, is not yet clear. It is conceivable that it originates from fastest growing modes about the zonostrophic instability threshold that possess a non-zero imaginary part, and are therefore latitudinally-unstable. Whilst the existence of such fastest growing modes is yet to be determined, Ruiz et al. (2016) demonstrated that modes with a non-zero imaginary part exist for a simpler forcing distribution, but made no reference to whether these modes were the fastest growing ones (a key point when considering zonostrophic instability). For these reasons, it would be interesting if jet migration could be demonstrated close to marginal stability, but the behaviour has so far only been observed far from the stability threshold at larger zonostrophy. Whatever the mechanism, it is clear, however, that the existence of zonons enhances the phenomenon of zonal jet migration due to their organisational role of the eddy field. This concludes our study of the dynamics of beta-plane turbulence, leaving open the additional question regarding the role that zonons play in other types of zonal jet variability.

# Chapter 7

## Introduction to stratified turbulence

### 7.1 Motivation

Geophysical and astrophysical fluid flows are strongly influenced and characterised by the effects of important ingredients such as rotation and stratification. In this second part of the thesis, we turn our attention towards this latter effect, meaning that there is a vertical gradient in the background equilibrium fluid density. Statically stable stratified flows, where the background density gradient decreases (at least on average) upwards in a gravitational field, are ubiquitous. Geophysical examples include planetary atmospheres, oceans and lakes, while such flows also occur on astrophysical scales in stellar interiors.

A key physical process in stratified flows is the effect of a restoring *buoyancy force* which induces internal wave motions when fluid parcels are vertically perturbed from their equilibrium position. Furthermore, such naturally occurring flows are rarely at rest, therefore it is generic that the fluid will also have a spatially and temporally varying background velocity distribution that is expected to interact with the stratification. In many cases, the flow becomes turbulent due to dynamical instabilities, leading to the phenomenon of *stratified turbulence*, a term that was coined by Lilly (1983) to describe three-dimensional turbulence where motion in the vertical is constrained by stable stratification.

This interaction between turbulence and stratification is a major source of vertical transport in geophysical flows (Ferrari and Wunsch, 2009; Ivey et al., 2008) as well as stellar interiors (Spiegel and Zahn, 1992; Zahn, 1974, 1992). In the geophysical literature, stratified turbulence exhibits a wide range of dynamical, and often counter-intuitive, behaviours, not least because it leads to complex, and still controversial, irreversible energetic exchange pathways between the kinetic, potential and internal energy reservoirs. Understanding and modelling these pathways, in particular the *efficiency* of mixing (associated with the irreversible conversion of kinetic energy into potential energy) is of great importance for the large-scale descriptions of geophysical flows, such as weather forecasts, ocean circulation simulation or indeed climate models, as well as astrophysical flows that regulate stellar evolution. Nevertheless, small-scale mixing processes, which play a significant role in the large-scale transport of angular momentum and chemical elements, cannot be directly resolved in GCMs and stellar evolution models. Understanding their properties is therefore crucial for the development of appropriate parameterisations.

In this chapter, we first describe the current understanding of stratified turbulence in geophysical flows, in which the diffusivities of heat and momentum are commensurate. This is followed by an explanation as to why these results are not directly applicable in the limit of strong thermal diffusion (which applies to astrophysical flows such as stellar interiors) and therefore why they need to be revisited.

## 7.2 Stratified turbulence in geophysical flows

### 7.2.1 A framework of idealised models of stratified flows

In the context of stratified flows, there has been a substantial amount of research examining the transition to turbulence, and its subsequent properties (including turbulent mixing) with a focus on the relevance to atmospheric and oceanic flows (see e.g. Ivey et al., 2008). The simplest idealised (yet commonly considered) situation incorporates three fundamental modelling assumptions. These stipulate that the fluid velocity is incompressible, i.e.  $\nabla \cdot \mathbf{u} = 0$ , that the density differences within the flow are sufficiently small such that the Boussinesq approximation applies, and that the density variations within the fluid are associated with a single stratifying agent, avoiding the occurrence of double diffusive phenomena. As we shall explain, this gives rise to a system that can be described by the set of equations

$$\frac{\partial \mathbf{u}}{\partial t} + \mathbf{u} \cdot \nabla \mathbf{u} + \frac{1}{\rho_0} \nabla p = \nu \nabla^2 \mathbf{u} + \alpha g (T - T_0) \mathbf{e}_z + \mathbf{F}, \quad (7.1)$$

$$\frac{\partial T}{\partial t} + \mathbf{u} \cdot \nabla T = \kappa \nabla^2 T, \quad (7.2)$$

$$\nabla \cdot \mathbf{u} = 0, \quad (7.3)$$

where  $\mathbf{u}$  is a three-dimensional velocity field,  $T$  is the temperature field and  $\mathbf{F}$  is a body force. Without loss of generality, the density field,  $\rho$ , may be assumed to be a function of temperature,  $T$ , alone, such that

$$\frac{(\rho - \rho_0)}{\rho_0} = -\alpha(T - T_0), \quad (7.4)$$

where  $\rho_0$  and  $T_0$  are reference densities and temperatures and  $\alpha$  is the thermal expansion coefficient. This implies that, since the temperature satisfies the advection-diffusion equation (7.2), the density fluctuations must also satisfy the same equation.

Both irreversible mixing and turbulent viscous dissipation, leading respectively to irreversible changes in the potential and internal energy of the flow, rely inherently on the action of diffusive processes. Under the three simplifying assumptions described above, the stratified fluid under consideration is associated with two relevant diffusivities: the kinematic viscosity,  $\nu$ , quantifying the diffusivity of momentum in equation (7.1), and  $\kappa$ , quantifying the diffusivity of density in equation (7.2). Together with these diffusivities, there are at least three additional dimensional parameters required to describe a stratified flow. These include a characteristic velocity scale,  $U_c$ , a characteristic length scale,  $L_c$ , and a characteristic buoyancy frequency,  $N_c$ , associated with the background buoyancy frequency profile,  $N_b(z)$ , which is defined as

$$N_b^2(z) \equiv -\frac{g}{\rho_0} \frac{d\rho_b}{dz} = \alpha g \frac{dT_b}{dz}. \quad (7.5)$$

Here,  $g$  is the acceleration due to gravity, and  $\rho_b$  and  $T_b$  are background profiles of density and temperature, respectively. We note that the Boussinesq approximation requires that the total variation of a background scalar quantity  $q_b(z)$  satisfies the condition  $L_c |dq_b/dz| \ll q_0$ .

This idealised system can be described by a set of three non-dimensional parameters. Natural choices include a Reynolds number,  $Re$ , quantifying the relative magnitude of inertia to momentum diffusion by viscosity, a Péclet number,  $Pe$ , quantifying the relative magnitude of inertia to the diffusion of the density,

and a Froude number,  $Fr$ , quantifying the relative magnitude of the inertia to the stratification. In terms of the original parameters, these are constructed as

$$Re \equiv \frac{U_c L_c}{\nu}, \quad Pe \equiv \frac{U_c L_c}{\kappa} = Pr Re, \quad \text{and} \quad Fr \equiv \frac{U_c}{N_c L_c}, \quad (7.6)$$

where  $Pr = \nu/\kappa$  is the Prandtl number. For consistency with the existing literature, we note that for vertically sheared flows, the Froude number is related to a bulk Richardson number,  $Ri$ , as

$$Ri = \frac{N_c^2 L_c^2}{U_c^2} = Fr^{-2}, \quad (7.7)$$

where the limit  $Ri \ll 1$  implies that stratification effects are unimportant. We also note that we have restricted our attention to a regime where the scales of motion are sufficiently small and fast such that the effects of rotation can be ignored, otherwise an additional parameter is necessary.

### 7.2.2 Stratified turbulence and general scaling arguments

Before proceeding, it is helpful to briefly review some concepts from the theory of three-dimensional turbulence, which behaves in a profoundly different way from that in two-dimensions, largely due to the presence of vortex stretching mechanisms. According to the spectral theory of Kolmogorov (1941), energy and enstrophy both cascade from large scales down to small scales, where they are ultimately dissipated by viscosity. The theory considers an isotropic, homogeneous (and unstratified) fluid that is stirred at scales that are sufficiently larger than the dissipation scale, such that there exist a range of intermediate scales which are effectively independent from the details of the forcing or dissipation, i.e. the *locality hypothesis*. If we consider that the rate of production of energy due to the stirring is given by  $\varepsilon$ , then in a steady state, this should also equal the rate of cascade of energy from large to small scales, in addition to the rate at which energy is dissipated by viscous processes. Consequently, on the grounds of dimensional arguments, Kolmogorov (1941) predicted an inertial range on the assumption that the energy spectrum should depend only on the local isotropic wavenumber,  $k = (k_x^2 + k_y^2 + k_z^2)^{1/2}$ , and the energy cascade rate,  $\varepsilon$ . The associated energy spectrum,  $\mathcal{E}(k)$ , for wavenumbers smaller than the forcing scale was predicted to be

$$\mathcal{E}(k) = \mathcal{K} \varepsilon^{2/3} k^{-5/3}, \quad (7.8)$$

where  $\mathcal{K}$  is a constant; this is the famous ‘Kolmogorov -5/3 spectrum’.

The presence of stratification, however, constrains vertical motions due to the buoyancy force, which induces anisotropy into the system, analogously to the  $\beta$ -effect in two-dimensional turbulence. The seminal papers by Dougherty (1961) and Ozmidov (1965) suggested that there exists a length scale constructed from  $\varepsilon$  and the characteristic buoyancy frequency,  $N_c$ , that should define the largest scale that can remain isotropic in the presence of stratification. This is the well-known *Ozmidov* scale,

$$L_O = \left( \frac{\varepsilon}{N^3} \right)^{1/2}, \quad (7.9)$$

which is also thought to be associated with the maximum length scale at which eddies can overturn before being inhibited by buoyancy. Another important length scale, known as the *Kolmogorov* scale, is associated with the smallest size of turbulent eddies. This emerges by equating the dissipation time scale due to

viscosity,  $\tau_v = k^{-2}\nu^{-1}$ , with the eddy turnover time,  $\tau_t = \varepsilon^{-1/3}k^{-2/3}$ , giving

$$L_v = \left(\frac{\nu^3}{\varepsilon}\right)^{1/4}, \quad (7.10)$$

where  $L_v = k_v^{-1}$ . This is the only length scale that can be deduced from  $\varepsilon$  and the kinematic viscosity,  $\nu$ .

Using these scales, a common approach to assessing the importance of turbulence in stratified flows is to consider a dimensionless quantity which is derived from their ratio:

$$Re_b \equiv \left(\frac{L_O}{L_v}\right)^{4/3} = \frac{\varepsilon}{\nu N^2}. \quad (7.11)$$

This is known as the *buoyancy Reynolds* number, and acts as a measure of the isotropic cascade range.

### 7.2.3 Towards an understanding of the sustainment of stratified turbulence

Atmospheric and oceanic flows are often very strongly stratified, as discussed in detail in Riley and Lelong (2000) and Brethouwer et al. (2007), in the specific sense that if both  $L_c$  and  $U_c$  are identified with typical scales of horizontal motions, then  $Fr \ll 1$  (or equivalently,  $Ri \gg 1$ ). Given that a necessary condition for a vertically-sheared flow to overcome the tendency to remain stratified, and thus transition to turbulence, requires  $Ri < O(1)$ , this would imply that such flows remain laminar. On the contrary, turbulence is observed in the atmosphere and the ocean, at least in spatio-temporally varying patches (Portwood et al., 2016), which has profound implications for understanding the dynamics of stratified flows.

In a bid towards understanding the dynamics of strongly stratified turbulent flows, Brethouwer et al. (2007), following Billant and Chomaz (2001), demonstrated that when both  $Re \gg 1$  and  $Fr \ll 1$ , several different flow regimes are possible. Each regime can be understood as a distinct dominant balance between various terms in the Navier-Stokes equations, dependent on their relative sizes. Of central significance to these balances, however, are two additional geophysically-motivated parameter choices. The first is motivated by the expectation (and empirical observation) that strong stratification leads to anisotropy in the flow, so that the characteristic vertical length scales,  $L_v$ , are expected to be very different from characteristic horizontal length scales,  $L_h \equiv L_c$ . The second relies on the fact that the Prandtl number is of order unity or larger in geophysical flows, with  $Pr \sim O(1)$  for gases and  $Pr \sim O(10)$  for fresh water.

With these two further choices, Brethouwer et al. (2007) discussed three particular regimes which we shall proceed to describe. The first, which was originally considered by Lilly (1983) and later discussed by Riley and Lelong (2000), considers the limit in which  $L_v/L_c \gg Fr$  while  $L_v/L_c \gg Re^{-1/2}$ . Together with the original assumption that  $Re \gg 1$  and  $Fr \ll 1$ , these scalings imply that all terms involving vertical derivatives are insignificant in the Navier-Stokes equations, and so the governing equations reduce to the evolution equations for an incompressible and inviscid two-dimensional horizontal velocity field,  $\mathbf{u}_h(x, y, t)$ . Furthermore, since  $Pr \gtrsim O(1)$ , the diffusive terms in the density equation can also be ignored, and quasi-two dimensional (although possibly layerwise) flow evolution is expected in this regime.

The other two regimes discussed in detail by Brethouwer et al. (2007) exploit the insight of Billant and Chomaz (2001) that the vertical length scale should not be externally imposed, but should emerge as a property of the flow dynamics. In that respect, a key parameter is the buoyancy Reynolds number, defined here as  $Re_b \equiv ReFr^2$ , noting that  $\varepsilon = U_c^3/L_c$  in expression (7.11). When  $Re_b \lesssim O(1)$ , a *viscously-affected* regime is expected, where horizontal advection is balanced by viscous diffusion, specifically associated

with vertical shearing. This regime, which is much more likely to be relevant in experiments or simulations rather than in geophysical applications, has  $L_v/L_c \sim Re^{-1/2}$ , and does not exhibit a conventional turbulent cascade, but rather exhibits the effects of viscosity (and density diffusion) even at large horizontal scales.

Conversely, Brethouwer et al. (2007) showed that when  $Re_b \gg 1$ , viscous effects (and density diffusion) are insignificant and the remaining terms (including the advection by the vertical velocity) become self-similar with respect to  $zN_c/U_c$ , with  $z$  being the vertical coordinate aligned with gravity. This suggests strongly that  $L_v \sim U_c/N_c$ , or equivalently that the Froude number based on the vertical scale  $L_v$ , defined as

$$Fr_v \equiv \frac{U_c}{L_v N_c}, \quad (7.12)$$

should be of order one, so  $L_v \ll L_c$ . Such a vertical layer scale has been commonly observed in a wide variety of sufficiently high Reynolds number stratified flows (e.g Billant and Chomaz, 2000; Brethouwer et al., 2007; Godeferd and Staquet, 2003; Holford and Linden, 1999; Lucas et al., 2017; Oglethorpe et al., 2013; Park et al., 1994; Zhou and Diamessis, 2019) and appears to be a generic property of high  $Re_b$  and high  $Pr$  stratified turbulence. This regime is characterised not only by anisotropic length scales but also by anisotropy in the velocity field, and hence the associated turbulence, leading Falder et al. (2016) to refer to this flow regime as the ‘layered anisotropic stratified turbulence’ (LAST) regime.

The vertical layering on the scale  $L_v$  is key to understanding how turbulence can be maintained in the LAST regime despite the fact that  $Fr \ll 1$ . Indeed, these ‘layers’ in the density distribution consist of relatively weakly stratified wider regions separated by relatively thinner ‘interfaces’ with substantially enhanced density gradient. As such, local values of the buoyancy frequency can vary widely from the characteristic value  $N_c$ . When the local vertical shear is sufficiently strong compared to the local density gradient, then the gradient Richardson number  $Ri_g$ , which is defined as

$$Ri_g \equiv \frac{-g}{\rho_0} \frac{\partial \rho / \partial z}{|\partial \mathbf{u}_h / \partial z|^2}, \quad (7.13)$$

can drop to values low enough for shear instabilities to be able to develop. If, in addition, the Reynolds number is sufficiently large for inertial effects to be dominant, this allows for the possibility of turbulence through the breakdown of shear instabilities, albeit with both spatial and temporal intermittency.

It is crucial to appreciate that this LAST regime relies inherently on the assumption that  $Pr \gtrsim O(1)$ , since high Reynolds number then implies high Péclet number (i.e. weak thermal diffusion), so localised turbulent events can erode the stratification and in turn participate in the formation or maintenance of the layers. Whilst these assumptions are appropriate for the atmosphere and the ocean, they certainly do not apply in the astrophysical context, where  $Pr \ll 1$  (see Section 7.3). As we proceed to demonstrate, density layering is prohibited in that case, suggesting that LAST dynamics cannot occur. This raises the interesting question of whether analogous or fundamentally different regimes exist when  $Pr \ll 1$ .

### 7.3 Stratified shear instabilities in astrophysical flows

Whilst turbulent mixing in geophysical (atmospheric and oceanic) GCMs has received much attention, it is usually either neglected or poorly parameterised in stellar evolution models. However, there is growing theoretical and observational evidence that such mixing is present and can affect the life cycle of a star, participating in the transport of both angular momentum and chemical elements. Inspired by the work

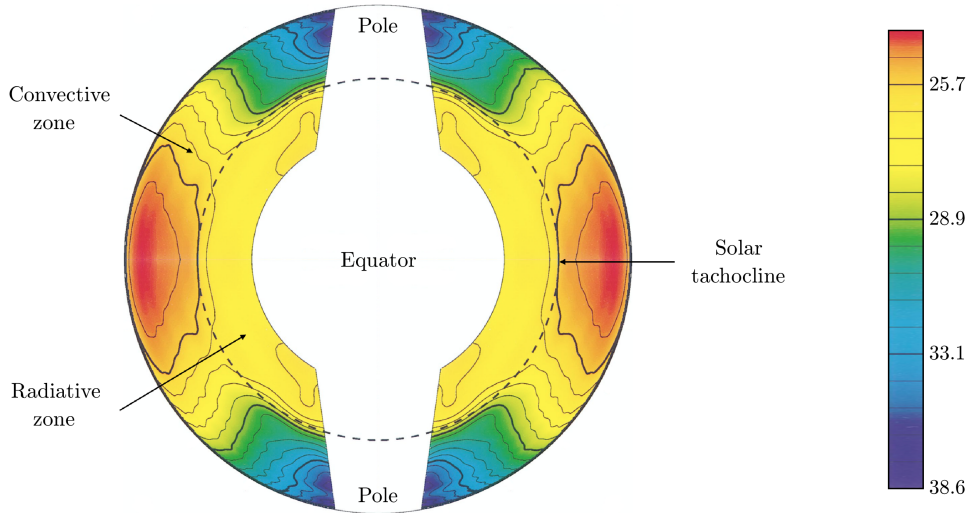


**Figure 7.1** The Sun's differential rotation, adapted from Schou et al. (1998). Colours represent the inferred rotation period in units of days, computed from 144 days of observations. The radiative zone rotates with approximately uniform angular velocity, while the angular velocity in the convective zone increases from the poles to the equator. This gives rise to an abrupt transition between these zones, known as the solar tachocline, which is characterised by both horizontal and vertical shear.

of Jean-Paul Zahn (Zahn, 1974, 1992), shear instabilities are conjectured to provide one such source of turbulent mixing in stars, with the origin of the shear attributed to the star's differential rotation. Indeed, the advent of helio- and astero-seismology have enabled the internal structure of the sun and Red Giant Branch (RGB) stars to be probed, revealing, for example, the existence of a *solar tachocline* (see Figure 7.1) which constitutes an abrupt transition between the differentially rotating outer convection zone and the uniformly rotating radiative inner zone. This region is associated with both strong radial (vertical) and horizontal shear, and it is also stably (and strongly) stratified.

When modelling astrophysical fluids, it is important to note that several key differences exist between these flows and their geophysical counterparts. For example, the fluid from which stars are made is a plasma comprised of photons, ions, and free electrons, giving rise to a Prandtl number which is much smaller than one, ranging between  $10^{-9}$  and  $10^{-5}$  in typical stellar radiative zones (see Garaud et al., 2015b). The microphysical explanation for this difference is that heat can be transported by photons efficiently while momentum transport usually requires collisions between ions (which comprise most of the mass), so  $\nu \ll \kappa$  and therefore  $Pr \ll 1$ . This crucially introduces the possibility of a new regime of flow dynamics where  $Re \gg 1$  while  $Pe = PrRe \ll 1$ , which is never realised in geophysical flows.

Another key difference is that astrophysical fluids are also not incompressible. However, under a set of assumptions that are almost always satisfied sufficiently far below the surface of stars, the Spiegel-Veronis-Boussinesq approximation (Spiegel and Veronis, 1960) can be used to reduce the governing equations to a form that is almost equivalent to that used for geophysical flows. In particular,  $\nabla \cdot \mathbf{u} \simeq 0$ ,  $(\rho - \rho_0)/\rho_0 \simeq -\alpha(T - T_0)$ , and the temperature equation (7.2) becomes

$$\frac{\partial T}{\partial t} + \mathbf{u} \cdot \nabla T + w \frac{g}{c_p} = \kappa \nabla^2 T, \quad (7.14)$$

where  $c_p$  is the specific heat at constant pressure. In comparison with (7.2), the new term  $wg/c_p$  accounts for compressional heating (or cooling) as the parcel of fluid contracts (or expands) to adjust to the ambient

pressure as it moves downwards (or upwards) in a gravitational field. As a result, the background buoyancy frequency profile,  $N_b(z)$ , is modified from expression (7.5) to incorporate this new term,

$$N_b^2(z) \equiv \alpha g \left( \frac{dT_b}{dz} + \frac{g}{c_p} \right), \quad (7.15)$$

from which a new characteristic buoyancy frequency,  $N_c$ , can be defined.

Due to these properties, there exist a couple of important consequences which are relevant to the study of stratified turbulence in astrophysical flows. Firstly, as previously mentioned, thermal dissipation greatly mitigates and modifies the effect of stratification in comparison to flows with  $Pr \gtrsim O(1)$ . In particular, as demonstrated by Lignières (1999) (see also Spiegel, 1962; Thual, 1992), a dominant balance emerges in the temperature equation whereby

$$w \left( \frac{dT_b}{dz} + \frac{g}{c_p} \right) \simeq \kappa \nabla^2 T, \quad (7.16)$$

(at least to leading order in  $Pe^{-1}$ ), showing that temperature fluctuations and vertical velocity fluctuations are slaved to one another. Mass conservation, combined with appropriate boundary conditions, then generally implies that the horizontal average of  $T$  should be zero. Physically, this implies that due to the very rapid diffusion of the temperature fluctuations (and hence density), these perturbations cannot modify the background state. Thus, density layering is inhibited which means that the local buoyancy frequency remains close to the background value,  $N_b(z)$ , everywhere.

Another important consequence is that the Péclet and Froude (or Richardson) numbers are no longer independent control parameters for the system dynamics, but always appear together as  $Pe/Pr^2$  or  $RiPe$  (Lignières, 1999). Zahn (1974) argued that, as a result, the threshold for vertical shear instability should be  $RiPe \lesssim Re/Re_c$  where  $Re_c$  is the critical Reynolds number for instability in unstratified, unbounded shear flows. This criterion, which is now commonly written as  $RiPr \lesssim K_Z$ , was recently confirmed using direct numerical simulations, giving  $K_Z \simeq 0.007$  (see Garaud et al., 2017; Prat et al., 2016; Prat and Lignières, 2013, 2014). With the aforementioned estimates for  $Pr$ , we see that shear-induced turbulence in low  $Pe$  vertical shear flows is therefore likely for  $Ri$  up to  $O(10^2)$  or higher. On the other hand, for astrophysical flows with  $RiPr \gg K_Z$ , or for horizontally-sheared flows, one may naturally ask whether any pathway to turbulence exists, since the density layering that is central to the LAST regime is not possible here.

We conclude this section with a review of the most commonly used model of shear-induced mixing in stars, proposed by Zahn (1992), who considered successively both vertically-sheared flows and horizontally-sheared flows. For a vertically-sheared flow with a characteristic shearing rate  $S_c$ , he argued, based on work by Townsend (1958) and Dudis (1974), that the largest unstable vertical scale in the flow would satisfy  $RiPe_t \sim O(1)$ , where  $Ri = N_c^2/S_c^2$  and  $Pe_t \equiv S_c l^2/\kappa$  is an eddy-scale Péclet number. This defines the characteristic Zahn scale,  $l_Z$ , as

$$Ri \frac{S_c l_Z^2}{\kappa} \sim O(1) \quad \Rightarrow \quad l_Z \sim \sqrt{\frac{\kappa}{Ri S_c}} \sim \sqrt{\frac{\kappa S_c}{N_c^2}}, \quad (7.17)$$

from which he proposed a simple expression for a turbulent diffusion coefficient on dimensional grounds:

$$D_{\text{turb}} \sim S_c l_Z^2 \sim \frac{\kappa}{Ri}. \quad (7.18)$$

The relevance of the Zahn scale to the dynamics of *low Péclet* number stratified turbulence in vertically-sheared flows was confirmed by Garaud et al. (2017) using direct numerical simulations. They also verified the applicability of the turbulent diffusion coefficient (7.18), provided that  $l_Z$  is much smaller than the domain scale, and  $RiPr \lesssim K_Z$  (see also Prat et al., 2016; Prat and Lignières, 2013, 2014).

In the horizontally-sheared case, Zahn (1992) postulated (following an argument attributed to Schatzman and Baglin, 1991), that while the turbulence would be mostly two-dimensional on the large scales owing to the strong stratification, it could become three-dimensional below a scale  $L_c$  where thermal dissipation becomes important. By definition, this is the Zahn scale, given by (7.17), where  $S_c = U_c/L_c$  (and  $U_c$  is the characteristic velocity of eddies on scale  $L_c$ ). Since  $Pr \ll 1$ , this scale is also unaffected by viscosity, so one would expect a turbulent cascade with a well-defined kinetic energy transfer rate of order  $U_c^3/L_c$ . If, in addition, dissipative irreversible conversions into the potential energy reservoir (associated with mixing) are negligible, then  $\varepsilon = U_c^3/L_c$ , where  $\varepsilon$  is the viscous energy dissipation rate. Solving for  $L_c$  and  $U_c$  yields

$$L_c \sim \left( \frac{k\varepsilon^{1/3}}{N_c^2} \right)^{3/8} \quad \text{and} \quad U_c^3 \sim L_c \varepsilon, \quad (7.19)$$

from which a turbulent diffusion coefficient can then be constructed as

$$D_{\text{turb}} \sim U_c L_c \sim \sqrt{\frac{k\varepsilon}{N_c^2}}. \quad (7.20)$$

These scalings for low Péclet (and Prandtl) number horizontal shear instabilities have never been verified.

## 7.4 Research questions

Understanding the pathways and transition to turbulence in stars is of central importance in the development of stellar evolution models. Due to the presence of strong radial and horizontal differential rotation, shear instabilities are thought to play a significant role, however, the majority of theoretical studies have focussed purely on the effect of vertical shear. The fact that vertical shear instabilities directly generate vertical fluid motion makes them natural choices as a source of vertical mixing, nevertheless, they do have a tendency to be suppressed by stratification (Garaud et al., 2015a). This study aims to address these ideas for the case of stratified horizontal shear instabilities, where we aim to test the Zahn (1992) model. In addition, we are also interested in testing the assumption that all energy dissipation is exclusively viscous, since there is growing evidence (Garanaik and Venayagamoorthy, 2019; Maffioli et al., 2016) for geophysical flows with  $Pr \gtrsim O(1)$  that non-trivial irreversible mixing converting kinetic energy into potential energy continues to occur even in the limit  $Fr \rightarrow 0$  of extremely strong stratification.

In Chapter 8 we study the simplest possible model of a stratified horizontal shear flow, focussing on the limit of strong thermal diffusion, or equivalently, small Péclet number. This limit is motivated by the fact that whilst  $Re$  is very large in stars such that the global-scale Péclet number is large, there must necessarily exist a length scale,  $L_c$ , below which the flow behaves diffusively (Zahn, 1992), and for which the limit is relevant. In addition, studying high  $Pe$  flows with  $Pr \ll 1$  is numerically challenging since it requires large values of  $Re$ . Thus, understanding the behaviour of low  $Pe$  flows is a first step towards this more challenging goal, and may provide a way of creating a model for mixing at small scales. Consequently, we seek to identify separate dynamical regimes along with a set of scaling laws that explain the numerical data.

## Chapter 8

# The dynamics of stratified horizontal shear flows at low Péclet number

### 8.1 Introduction

In this Chapter, following the hypothesis of Zahn (1992), we explore the contribution of horizontal shear instabilities to turbulent mixing processes in stellar interiors. This study, which was initiated as a project at the Woods Hole Oceanographic Institute GFD summer programme in 2018, has recently been published (Cope et al., 2020). After presenting the model set-up, we begin by summarising the results of a linear stability analysis of the problem, where we seek to identify possible mechanisms for the transition to turbulence in the limit of strong thermal diffusion. The subsequent nonlinear evolution is studied numerically using direct numerical simulations, allowing for the identification of separate dynamical regimes, each with their own characteristic properties. These are then systematically reviewed, where we study the dominant balances for each regime and derive pertinent scaling laws that are then compared with the numerical data.

### 8.2 Mathematical formulation

#### 8.2.1 Mathematical model

Seeking the simplest possible model, and neglecting the effects of rotation and magnetism, we consider an incompressible, body-forced, stably stratified flow with streamwise velocity field aligned with the  $x$ -axis. In accordance with the Spiegel-Veronis-Boussinesq approximation (Spiegel and Veronis, 1960), we assume that the basic state comprises a linearised temperature distribution,  $T_b(z)$ , given by  $T_b(z) = T_0 + z(dT_b/dz)$ , where  $T_0$  is a reference temperature, along with a body-forced laminar velocity field,  $\mathbf{u}_L(y)$ . The total temperature field,  $T$ , includes perturbations  $T'(x, y, z, t)$  away from the basic state such that  $T = T_b(z) + T'(x, y, z, t)$ . As discussed in Chapter 7, the density fluctuations,  $\rho'$ , and temperature fluctuations,  $T'$ , are related by the linearised equation of state

$$\frac{\rho'}{\rho_0} = -\alpha T', \quad (8.1)$$

where  $\rho_0$  is a reference density and  $\alpha = -\rho_0^{-1}(\partial\rho/\partial T)$  is the coefficient of thermal expansion. The three-dimensional velocity field is given by  $\mathbf{u}(x, y, z, t) = u\mathbf{e}_x + v\mathbf{e}_y + w\mathbf{e}_z$ . For numerical efficiency and mathemati-

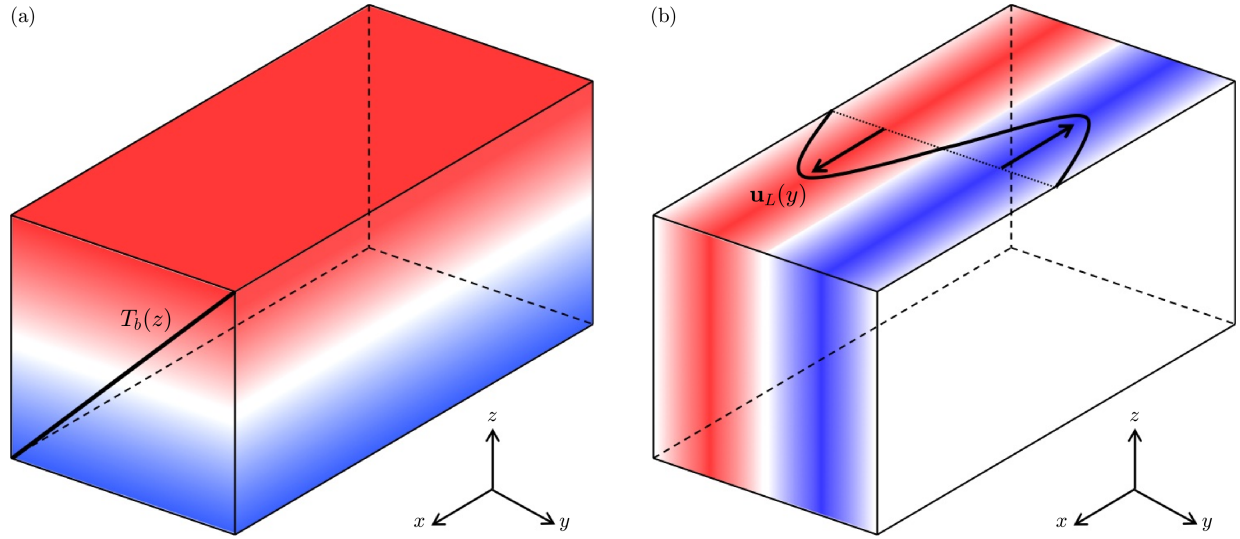


**Figure 8.1** Schematics of the basic state set-up showing (a) the linearised background temperature distribution  $T_b(z)$  and (b) the laminar Kolmogorov velocity profile  $\mathbf{u}_L(y)$  driven by a monochromatic sinusoidal body force.

cal simplicity, we impose triply-periodic boundary conditions on the body force,  $\mathbf{F}$ , and the variables  $T'$  and  $\mathbf{u}$  such that  $(x, y, z) \in [0, L_x) \times [0, L_y) \times [0, L_z)$ . A suitable candidate for the applied force is a monochromatic sinusoidal forcing with spanwise wavenumber  $k_y = 1$  driving a horizontal Kolmogorov flow,

$$\mathbf{F} \propto \sin\left(\frac{2\pi y}{L_y}\right) \mathbf{e}_x. \quad (8.2)$$

This choice of forcing is computationally straightforward to implement and was selected following the work of Lucas et al. (2017), who studied horizontally-sheared stratified flows in the geophysical regime with  $Pr = 1$ . Monochromatic Kolmogorov forcing was also used by Balmforth and Young (2002) to study vertically-sheared stratified flows at high  $Pr$ , and by Garaud et al. (2015a) and Garaud and Kulenthirarajah (2016) for vertically-sheared stratified flows at low  $Pr$  (and in the low  $Pe$  limit). It has the advantage of being linearly unstable, in contrast with other setups such as the shearing box that only have finite amplitude instabilities. Figure 8.1 illustrates the basic laminar state in this idealised system.

As discussed in Chapter 7, astrophysical flows are not incompressible, however, under the Spiegel-Veronis-Boussinesq approximation (Spiegel and Veronis, 1960), the governing equations can be reduced to a form that is virtually equivalent to that used for geophysical systems. For our model setup, these are:

$$\frac{\partial \mathbf{u}}{\partial t} + \mathbf{u} \cdot \nabla \mathbf{u} + \frac{1}{\rho_0} \nabla p = \nu \nabla^2 \mathbf{u} + \alpha g T' \mathbf{e}_z + \chi \sin\left(\frac{2\pi y}{L_y}\right) \mathbf{e}_x, \quad (8.3)$$

$$\frac{\partial T'}{\partial t} + \mathbf{u} \cdot \nabla T' + w \left( \frac{dT_b}{dz} + \frac{g}{c_p} \right) = \kappa \nabla^2 T', \quad (8.4)$$

$$\nabla \cdot \mathbf{u} = 0, \quad (8.5)$$

where  $\nu$  is the kinematic viscosity,  $\kappa$  is the thermal diffusivity,  $\chi$  is the forcing amplitude,  $p$  is the pressure,  $c_p$  is the specific heat at constant pressure and gravity  $g$  acts in the negative  $z$ -direction. In this study, we specify that  $L_y = L_z$  while  $L_x$  may vary continuously such that the aspect ratio of the domain is given by  $\lambda = L_x/L_y$ . The case  $\lambda > 1$  corresponds to domains which are longer in the streamwise direction.

### 8.2.2 Non-dimensionalisation and model parameters

It is helpful to simplify equations (8.3)-(8.5) by non-dimensionalising the variables. In equilibrium, we anticipate a balance between the body force and fluid inertia such that  $\mathbf{u} \cdot \nabla \mathbf{u} \sim \chi \sin(2\pi y/L_y) \mathbf{e}_x$  in the streamwise direction. For a characteristic length scale  $L_y/2\pi$ , this gives a characteristic velocity scale  $\sqrt{\chi L_y/2\pi}$  and a characteristic time scale  $\sqrt{L_y/2\pi\chi}$ . Combined with the vertical temperature gradient scale,  $dT_b/dz + g/c_p$ , we choose to use the equivalent non-dimensionalisation as in Lucas et al. (2017) to give the following system of equations, in which all quantities are non-dimensional:

$$\frac{\partial \mathbf{u}}{\partial t} + \mathbf{u} \cdot \nabla \mathbf{u} + \nabla p = \frac{1}{Re} \nabla^2 \mathbf{u} + BT' \mathbf{e}_z + \sin(y) \mathbf{e}_x, \quad (8.6)$$

$$\frac{\partial T'}{\partial t} + \mathbf{u} \cdot \nabla T' + w = \frac{1}{RePr} \nabla^2 T', \quad (8.7)$$

$$\nabla \cdot \mathbf{u} = 0. \quad (8.8)$$

Consequently, there are three non-dimensional numbers, given by the Reynolds number,  $Re$ , the buoyancy parameter,  $B$ , and the Prandtl number,  $Pr$ , which determine the dynamics of the system:

$$Re := \frac{\sqrt{\chi}}{\nu} \left( \frac{L_y}{2\pi} \right)^{\frac{3}{2}}, \quad B := \frac{\alpha g (dT_b/dz + g/c_p) L_y}{2\pi\chi} = \frac{N_b^2 L_y}{2\pi\chi}, \quad Pr := \frac{\nu}{\kappa}. \quad (8.9)$$

Here,  $N_b$  is the dimensional buoyancy frequency defined in expression (7.15), which is now constant by construction. Note that the buoyancy parameter,  $B$ , is related to the Froude number,  $Fr$ , as

$$B = Fr^{-2}. \quad (8.10)$$

It is also convenient to introduce the Péclet number,  $Pe$ , which in this system is defined as

$$Pe := RePr = \frac{\sqrt{\chi}}{\kappa} \left( \frac{L_y}{2\pi} \right)^{\frac{3}{2}}. \quad (8.11)$$

Both sets of parameters,  $(Re, B, Pr)$  or  $(Re, B, Pe)$ , uniquely define the system and will be used interchangeably throughout this study. In all that follows, the domain is a cuboid such that  $(x, y, z) \in [0, 2\pi\lambda) \times [0, 2\pi) \times [0, 2\pi)$ , and variables  $p$ ,  $T'$  and  $\mathbf{u}$  have triply-periodic boundary conditions. This system, defined by equations (8.6), (8.7) and (8.8), will henceforth be referred to as the standard system of equations.

### 8.2.3 Low-Péclet number approximation

As discussed in Chapter 7, when the thermal diffusion timescale is much shorter than the advective timescale, a *quasi-static* regime is established where temperature fluctuations are slaved to the vertical velocity field. Motivated by astrophysical applications, we consider the standard set of equations (8.6)-(8.8) in the asymptotic limit of low Péclet number (LPN). This limit was studied by Spiegel (1962) and Thual (1992) in the context of thermal convection, and more recently by Lignières (1999) in the context of stably stratified flows. Lignières proposed that the standard equations can be approximated by a reduced set of equations called the *low-Péclet number* equations (LPN equations hereafter), in which the density

fluctuations are slaved to the vertical velocity field:

$$\frac{\partial \mathbf{u}}{\partial t} + \mathbf{u} \cdot \nabla \mathbf{u} + \nabla p = \frac{1}{Re} \nabla^2 \mathbf{u} + BT' \mathbf{e}_z + \sin(y) \mathbf{e}_x, \quad (8.12)$$

$$w - \frac{1}{Pe} \nabla^2 T' = 0, \quad (8.13)$$

$$\nabla \cdot \mathbf{u} = 0. \quad (8.14)$$

These can be derived by assuming a regular asymptotic expansion of  $T'$  in powers of the small parameter  $Pe$ , i.e.  $T' = T'_0 + T'_1 Pe + O(Pe^2)$ , and by assuming that the velocity field is of order unity. At lowest order ( $Pe^{-1}$ ), we get  $\nabla^2 T'_0 = 0$ , implying that  $T'_0 = 0$  is required to satisfy the boundary conditions, while at the next order ( $Pe^0$ ), the equations yield  $w = \nabla^2 T'_1 \approx Pe^{-1} \nabla^2 T'$  as required.

Noting that (8.13) can be re-written as  $T' = Pe \nabla^{-2} w$ , we derive the reduced set of LPN equations:

$$\frac{\partial \mathbf{u}}{\partial t} + \mathbf{u} \cdot \nabla \mathbf{u} + \nabla p = \frac{1}{Re} \nabla^2 \mathbf{u} + BPe \nabla^{-2} w \mathbf{e}_z + \sin(y) \mathbf{e}_x, \quad (8.15)$$

$$\nabla \cdot \mathbf{u} = 0. \quad (8.16)$$

These equations explicitly demonstrate that under the LPN approximation (and in contrast to the standard equations), there are only two non-dimensional parameters governing the flow dynamics, notably the Reynolds number,  $Re$ , and the product of the buoyancy parameter and the Péclet number,  $BPe = PeFr^{-2}$ . This combined parameter, which we consider to be a measure of the stratification, can take any value (even for small Péclet numbers) because  $B$  can be arbitrarily large, or equivalently  $Fr$  can be arbitrarily small, as the stratification becomes strong.

There are advantages to studying the LPN equations rather than the standard equations. For example, this reduced set of equations allows for the derivation of mathematical results such as an energy stability threshold that explicitly depends on  $BPe$  (see Garaud et al., 2015a). Throughout this study, we will discuss both systems of equations, verifying the validity of the LPN equations where possible.

### 8.3 Linear stability analysis of a horizontal shear flow

In this section, we carry out a linear stability analysis of both the standard set of equations and the reduced set of LPN equations, where we seek to demonstrate the instability properties in the LPN limit, in addition to verifying the validity of the LPN equations.

#### 8.3.1 Standard equations

With initial focus on the standard set of equations (8.6)-(8.8), we begin by considering the stability of a laminar flow to infinitesimal perturbations. The background flow  $\mathbf{u}_L(y)$ , which satisfies the equation  $Re^{-1} \nabla^2 \mathbf{u}_L + \sin(y) \mathbf{e}_x = 0$ , has amplitude  $Re$  and is given by the expression

$$\mathbf{u}_L(y) = Re \sin(y) \mathbf{e}_x. \quad (8.17)$$

Note that if one wishes to consider a basic state with generic amplitude  $aRe$  instead of  $Re$ , it is straightforward to apply a rescaling using the method described in Appendix E. For small perturbations  $\mathbf{u}'(x, y, z, t)$

away from this laminar flow, i.e. letting  $\mathbf{u} = \mathbf{u}_L(y) + \mathbf{u}'(x, y, z, t)$ , the linearised perturbation equations are

$$\frac{\partial \mathbf{u}'}{\partial t} + Re \cos(y) v' \mathbf{e}_x + Re \sin(y) \frac{\partial \mathbf{u}'}{\partial x} + \nabla p = \frac{1}{Re} \nabla^2 \mathbf{u}' + BT' \mathbf{e}_z, \quad (8.18)$$

$$\frac{\partial T'}{\partial t} + Re \sin(y) \frac{\partial T'}{\partial x} + w' = \frac{1}{RePr} \nabla^2 T', \quad (8.19)$$

$$\nabla \cdot \mathbf{u}' = 0. \quad (8.20)$$

In this set of partial differential equations, the coefficients are periodic in  $y$  but independent of  $x, z$  and  $t$ . Consequently, and in the conventional fashion, we consider normal mode disturbances of the form

$$q(x, y, z, t) = \tilde{q}(y) e^{ik_x x + ik_z z + \sigma t}, \quad (8.21)$$

where  $q \in (u', v', w', T', p)$ ,  $\sigma$  is the growth rate of the disturbance and  $k_x$  and  $k_z$  are the perturbation wavenumbers in the  $x$  and  $z$ -directions respectively. Note that the geometry of the model set-up requires that  $k_x \in \mathbb{R}$  and  $k_z \in \mathbb{Z}$ . The spanwise structures can be decomposed into their individual Fourier components, such that we seek periodic solutions for  $\tilde{q}(y)$  given by

$$\tilde{q}(y) = \sum_{k_y=-L}^L q_{k_y} e^{ik_y y}. \quad (8.22)$$

Substituting this ansatz into equations (8.18)-(8.20) and using the orthogonality property of complex exponentials, we obtain a  $5 \times (2L + 1) = (10L + 5)$  algebraic system of equations for the individual Fourier components  $u_{k_y}, v_{k_y}, w_{k_y}, T_{k_y}$  and  $p_{k_y}$  for  $k_y \in (-L, L)$ :

$$\frac{1}{2} Re k_x (u_{k_y+1} - u_{k_y-1}) - \frac{k_x^2 + k_y^2 + k_z^2}{Re} u_{k_y} - \frac{1}{2} Re (v_{k_y-1} + v_{k_y+1}) - ik_x p_{k_y} = \sigma u_{k_y}, \quad (8.23)$$

$$\frac{1}{2} Re k_x (v_{k_y+1} - v_{k_y-1}) - \frac{k_x^2 + k_y^2 + k_z^2}{Re} v_{k_y} - ik_y p_{k_y} = \sigma v_{k_y}, \quad (8.24)$$

$$\frac{1}{2} Re k_x (w_{k_y+1} - w_{k_y-1}) - \frac{k_x^2 + k_y^2 + k_z^2}{Re} w_{k_y} + BT_{k_y} - ik_z p_{k_y} = \sigma w_{k_y}, \quad (8.25)$$

$$\frac{1}{2} Re k_x (T_{k_y+1} - T_{k_y-1}) - w_{k_y} - \frac{k_x^2 + k_y^2 + k_z^2}{RePr} T_{k_y} = \sigma T_{k_y}, \quad (8.26)$$

$$k_x u_{k_y} + k_y v_{k_y} + k_z w_{k_y} = 0. \quad (8.27)$$

This system can be re-formulated as a generalised eigenvalue problem for the complex growth rates  $\sigma$ ,

$$\mathbf{A}(k_x, k_z, Re, B, Pr) \mathbf{X} = \sigma \mathbf{B} \mathbf{X}, \quad (8.28)$$

where  $\mathbf{X} = (u_{-L}, \dots, u_L, v_{-L}, \dots, v_L, w_{-L}, \dots, w_L, T_{-L}, \dots, T_L, p_{-L}, \dots, p_L)$ ,  $\mathbf{A}$  and  $\mathbf{B}$  are  $(10L + 5) \times (10L + 5)$  square matrices and  $\mathbf{B}_{i,j} = \{\delta_{ij}, i, j \leq (8L + 4); 0, \text{ otherwise}\}$ . Equation (8.28) has  $(10L + 5)$  eigenvalues  $\sigma$ . For perturbation wavenumbers  $k_x$  and  $k_z$  and system parameters  $Re, B$  and  $Pr$ , the eigenvalue with the largest real part determines the growth rate of the linear instability. The eigenvalue problem must be solved numerically, with  $L$  chosen such that convergence is achieved.

### 8.3.1.1 Comparison with previous results at $Pr = 1$

We first consider the geophysically-relevant case of  $Pr = 1$  for ease of comparison with previous work. Deloncle et al. (2007), Arobone and Sarkar (2012) and Park et al. (2020) each considered the linear stability of horizontal shear layers with somewhat different base flows, and Lucas et al. (2017) considered the linear stability of the specific horizontally-sheared Kolmogorov flow considered here, exclusively for  $Pr = 1$ . Letting  $B = 100$  in our system, we consider the linear stability of the basic state flow  $\mathbf{u}_L$  (defined in (8.17)) across a range of Reynolds numbers for both 2D ( $k_z = 0$ ) and 3D ( $k_z \neq 0$ ) perturbation modes.

Figure 8.2(a) shows the neutral stability curves ( $\sigma = 0$ ) for varying vertical wavenumbers  $k_z \in (0, \dots, 6)$  in the  $(Re, k_x)$  space, where our results are in agreement with Lucas et al. (2017). Stability ( $\sigma < 0$ ) is found to the left and above the curves whilst instability ( $\sigma > 0$ ) occurs to the right and below. The black curve illustrates the 2D ( $k_z = 0$ ) mode. This neutral stability curve intercepts the  $x$ -axis when  $Re = 2^{1/4} \approx 1.19$ , implying that the system is linearly stable when  $Re < 2^{1/4}$ . As we shall explain in Section 8.3.3, this is in agreement with Beaumont (1981) and Balmforth and Young (2002), once the correct rescaling is applied. For large  $Re$ , it asymptotes to  $k_x = 1$  but, in agreement with Lucas et al. (2017), always lies below this line, leading to the conclusion that domains such that  $\lambda = L_x/L_y \leq 1$  are linearly stable to the 2D mode.

The coloured curves show the neutral stability curves for the first six 3D modes ( $k_z \in (1, \dots, 6)$ ). The onset of instability in the 3D modes is found to occur for higher Reynolds numbers than the 2D mode, with the critical Reynolds number for instability of these 3D modes increasing monotonically with increasing  $k_z$ . For a range of  $Re \sim O(100)$  (corresponding to  $Pe \sim O(100)$ ), the 3D curves actually cross the line  $k_x = 1$  implying that these modes are unstable for domains where  $\lambda = 1$ , i.e. cubic domains.

Figures 8.2(b-c) further analyse the information in Figure 8.2(a) by computing, for each Reynolds number and  $k_z$ , the largest (positive) growth rate,  $\sigma_{max}$ , across all values of  $k_x$  and the value of  $k_x$  for which that maximum is achieved,  $k_{x,max}$ . We see that, as well as being the mode that becomes unstable first, the 2D mode is always the fastest growing one, a result of Squire's theorem (Squire, 1933). In addition, the ratio of the growth rate of the 2D mode to that of the 3D modes increases with  $Re$ . We therefore predict

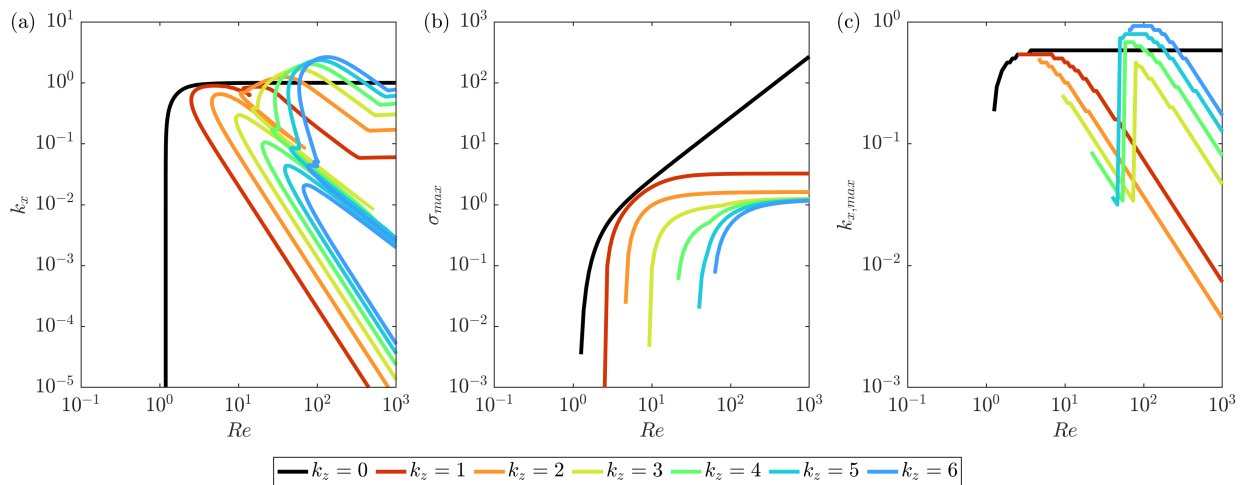


**Figure 8.2** (a) Neutral stability curves for a range of  $k_z$  wavenumbers as a function of Reynolds number and  $k_x$  wavenumber, with instability occurring to the right and below the curves. Variation with Reynolds number for a collection of  $k_z$  wavenumbers of: (b) the largest growth rate  $\sigma_{max}$  maximised across all horizontal wavenumbers  $k_x$ ; (c) the associated horizontal wavenumber  $k_{x,max}$ . The curves plotted include  $k_z = 0$  (black) and  $k_z = 1, 2, 3, 4, 5, 6$  (coloured) and the standard equations were used with  $B = 100$  and  $Pr = 1$  fixed (so  $Pe = Re$ ).

that the 2D mode would strongly influence the dynamics when it is unstable (i.e. for domain sizes such that  $\lambda > 1$ ). Finally, we note that the corresponding streamwise wavenumbers of the fastest growing 3D modes satisfy  $k_{x,max} \rightarrow 0$  in the limit  $Re \rightarrow \infty$ , while those of the fastest growing 2D mode remain constant.

### 8.3.1.2 Linear stability at low $Pr$

Astrophysical applications motivate an understanding of the effects of the stratification parameter,  $B$ , and the Prandtl number,  $Pr$ , on the linear stability of the basic state. Consequently, in Figures 8.3(a-c) we plot the neutral stability curves in exactly the same fashion as those in Figure 8.2(a), for three different Prandtl numbers:  $Pr = 0.1$  (first column),  $Pr = 0.01$  (second column) and  $Pr = 0.001$  (third column), keeping  $B = 100$  constant. Whilst the neutral stability curves for the 2D mode are identical, clear trends exist for the 3D modes. A reduction in the value of  $Pr$  shifts the critical Reynolds numbers for the onset of instability of the 3D modes towards higher values, thereby making these modes less unstable. This result is consistent with Arobone and Sarkar (2012) and Park et al. (2020), who investigated the stability of a diffusive, stratified, horizontally-sheared hyperbolic flow. We also note that the same trend is found by letting  $B \rightarrow 0$  and keeping  $Pr$  constant (not plotted).

Thus, the limits  $B \rightarrow 0$  (at fixed  $Pr$ ) and  $Pr \rightarrow 0$  (at fixed  $B$ ) have the same effect: the 3D modes of instability are suppressed while the 2D mode remains unstable. The explanation for this emerges from consideration of equation (8.7). As the Prandtl number tends to zero (keeping the Reynolds number finite),

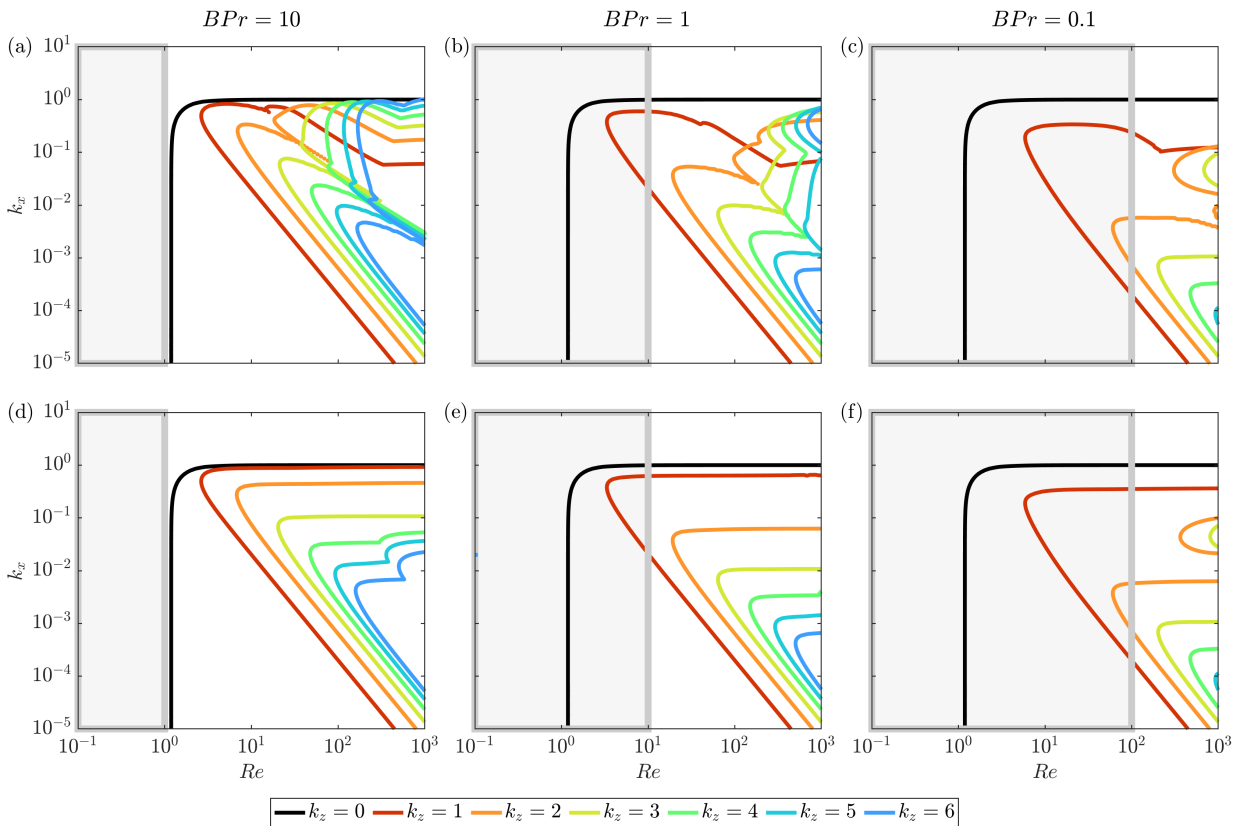


**Figure 8.3** A comparison of linear stability analysis results between the standard equations (top row) and the LPN equations (bottom row). Neutral stability curves for a range of  $k_z$  wavenumbers ( $k_z = 0$  (black) and  $k_z = 1, 2, 3, 4, 5, 6$  (coloured)) are plotted as a function of Reynolds number and  $k_x$ . Instability occurs to the right and below the curves. Parameter values used are (a)  $B = 100$ ,  $Pr = 0.1$ , (b)  $B = 100$ ,  $Pr = 0.01$ , (c)  $B = 100$ ,  $Pr = 0.001$ , (d)  $BPr = 10$ , (e)  $BPr = 1$ , (f)  $BPr = 0.1$ . Grey rectangles indicate regions where  $Pe \leq 0.1$ .

the Péclet number becomes small and so the buoyancy diffusion becomes important. In this case, a parcel of fluid that is advected into surrounding fluid of a different density will adjust very rapidly to its surroundings, thereby reducing the buoyancy force and so approximating an unstratified system. However, it is important to note that another distinguished limit exists in which  $B \rightarrow \infty$  and  $Pr \rightarrow 0$ , while the product  $BPr$  remains finite. This limit is relevant to stellar interiors, and behaves quite differently from the case where  $B$  is fixed while  $Pr \rightarrow 0$ , as we now demonstrate.

### 8.3.2 Low-Péclet number equations

We now examine the linear stability of the LPN equations, given by (8.15) and (8.16). Following the same steps as for the standard equations, this time we find ourselves working with a reduced set of four equations rather than five. Thus, we obtain a  $4 \times (2L + 1) = (8L + 4)$  algebraic system of equations for the individual Fourier components  $u_{k_y}$ ,  $v_{k_y}$ ,  $w_{k_y}$  and  $p_{k_y}$  for  $k_y \in (-L, L)$ :

$$\frac{1}{2}Rek_x(u_{k_y+1} - u_{k_y-1}) - \frac{k_x^2 + k_y^2 + k_z^2}{Re}u_{k_y} - \frac{1}{2}Re(v_{k_y-1} + v_{k_y+1}) - ik_x p_{k_y} = \sigma u_{k_y}, \quad (8.29)$$

$$\frac{1}{2}Rek_x(v_{k_y+1} - v_{k_y-1}) - \frac{k_x^2 + k_y^2 + k_z^2}{Re}v_{k_y} - ik_y p_{k_y} = \sigma v_{k_y}, \quad (8.30)$$

$$\frac{1}{2}Rek_x(w_{k_y+1} - w_{k_y-1}) - \frac{k_x^2 + k_y^2 + k_z^2}{Re}w_{k_y} - \frac{BPe}{k_x^2 + k_z^2}w_{k_y} - ik_z p_{k_y} = \sigma w_{k_y}, \quad (8.31)$$

$$k_x u_{k_y} + k_y v_{k_y} + k_z w_{k_y} = 0. \quad (8.32)$$

As before, this can be re-formulated as a generalised eigenvalue problem for the complex growth rates  $\sigma$ ,

$$\mathbf{A}(k_x, k_z, Re, BPe)\mathbf{X} = \sigma\mathbf{B}\mathbf{X}, \quad (8.33)$$

where  $\mathbf{X} = (u_{-L}, \dots, u_L, v_{-L}, \dots, v_L, w_{-L}, \dots, w_L, p_{-L}, \dots, p_L)$ ,  $\mathbf{A}$  and  $\mathbf{B}$  are  $(8L + 4) \times (8L + 4)$  square matrices and  $\mathbf{B}_{i,j} = \{\delta_{ij}, i, j \leq (6L + 3); 0, \text{ otherwise}\}$ . We follow the same procedure as before, solving the eigenvalue problem numerically with  $L$  chosen such that convergence is achieved.

In order to test the validity of the LPN equations, we first compare the results of the linear stability analysis in the LPN limit to that obtained using the standard equations. Figure 8.3 illustrates this comparison. The top row (as already discussed) shows the neutral stability curves from the standard equations and the bottom row shows the equivalent results from the LPN equations. The value of  $BPr = BPe/Re$  in the bottom row decreases from left to right by two orders of magnitude, in line with reductions in the value of  $BPe$  at fixed  $Re$  in the standard equations in the top row. As demonstrated in Section 8.2.3, the LPN equations are asymptotically correct in the limit where  $Pe \rightarrow 0$ . Figure 8.3 shows that they remain valid up to  $Pe \approx 0.1$  (i.e. within the regions shown in grey). Outside of these regions, increasingly large differences emerge, especially as  $Pe$  increases above one. In particular, the neutral stability curves for the 3D modes never cross the line  $k_x = 1$  in the LPN equations, suggesting that horizontal shear instabilities do not arise for cubic domains when the LPN approximation is used.

The LPN system of equations depend on the combined parameter  $BPr = BPe/Re$ , which can be seen by removing the dependence on the independent parameter,  $Re$ , from  $BPe$ . In the astrophysically-relevant limit of strong stratification ( $B \rightarrow \infty$ ) and strong thermal diffusion ( $Pr \rightarrow 0$ ), this parameter remains finite

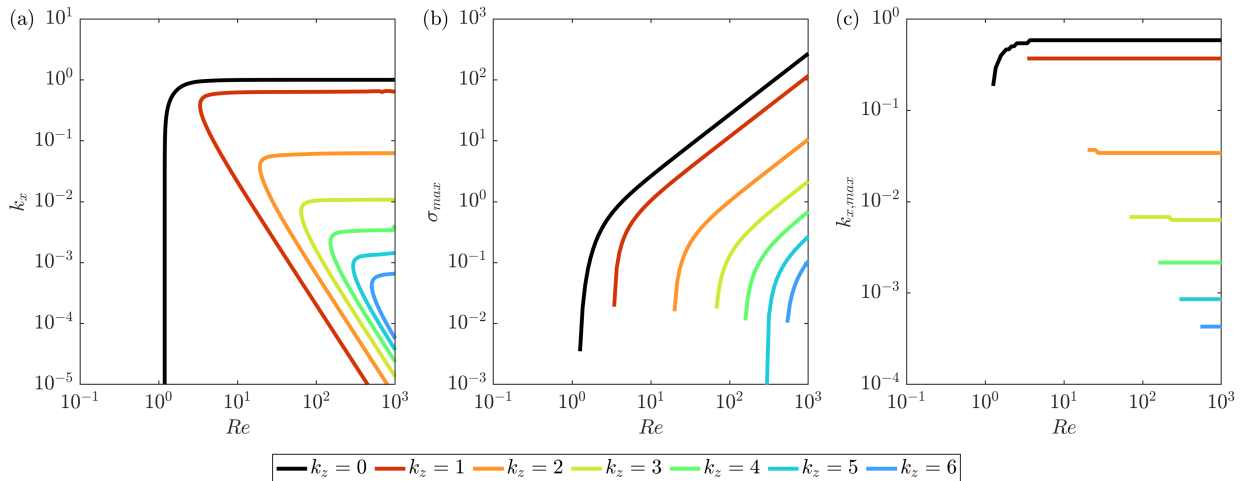


**Figure 8.4** (a) Neutral stability curves for a range of  $k_z$  wavenumbers as a function of  $Re$  and  $k_x$ , with instability occurring to the right and below the curves. This time we used the LPN equations, with  $BPr = 1$  fixed. Variation with Reynolds number for a collection of  $k_z$  wavenumbers of: (b) the largest growth rate  $\sigma_{max}$  maximised across all horizontal wavenumbers  $k_x$ ; (c) the associated horizontal wavenumber  $k_{x,max}$ . The curves plotted include  $k_z = 0$  (black) and  $k_z = 1, 2, 3, 4, 5, 6$  (coloured).

and is not necessarily small. As can be seen in Figure 8.3, the 3D modes remain unstable in this limit, in agreement with the results from the standard system of equations, suggesting that a potential route to turbulence via horizontal shear instabilities exists for arbitrarily large stratification.

In order to see this more clearly, we now focus on the case when  $BPr = 1$ . By way of comparison with the standard equations at  $Pr = 1$ , Figures 8.4(b-c) show, for each Reynolds number and  $k_z$  wavenumber, the largest (positive) growth rate,  $\sigma_{max}$ , across all values of  $k_x$  and the value of  $k_x$  for which that maximum is achieved,  $k_{x,max}$ . As before, we observe that the 2D mode is both the first mode to become unstable, and is always the fastest growing mode. There are, however, two significant differences between high and low Prandtl number dynamics. Firstly, in the LPN limit, Figure 8.4(b) shows that the growth rates of the fastest growing 3D modes increase in line with those of the fastest growing 2D mode. Secondly, the corresponding values of  $k_{x,max}$  remain constant as  $Re \rightarrow \infty$ . Consequently, the 3D modes remain important relative to the 2D mode and we therefore predict that, in contrast to the case when  $Pr = 1$ , both the 2D and 3D modes would strongly influence the dynamics in this limit. These results have important consequences for the nonlinear dynamics, as we shall discuss in Section 8.4.

### 8.3.3 Critical Reynolds number for the onset of linear instability

To conclude this section, we remark that an important finding, determined numerically across a broad spectrum of parameters, is the fact that the critical Reynolds number,  $Re_c$ , for the onset of linear instability, as given by the 2D mode ( $k_z = 0$ ), is independent of both the stratification and the Prandtl number, being fixed at  $Re_c = 2^{1/4}$ . This result holds for both the standard equations and the LPN equations and differs quite substantially from that obtained in Garaud et al. (2015a) for the case of a vertically-orientated shear, where stratification was found to be able to stabilise the system.

To see why this is the case, we observe in equations (8.23)-(8.27) (or the equivalent LPN equations (8.29)-(8.32)) that setting  $k_z = 0$  reduces the problem to the study of equations (8.23), (8.24) and (8.27) (or equivalently (8.29), (8.30) and (8.32)). This reduced problem is well studied (Balmforth and Young, 2002; Beaumont, 1981), being the linear stability of an unstratified ( $B = 0$ ) flow. The critical Reynolds

number for instability around a basic state of  $\mathbf{u}_L(y) = \sin(y)\mathbf{e}_x$  has been shown to be  $Re_c = \sqrt{2}$  (Beaumont, 1981). As detailed in Appendix E, a simple transformation given by relations (E.8) (for  $a = Re^{-1}$ ) gives the corresponding critical Reynolds number for 2D modes in this study to be  $2^{1/4}$ , which corresponds to the result obtained numerically. Consequently, we note that horizontally-sheared Kolmogorov flows with  $Re > 2^{1/4}$  are always unstable, irrespective of the stratification, and thus form a convenient basis from which to study the subsequent nonlinear evolution of stratified, low-Péclet number flows.

## 8.4 Direct numerical simulations

We now present the results from a series of direct numerical simulations (DNS) of horizontal shear flows at low Péclet number following the model setup and equations described in Section 8.2. As we shall demonstrate, the system presents a rich ecosystem of instabilities that feed off each other, leading to a number of distinct dynamical regimes that will be further characterised in Section 8.5.

### 8.4.1 Numerical formulation

The simulations are performed using the PADDI code that was first introduced by Traxler et al. (2011) and Stellmach et al. (2011) to study double-diffusive fingering. The code has since then been modified to study many different kinds of instabilities, including body-forced vertical shear instabilities, using both the standard equations and the LPN approximation (Gagnier and Garaud, 2018; Garaud et al., 2015a; Garaud and Kulenthirarajah, 2016; Kulenthirarajah and Garaud, 2018). PADDI is a triply-periodic pseudo-spectral algorithm that uses pencil-based Fast Fourier Transforms, and third order Backward-Differentiation Adams-Bashforth adaptive time-stepping (Peyret, 2002) in which diffusive terms are treated implicitly while all other terms are treated explicitly. The velocity field is made divergence-free at every timestep by solving the relevant Poisson equation for the pressure. Two versions of the code exist: one that solves the standard equations (8.6)-(8.8), and one that solves the LPN equations (8.15)-(8.16).

Based on the linear stability analysis performed in Section 8.3, where instability in the low Péclet number limit required  $\gamma > 1$ , we have selected a domain size such that  $L_y = L_z = 2\pi$  and  $L_x = 4\pi$ . This allows for the natural development of a single 2D mode of instability (for which  $k_x = 0.5$ ), without being computationally prohibitive at high Reynolds number (see below). Justification comes from a comparison of simulation outcomes for different domain lengths that is presented in Cope (2019) (but only for  $Re = 50$ ), for which only two dynamical regimes were found to exist depending on whether  $\gamma = 1$  or  $\gamma > 1$ .

Tables 8.1 and 8.2 present the data from all the simulations that have been performed with this model set-up, using equations (8.6)-(8.8) and (8.15)-(8.16), respectively. To save on computational time, only one of the simulations at each Reynolds number was initiated from the original initial conditions (i.e.  $\mathbf{u} = \sin(y)\mathbf{e}_x$  plus some small amplitude white noise). All of the others were restarted from the end point of a simulation at nearby values of  $Pe$  or  $B$ . In all cases, we have run the simulations until they reach a statistically stationary state, except where explicitly mentioned. Note that for very large values of  $B$  or very small values of  $Pr$ , it was necessary to decrease the value of the maximum allowable timestep substantially. This is because the system of equations becomes increasingly stiff and is otherwise susceptible to the development of spurious elevator modes (i.e. modes that are invariant in the vertical direction). To save on computational time, we only ran simulations using the standard equations in that limit.

$Re$	$Pe$	$B$	$Re_\lambda$	$l_z \pm \delta l_z$	$w_{rms} \pm \delta w_{rms}$	$T'_{rms} \pm \delta T'_{rms}$	$\eta \pm \delta \eta$
600	0.1	6,000	280	$0.25 \pm 0.02$	$0.24 \pm 0.03$	$(3.5 \pm 0.3) \times 10^{-4}$	$0.36 \pm 0.03$
600	0.1	12,000	359	$0.19 \pm 0.02$	$0.21 \pm 0.03$	$(2.3 \pm 0.3) \times 10^{-4}$	$0.31 \pm 0.02$
600	0.1	100,000	465	$0.11 \pm 0.005$	$0.038 \pm 0.003$	$(4.0 \pm 0.4) \times 10^{-5}$	$0.18 \pm 0.02$
300	0.1	1	173	$1.88 \pm 0.29$	$0.91 \pm 0.10$	$(3.1 \pm 0.8) \times 10^{-2}$	$0.029 \pm 0.007$
300	0.1	100	171	$0.99 \pm 0.08$	$0.56 \pm 0.03$	$(6.9 \pm 0.9) \times 10^{-3}$	$0.43 \pm 0.05$
300	0.1	1,000	173	$0.45 \pm 0.02$	$0.34 \pm 0.03$	$(1.4 \pm 0.1) \times 10^{-3}$	$0.42 \pm 0.03$
300	0.1	3,000	227	$0.32 \pm 0.05$	$0.25 \pm 0.03$	$(6.5 \pm 0.6) \times 10^{-4}$	$0.35 \pm 0.02$
300	0.1	6,000	300	$0.24 \pm 0.01$	$0.17 \pm 0.03$	$(4.1 \pm 0.6) \times 10^{-4}$	$0.30 \pm 0.03$
300	0.1	10,000	319	$0.19 \pm 0.02$	$0.11 \pm 0.04$	$(2.7 \pm 0.7) \times 10^{-4}$	$0.23 \pm 0.04$
300	0.1	30,000	281	$0.15 \pm 0.01$	$0.05 \pm 0.004$	$(9.7 \pm 0.8) \times 10^{-5}$	$0.18 \pm 0.02$
300	0.1	100,000	265	$0.13 \pm 0.01$	$0.03 \pm 0.003$	$(4.2 \pm 0.4) \times 10^{-5}$	$0.16 \pm 0.02$
300	0.1	300,000	219	$0.11 \pm 0.000$	$0.02 \pm 0.002$	$(2.1 \pm 0.2) \times 10^{-5}$	$0.15 \pm 0.01$
100	0.01	1	102	$1.94 \pm 0.27$	$0.91 \pm 0.11$	$(5.3 \pm 2.2) \times 10^{-3}$	$0.004 \pm 0.002$
100	0.01	10	98	$1.94 \pm 0.34$	$0.89 \pm 0.09$	$(3.3 \pm 0.9) \times 10^{-3}$	$0.031 \pm 0.007$
100	0.01	100	91	$1.62 \pm 0.14$	$0.83 \pm 0.09$	$(2.0 \pm 0.3) \times 10^{-3}$	$0.18 \pm 0.04$
100	0.1	100	93	$0.96 \pm 0.07$	$0.49 \pm 0.06$	$(7.5 \pm 1.0) \times 10^{-3}$	$0.45 \pm 0.04$
100	0.1	1,000	201	$0.39 \pm 0.03$	$0.17 \pm 0.03$	$(1.4 \pm 0.2) \times 10^{-3}$	$0.26 \pm 0.04$
100	0.1	3,000	161	$0.28 \pm 0.02$	$0.09 \pm 0.01$	$(5.4 \pm 0.8) \times 10^{-4}$	$0.20 \pm 0.03$
100	0.1	10,000	172	$0.22 \pm 0.02$	$0.06 \pm 0.01$	$(2.2 \pm 0.5) \times 10^{-4}$	$0.15 \pm 0.03$
100	0.1	100,000	112	$0.16 \pm 0.004$	$0.02 \pm 0.001$	$(4.4 \pm 0.3) \times 10^{-5}$	$0.105 \pm 0.006$
100	1	100	152	$0.42 \pm 0.03$	$0.20 \pm 0.035$	$(1.6 \pm 0.3) \times 10^{-2}$	$0.29 \pm 0.04$
100	1	300	165	$0.28 \pm 0.02$	$0.08 \pm 0.011$	$(5.2 \pm 0.8) \times 10^{-3}$	$0.19 \pm 0.03$
100	1	500	151	$0.26 \pm 0.01$	$0.06 \pm 0.006$	$(3.4 \pm 0.4) \times 10^{-3}$	$0.17 \pm 0.02$
100	1	1,000	140	$0.23 \pm 0.000$	$0.05 \pm 0.005$	$(2.2 \pm 0.3) \times 10^{-3}$	$0.17 \pm 0.02$
100	1	10,000	117	$0.18 \pm 0.02$	$0.015 \pm 0.001$	$(4.5 \pm 0.5) \times 10^{-4}$	$0.11 \pm 0.01$
100	1	30,000	245	$0.19 \pm 0.02$	$0.007 \pm 0.002$	$(2.7 \pm 0.7) \times 10^{-4}$	$0.09 \pm 0.03$
100	1	50,000	362	$0.20 \pm 0.03$	$0.005 \pm 0.002$	$(1.9 \pm 0.6) \times 10^{-4}$	$0.08 \pm 0.04$
100	1	100,000	437	$0.21 \pm 0.02$	$0.003 \pm 0.001$	$(1.2 \pm 0.4) \times 10^{-4}$	$0.05 \pm 0.02$
100	1	1,000,000	554	$0.30 \pm 0.04$	$0.0002 \pm 0.00004$	$(1.2 \pm 0.2) \times 10^{-5}$	$0.005 \pm 0.002$
50	0.1	0.3	68	$2.05 \pm 0.30$	$0.85 \pm 0.11$	$(4.5 \pm 1.8) \times 10^{-2}$	$0.013 \pm 0.004$
50	0.1	1	68	$2.02 \pm 0.37$	$0.82 \pm 0.09$	$(3.6 \pm 0.9) \times 10^{-2}$	$0.04 \pm 0.008$
50	0.1	10	63	$1.59 \pm 0.17$	$0.71 \pm 0.09$	$(2.0 \pm 0.4) \times 10^{-2}$	$0.19 \pm 0.03$
50	0.1	30	64	$1.28 \pm 0.13$	$0.55 \pm 0.06$	$(1.3 \pm 0.2) \times 10^{-2}$	$0.32 \pm 0.04$
50	0.1	100	67	$0.89 \pm 0.07$	$0.39 \pm 0.05$	$(7.2 \pm 1.2) \times 10^{-3}$	$0.33 \pm 0.04$
50	0.1	300	102	$0.57 \pm 0.05$	$0.24 \pm 0.04$	$(3.3 \pm 0.7) \times 10^{-3}$	$0.21 \pm 0.04$
50	0.1	1,000	92	$0.38 \pm 0.03$	$0.11 \pm 0.02$	$(1.2 \pm 0.2) \times 10^{-3}$	$0.15 \pm 0.02$
50	0.1	3,000	95	$0.29 \pm 0.03$	$0.08 \pm 0.02$	$(5.2 \pm 1.2) \times 10^{-4}$	$0.13 \pm 0.03$
50	0.1	10,000	81	$0.28 \pm 0.03$	$0.04 \pm 0.006$	$(2.8 \pm 0.5) \times 10^{-4}$	$0.17 \pm 0.04$
50	0.1	30,000	122	$0.28 \pm 0.03$	$0.016 \pm 0.002$	$(1.1 \pm 0.3) \times 10^{-4}$	$0.09 \pm 0.03$
50	0.1	100,000	344	$0.26 \pm 0.000$	$0.007 \pm 0.001$	$(4.7 \pm 0.7) \times 10^{-5}$	$0.05 \pm 0.01$
50	1	3	63	$1.39 \pm 0.16$	$0.60 \pm 0.06$	$(1.3 \pm 0.2) \times 10^{-1}$	$0.32 \pm 0.05$
50	1	10	70	$1.03 \pm 0.1$	$0.43 \pm 0.05$	$(7.8 \pm 1.2) \times 10^{-2}$	$0.34 \pm 0.03$
50	1	30	97	$0.65 \pm 0.08$	$0.27 \pm 0.05$	$(3.7 \pm 0.8) \times 10^{-2}$	$0.24 \pm 0.04$
50	1	100	90	$0.38 \pm 0.03$	$0.12 \pm 0.02$	$(1.2 \pm 0.2) \times 10^{-2}$	$0.15 \pm 0.03$
50	1	300	97	$0.29 \pm 0.04$	$0.07 \pm 0.02$	$(5.2 \pm 1.3) \times 10^{-3}$	$0.13 \pm 0.03$
50	1	1,000	68	$0.27 \pm 0.03$	$0.04 \pm 0.003$	$(2.5 \pm 0.4) \times 10^{-3}$	$0.14 \pm 0.02$
50	1	3,000	99	$0.28 \pm 0.03$	$0.02 \pm 0.003$	$(1.2 \pm 0.3) \times 10^{-3}$	$0.10 \pm 0.02$
50	1	100,000	474	$0.62 \pm 0.4$	$0.0008 \pm 0.0004$	$(7.0 \pm 2.9) \times 10^{-5}$	$0.006 \pm 0.003$

**Table 8.1** Summary of all the data from the DNSs run using the standard equations, with parameters  $Re$ ,  $Pe$  and  $B$ .

$Re$	$BPe$	$Re_\lambda$	$l_z \pm \delta l_z$	$w_{rms} \pm \delta w_{rms}$	$\eta \pm \delta \eta$
600	1	236	$1.451 \pm 0.184$	$0.814 \pm 0.084$	$0.16 \pm 0.04$
600	10	246	$0.962 \pm 0.074$	$0.566 \pm 0.045$	$0.38 \pm 0.07$
600	40	276	$0.613 \pm 0.028$	$0.485 \pm 0.041$	$0.37 \pm 0.05$
600	100	266	$0.455 \pm 0.029$	$0.379 \pm 0.037$	$0.40 \pm 0.05$
600	300	281	$0.319 \pm 0.012$	$0.297 \pm 0.038$	$0.38 \pm 0.04$
600	600	383	$0.254 \pm 0.016$	$0.249 \pm 0.041$	$0.35 \pm 0.03$
300	1	166	$1.609 \pm 0.191$	$0.864 \pm 0.104$	$0.17 \pm 0.04$
300	10	167	$0.992 \pm 0.093$	$0.609 \pm 0.042$	$0.38 \pm 0.04$
300	40	202	$0.619 \pm 0.028$	$0.457 \pm 0.036$	$0.41 \pm 0.04$
300	100	262	$0.458 \pm 0.020$	$0.378 \pm 0.048$	$0.40 \pm 0.03$
300	300	427	$0.312 \pm 0.015$	$0.256 \pm 0.030$	$0.36 \pm 0.02$
300	600	182	$0.218 \pm 0.000$	$0.122 \pm 0.005$	$0.40 \pm 0.02$
100	1	98	$1.731 \pm 0.376$	$0.771 \pm 0.059$	$0.18 \pm 0.04$
100	10	96	$0.933 \pm 0.064$	$0.478 \pm 0.036$	$0.43 \pm 0.04$
100	100	184	$0.411 \pm 0.029$	$0.198 \pm 0.035$	$0.29 \pm 0.04$
100	300	87	$0.309 \pm 0.008$	$0.096 \pm 0.007$	$0.26 \pm 0.03$
100	600	87	$0.255 \pm 0.011$	$0.063 \pm 0.006$	$0.21 \pm 0.03$

**Table 8.2** Summary of all the data from the DNSs run using the LPN equations, with parameters  $Re$  and  $BPe$ .

The number of Fourier modes used in each direction (after dealiasing) depended on the Reynolds number  $Re$  selected. In terms of equivalent grid points, the resolution used was  $192 \times 96 \times 96$  ( $Re = 50$ ),  $384 \times 192 \times 192$  ( $Re = 100$ ),  $576 \times 288 \times 288$  ( $Re = 300$ ) and  $768 \times 384 \times 384$  ( $Re = 600$ ), regardless of the values of  $B$  and  $Pe$ . As a simple check of the suitability of these choices, we have verified that the product of the maximum wavenumber and the Kolmogorov scale,  $L_v$ , was always greater than one (it was about 1.1 for the  $Re = 600$  simulations, and increased with decreasing  $Re$ ).

#### 8.4.2 Typical simulations: early phase

We begin our analysis of the simulations by considering the early phases of development of the horizontal shear instabilities in two typical simulations at moderately large Reynolds number ( $Re = 300$ ), strong stratification ( $B = 30,000$  and  $300,000$ , respectively) and relatively low Péclet number ( $Pe = 0.1$ ). Both simulations were initialised with  $\mathbf{u} = \sin(y)\mathbf{e}_x$  plus small amplitude white noise, therefore the linear stability analysis in Section 8.3 can be extended to depend on the amplitude of  $u(y)$  by applying the rescaling described in Appendix E. Figures 8.5(a) and 8.5(d) show the root mean square (r.m.s.) values of the streamwise ( $u_{rms}$ ), spanwise ( $v_{rms}$ ) and vertical ( $w_{rms}$ ) velocities for each simulation, computed at each instant in time as

$$q_{rms}(t) = \langle q^2 \rangle^{1/2}, \quad (8.34)$$

where the angular brackets denote a volume average over the domain such that

$$\langle q \rangle = \frac{1}{L_x L_y L_z} \int q(x, y, z, t) dx dy dz. \quad (8.35)$$

For both values of  $B$ , we clearly see the growth of the streamwise flow due to the forcing. Spanwise and vertical fluid motions at first decay, until the onset of the 2D mode of instability, whereby  $v_{rms}$  begins to

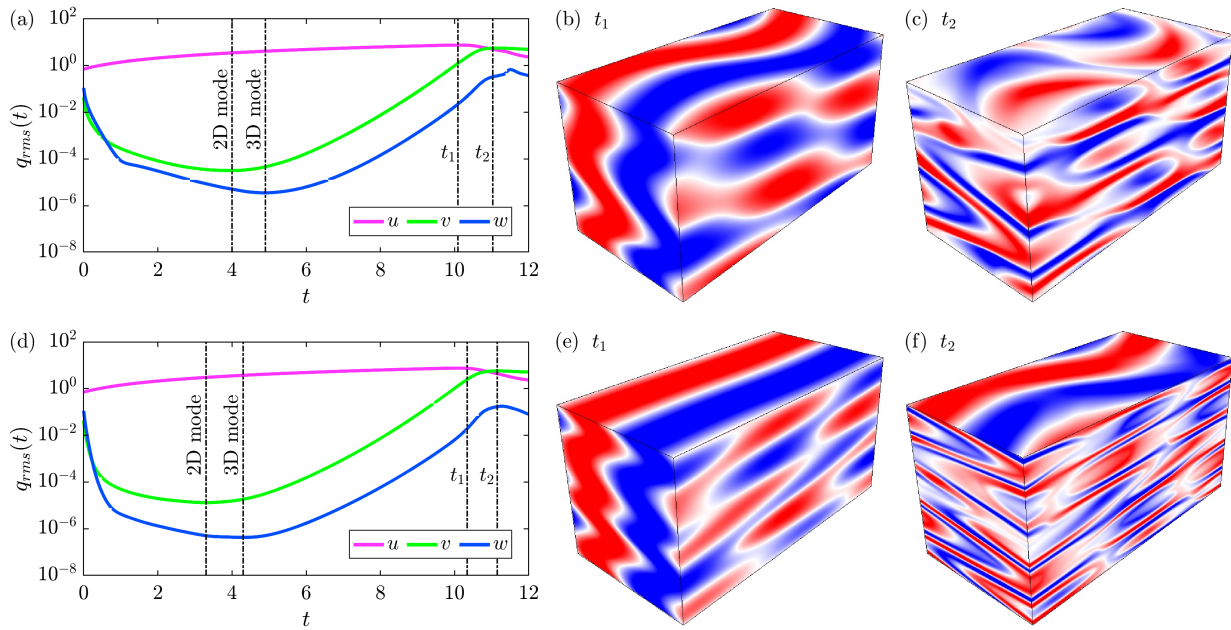


**Figure 8.5** (a) Time evolution of the r.m.s. velocities in a simulation with  $Re = 300$ ,  $Pe = 0.1$  and  $B = 30,000$ . The onset of the 2D modes ( $k_z = 0$ ) and 3D modes ( $k_z \neq 0$ ) of instability are indicated. (b) and (c): Snapshots of the streamwise velocity at times  $t_1$  and  $t_2$  for the same simulation as panel (a). (d) As in (a), except with  $B = 300,000$ . (e) and (f): Snapshots of the streamwise velocity at times  $t_1$  and  $t_2$  for the same simulation as in panel (d). We draw attention to the change in the vertical scale as  $B$  increases.

grow while  $w_{rms}$  continues to decay. This is rapidly followed by the 3D mode of instability, for which  $w_{rms}$  finally also begins to grow.

Snapshots of the streamwise velocity fields near the saturation of these instabilities are presented in Figures 8.5(b-c) and 8.5(e-f). In both cases, the snapshot at time  $t_1$  illustrates the early development of the 2D and 3D modes of instability. The 2D mode causes a meandering of the background flow, and the 3D mode causes a vertical modulation of the position of the meanders. We also see that the 3D mode has a substantially smaller vertical scale for larger  $B$ . The snapshots at time  $t_2$  show how these instabilities further evolve with time, where we observe that the meanders and their vertical modulations both grow in amplitude, leading to the development of substantial vertical shear of the streamwise flow. Whilst similar early-time dynamics are observed at all parameter values (assuming the 2D mode is unstable), the various regimes that emerge beyond that depend on the values of  $Re$ ,  $B$  and  $Pe$ , as we now proceed to describe.

### 8.4.3 Typical simulations: nonlinear saturation

The nonlinear saturation of this body-forced horizontal shear flow depends crucially on the selected value of the stratification parameter,  $B$ . This is illustrated in Figure 8.6 using snapshots of the streamwise velocity,  $u$ , vertical velocity,  $w$ , and local viscous dissipation rate,  $Re^{-1}|\nabla\mathbf{u}|^2$ , taken during the statistically stationary state after equilibration. In all but the last row,  $Re = 300$ , and  $Pe = 0.1$ , while for the last row,  $Re = 50$ .

For very large values of  $B$  (bottom row in Figure 8.6), the vertical scale of the 3D mode of instability is relatively small. Even though substantial shear develops between successive meanders of the streamwise jets, this shear is too small to overcome the stabilising effect of viscosity, and remains stable. The resulting flow takes the form of thin vertical layers, crucially in the *velocity* field, each of which presents a meandering jet-like structure with its own distinct phase. These jets are weakly coupled in the vertical direction through

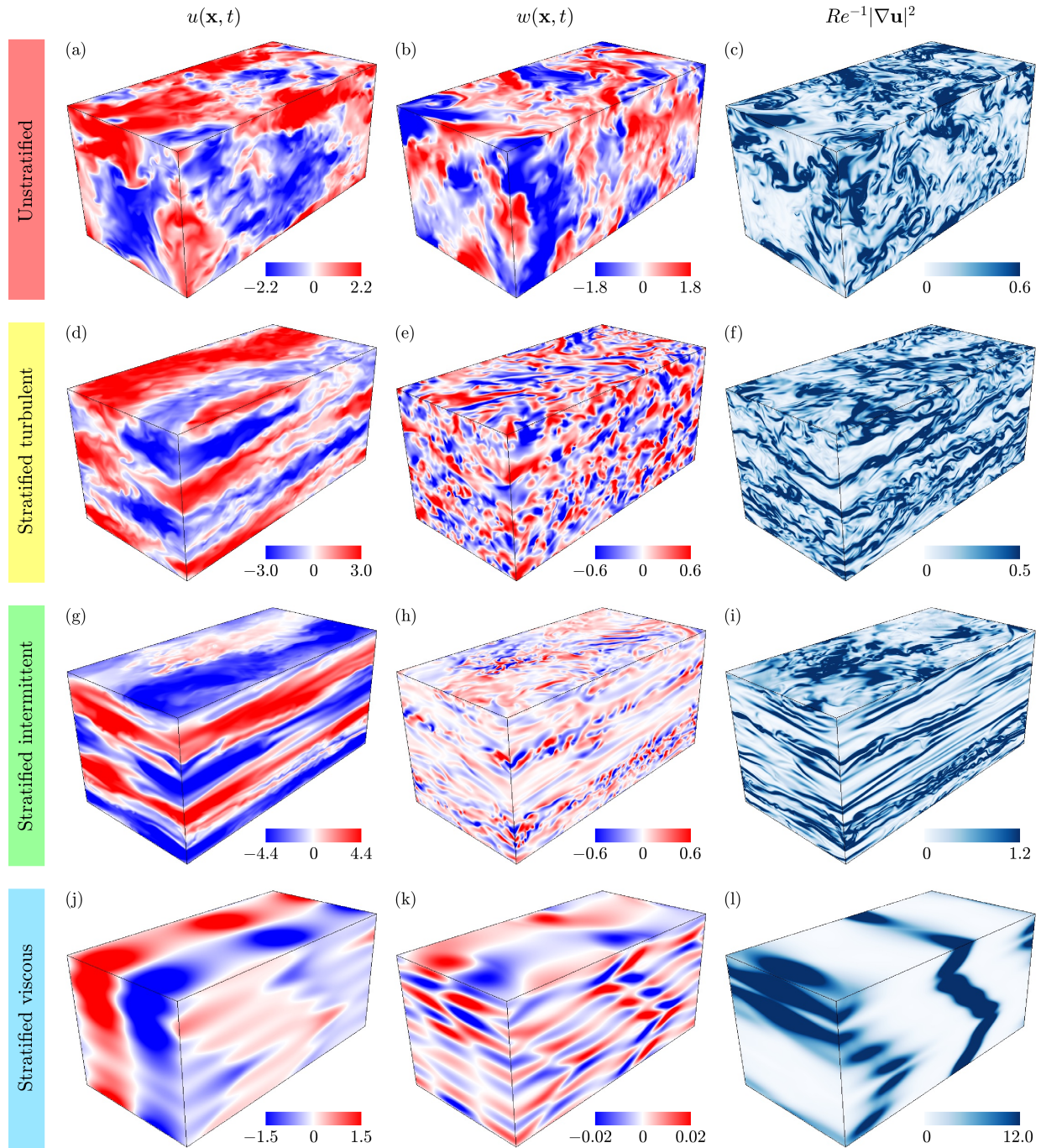


**Figure 8.6** Snapshots of the streamwise velocity (left), vertical velocity (centre) and local viscous dissipation rate (right) during the statistically stationary states of direct numerical simulations with  $Pe = 0.1$  and: (a-c)  $Re = 300$ ,  $B = 1$ ; (d-f)  $Re = 300$ ,  $B = 100$ ; (g-i)  $Re = 300$ ,  $B = 10,000$ ; (j-l)  $Re = 50$ ,  $B = 100,000$ . Each of these examples are characteristic of a particular dynamical regime, listed on the left-hand side.

viscosity. The vertical velocity field is small but non-zero, however, and is presumably generated by the weak horizontal divergence of the flow within each jet.

As  $B$  decreases (i.e. moving up in Figure 8.6), the reduced stratification now allows for the intermittent development of secondary vertical shear instabilities between the meanders associated with the layers, with correspondingly larger vertical velocities in these regions. These spatially localised overturns (i.e. turbulent regions) can be seen in Figures 8.6(g-i), where we note that they become more numerous and more frequent

as  $B$  continues to decrease. The local viscous dissipation rate is clearly enhanced in the turbulent regions compared with the laminar regions.

For intermediate values of  $B$  (see Figures 8.6(d-f)), the flow becomes fully turbulent. The vertical scale of the eddies, however, remains relatively small, which is consistent with stratification playing a role in shaping the dynamics of the turbulence. In this regime, the meandering streamwise jets are still clearly visible in Figure 8.6(d). These are accompanied by approximately isotropic turbulent eddies which are associated with small scales in both the horizontal and vertical directions, as shown in the vertical velocity field and the dissipation rate snapshots.

Finally, for low values of  $B$ , the scale of the eddies is now commensurate with the size of the domain, and the turbulence is unaffected by stratification. In fact, this system bears strong similarities with the one obtained in weakly-stratified vertically-sheared flows (see Garaud and Kulenthirarajah, 2016), except for the horizontally-averaged mean flow (which varies with  $y$  in our case instead of  $z$  for vertical shears).

These observations therefore suggest the existence of at least four distinct LPN dynamical regimes: unstratified turbulence for very low  $B$ ; stratified turbulence for intermediate values of  $B$ ; intermittent turbulence for higher values of  $B$ ; and finally, viscously-dominated stratified laminar flow for the highest values of  $B$ . We will now proceed to characterise these different regimes more quantitatively.

#### 8.4.4 Data extraction

Each of the simulations that we have performed was integrated until the system had reached a statistically stationary state. This can take a long time, especially for the very strongly stratified systems, so data in that limit is scarce except for the lowest values of  $Re$ . Once such a state had been reached, we computed the time average, and deviations around that average, of a number of quantities. These include  $w_{rms}(t)$  and  $T'_{rms}(t)$ , which are reported as  $w_{rms} \pm \delta w_{rms}$  and  $T'_{rms} \pm \delta T'_{rms}$ , respectively, in Tables 8.1 and 8.2.

We also computed the instantaneous temperature flux,  $F_T(t)$ , given by

$$F_T(t) = \langle wT' \rangle, \quad (8.36)$$

for simulations that used the standard equations, and equivalently

$$Pe^{-1}F_T(t) = \langle w\nabla^{-2}w \rangle, \quad (8.37)$$

for simulations that used the LPN equations, where the angular bracket was defined in (8.35). In addition, we computed the instantaneous viscous energy dissipation rate as

$$\epsilon(t) = Re^{-1} \langle |\nabla \mathbf{u}|^2 \rangle, \quad (8.38)$$

where  $\epsilon$  is the non-dimensional version of  $\varepsilon$  that was introduced in Chapter 7. These quantities can be used to diagnose the dominant energetic balance taking place between the different energy reservoirs in the system. Indeed, dotting the momentum equation (8.6) with  $\mathbf{u}$  and integrating over the domain, we obtain

$$\frac{\partial}{\partial t} \left\langle \frac{1}{2} |\mathbf{u}|^2 \right\rangle = B \langle wT' \rangle - \frac{1}{Re} \langle |\nabla \mathbf{u}|^2 \rangle + \langle u \sin(y) \rangle, \quad (8.39)$$

$$= BF_T - \epsilon + \langle u \sin(y) \rangle. \quad (8.40)$$

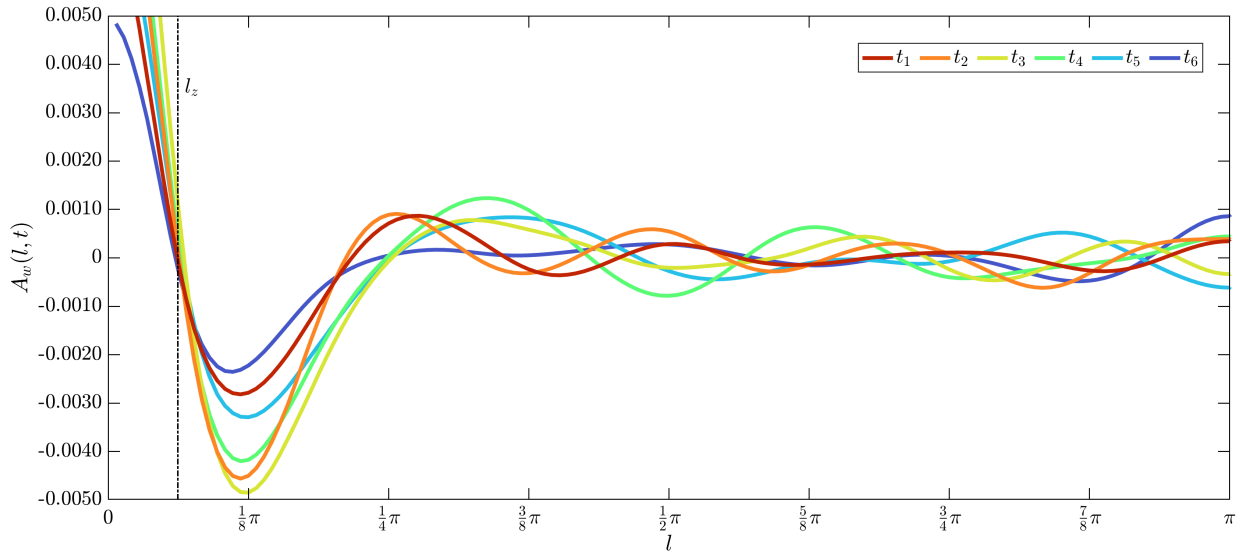


**Figure 8.7** Autocorrelation function  $A_w(l, t)$  as defined in (8.43) computed at six randomly selected times during the statistically stationary state of a simulation with parameters  $Re = 300$ ,  $B = 10,000$  and  $Pe = 0.1$ . Note how  $A_w(l, t)$  has a well-defined first zero, whose time-average defines the vertical eddy scale  $l_z$ .

In a steady state, this shows that the rate at which energy is injected into the flow by the body force,  $\langle u \sin(y) \rangle$ , is partitioned between energy that is dissipated viscously (through  $\epsilon$ ), and energy that is converted into potential energy (at a rate  $BF_T$ ). The fate of the latter can be established by multiplying the temperature equation by  $T'$  and integrating over the domain, which reveals that

$$\frac{\partial}{\partial t} \left\langle \frac{1}{2} T'^2 \right\rangle + BF_T = -\frac{1}{Pe} \langle |\nabla T'|^2 \rangle, \quad (8.41)$$

for the full equations (while in the LPN limit, the time derivative simply disappears). This shows that  $BF_T$  is ultimately dissipated thermally at a rate  $Pe^{-1} \langle |\nabla T'|^2 \rangle$ .

From these energy balance considerations, it is common to define a so-called instantaneous mixing efficiency (see, for example, Maffioli et al., 2016),

$$\eta(t) = \frac{-BF_T(t)}{-BF_T(t) + \epsilon(t)} = \frac{-BF_T(t)}{\langle u \sin(y) \rangle}, \quad (8.42)$$

which measures the efficiency with which kinetic energy, produced by the applied forcing, is converted into potential energy as opposed to being dissipated viscously. Thus, we have computed  $\eta(t)$  for all simulations produced, and report its time average and deviation from that average, while in a statistically stationary state, as  $\eta \pm \delta\eta$  in Tables 8.1 and 8.2.

Finally, another useful diagnostic of the flow is the typical vertical scale of the turbulent eddies. As discussed in Garaud and Kulenthirarajah (2016) and Garaud et al. (2017), there are many different ways of extracting such a length scale, either from weighted averages over the turbulent energy spectrum, or from spatial autocorrelation functions of the velocity field. Garaud et al. (2017) compared these different methods and concluded that the spatial autocorrelation function was a more physical and reliable way of extracting the vertical length scale. In what follows, we therefore compute the function

$$A_w(l, t) = \frac{1}{L_x L_y L_z} \int w(x, y, z, t) w(x, y, z + l, t) dx dy dz, \quad (8.43)$$

at each timestep for which the full fields are available, using periodicity of  $w$  to deal with points near the domain boundaries. Sample functions for six randomly selected times during the statistically stationary state are shown in Figure 8.7 for a simulation with parameters  $Re = 300$ ,  $B = 10,000$  and  $Pe = 0.1$  (a simulation from the stratified intermittent regime, snapshots from which are shown in Figures 8.6(g-i)). We clearly see that  $A_w(l, t)$  has a well-defined first zero at each timestep, which we call  $l_z(t)$ . The vertical eddy scale thus obtained is then averaged over all available timesteps during the statistically stationary state to obtain the mean vertical eddy scale,  $l_z$ , and its standard deviation,  $\delta l_z$ .

## 8.5 Scaling regimes for nonlinear saturation

In our quest for a quantitative description of the four dynamical regimes described in Section 8.4.3, we endeavour to derive scaling laws that explain our data, in an analogous fashion to the approach of Brethouwer et al. (2007) in which the focus was on geophysically-relevant parameters ( $Pr \gtrsim O(1)$ ). Consistent with our goal to study systems in which the Péclet number,  $Pe$ , is small, our data set comprises a range of simulations using the standard equations (8.6)-(8.8) for three different Péclet numbers,  $Pe \in \{0.01, 0.1, 1\}$ , which we compare alongside simulations using the LPN equations (8.15) and (8.16), noting excellent agreement. Using both sets of equations, we consider four different Reynolds numbers,  $Re \in \{50, 100, 300, 600\}$ , and investigate a wide range of background stratifications, with full details presented in Tables 8.1 and 8.2.

### 8.5.1 Effects of stratification on mixing and the vertical scale of eddies

The first flow diagnostic that we discuss is the vertical eddy scale,  $l_z$ , computed using the method described in Section 8.4.4. Figure 8.8(a) shows  $l_z$  as a function of the parameter  $BPe$ , consistent with our expectations on the potential relevance of this parameter for low Péclet number flows (as discussed in Section 8.2.3). For all but the largest values of  $BPe$  (which corresponds to the viscous regime discussed in Section 8.4.3), we confirm that  $BPe$  is indeed the relevant parameter, and that  $l_z$  is independent of  $Re$ . As a result, all of the data collapse onto a single universal curve. For weak stratification, which we refer to as the *unstratified regime*, the vertical eddy scale is invariant with respect to both stratification and Reynolds number, such that  $l_z \simeq 2$ , which is of the order of the size of the periodic domain. For intermediate values of  $BPe$ , corresponding to the *stratified turbulent* regime described in Section 8.4.3, we find that

$$l_z \simeq 2(BPe)^{-1/3}, \quad (8.44)$$

with some uncertainty in both the prefactor and the exponent due to the inherent variability of the flow.

Finally, for very strong stratification in the *stratified viscous* regime, the vertical eddy scale appears to become independent of  $BPe$ , where it depends solely on Reynolds number with the empirical relationship

$$l_z \simeq 2Re^{-1/2}, \quad (8.45)$$

again with some uncertainty in the scaling and exponent. This scaling is analogous to the viscously-affected stratified regime considered by Brethouwer et al. (2007) which we discussed in Chapter 7 (since  $l_z$  in (8.45) is non-dimensional and scaled by a characteristic horizontal length scale). While only three clear regimes are evident in this plot, data from the *stratified intermittent* regime discussed in Section 8.4.3 lie in the

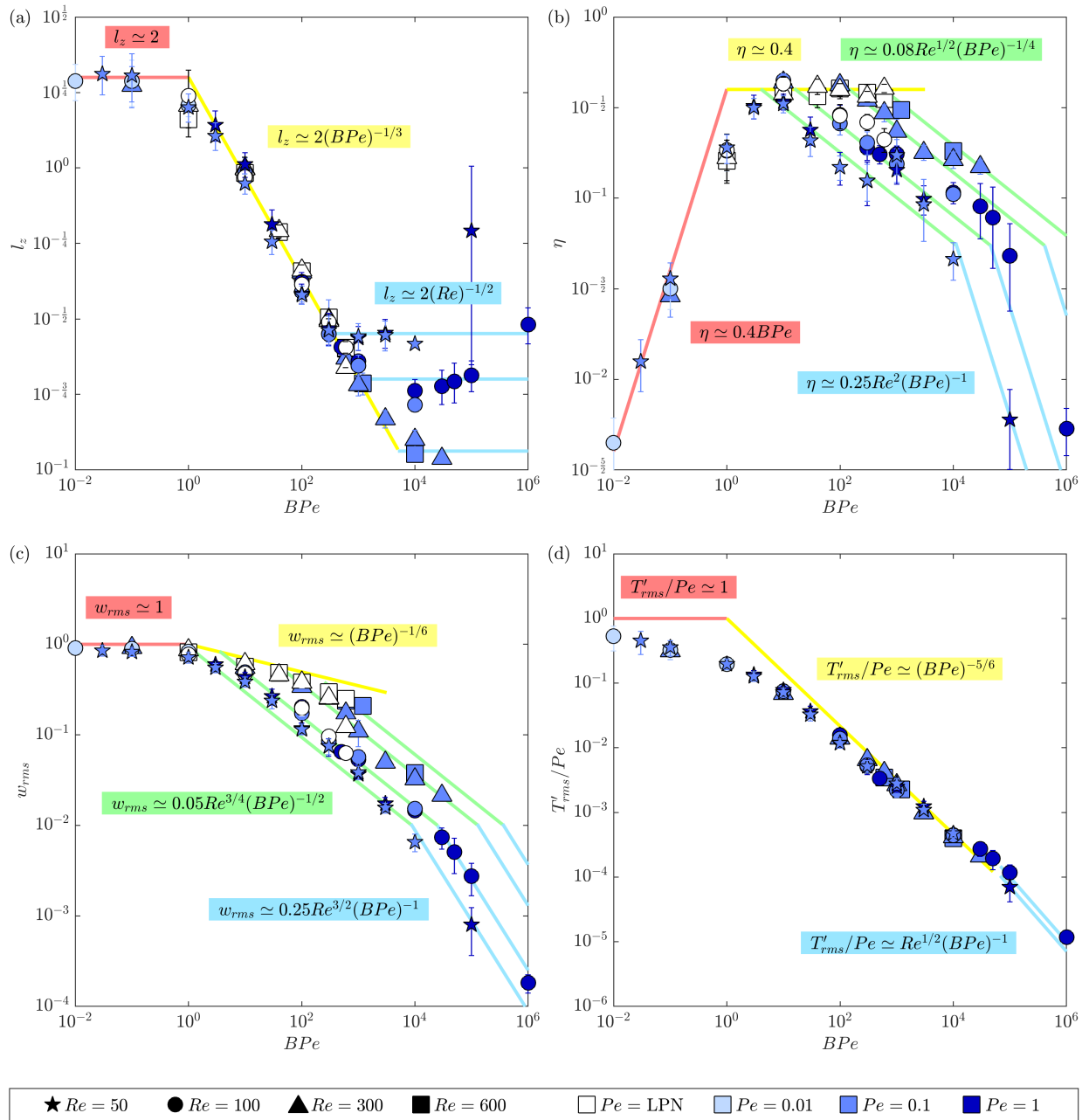


**Figure 8.8** Variation with  $BPe$  of four diagnostics, defined in Section 8.4.4: (a)  $l_z$ , (b)  $\eta$ , (c)  $w_{rms}$ , (d)  $T'_{rms}/Pe$ . All simulations listed in Tables 8.1 and 8.2 are plotted with error bars, using shapes to indicate the Reynolds number and colours to indicate the Péclet number. Coloured lines illustrate our proposed scalings for the (red) unstratified, (yellow) stratified turbulent, (green) stratified intermittent and (blue) stratified viscous regimes.

region of parameter space between the  $l_z \sim (BPe)^{-1/3}$  and  $l_z \sim Re^{-1/2}$  regimes, as the simulations begin to feel the effects of viscosity, and hence the Reynolds number  $Re$ .

It is also of interest to observe how the mixing efficiency,  $\eta$ , discussed in Section 8.4.4, depends on the stratification,  $BPe$ , and the Reynolds number,  $Re$ . Figure 8.8(b) shows  $\eta$  plotted as a function of  $BPe$  for each of our simulations. This time, the four regimes can be clearly identified. For the unstratified regime, the mixing efficiency depends only on  $BPe$ , and is given by

$$\eta \approx 0.4BPe. \quad (8.46)$$

As the stratification increases, the mixing efficiency increases until it reaches a plateau at  $\eta \simeq 0.4$  which, as we argue below, is a defining property of the stratified turbulent regime. The range of values of  $BPe$  for which  $\eta$  is approximately constant is very small for  $Re = 50$ , but clearly increases with  $Re$ , and is quite substantial for  $Re = 600$ . However, in all cases, a threshold is reached where  $\eta$  begins to decrease again. To understand why this is the case, note that the vertical eddy scale decreases rapidly (as discussed above) as the stratification increases and inevitably reaches a point where the effects of viscosity begin to play a role. This is manifest in the fact that  $\eta$  begins to develop a dependency on  $Re$  when the system enters the intermittently turbulent regime. Here, we observe the new empirical scaling

$$\eta \simeq 0.08Re^{1/2}(BPe)^{-1/4}, \quad (8.47)$$

with significant uncertainty in the scalings owing to the high variability of  $\eta$  in this intermittent regime. Finally, for even larger values of  $BPe$ , our simulations suggest a fourth regime for very large stratification, which is characteristic of the stratified viscous regime. Here, we tentatively observe the scaling

$$\eta \simeq 0.25Re^2(BPe)^{-1}, \quad (8.48)$$

which is associated with some uncertainty since very little data is available in this regime. Analogous empirical scalings are evident in Figures 8.8(c) and 8.8(d) for the respective variations with  $BPe$  of the vertical velocity field,  $w_{rms}$ , and the temperature perturbation field,  $T'_{rms}/Pe$ .

## 8.5.2 Derivation of scaling regimes

These observations inspire us to attempt to derive scaling laws by considering dominant balances in the governing equations. In the following analysis, and consistent with our study of low Péclet number systems, we will always assume a LPN balance in equation (8.7) such that

$$w \simeq \frac{1}{Pe} \nabla^2 T'. \quad (8.49)$$

Our approach, therefore, is to consider the dominant balance between terms in the momentum equation (8.6), specifically the relative importance of stratification, inertia and viscosity.

### 8.5.2.1 Unstratified regime

We begin by considering the unstratified regime which was illustrated in Figures 8.6(a-c). Motivated by the qualitative observation of the domain-filling eddies in Figures 8.6(a) and 8.6(b), we make the assumptions that each of the three velocity components and eddy length scales are approximately isotropic with

$$u_{rms}, v_{rms}, w_{rms} \sim O(1), \quad l_x, l_y, l_z \sim O(1). \quad (8.50)$$

These assumptions for  $w_{rms}$  and  $l_z$  are confirmed in Figures 8.8(a) and 8.8(c), indicated by the red lines. By combining the LPN approximation (8.49) with assumptions (8.50), we deduce that a scaling for the typical temperature perturbations is given by

$$\frac{T'_{rms}}{Pe} \sim O(1). \quad (8.51)$$

In terms of the mixing efficiency,  $\eta$ , we note that (8.50) implies  $\langle u \sin(y) \rangle \sim O(1)$ . Thus

$$\eta \sim \frac{B \langle w T' \rangle}{\langle u \sin(y) \rangle} \sim B w_{rms} T'_{rms} \sim B Pe. \quad (8.52)$$

The theoretically derived scalings (8.51) and (8.52) are consistent with the empirical scalings determined using our simulations, shown using the red lines in Figures 8.8(d) and 8.8(b) respectively, where we note that the lack of  $Re$ -dependence affirms the irrelevance of viscosity in this regime.

Finally, it is of interest to compute the condition of validity for this unstratified regime. In the vertical momentum equation (8.6), we have assumed that stratification is weak relative to fluid inertia, such that  $BT' \ll \mathbf{u} \cdot \nabla w$ . Using the scalings derived above, we find that this is true when

$$B Pe \ll O(1). \quad (8.53)$$

Condition (8.53), combined with the condition for linear instability ( $Re > 2^{1/4}$ ), defines the region of parameter space in which we would expect to observe this regime of unstratified turbulence.

### 8.5.2.2 Stratified turbulent regime

As the stratification increases, the system transitions into the stratified turbulent regime, first presented in Section 8.4.3, which we believe is defined by a constant mixing efficiency. Inspection of the snapshots in Figures 8.6(d) and 8.6(e) reveals that the vertical velocity field, which is generated by localised shear-driven Kelvin-Helmholtz type instabilities, is mostly small-scale. On the other hand, the horizontal velocity field contains both large scales (due to the modulated meanders of the jets) and small scales (associated with the small vertical scales). Consequently, in this regime we assume that

$$u_{rms}, v_{rms} \sim O(1), \quad l_x \sim l_y \sim l_z, \quad (8.54)$$

from which it then follows that the LPN approximation is given by

$$w_{rms} \sim Pe^{-1} \frac{T'_{rms}}{l_z^2}. \quad (8.55)$$

Since the vertical flow is generated by vertical shear instabilities of the horizontal flow, and since stratification is now important, we anticipate that the dominant balance in the vertical momentum equation should be between the inertial and stratification terms,  $\mathbf{u} \cdot \nabla w \sim BT'$ , implying that

$$u_{rms} w_{rms} l_z^{-1} \sim BT'_{rms}. \quad (8.56)$$

We note that this implicitly assumes that the vertical pressure gradient,  $\partial p / \partial z$ , is either of the same order of magnitude as  $BT'_{rms}$  or else is much smaller, which on the surface appears to contradict the fact that the pressure,  $p$ , ought to be  $O(1)$  based on the horizontal component of the momentum equation. However, the contradiction can be resolved by noting that  $p$ , similar to  $u$  and  $v$ , has both a large-scale and a small scale component, and that only the large-scale component is  $O(1)$  while it is the small-scale component (of unknown amplitude) that mostly contributes to the vertical derivative. Whilst a rigorous multi-scale analysis would be required to formalise this argument, we note that since both the inertial and the buoyancy

terms must play a role in the dynamics of the flow, then the  $\partial p/\partial z$  term cannot replace either  $\mathbf{u} \cdot \nabla w$  or  $BT'$  in the dominant balance (at best, it can be of the same order of magnitude). Consequently, combining (8.56) with (8.55) and  $u_{rms} \sim O(1)$  leads to the vertical eddy length scale

$$l_z \sim (BPe)^{-1/3}, \quad (8.57)$$

which is confirmed by the yellow line in Figure 8.8(a). Empirically, we find that the prefactor is close to 2, and confirm that this scaling is independent of the Reynolds number.

As mentioned earlier,  $\eta \sim O(1)$  is believed to be a defining property of the stratified turbulent regime, representing a roughly equal partitioning between viscous dissipation and thermal dissipation. The yellow line in Figure 8.8(b) suggests that this constant value of the mixing efficiency is

$$\eta \simeq 0.4. \quad (8.58)$$

Since  $\langle u \sin(y) \rangle \sim O(1)$  from assumption (8.54), then  $\eta \sim B\langle wT' \rangle$ , which implies that

$$Bw_{rms}T'_{rms} \sim O(1). \quad (8.59)$$

Combining (8.59) with the LPN approximation (8.49) and the vertical momentum equation balance (8.56) leads to the additional scalings for the temperature fluctuations and the vertical velocity field:

$$\frac{T'_{rms}}{Pe} \sim (BPe)^{-5/6}, \quad w_{rms} \sim (BPe)^{-1/6}. \quad (8.60)$$

There is strong evidence for both of these scalings, as illustrated by the yellow lines in Figures 8.8(d) and 8.8(c) respectively, where we note that the empirical data are consistent with the associated prefactors being close to one in each case. Once again, we highlight the lack of dependence on  $Re$  in (8.60).

In this stratified turbulent regime, we can finally estimate a generic non-dimensional turbulent diffusivity for the vertical transport of a passive scalar as

$$D_{\text{turb}} \sim w_{rms}l_z \sim (BPe)^{-1/2}, \quad (8.61)$$

with a prefactor that is expected to be of order unity. This result can be compared with the mixing coefficient expected in low Péclet number stratified turbulence caused by vertical shear, which scales as  $(RiPe)^{-1}$  instead (see expression (7.18) when cast in non-dimensional form). Thus, we see that  $D_{\text{turb}}$  decreases much less rapidly with increasing stratification in horizontally-sheared flows than in vertically-sheared flows, at least while the system is in this stratified turbulent regime.

The assumptions that we made in the vertical momentum equation balance, i.e. that the viscous terms are negligible ( $Re^{-1}\nabla^2 w \ll BT'$ ), along with scalings for  $l_z$ ,  $u_{rms}$  and  $T'_{rms}$ , lead to the condition that  $BPe \ll Re^2$ . This suggests that the stratified turbulent regime scalings should apply when

$$1 \ll BPe \ll Re^2. \quad (8.62)$$

Condition (8.62), which is computed more precisely in Section 8.5.3, uniquely defines the region of parameter space in which we would expect to observe this particular type of stratified turbulence in flows at low Péclet number.

### 8.5.2.3 Stratified viscous regime

As discussed in Section 8.4.3, for very strong stratification we observe the formation of thin and viscously coupled layers, each containing almost two-dimensional flow. Consequently, we expect that horizontal and vertical velocity components and length scales will both be strongly anisotropic. Denoting horizontal length scales as  $l_h$ , we make the following assumptions:

$$l_h \sim O(1), \quad l_z \ll l_h, \quad (8.63)$$

$$u_{rms}, v_{rms} \sim O(1), \quad w_{rms} \ll u_{rms}, v_{rms}. \quad (8.64)$$

In the following analysis, we split the three-dimensional velocity field into horizontal and vertical components,  $\mathbf{u} = \mathbf{u}_h + w\mathbf{e}_z$ , with a corresponding decomposition of the gradient operator  $\nabla = (\nabla_h, \partial/\partial z)$ . The momentum equation can then be split into its horizontal and vertical components as

$$\frac{\partial \mathbf{u}_h}{\partial t} + \mathbf{u}_h \cdot \nabla_h \mathbf{u}_h + w \frac{\partial \mathbf{u}_h}{\partial z} + \nabla_h p = \frac{1}{Re} \left( \nabla_h^2 \mathbf{u}_h + \frac{\partial^2 \mathbf{u}_h}{\partial z^2} \right) + \sin(y)\mathbf{e}_x, \quad (8.65)$$

$$\frac{\partial w}{\partial t} + \mathbf{u}_h \cdot \nabla_h w + w \frac{\partial w}{\partial z} + \frac{\partial p}{\partial z} = \frac{1}{Re} \left( \nabla_h^2 w + \frac{\partial^2 w}{\partial z^2} \right) + BT'. \quad (8.66)$$

If we assume a dominant balance between viscosity and the forcing in the horizontal momentum equation (8.65), then  $Re^{-1} \partial_z^2 \mathbf{u}_h \sim \sin(y)\mathbf{e}_x \sim O(1)$ . This balance, combined with  $\mathbf{u}_h \sim O(1)$ , leads to the classical viscous scaling for the vertical length scales discussed in Section 7.2.3 (cf. Brethouwer et al., 2007):

$$l_z \sim Re^{-1/2}. \quad (8.67)$$

Substantial evidence for this scaling is visible in Figure 8.8(a), where the series of blue lines correspond to  $l_z \simeq 2Re^{-1/2}$  for each individual Reynolds number. Note that these strongly stratified simulations exhibit large amplitude quasi-time-periodic behaviour, a feature that we believe to be an intrinsic property of such flows. We consequently attribute the large error bars associated with some simulations to this observation.

In the vertical momentum equation, we assume that the dynamics are hydrostatic, therefore  $\partial_z p \sim BT'$  implies that  $p l_z^{-1} \sim BT'_{rms}$ . This approximation, combined with the requirement from the balance in the horizontal momentum equation that  $p \sim O(1)$ , and with the scaling (8.67) for  $l_z$ , gives us a scaling for the temperature perturbations:

$$\frac{T'_{rms}}{Pe} \sim Re^{1/2} (BPe)^{-1}. \quad (8.68)$$

As previously mentioned, this stratified viscous regime is considerably more challenging to simulate than the other three regimes, a consequence of the very small time steps required and long integration times. However, we see in Figure 8.8(d) that the blue lines, which represent the scalings in (8.68), fit the few available data points well, once again with a prefactor that is close to one.

A scaling for the vertical velocity results from the LPN approximation (8.55) combined with (8.67):

$$w_{rms} \sim Re^{3/2} (BPe)^{-1}. \quad (8.69)$$

Again, we see a good correspondence between the blue curves in Figure 8.8(c) which represent this scaling, and the simulation data, where the prefactor is approximately 0.25.

Using these results, we can finally deduce a scaling for the mixing efficiency,

$$\eta \sim \frac{B\langle wT' \rangle}{\langle u \sin(y) \rangle} \sim Bw_{rms}T'_{rms} \sim Re^2(BPe)^{-1}, \quad (8.70)$$

with a prefactor of 0.25 for consistency with the data obtained for  $w_{rms}$  and  $T'_{rms}$ . This is found to be consistent with observations for  $Re = 50$  and  $Re = 100$  in Figure 8.8(b). We can also estimate a generic non-dimensional turbulent diffusivity for vertical transport of a passive scalar as

$$D_{turb} \sim w_{rms}l_z \sim Re(BPe)^{-1} \sim (BPr)^{-1}, \quad (8.71)$$

with a prefactor that is again expected to be of order unity.

The viscous regime is achieved in the opposite limit to the one derived in (8.62) for the stratified turbulent regime, namely when  $BPe \gg Re^2$ . Thus, we find that the system parameters must satisfy

$$2^{1/2} < Re^2 \ll BPe, \quad (8.72)$$

when combined with the condition for linear instability. Condition (8.72), computed more precisely in Section 8.5.3, defines the region of parameter space in which we would expect to observe this stratified viscous regime. We note for consistency that each of the scalings obtained here do depend on the value of the Reynolds number, as one would expect.

#### 8.5.2.4 Stratified intermittent regime

There also exists a fourth regime, visible both in the simulations and the results presented in Figures 8.8(a-d). This final regime is a transitional regime that occurs between the stratified turbulent regime and the stratified viscous regime. As discussed in Section 8.4.3, it is inherently intermittent in the sense that we observe spatially and temporally localised patches of small-scale turbulence generated via vertical shear instabilities, surrounded by more laminar, viscously dominated flow. Whilst we have been unable to derive satisfactory scalings for this regime, we can nevertheless deduce some of them empirically from Figures 8.8(b) and 8.8(c).

For instance, we see in Figure 8.8(b) that the onset of this stratified intermittent regime (indicated by the green lines) is characterised by a sudden change in the dependence of the mixing efficiency,  $\eta$ , on  $BPe$ , from the constant value of 0.4 observed in the stratified turbulent regime to a regime where  $\eta$  is given by (8.47). It is interesting and perhaps reassuring to note that the parameter group  $BPe/Re^2$ , which controls  $\eta$  in this regime, is the same parameter group that appears in the viscous regime. Note that for  $\eta \approx 0.1$ , we observe a temporary flattening of this scaling just before the onset of the viscous regime. Whilst it is certainly possible that this feature is an artefact of inherent variability in the simulations (and therefore the measurement of  $\eta$  has larger associated error bars), it is interesting to note that this ‘knee’ in the curve does occur for flows with at least three different Reynolds numbers.

An additional scaling can be inferred from Figure 8.8(c) which suggests that  $w_{rms}$  scales as

$$w_{rms} \approx 0.05Re^{3/4}(BPe)^{-1/2}. \quad (8.73)$$

No clear scalings for  $l_z$  or  $T'_{rms}/Pe$  appear to be deducible from the numerical results.

### 8.5.3 A regime diagram

We conclude this section by summarising in Figure 8.9 the delineation of the four dynamical regimes of nonlinear saturation that were described in Section 8.5.2, along with the inclusion of the linearly stable regime that was discussed in Section 8.3. The unstratified regime, indicated in red, occurs when

$$BPe \ll O(1), \quad Re > 2^{1/4}. \quad (8.74)$$

The stratified turbulent regime, indicated by the yellow region, and the stratified viscous regime, indicated by the blue region, exist when  $BPe \ll Re^2$  and  $BPe \gg Re^2$  respectively, with the stratified intermittent regime (green) lying at the transition. Written in terms of the buoyancy Reynolds number  $Re_b = Re/B$ , which Brethouwer et al. (2007) identified as a key parameter for delineating parameter regimes when  $Pr \gtrsim 1$ , these regime boundaries become  $Re_b \gg Pr$  and  $Re_b \ll Pr$  respectively. Thus, we observe that at low  $Pr$ , the stratified turbulent regime can be realised even if  $Re_b$  is very small (and less than one), unlike for geophysical flows which require  $Re_b \gg 1$  for the existence of stratified turbulence.

Greater precision on these regime boundaries, permitting the identification of the domain of validity of the stratified intermittent regime, can be determined from Figure 8.8(b). If we assume that, for each Reynolds number, the transition between the stratified turbulent and stratified intermittent regimes occurs

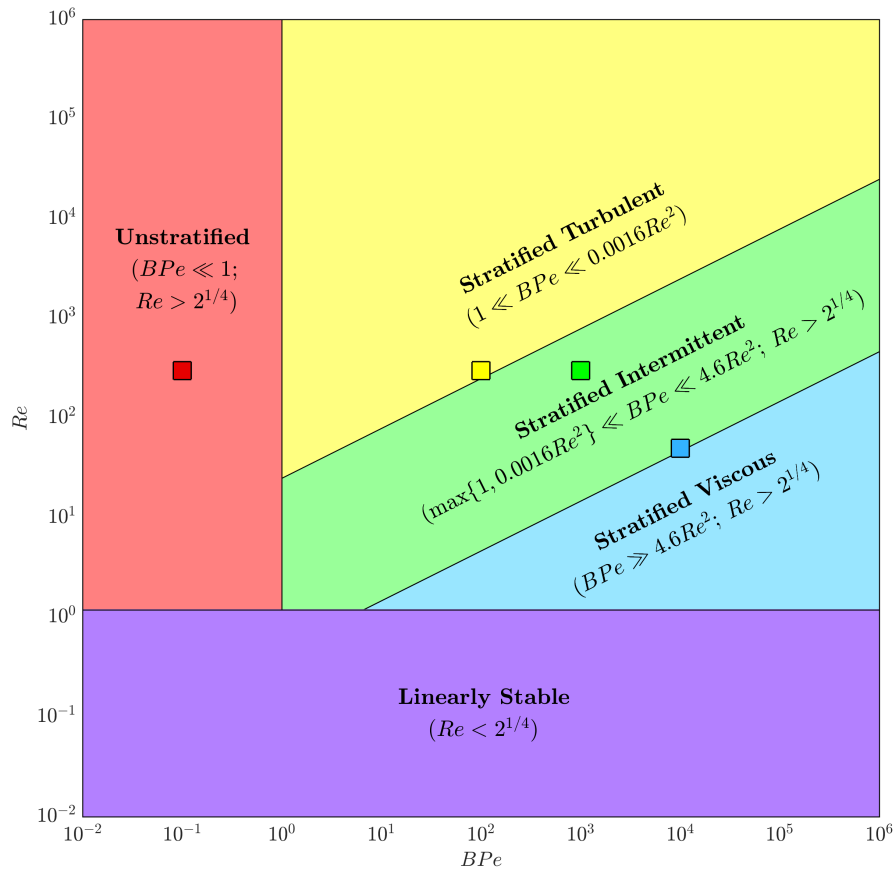


**Figure 8.9** A regime diagram, applicable in the LPN limit, illustrating five dynamical regimes across the system parameters  $BPe$  (horizontal axis) and  $Re$  (vertical axis). Each regime is associated with a colour: linearly stable (purple); unstratified (red); stratified turbulent (yellow); stratified intermittent (green); stratified viscous regime (blue). The four example simulations presented in Figure 8.6 are associated with parameters corresponding to the red, yellow, green and blue squares.

when  $\eta \simeq 0.4$ , then the boundary is given by  $BPe \simeq 0.0016Re^2$ . This provides the more precise condition

$$1 \ll BPe \ll 0.0016Re^2, \quad (8.75)$$

for the stratified turbulent regime, labelled in Figure 8.9. We note that this regime does not intersect the region of linear stability, indicating that for certain Reynolds numbers for which instability occurs ( $2^{1/4} < Re < 25$ ) this particular type of stratified turbulence does not exist.

From Figure 8.8(b) we can also estimate that the transition between the stratified intermittent regime and the stratified viscous regime approximately occurs when  $\eta \simeq 0.05$  irrespective of the Reynolds number, which would imply that the boundary is given by  $BPe \simeq 4.6Re^2$ . Thus, a more precise condition for the existence of the stratified viscous regime is given by

$$BPe \gg 4.6Re^2, \quad Re > 2^{1/4}. \quad (8.76)$$

For each Reynolds number, the stratified intermittent regime exists for intermediate values of  $BPe$  between conditions (8.75) and (8.76). When combined with the converse of the condition for the unstratified regime (i.e.  $BPe \gg 1$ ) and the condition for linear instability ( $Re > 2^{1/4}$ ), this regime condition becomes

$$\max\{1, 0.0016Re^2\} \ll BPe \ll 4.6Re^2, \quad Re > 2^{1/4}. \quad (8.77)$$

As shown in Figure 8.9, the stratified intermittent regime can exist for any value of  $Re$ , provided that the system is linearly unstable.

## 8.6 Discussion

In this chapter we have studied the linear instability and subsequent nonlinear evolution of stratified horizontal Kolmogorov flows at high Reynolds number but low Péclet number. As summarised in Section 8.5.3, our numerical simulations have revealed that such flows exhibit (at least) four different non-trivial dynamical regimes, depending on the respective values of the parameters  $BPe$  and  $Re$  (where the buoyancy parameter,  $B$ , the Péclet number,  $Pe$ , and the Reynolds number,  $Re$ , were defined in (8.9) and (8.11)). In all but one of these regimes, well-defined dominant balances in the momentum equation lead to simple scaling laws for the turbulent properties of the flow. We now first compare our results with previous studies of stratified mixing in the geophysical context, and then discuss the implications of our findings for stratified mixing in stars, whose understanding motivated this study.

### 8.6.1 Comparison between stratified mixing in geophysical and astrophysical flows

As we have demonstrated in this work, geophysical and astrophysical stratified turbulence is fundamentally different due to the fact that the former has a Prandtl number  $Pr \gtrsim O(1)$  while the latter has  $Pr \ll 1$ . This has important consequences, since a high Reynolds number flow in geophysics necessarily also has a high Péclet number, meanwhile, in astrophysical flows it is possible to have both  $Re \gg 1$  and  $Pe \ll 1$  such that the effect of thermal diffusion can become a dominant factor in the system dynamics. As demonstrated by Lignières (1999) (see also Spiegel, 1962; Thual, 1992), temperature and velocity fluctuations in the low Péclet number limit are slaved to one another, and density layering is prohibited (see Section 7.3). This is

in stark contrast with geophysical flows, where density layering (or at the very least, the propensity to form alternating regions of shallower and steeper density gradients) is key to understanding the properties of stratified turbulence in the LAST regime.

Indeed, in geophysical flows (in particular in the Earth's atmosphere and ocean), the standard Miles-Howard stability criterion (Howard, 1961; Miles, 1961) for linear instability to vertical shear, namely  $Ri_g < \frac{1}{4}$  (where the local gradient Richardson number,  $Ri_g$ , is defined in (7.13)), is at first glance incompatible with the ubiquitous presence of turbulence in most large-scale stratified shear flows, where typically  $Ri_g \gg 1$ , or indeed is irrelevant in the case of horizontally-sheared flows. However, small-scale layering releases this constraint by creating regions where the stratification is locally reduced, and the instability that is now allowed to develop continues to mix the layer, thereby allowing the turbulence to sustain itself. This process, as reviewed in Section 7.2, can lead to the formation of layers on the scale  $U_c/N_c$ , and is controlled by the buoyancy Reynolds number,  $Re_b = ReFr^2 = Re/B$ .

In astrophysical flows, typical values of the gradient Richardson number are also very large, but density layering is prohibited so this pathway to turbulence is not available. Instead, we have shown that three-dimensional perturbations of the horizontal shear (see also Arobone and Sarkar, 2012; Deloncle et al., 2007; Lucas et al., 2017) cause the flow to develop layers in the velocity field that enhance the vertical shear (or create it when it is not initially present). For sufficiently thin velocity layers, thermal diffusion reduces the effect of stratification, allowing vertical shear instabilities to develop in between the layers. The combination of these two effects drives turbulence which can cause substantial vertical mixing, even when the background flow has no vertical shear. The dynamics of this thermally diffusive system are no longer controlled by the geophysically-relevant parameter  $ReFr^2$ , but instead, first by  $BPe = Pe/Fr^2$  in the limit where  $BPe \ll Re^2$ , and then by the ratio  $BPe/Re^2$  in the limit where  $BPe \gg Re^2$ , thus partitioning parameter space into the four different dynamical regimes discussed in Section 8.5.

A comparison between low and high  $Pe$  dynamics reveals that the viscous regime that we have identified (when  $BPe \gg Re^2$ ) is analogous to the viscously affected  $Re_b \lesssim O(1)$  regime discussed by Brethouwer et al. (2007), in the sense that it relies on the same dominant balances in the momentum equation. As a result, it exhibits the same scaling in terms of the vertical length scale,  $l_z \sim Re^{-1/2}$ . It differs, however, in the treatment of the buoyancy equation, which is not surprising given the low Péclet number limit appropriate in our case. On the other hand, the stratified turbulent regime identified here bears little resemblance with the  $Re_b \gg 1$  and high  $Pe$  regime of Brethouwer et al. (2007) (i.e. the LAST regime), where  $l_z \sim U_c/N_c$ . Indeed, for this new low Péclet number stratified turbulent regime, we find that, dimensionally,

$$l_z \sim (BPe)^{-1/3} L_c \sim \left( \frac{U_c \kappa}{N_c^2} \right)^{1/3}, \quad (8.78)$$

as found in Section 8.5. From a dimensional analysis point of view, this new scaling can be understood as the only combination of  $U_c$  and  $N_c$  that can be created to form a length scale given the constraint that  $N_c^2$  and  $\kappa$  can only appear together as  $N_c^2/\kappa$  in the low Péclet number limit (as is apparent from (7.16)). But more importantly, we also saw that this scaling emerges from the assumption that the turbulent eddies are isotropic on the small scales, with  $l_x \sim l_y \sim l_z$  (see Section 8.5.2.2), which is quite different from the inherently anisotropic scalings discussed in Brethouwer et al. (2007) where  $l_x, l_y \gg l_z$ . In other words, the stratified turbulent regime identified here is (we believe) a genuinely new regime of turbulence, that can only exist at low Péclet number, and so we refer to it as *low Péclet number stratified turbulence*, LPNST.

### 8.6.2 Implications for mixing in stars

In order to discuss the implications of our findings for mixing in stars, we begin by comparing our numerical results to the theory proposed by Zahn (1992) for turbulence driven by horizontal shear in stellar radiation zones. Recall (see Section 7.3) that the characteristic flow length scale and amplitude in his model are given by (7.19). Written in terms of the non-dimensionalisation used in this work (see Section 8.2), these are

$$L_c \sim \left( \frac{\epsilon^{1/3}}{BPe} \right)^{3/8} \quad \text{and} \quad U_c \sim \left( \frac{\epsilon^3}{BPe} \right)^{1/8}, \quad (8.79)$$

where  $\epsilon$  is the non-dimensional dissipation rate (see also Lignières, 2018). Zahn assumed that all of the energy that was input into the system (i.e.  $\langle u \sin(y) \rangle$ , which is always of order one in the chosen units) would be dissipated viscously, such that there would be negligible irreversible conversion of kinetic energy into the potential energy reservoir associated with mixing. This means that  $\epsilon \simeq 1$ , from which it follows that the corresponding non-dimensional turbulent diffusivity in Zahn's model would scale as

$$D_{\text{turb}} \sim U_c L_c \sim (BPe)^{-1/2}, \quad (8.80)$$

which is indeed what we find in the stratified turbulent regime (see expression (8.61)). It is interesting to note, however, that  $L_c \sim (BPe)^{-3/8}$  in Zahn's model, and that this does not fit the data as well as our proposed  $l_z \sim (BPe)^{-1/3}$  scaling. We believe that both scalings are relevant, with the discrepancy emerging due to the different choices for the characteristic velocity  $U_c$ . In (8.78), we have assumed that  $U_c$  is the r.m.s. horizontal velocity which is approximately constant in our simulations. By contrast, Zahn assumes a constant dissipation rate,  $\epsilon$ , in (7.19), giving a modified Ozmidov scale,  $L_O = (\epsilon/N^3)^{1/2}$ , representing the scale below which an isotropic turbulent cascade can exist (see Lignières, 2018).

Whilst we believe our results are a step forward in the study of stratified mixing in stars, they are nevertheless not yet applicable *as is* for a number of reasons. First and foremost is the fact that the majority of stars (i.e. all stars except the most massive ones) are actually in the *high Péclet* number yet low Prandtl number regime, while the simulations presented in this study only probe the low Péclet number regime. Indeed, a classic example of a stellar shear layer is the solar tachocline, which, as mentioned in Section 7.3, is located just below the base of the solar convective envelope (Christensen-Dalsgaard and Schou, 1988; Goode et al., 1991). This layer contains a horizontal shear flow with characteristic values associated with the base flow being  $U_c \simeq 150 \text{ m s}^{-1}$  and  $L_c \simeq 5 \times 10^8 \text{ m}$ , while the buoyancy frequency is of the order of  $N_c \simeq 10^{-3} \text{ s}^{-1}$  (Hughes et al., 2007). With diffusivities given by  $\nu \simeq 0.001 \text{ m}^2 \text{ s}^{-1}$  and  $\kappa \simeq 1000 \text{ m}^2 \text{ s}^{-1}$ , this implies that  $Re \sim O(10^{14})$ ,  $Pe \sim O(10^8)$ , and  $B \sim O(10^7)$ , with  $Pr \sim O(10^{-6})$ . Corresponding numbers for other main sequence low-mass and-intermediate mass stars are in the same parameter regime.

Our low Péclet number findings are not to be casually dismissed, however. As shown in a more recent study by Garaud (2020), flows with  $Pe \gg 1$  and  $Pr \ll 1$  can still be governed by low Péclet number dynamics (and therefore all the scalings derived in this work) when the turbulent Péclet number associated with the eddies is small, i.e.  $Pe_t = w_{rms} l_z Pe \ll 1$  (noting that  $w_{rms}$  and  $l_z$  are non-dimensionalised). This is likely because the effective local Péclet number of the flow (written in terms of the actual vertical eddy scale  $l_z$  instead of  $L_c$ ) is low even though the Péclet number based on the global scale itself is large.

More crucially, however, is the fact that other effects will need to be taken into account before a comprehensive model of stratified mixing in stars can be created. The main source of shear in stars is

their differential rotation, where the mean rotation rate is typically substantially larger than the shearing rate, and where the horizontal shear is usually global (i.e. with a length scale of the order of the stellar radius). This implies that the effects of curvature and angular momentum conservation must be taken into account to determine whether the horizontal shear is unstable in the first place. Two-dimensional horizontal shear flows in a rotating spherical shell were first studied by Watson (1980) (see also Garaud, 2001), who found that the shearing rate must exceed a critical threshold for instability to proceed. In the context of our work, this implies that rotation could in principle inhibit the development of the primary instability. If the latter does take place, however, we anticipate that the same sequence of instabilities resulting in the development of small-scale eddies of size  $l_z$  would ensue. The Rossby number based on  $l_z$  is likely to be very large ( $Ro \sim U_c/\Omega l_z \sim O(10^4)$  in the tachocline, where  $\Omega \sim 3 \times 10^{-6} \text{ s}^{-1}$  is the mean rotation rate of the Sun), suggesting that rotation would not have a significant effect on the flow dynamics in any stratified turbulent regime. It may be relevant in the intermittent and viscous regimes on the other hand, where the horizontal eddy scale is of the order of the scale of the background flow.

Stars are also subject to vertical shear as well as horizontal shear, and the dynamics of shear-induced turbulence are notably different in the two cases (see Section 7.3). A question of interest will therefore be to establish what controls the outcome when vertical and horizontal shear are both present. Finally, most stars are expected to be magnetised to some extent (Mestel, 2012), either by the presence of a primordial magnetic field or by the action of a dynamo in a nearby convective zone. The effect of these magnetic fields will need to be taken into account in order to construct an astrophysically-relevant theory of stratified turbulence.

## Chapter 9

# Conclusions and future work

Turbulence is ubiquitous within geophysical and astrophysical fluid flows. Its interaction with physical ingredients such as rotation and stratification gives rise to spectacular dynamics, including the layering of material properties, which in turn have important consequences for the transport and distribution of heat, momentum and tracers. In this thesis, we have considered these effects individually via the study of two different problems of scientific interest. Focussing initially on the effect of rotation in geophysical fluid dynamics, we have studied the paradigm problem of beta-plane turbulence as a simple model of jet stream dynamics in planetary atmospheres and oceans. This was followed by a consideration of stratification in astrophysical fluid flows, and its effect on the vertical transport properties of flows in stellar interiors.

### 9.1 Jet stream variability in beta-plane turbulence

In our first problem, we considered the dynamics of jet streams, which play a significant role in the climate system, transporting geophysically important quantities such as momentum and heat that influence the patterns of weather and climate. The behaviours of naturally-occurring jet streams differ substantially between different planetary systems, and a current leading order question concerns their time variability. The novelty in the first part of this thesis involved the study of the fundamental properties and physical mechanisms governing the dynamics of zonal jet variability within the context of a framework of idealised models. This is an important step towards understanding the variability of jet streams in more complex systems.

Using a succession of idealised barotropic beta-plane models of decreasing complexity - arguably the simplest systems that exhibit the relevant variability - we were able to draw comparisons and elucidate the fundamental ingredients necessary for different aspects of zonal jet variability. The most complex of these models was a fully nonlinear (NL) system in which an idealisation of two-dimensional turbulence was modelled using a stochastic forcing function and energy was predominantly dissipated at the largest scales using linear friction. Comparisons with this NL system were made with a quasilinear (QL) version, which was also stochastic and in which eddy-eddy interactions were neglected, in addition to a statistical formulation of the QL model, known as CE2, in which the neglect of some aspects of random fluctuations leads to the construction of a relatively simple, deterministic system. By successively neglecting these different components in an analysis of a large number of numerical simulations across a broad range of parameters, notably the Rhines scale,  $k_{Rh}$ , which was found to be linearly related to the number of jets, and the zonostrophy parameter,  $R_\beta$ , our objective was to understand the phenomena observed in the NL model.

Each of the models revealed a rich zoology of different types of behaviour in the zonostrophic regime ( $R_\beta \gtrsim 2$ ) which we endeavoured to classify based on the time evolution of the zonal mean zonal velocity. Our taxonomy, illustrated in Figure 9.1, consists of three distinct types of behaviour at the most fundamental level, along with various sub-categories, each of which were reproduced to varying degrees by the different models according to whether the necessary ingredients were retained. Firstly, we identified *unsteady* regimes which comprise randomly wandering behaviour. Here, the latitudinal positions of the jets appear to behave like a random walk, showing no predictability. This behaviour was reproduced by the DNS (NL and QL) models but not by the CE2 model, indicating that random fluctuations in the eddy field are an essential component. The CE2 model instead gave rise to time-periodic behaviour, illustrating its capacity to generate time dependent behaviour for fixed external parameters.

Secondly, we observed the existence of stable attractors within our models, where the jets assume a particular configuration that persists over time scales far in excess of the damping time scale. A more detailed classification of these *quasi-steady* states (so named due to the presence of small-amplitude fluctuations) revealed that they can be categorised according to the symmetries associated with the relative spacings and strengths of the jets. Symmetric states, which obey a certain sort of translational symmetry due to the fact that the jets are equally strong and equally spaced, are distinct from asymmetric states, where the jet spacings or strengths display asymmetries. Eddy-eddy interactions were found to be essential for the existence of these symmetric states, which were only observed in the NL model. On the other hand, all models reproduced the asymmetric states, although we note that the persistency of these regimes was quite weak in the QL model.

The quasi-steady states were not found to be unique in any of our models for a given set of parameters. Instead, we demonstrated the existence of multiple stable attractors (both in terms of the numbers of jets and

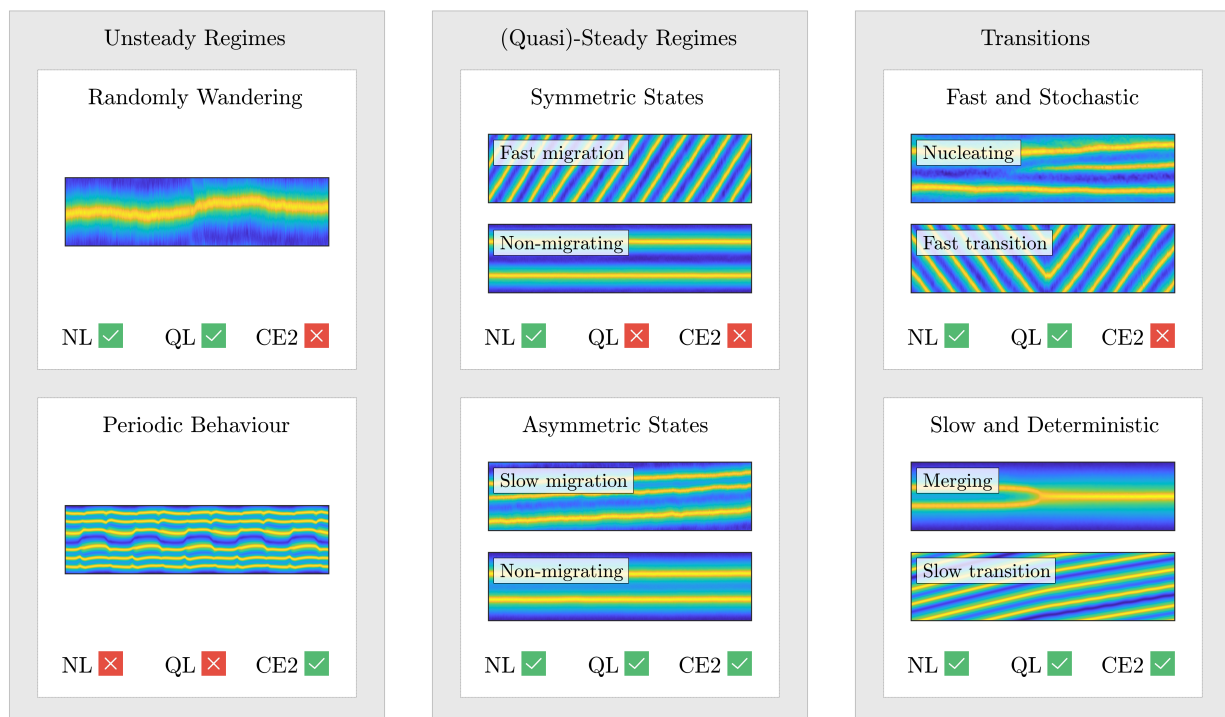


**Figure 9.1** A taxonomy of the zoology of zonal jet dynamics in barotropic beta-plane turbulence, showing three distinct types of behaviour at the most fundamental level, along with various sub-categories. The individual latitude-time plots show representative examples of the evolution of the zonal mean zonal velocity in each case.

their configurations) via the choice of different initial conditions. Furthermore, the systems demonstrated the capacity to spontaneously transition between these different attractors, even in the absence of external impulses. Somewhat surprisingly, certain types of transitions were reproduced by the CE2 system due to the persistent, but often weak, time dependency of its solutions, suggesting that these transitions can be categorised according to two different types. These include *fast* transitions that are stochastically driven (and which only occur in the DNS models) and *slow* transitions that are preceded by very slow time scales of evolution (and which occur in all of the models). Two important examples include the merging and nucleating of jets, which are the only mechanisms by which the number of jets can increase or decrease. Jet nucleations, which were not observed in the CE2 model, were deduced to fall under the fast type, while jet mergers, which followed the slow translation of jets towards each other, were associated with the slow type.

Whilst various elements of the above analysis have been observed in previous studies of beta-plane turbulence, the final insights from this study concerned the discovery of a new quasi-steady regime, notably *migrating* behaviour. This is a phenomenon that has previously been observed in more complex systems in which a naturally occurring symmetry-breaking mechanism (such as that associated with the geometry of the domain) induces migration purely in one direction. In this study, where jets are observed to systematically migrate north or south with equal probability, occasionally changing their direction of translation, we have demonstrated that these external conditions are not essential. Further analysis revealed the existence of two types of migration, depending on the symmetry properties of the relative spacings and strengths of the jets. A fast and symmetric type of migration, which was only observed in the NL model, was so named because the translation speeds of the jets (found to be proportional to the damping rate and Rhines scale) were significantly faster than a slow and asymmetric type that was observed in all of the models.

Wishing to understand this distinction, we conducted a detailed study of the fast type of migration using a hybrid model that generalised the quasilinear approximation, providing a systematic way of restoring eddy-eddy interactions to the QL model. This generalised quasilinear (GQL) model revealed the necessity of nonlinear triad interactions that generate modes with zonal wavenumber  $k_x = 1$ , which we related to a class of nonlinear waves known as zonons (the generalisation of Rossby waves to systems with latitudinal shear). In our domain, the zonons were associated with both the jet meanders and a wave-like pattern of vorticity anomalies that propagated alongside the jets, accounting for a significant fraction of the total kinetic energy. This led to a new theory for the fast type of zonal jet migration, where the zonons were deduced to be essential, playing an organisational role of the smaller scale eddy field. The relative alignment of the jets and zonons allowed for a persistent state of latitudinal asymmetry in the eddy momentum flux convergence, and a corresponding net force on the jets.

In summary, significant progress has been made in understanding the fundamental properties and dynamics of zonal jets. Whilst we believe that our results present an important contribution, they also open up a range of possible avenues for future research. These include an investigation of the role of zonons (or long waves more generally) in other aspects of zonal jet variability, the importance of which was suggested by the discrepancies between the NL and QL models, in addition to the behaviour-dependent zmf indices in the NL model. Further analytical or numerical insights could be investigated using other reduced zonon-permitting models, such as the ensemble-CE2 model or a statistical formulation of the GQL model. Another potential area of research concerns the dynamical pathways associated with the stochastically-driven (fast) regime transitions, and their associated probabilities of occurrence. These transitions, which share an analogy with the idea of multiple stochastic potential wells, may be amenable to the opportunities presented

by recent developments in the field of large deviation theory. Finally, and perhaps most importantly, the applicability of our results should be established in the context of more complex systems, where the additional effects of baroclinicity, non-periodic boundary conditions or spherical geometry need to be taken into account in order to develop a more complete theory of zonal jet variability. Our results suggest that long waves play an essential role in aspects of jet behaviour, therefore any complete theory based on some kind of statistical closure scheme must include the effects of these waves.

## 9.2 Turbulent mixing in stratified, thermally diffusive shear flows

Our second problem studied the dynamics of stratified turbulence, which is key to transport processes in geophysical flows and also thought to play a crucial role in stellar interiors. Geophysical flows, in which the Prandtl number  $Pr \gtrsim O(1)$ , are often very strongly stratified, nevertheless, turbulence still occurs. Density layering is key to understanding the properties of this ‘layered anisotropic stratified turbulence’ (LAST) regime. On the other hand, astrophysical flows are characterised by  $Pr \ll 1$ , inhibiting the formation of density layers. This suggests that LAST dynamics cannot occur, raising the interesting question of whether analogous or fundamentally different regimes exist in the limit of strong thermal diffusion. Inspired by the work of Zahn (1992), who conjectured that shear instabilities provide one such source of turbulent mixing in stars, and following work investigating stratified vertically-sheared flows (Garaud et al., 2015a), this study considered horizontally-sheared flows in the limit of small Prandtl (and hence small Péclet) number.

Seeking the simplest possible model and neglecting the effects of rotation and magnetism, we considered the dynamics of a vertically-stratified, horizontally-forced Kolmogorov flow with a linearised background temperature distribution. This was studied alongside a reduced system that can be derived in the asymptotic limit of low Péclet number (LPN), giving a set of LPN equations that depend only on two non-dimensional parameters, notably the Reynolds number,  $Re$ , and the parameter  $BPe$ . Results from a linear stability analysis about the laminar background flow found that the stability of two-dimensional modes ( $k_z = 0$ ) to infinitesimal perturbations was independent of the stratification, whilst three-dimensional modes ( $k_z \neq 0$ ) were always unstable in the limit of strong stratification ( $B \rightarrow \infty$ ) and strong thermal diffusion ( $Pr \rightarrow 0$ ).

The subsequent nonlinear evolution and transition to turbulence were studied numerically using DNS. We observed that three-dimensional perturbations of the horizontal shear caused the flow to develop layers in the velocity field that generated vertical shear. For sufficiently thin velocity layers, thermal diffusion reduced the effect of stratification, allowing vertical shear instabilities to develop at sufficiently large  $Re$ . These two effects combined to drive turbulence that can cause substantial vertical mixing. We found that four distinct dynamical regimes naturally emerged, depending upon  $Re$  and the strength of the stratification.

The importance of the parameter  $BPe$  that emerged in the LPN equations was confirmed using turbulent flow diagnostics from a broad range of simulations. By considering dominant balances in the governing equations, we derived scaling laws which explained these empirical observations. In particular, the stratified turbulent regime, defined by a constant mixing efficiency  $\eta \simeq 0.4$ , was associated with vertical eddy length scales  $l_z \sim (BPe)^{-1/3}$  and velocity scales  $w_{rms} \sim (BPe)^{-1/3}$ , giving a non-dimensional vertical transport diffusivity  $D_{turb} \sim (BPe)^{-1/2}$  that matched the prediction from Zahn’s model. Nevertheless, most stars are actually in the high  $Pe$  but low  $Pr$  limit and are subject to additional ingredients including rotation, magnetism and the presence of vertical shear, all of which will need to be accounted for in future research in order to construct a truly astrophysically-relevant theory of stratified turbulence.

# References

- Allawala, A., Tobias, S. M., and Marston, J. B. (2020). Dimensional reduction of direct statistical simulation. *Journal of Fluid Mechanics*, 898:A21.
- Andrews, D. G. and McIntyre, M. E. (1976). Planetary waves in horizontal and vertical shear: The generalized Eliassen-Palm relation and the mean zonal acceleration. *Journal of the Atmospheric Sciences*, 33(11):2031–2048.
- Arobone, E. and Sarkar, S. (2012). Evolution of a stratified rotating shear layer with horizontal shear. Part I. Linear stability. *J. Fluid Mech.*, 703:29–48.
- Asay-Davis, X. S., Marcus, P. S., Wong, M. H., and de Pater, I. (2011). Changes in Jupiter's zonal velocity between 1979 and 2008. *Icarus*, 211(2):1215–1232.
- Ashkenazy, Y. and Tziperman, E. (2016). Variability, instabilities, and eddies in a snowball ocean. *Journal of Climate*, 29(2):869–888.
- Bakas, N. A., Constantinou, N. C., and Ioannou, P. J. (2015). S3T stability of the homogeneous state of barotropic beta-plane turbulence. *Journal of the Atmospheric Sciences*, 72(5):1689–1712.
- Bakas, N. A. and Ioannou, P. J. (2013). Emergence of large scale structure in barotropic  $\beta$ -plane turbulence. *Phys. Rev. Lett.*, 110:224501.
- Bakas, N. A. and Ioannou, P. J. (2014). A theory for the emergence of coherent structures in beta-plane turbulence. *Journal of Fluid Mechanics*, 740:312–341.
- Balmforth, N. J. and Young, Y.-N. (2002). Stratified Kolmogorov flow. *J. Fluid Mech.*, 450:131–167.
- Barnes, E. A. and Polvani, L. (2013). Response of the midlatitude jets, and of their variability, to increased greenhouse gases in the cmip5 models. *Journal of Climate*, 26(18):7117–7135.
- Barrado-Izaguirre, N., Pérez-Hoyos, S., and Sánchez-Lavega, A. (2009). Brightness power spectral distribution and waves in Jupiter's upper cloud and hazes. *Icarus*, 202(1):181–196.
- Batchelor, G. K. (1969). Computation of the energy spectrum in homogeneous two-dimensional turbulence. *The Physics of Fluids*, 12(12):II-233–II-239.
- Beaumont, D. N. (1981). The stability of spatially periodic flows. *J. Fluid Mech.*, 108:461–474.
- Beck, P. G., Montalbán, J., Kallinger, T., De Ridder, J., Aerts, C., García, R. A., Hekker, S., Dupret, M.-A., Mosser, B., Eggenberger, P., Stello, D., Elsworth, Y., Frandsen, S., Carrier, F., Hillen, M., Gruberbauer, M., Christensen-Dalsgaard, J., Miglio, A., Valentini, M., Bedding, T. R., Kjeldsen, H., Girouard, F. R., Hall, J. R., and Ibrahim, K. A. (2012). Fast core rotation in red-giant stars as revealed by gravity-dominated mixed modes. *Nature*, 481(7379):55–57.
- Beebe, R. F., Ingersoll, A. P., Hunt, G. E., Mitchell, J. L., and Müller, J.-P. (1980). Measurements of wind vectors, eddy momentum transports, and energy conversions in Jupiter's atmosphere from Voyager 1 images. *Geophysical Research Letters*, 7(1):1–4.
- Bellman, R. E. (1957). *Dynamic Programming*. Princeton University Press.
- Bellman, R. E. (1961). *Adaptive Control Processes: A Guided Tour*. Princeton University Press.

- Benomar, O., Bazot, M., Nielsen, M. B., Gizon, L., Sekii, T., Takata, M., Hotta, H., Hanasoge, S., Sreenivasan, K., and Christensen-Dalsgaard, J. (2018). Asteroseismic detection of latitudinal differential rotation in 13 sun-like stars. *Science*, 361(6408):1231–1234.
- Berloff, P., Kamenkovich, I., and Pedlosky, J. (2009). A model of multiple zonal jets in the oceans: Dynamical and kinematical analysis. *Journal of Physical Oceanography*, 39(11):2711–2734.
- Berloff, P., Karabasov, S., Farrar, J. T., and Kamenkovich, I. (2011). On latency of multiple zonal jets in the oceans. *Journal of Fluid Mechanics*, 686:534–567.
- Billant, P. and Chomaz, J. (2000). Experimental evidence for a new instability of a vertical columnar vortex pair in a strongly stratified fluid. *J. Fluid Mech.*, 418:167–188.
- Billant, P. and Chomaz, J. (2001). Self-similarity of strongly stratified inviscid flows. *Phys. Fluids*, 13:1645–1651.
- Boffetta, G. and Ecke, R. E. (2012). Two-dimensional turbulence. *Annual Review of Fluid Mechanics*, 44(1):427–451.
- Bolton, S. J., Adriani, A., Adumitroaie, V., Allison, M., Anderson, J., Atreya, S., Bloxham, J., Brown, S., Connerney, J. E. P., DeJong, E., Folkner, W., Gautier, D., Grassi, D., Gulkis, S., Guillot, T., Hansen, C., Hubbard, W. B., Iess, L., Ingersoll, A., Janssen, M., Jorgensen, J., Kaspi, Y., Levin, S. M., Li, C., Lunine, J., Miguel, Y., Mura, A., Orton, G., Owen, T., Ravine, M., Smith, E., Steffes, P., Stone, E., Stevenson, D., Thorne, R., Waite, J., Durante, D., Ebert, R. W., Greathouse, T. K., Hue, V., Parisi, M., Szalay, J. R., and Wilson, R. (2017). Jupiter’s interior and deep atmosphere: The initial pole-to-pole passes with the juno spacecraft. *Science*, 356(6340):821–825.
- Bouchet, F., Grafke, T., Tangarife, T., and Vanden-Eijnden, E. (2016). Large deviations in fast–slow systems. *Journal of Statistical Physics*, 162:793–812.
- Bouchet, F., Marston, J. B., and Tangarife, T. (2018). Fluctuations and large deviations of reynolds stresses in zonal jet dynamics. *Physics of Fluids*, 30(1):015110.
- Bouchet, F., Nardini, C., and Tangarife, T. (2013). Kinetic theory of jet dynamics in the stochastic barotropic and 2D navier-stokes equations. *Journal of Statistical Physics*, 153(4):572–625.
- Bouchet, F., Nardini, C., and Tangarife, T. (2014). Stochastic averaging, large deviations and random transitions for the dynamics of 2D and geostrophic turbulent vortices. *Fluid Dynamics Research*, 46(6):061416.
- Bouchet, F., Rolland, J., and Simonnet, E. (2019). Rare event algorithm links transitions in turbulent flows with activated nucleations. *Phys. Rev. Lett.*, 122:074502.
- Bouchet, F. and Simonnet, E. (2009). Random changes of flow topology in two-dimensional and geophysical turbulence. *Phys. Rev. Lett.*, 102:094504.
- Bouchet, F. and Venaille, A. (2012). Statistical mechanics of two-dimensional and geophysical flows. *Physics Reports*, 515(5):227–295.
- Brethouwer, G., Billant, P., Lindborg, E., and Chomaz, J. M. (2007). Scaling analysis and simulation of strongly stratified turbulent flows. *J. Fluid Mech.*, 585:343–368.
- Bühler, O. (2014). *Waves and Mean Flows*. Cambridge Monographs on Mechanics. Cambridge University Press, 2 edition.
- Cérou, F., Guyader, A., and Rousset, M. (2019). Adaptive multilevel splitting: Historical perspective and recent results. *Chaos: An Interdisciplinary Journal of Nonlinear Science*, 29(4):043108.
- Chan, C. J., Plumb, R. A., and Cerovecki, I. (2007). Annular modes in a multiple migrating zonal jet regime. *Journal of the Atmospheric Sciences*, 64(11):4053–4068.

- Chang, E. K. M., Guo, Y., and Xia, X. (2012). CMIP5 multimodel ensemble projection of storm track change under global warming. *Journal of Geophysical Research: Atmospheres*, 117(D23):D23118.
- Charney, J. G. (1948). On the scale of atmospheric motions. *Geofys. Publ. Oslo.*, 17(2):1–17.
- Chekhlov, A., Orszag, S. A., Sukoriansky, S., Galperin, B., and Staroselsky, I. (1996). The effect of small-scale forcing on large-scale structures in two-dimensional flows. *Physica D: Nonlinear Phenomena*, 98(2):321–334.
- Chemke, R. and Kaspi, Y. (2015a). The latitudinal dependence of atmospheric jet scales and macroturbulent energy cascades. *Journal of the Atmospheric Sciences*, 72(10):3891–3907.
- Chemke, R. and Kaspi, Y. (2015b). Poleward migration of eddy-driven jets. *Journal of Advances in Modeling Earth Systems*, 7(3):1457–1471.
- Christensen-Dalsgaard, J. and Schou, J. (1988). Differential rotation in the solar interior. In Rolfe, E. J., editor, *Seismology of the Sun and Sun-Like Stars*, volume 286 of *ESA Special Publication*, pages 149–153.
- Connaughton, C. P., Nadiga, B. T., Nazarenko, S. V., and Quinn, B. E. (2010). Modulational instability of rossby and drift waves and generation of zonal jets. *Journal of Fluid Mechanics*, 654:207–231.
- Constantinou, N. C., Farrell, B. F., and Ioannou, P. J. (2014). Emergence and equilibration of jets in beta-plane turbulence: Applications of stochastic structural stability theory. *Journal of the Atmospheric Sciences*, 71(5):1818–1842.
- Constantinou, N. C., Farrell, B. F., and Ioannou, P. J. (2016). Statistical state dynamics of jet–wave coexistence in barotropic beta-plane turbulence. *Journal of the Atmospheric Sciences*, 73(5):2229–2253.
- Cope, L. (2019). Horizontal shear instabilities in the stellar regime. Technical report, 2018 Geophysical Fluid Dynamics Program of Study, Woods Hole Oceanographic Institution Technical Report. (in press).
- Cope, L., Garaud, P., and Caulfield, C. P. (2020). The dynamics of stratified horizontal shear flows at low pécllet number. *Journal of Fluid Mechanics*, 903:A1.
- Coumou, D., Lehmann, J., and Beckmann, J. (2015). The weakening summer circulation in the northern hemisphere mid-latitudes. *Science*, 348(6232):324–327.
- Cravatte, S., Kestenare, E., and Marin, F. (2017). Subthermocline and intermediate zonal currents in the tropical pacific ocean: Paths and vertical structure. *Journal of Physical Oceanography*, 47(9):2305–2324.
- Danilov, S. and Gurarie, D. (2004). Scaling, spectra and zonal jets in beta-plane turbulence. *Physics of Fluids*, 16(7):2592–2603.
- Deloncle, A., Chomaz, J. M., and Billant, P. (2007). Three-dimensional stability of a horizontally sheared flow in a stably stratified fluid. *J. Fluid Mech.*, 570:297–305.
- DelSole, T. (2004). Stochastic models of quasigeostrophic turbulence. *Surveys in Geophysics*, 25(2):107–149.
- DelSole, T. and Farrell, B. F. (1996). The quasi-linear equilibration of a thermally maintained, stochastically excited jet in a quasigeostrophic model. *Journal of the Atmospheric Sciences*, 53(13):1781–1797.
- Dickey, J., Marcus, S., and Hide, R. (1992). Global propagation of interannual fluctuations in atmospheric angular momentum. *Nature*, 357(6378):484–488.
- Dickinson, R. E. (1969). Theory of planetary wave-zonal flow interaction. *Journal of the Atmospheric Sciences*, 26(1):73–81.
- Dougherty, J. (1961). The anisotropy of turbulence at the meteor level. *Journal of Atmospheric and Terrestrial Physics*, 21(2):210 – 213.

- Dritschel, D. G. and McIntyre, M. E. (2008). Multiple jets as pv staircases: The phillips effect and the resilience of eddy-transport barriers. *Journal of the Atmospheric Sciences*, 65(3):855–874.
- Dritschel, D. G. and Scott, R. K. (2011). Jet sharpening by turbulent mixing. *Philosophical Transactions of the Royal Society A: Mathematical, Physical and Engineering Sciences*, 369(1937):754–770.
- Dudis, J. J. (1974). The stability of a thermally radiating stratified shear layer, including self-absorption. *J. Fluid Mech.*, 64:65–83.
- Dunkerton, T. J. and Scott, R. K. (2008). A barotropic model of the angular momentum–conserving potential vorticity staircase in spherical geometry. *Journal of the Atmospheric Sciences*, 65(4):1105–1136.
- Eichelberger, S. J. and Hartmann, D. L. (2007). Zonal jet structure and the leading mode of variability. *Journal of Climate*, 20(20):5149–5163.
- Eliassen, A. and Palm, E. (1960). On the transfer of energy in stationary mountain waves. *Geofys Publ.*, 22(3):1–23.
- Falder, M., White, N. J., and Caulfield, C. P. (2016). Seismic imaging of rapid onset of stratified turbulence in the South Atlantic Ocean. *Journal of Physical Oceanography*, 46:1023–1044.
- Farrell, B. F. and Ioannou, P. J. (2003). Structural stability of turbulent jets. *Journal of the Atmospheric Sciences*, 60(17):2101–2118.
- Farrell, B. F. and Ioannou, P. J. (2007). Structure and spacing of jets in barotropic turbulence. *Journal of the Atmospheric Sciences*, 64(10):3652–3665.
- Feldstein, S. B. (1998). An observational study of the intraseasonal poleward propagation of zonal mean flow anomalies. *Journal of the Atmospheric Sciences*, 55(15):2516–2529.
- Ferrari, R. and Wunsch, C. (2009). Ocean circulation kinetic energy: reservoirs, sources, and sinks. *Annu. Rev. Fluid Mech.*, 41:253–282.
- Fjørtoft, R. (1953). On the changes in the spectral distribution of kinetic energy for twodimensional, nondivergent flow. *Tellus*, 5(3):225–230.
- Frishman, A., Laurie, J., and Falkovich, G. E. (2017). Jets or vortices - what flows are generated by an inverse turbulent cascade? *Physical Review Fluids*, 2(3):032602.
- Gagnier, D. and Garaud, P. (2018). Turbulent transport by diffusive stratified shear flows: from local to global Models. II. Limitations of local models. *Astrophys. J.*, 862(1):36.
- Galperin, B. and Read, P. L. (2019). *Zonal Jets: Phenomenology, Genesis, and Physics*. Cambridge University Press.
- Galperin, B., Sukoriansky, S., and Dikovskaya, N. (2008). Zonostrophic turbulence. *Physica Scripta*, T132:014034.
- Galperin, B., Sukoriansky, S., and Dikovskaya, N. (2010). Geophysical flows with anisotropic turbulence and dispersive waves: flows with a  $\beta$ -effect. *Ocean Dynamics*, 60(2):427–441.
- Galperin, B., Sukoriansky, S., Dikovskaya, N., Read, P. L., Yamazaki, Y. H., and Wordsworth, R. (2006). Anisotropic turbulence and zonal jets in rotating flows with a  $\beta$ -effect. *Nonlinear Processes in Geophysics*, 13(1):83–98.
- Galperin, B., Sukoriansky, S., and Huang, H.-P. (2001). Universal  $n^{-5}$  spectrum of zonal flows on giant planets. *Physics of Fluids*, 13(6):1545–1548.
- Galperin, B., Sukoriansky, S., Young, R. M. B., Chemke, R., Kaspi, Y., Read, P. L., and Dikovskaya, N. (2019). Barotropic and zonostrophic turbulence. In Galperin, B. and Read, P. L. E., editors, *Zonal Jets: Phenomenology, Genesis, and Physics*, page 220–237. Cambridge University Press.

- Galperin, B., Young, R. M., Sukoriansky, S., Dikovskaya, N., Read, P. L., Lancaster, A. J., and Armstrong, D. (2014). Cassini observations reveal a regime of zonostrophic macroturbulence on jupiter. *Icarus*, 229:295–320.
- Garanaik, A. and Venayagamoorthy, S. K. (2019). On the inference of the state of turbulence and mixing efficiency in stably stratified flows. *J. Fluid Mech.*, 867:323–333.
- Garaud, P. (2001). Latitudinal shear instability in the solar tachocline. *Mon. Not. Roy. Ast. Soc.*, 324(1):68–76.
- Garaud, P. (2020). Horizontal shear instabilities at low prandtl number. *Astrophys. J.* (in press).
- Garaud, P., Gagnier, D., and Verhoeven, J. (2017). Turbulent transport by diffusive stratified shear flows: from local to global models. I. Numerical simulations of a stratified plane couette flow. *Astrophys. J.*, 837:133.
- Garaud, P., Gallet, B., and Bischoff, T. (2015a). The stability of stratified spatially periodic shear flows at low pécelet number. *Physics of Fluids*, 27(8):084104.
- Garaud, P. and Kulenthirarajah, L. (2016). Turbulent transport in a strongly stratified forced shear layer with thermal diffusion. *Astrophys. J.*, 821:49.
- Garaud, P., Medrano, M., Brown, J. M., Mankovich, C., and Moore, K. (2015b). Excitation of gravity waves by fingering convection, and the formation of compositional staircases in stellar interiors. *Astrophys. J.*, 808:89.
- García-Melendo, E., Arregi, J., Rojas, J., Hueso, R., Barrado-Izagirre, N., Gómez-Forrellad, J., Pérez-Hoyos, S., Sanz-Requena, J., and Sánchez-Lavega, A. (2011). Dynamics of jupiter’s equatorial region at cloud top level from cassini and hst images. *Icarus*, 211(2):1242–1257.
- Godeferd, F. S. and Staquet, C. (2003). Statistical modelling and direct numerical simulations of decaying stably stratified turbulence. Part 2. large-scale and small-scale anisotropy. *J. Fluid Mech.*, 486:115–159.
- Goode, P. R., Dziembowski, W. A., Korzennik, S. G., and Rhodes, E. J., J. (1991). What we know about the Sun’s internal rotation from solar oscillations. *Astrophys. J.*, 367:649.
- Guervilly, C. and Hughes, D. W. (2017). Jets and large-scale vortices in rotating rayleigh-bénard convection. *Phys. Rev. Fluids*, 2:113503.
- Hadley, G. (1735). Concerning the cause of the general trade-winds. *Philosophical Transactions of the Royal Society of London*, 39(437):58–62.
- Haynes, P. H., Poet, D. A., and Shuckburgh, E. F. (2007). Transport and mixing in kinematic and dynamically consistent flows. *Journal of the Atmospheric Sciences*, 64(10):3640–3651.
- Heimpel, M., Aurnou, J., and Wicht, J. (2005). Simulation of equatorial and high-latitude jets on jupiter in a deep convection model. *Nature*, 438(7065):193–196.
- Held, I. M. (1999). The macroturbulence of the troposphere. *Tellus A: Dynamic Meteorology and Oceanography*, 51(1):59–70.
- Held, I. M. and Hoskins, B. J. (1985). Large-scale eddies and the general circulation of the troposphere. In Saltzman, B., editor, *Issues in Atmospheric and Oceanic Modeling*, volume 28 of *Advances in Geophysics*, pages 3–31. Elsevier.
- Heywood, K. J., Sparrow, M. D., Brown, J., and Dickson, R. R. (1999). Frontal structure and antarctic bottom water flow through the princess elizabeth trough, antarctica. *Deep Sea Research Part I: Oceanographic Research Papers*, 46(7):1181–1200.
- Hide, R. (1966). On the circulation of the atmospheres of jupiter and saturn. *Planetary and Space Science*, 14(8):669–675.

- Hide, R. (1969). Dynamics of the atmospheres of the major planets with an appendix on the viscous boundary layer at the rigid bounding surface of an electrically-conducting rotating fluid in the presence of a magnetic field. *Journal of the Atmospheric Sciences*, 26(5):841–853.
- Holford, J. M. and Linden, P. (1999). Turbulent mixing in stratified fluid. *Dyn. Atmos. Oceans*, 30:173–198.
- Howard, L. N. (1961). Note on a paper of John W. Miles. *J. Fluid Mech.*, 10:509–512.
- Huang, H.-P., Galperin, B., and Sukoriansky, S. (2001). Anisotropic spectra in two-dimensional turbulence on the surface of a rotating sphere. *Physics of Fluids*, 13(1):225–240.
- Huang, H.-P. and Robinson, W. A. (1998). Two-dimensional turbulence and persistent zonal jets in a global barotropic model. *Journal of the Atmospheric Sciences*, 55(4):611–632.
- Hughes, D. W., Rosner, R., and Weiss, N. O. (2007). *The Solar Tachocline*. Cambridge University Press.
- Ingersoll, A. P., Beebe, R. F., Mitchell, J. L., Garneau, G. W., Yagi, G. M., and Müller, J.-P. (1981). Interaction of eddies and mean zonal flow on jupiter as inferred from voyager 1 and 2 images. *Journal of Geophysical Research: Space Physics*, 86(A10):8733–8743.
- Ingersoll, A. P., Gierasch, P. J., Banfield, D., Vasavada, A. R., and Galileo Imaging Team (2000). Moist convection as an energy source for the large-scale motions in jupiter’s atmosphere. *Nature*, 403(6770):630–632.
- Ivey, G. N., Winters, K. B., and Koseff, J. R. (2008). Density stratification, turbulence, but how much mixing? *Annu. Rev. Fluid Mech.*, 40:169–184.
- James, I. N. and Dodd, J. P. (1996). A mechanism for the low-frequency variability of the mid-latitude troposphere. *Quarterly Journal of the Royal Meteorological Society*, 122(533):1197–1210.
- James, P. M., Fraedrich, K., and James, I. N. (1994). Wave-zonal-flow interaction and ultra-low-frequency variability in a simplified global circulation model. *Quarterly Journal of the Royal Meteorological Society*, 120(518):1045–1067.
- Jeffreys, H. (1926). On the dynamics of geostrophic winds. *Quarterly Journal of the Royal Meteorological Society*, 52(217):85–104.
- Kaspi, Y. and Flierl, G. R. (2007). Formation of jets by baroclinic instability on gas planet atmospheres. *Journal of the Atmospheric Sciences*, 64(9):3177–3194.
- Kaspi, Y., Galanti, E., Hubbard, W. B., Stevenson, D. J., Bolton, S. J., Iess, L., Guillot, T., Bloxham, J., Connerney, J. E. P., Cao, H., Durante, D., Folkner, W. M., Helled, R., Ingersoll, A. P., Levin, S. M., Lunine, J. I., Miguel, Y., Militzer, B., Parisi, M., and Wahl, S. M. (2018). Jupiter’s atmospheric jet streams extend thousands of kilometres deep. *Nature*, 555(7695):223–226.
- Kolmogorov, A. N. (1941). The local structure of turbulence in incompressible viscous fluid for very large reynolds’ numbers. *Akademiia Nauk SSSR Doklady*, 30:301–305.
- Kolmogorov, A. N. (1962). A refinement of previous hypotheses concerning the local structure of turbulence in a viscous incompressible fluid at high reynolds number. *Journal of Fluid Mechanics*, 13(1):82–85.
- Kong, D., Zhang, K., Schubert, G., and Anderson, J. D. (2018). Origin of jupiter’s cloud-level zonal winds remains a puzzle even after juno. *Proceedings of the National Academy of Sciences*, 115(34):8499–8504.
- Kraichnan, R. H. (1967). Inertial ranges in two-dimensional turbulence. *The Physics of Fluids*, 10(7):1417–1423.
- Kulenthirarajah, L. and Garaud, P. (2018). Turbulent transport by diffusive stratified shear flows: from local to global models. III. A closure model. *Astrophys. J.*, 864(2):107.
- Kuo, H.-I. (1951). Vorticity transfer as related to the development of the general circulation. *Journal of Meteorology*, 8(5):307–315.

- Laurie, J., Boffetta, G., Falkovich, G., Kolokolov, I., and Lebedev, V. (2014). Universal profile of the vortex condensate in two-dimensional turbulence. *Phys. Rev. Lett.*, 113:254503.
- Lee, S. (1997). Maintenance of multiple jets in a baroclinic flow. *Journal of the Atmospheric Sciences*, 54(13):1726–1738.
- Leith, C. E. (1968). Diffusion approximation for two-dimensional turbulence. *The Physics of Fluids*, 11(3):671–672.
- Lignières, F. (1999). The small-Péclet-number approximation in stellar radiative zones. *Astron. Astrophys.*, 348:933–939.
- Lignières, F. (2018). Turbulence in stably stratified radiative zones. In M. Rieutord, I. Baraffe, Y. L., editor, *Multi-Dimensional processes in stellar physics*, *Proceedings of the Evry Schatzman School 2018*, EDP Sciences Proceedings.
- Lilly, D. K. (1969). Numerical simulation of two-dimensional turbulence. *The Physics of Fluids*, 12(12):240–249.
- Lilly, D. K. (1983). Stratified turbulence and the mesoscale variability of the atmosphere. *J. Atmos. Sci.*, 40:749–761.
- Limaye, S. S. (1986). Jupiter: New estimates of the mean zonal flow at the cloud level. *Icarus*, 65(2):335–352.
- Lindborg, E. (2006). The energy cascade in a strongly stratified fluid. *Journal of Fluid Mechanics*, 550:207–242.
- Liu, J., Goldreich, P. M., and Stevenson, D. J. (2008). Constraints on deep-seated zonal winds inside jupiter and saturn. *Icarus*, 196(2):653 – 664.
- Lorenz, E. N. (1967). *The Nature and Theory of the General Circulation of the Atmosphere*, volume 218. World Meteorological Organization.
- Lucas, D., Caulfield, C. P., and Kerswell, R. R. (2017). Layer formation in horizontally forced stratified turbulence: connecting exact coherent structures to linear instabilities. *J. Fluid Mech.*, 832:409–437.
- Maffioli, A., Brethouwer, G., and Lindborg, E. (2016). Mixing efficiency in stratified turbulence. *J. Fluid Mech.*, 794:R3.
- Maltrud, M. E. and Vallis, G. K. (1991). Energy spectra and coherent structures in forced two-dimensional and beta-plane turbulence. *Journal of Fluid Mechanics*, 228:321–342.
- Manfroi, A. J. and Young, W. R. (1999). Slow evolution of zonal jets on the beta plane. *Journal of the Atmospheric Sciences*, 56(5):784–800.
- Marston, J. B., Chini, G. P., and Tobias, S. M. (2016). Generalized quasilinear approximation: Application to zonal jets. *Phys. Rev. Lett.*, 116:214501.
- Marston, J. B., Conover, E., and Schneider, T. (2008). Statistics of an unstable barotropic jet from a cumulant expansion. *Journal of the Atmospheric Sciences*, 65(6):1955–1966.
- Marston, J. B., Qi, W., and Tobias, S. M. (2019). Direct statistical simulation of a jet. In Galperin, B. and Read, P. L. E., editors, *Zonal Jets: Phenomenology, Genesis, and Physics*, page 332–346. Cambridge University Press.
- Maximenko, N. A., Bang, B., and Sasaki, H. (2005). Observational evidence of alternating zonal jets in the world ocean. *Geophysical Research Letters*, 32(12):L12607.
- Maximenko, N. A., Melnichenko, O. V., Niiler, P. P., and Sasaki, H. (2008). Stationary mesoscale jet-like features in the ocean. *Geophysical Research Letters*, 35(8):L08603.

- McWilliams, J. C. (1984). The emergence of isolated coherent vortices in turbulent flow. *Journal of Fluid Mechanics*, 146:21–43.
- Mestel, L. (2012). *Stellar magnetism*. Oxford University Press.
- Miles, J. W. (1961). On the stability of heterogeneous shear flows. *J. Fluid Mech.*, 10:496–508.
- Naveira Garabato, A. C., Ferrari, R., and Polzin, K. L. (2011). Eddy stirring in the southern ocean. *Journal of Geophysical Research: Oceans*, 116(C9):C09019.
- Nozawa, T. and Yoden, S. (1997). Formation of zonal band structure in forced two-dimensional turbulence on a rotating sphere. *Physics of Fluids*, 9(7):2081–2093.
- Oetzel, K. G. and Vallis, G. K. (1997). Strain, vortices, and the enstrophy inertial range in two-dimensional turbulence. *Physics of Fluids*, 9(10):2991–3004.
- Ogletorpe, R. L. F., Caulfield, C. P., and Woods, A. W. (2013). Spontaneous layering in stratified turbulent Taylor-Couette flow. *J. Fluid Mech.*, 721:R3.
- O’Gorman, P. A. and Schneider, T. (2007). Recovery of atmospheric flow statistics in a general circulation model without nonlinear eddy-eddy interactions. *Geophysical Research Letters*, 34(22):L22801.
- Orszag, S. A. (1971). On the elimination of aliasing in finite-difference schemes by filtering high-wavenumber components. *Journal of the Atmospheric Sciences*, 28(6):1074–1074.
- Ozmidov, R. V. (1965). On the turbulent exchange in a stably stratified ocean. *Atmos. Oceanic Phys.*, 1:853–860.
- Panetta, R. L. (1993). Zonal jets in wide baroclinically unstable regions: Persistence and scale selection. *Journal of the Atmospheric Sciences*, 50(14):2073–2106.
- Park, J., Prat, V., and Mathis, S. (2020). Horizontal shear instabilities in rotating stellar radiation zones. *Astron. Astrophys.*, 635:A133.
- Park, Y., Whitehead, J. A., and Gnanadeskian, A. (1994). Turbulent mixing in stratified fluids: layer formation and energetics. *J. Fluid Mech.*, 279:279–311.
- Parker, J. B. and Krommes, J. A. (2013). Zonal flow as pattern formation. *Physics of Plasmas*, 20(10):100703.
- Peixóto, J. P. and Oort, A. H. (1984). Physics of climate. *Rev. Mod. Phys.*, 56:365–429.
- Peyret, R. (2002). *Spectral Methods for Incompressible Viscous Flow*. Springer.
- Phillips, O. (1972). Turbulence in a strongly stratified fluid—is it unstable? *Deep Sea Research and Oceanographic Abstracts*, 19(1):79–81.
- Portwood, G. D., de Bruyn Kops, S. M., Taylor, J. R., Salehipour, H., and Caulfield, C. P. (2016). Robust identification of dynamically distinct regions in stratified turbulence. *J. Fluid Mech.*, 807:R2.
- Prat, V., Guilet, J., Viallet, M., and Müller, E. (2016). Shear mixing in stellar radiative zones. II. Robustness of numerical simulations. *Astron. Astrophys.*, 592:A59.
- Prat, V. and Lignières, F. (2013). Turbulent transport in radiative zones of stars. *Astron. Astrophys.*, 551:L3.
- Prat, V. and Lignières, F. (2014). Shear mixing in stellar radiative zones. I. Effect of thermal diffusion and chemical stratification. *Astron. Astrophys.*, 566:A110.
- Read, P., Kennedy, D., Lewis, N., Scolan, H., Tabataba-Vakili, F., Wang, Y., Wright, S., and Young, R. (2020). Baroclinic and barotropic instabilities in planetary atmospheres: energetics, equilibration and adjustment. *Nonlinear Processes in Geophysics*, 27(2):147–173.
- Rhines, P. B. (1975). Waves and turbulence on a beta-plane. *Journal of Fluid Mechanics*, 69(3):417–443.

- Riehl, H., Yeh, T. C., and La seur, N. E. (1950). A study of variations of the general circulation. *Journal of Meteorology*, 7(3):181–194.
- Riley, J. J. and Lelong, M. (2000). Fluid Motions in the Presence of Strong Stable Stratification. *Annu. Rev. Fluid Mech.*, 32:613–657.
- Rolland, J. and Simonnet, E. (2015). Statistical behaviour of adaptive multilevel splitting algorithms in simple models. *Journal of Computational Physics*, 283:541–558.
- Rossby, C.-G. (1939). Relation between variations in the intensity of the zonal circulation of the atmosphere and the displacements of the semi-permanent centers of action. *Journal of Marine Research*, 2(1):38–55.
- Ruddick, B., McDougall, T., and Turner, J. (1989). The formation of layers in a uniformly stirred density gradient. *Deep Sea Research Part A. Oceanographic Research Papers*, 36(4):597–609.
- Ruiz, D. E., Parker, J. B., Shi, E. L., and Dodin, I. Y. (2016). Zonal-flow dynamics from a phase-space perspective. *Physics of Plasmas*, 23(12):122304.
- Salyk, C., Ingersoll, A. P., Lorre, J., Vasavada, A., and Del Genio, A. D. (2006). Interaction between eddies and mean flow in jupiter’s atmosphere: Analysis of cassini imaging data. *Icarus*, 185(2):430–442.
- Scaife, A. A., Camp, J., Comer, R., Davis, P., Dunstone, N., Gordon, M., MacLachlan, C., Martin, N., Nie, Y., Ren, H.-L., Roberts, M., Robinson, W., Smith, D., and Vidale, P. L. (2019). Does increased atmospheric resolution improve seasonal climate predictions? *Atmospheric Science Letters*, 20(8):e922.
- Schatzman, E. and Baglin, A. (1991). On the physics of lithium depletion. *Astron. Astrophys.*, 249:125.
- Schneider, T. and Walker, C. C. (2006). Self-organization of atmospheric macroturbulence into critical states of weak nonlinear eddy–eddy interactions. *Journal of the Atmospheric Sciences*, 63(6):1569–1586.
- Schou, J., Antia, H. M., Basu, S., Bogart, R. S., Bush, R. I., Chitre, S. M., Christensen-Dalsgaard, J., Mauro, M. P. D., Dziembowski, W. A., Eff-Darwich, A., Gough, D. O., Haber, D. A., Hoeksema, J. T., Howe, R., Korzennik, S. G., Kosovichev, A. G., Larsen, R. M., Pijpers, F. P., Scherrer, P. H., Sekii, T., Tarbell, T. D., Title, A. M., Thompson, M. J., and Toomre, J. (1998). Helioseismic studies of differential rotation in the solar envelope by the solar oscillations investigation using the michelson doppler imager. *The Astrophysical Journal*, 505(1):390–417.
- Scott, R. K. and Dritschel, D. G. (2012). The structure of zonal jets in geostrophic turbulence. *Journal of Fluid Mechanics*, 711:576–598.
- Scott, R. K. and Polvani, L. M. (2007). Forced-dissipative shallow-water turbulence on the sphere and the atmospheric circulation of the giant planets. *Journal of the Atmospheric Sciences*, 64(9):3158–3176.
- Scott, R. K. and Polvani, L. M. (2008). Equatorial superrotation in shallow atmospheres. *Geophysical Research Letters*, 35(24):L24202.
- Scott, R. K. and Tissier, A.-S. (2012). The generation of zonal jets by large-scale mixing. *Physics of Fluids*, 24(12):126601.
- Simmons, A. J. and Hoskins, B. J. (1978). The life cycles of some nonlinear baroclinic waves. *Journal of the Atmospheric Sciences*, 35(3):414–432.
- Smith, S. A. and Hammett, G. W. (1997). Eddy viscosity and hyperviscosity in spectral simulations of 2D drift wave turbulence. *Physics of Plasmas*, 4(4).
- Sokolov, S. and Rintoul, S. R. (2007). Multiple jets of the antarctic circumpolar current south of australia. *Journal of Physical Oceanography*, 37(5):1394–1412.
- Spiegel, E. A. (1962). Thermal turbulence at very small Prandtl number. *J. Geophys. Res.*, 67:3063–3070.
- Spiegel, E. A. and Veronis, G. (1960). On the Boussinesq Approximation for a Compressible Fluid. *Astrophys. J.*, 131:442.

- Spiegel, E. A. and Zahn, J.-P. (1992). The solar tachocline. *Astronomy and Astrophysics*, 265:106–114.
- Squire, H. B. (1933). On the stability for three-dimensional disturbances of viscous fluid flow between parallel walls. *Proc. R. Soc. Lond. A*, 142:621–628.
- Srinivasan, K. and Young, W. R. (2012). Zonostrophic instability. *Journal of the Atmospheric Sciences*, 69(5):1633–1656.
- Srinivasan, K. and Young, W. R. (2014). Reynolds stress and eddy diffusivity of  $\beta$ -plane shear flows. *Journal of the Atmospheric Sciences*, 71(6):2169–2185.
- Starr, V. P. (1953). Note concerning the nature of the large-scale eddies in the atmosphere. *Tellus*, 5(4):494–498.
- Starr, V. P. (1968). *Physics of negative viscosity phenomena*. Earth and planetary science series. McGraw-Hill.
- Stellmach, S., Traxler, A., Garaud, P., Brummell, N., and Radko, T. (2011). Dynamics of fingering convection. Part 2 The formation of thermohaline staircases. *J. Fluid Mech.*, 677:554–571.
- Sukoriansky, S., Dikovskaya, N., and Galperin, B. (2007). On the arrest of inverse energy cascade and the rhines scale. *Journal of the Atmospheric Sciences*, 64(9):3312–3327.
- Sukoriansky, S., Dikovskaya, N., and Galperin, B. (2008). Nonlinear waves in zonostrophic turbulence. *Phys. Rev. Lett.*, 101:178501.
- Sukoriansky, S., Dikovskaya, N., Grimshaw, R., and Galperin, B. (2012). Rossby waves and zonons in zonostrophic turbulence. *AIP Conference Proceedings*, 1439(1):111–122.
- Sukoriansky, S., Galperin, B., and Dikovskaya, N. (2002). Universal spectrum of two-dimensional turbulence on a rotating sphere and some basic features of atmospheric circulation on giant planets. *Phys. Rev. Lett.*, 89:124501.
- Taylor, G. I. (1915). Eddy motion in the atmosphere. *Philosophical Transactions of the Royal Society of London. Series A*, 215(523-537):1–26.
- Thompson, M. J., Toomre, J., Anderson, E. R., Antia, H. M., Berthomieu, G., Burtonclay, D., Chitre, S. M., Christensen-Dalsgaard, J., Corbard, T., DeRosa, M., Genovese, C. R., Gough, D. O., Haber, D. A., Harvey, J. W., Hill, F., Howe, R., Korzennik, S. G., Kosovichev, A. G., Leibacher, J. W., Pijpers, F. P., Provost, J., Rhodes, E. J., Schou, J., Sekii, T., Stark, P. B., and Wilson, P. R. (1996). Differential rotation and dynamics of the solar interior. *Science*, 272(5266):1300–1305.
- Thual, O. (1992). Zero-Prandtl-number convection. *J. Fluid Mech.*, 240:229–258.
- Tobias, S. M., Dagon, K., and Marston, J. B. (2011). Astrophysical fluid dynamics via direct statistical simulation. *The Astrophysical Journal*, 727(2):127.
- Tobias, S. M. and Marston, J. B. (2013). Direct statistical simulation of out-of-equilibrium jets. *Phys. Rev. Lett.*, 110:104502.
- Tobias, S. M. and Marston, J. B. (2017). Direct statistical simulation of jets and vortices in 2D flows. *Physics of Fluids*, 29(11):111111.
- Tollefson, J., Wong, M. H., de Pater, I., Simon, A. A., Orton, G. S., Rogers, J. H., Atreya, S. K., Cosentino, R. G., Januszewski, W., Morales-Juberías, R., and Marcus, P. S. (2017). Changes in jupiter’s zonal wind profile preceding and during the juno mission. *Icarus*, 296:163–178.
- Townsend, A. A. (1958). The effects of radiative transfer on turbulent flow of a stratified fluid. *J. Fluid Mech.*, 4:361–375.
- Traxler, A., Stellmach, S., Garaud, P., Radko, T., and Brummell, N. (2011). Dynamics of fingering convection. Part 1 Small-scale fluxes and large-scale instabilities. *J. Fluid Mech.*, 677:530–553.

- Turner, M. R., Bassom, A. P., and Gilbert, A. D. (2009). Diffusion and the formation of vorticity staircases in randomly strained two-dimensional vortices. *Journal of Fluid Mechanics*, 638:49–72.
- Vallis, G. K. (2017). *Atmospheric and Oceanic Fluid Dynamics: Fundamentals and Large-Scale Circulation*. Cambridge University Press, 2 edition.
- Vallis, G. K. and Maltrud, M. E. (1993). Generation of mean flows and jets on a beta plane and over topography. *Journal of Physical Oceanography*, 23(7):1346–1362.
- van Sebille, E., Kamenkovich, I., and Willis, J. K. (2011). Quasi-zonal jets in 3-D argo data of the northeast atlantic. *Geophysical Research Letters*, 38(2):L02606.
- Vasavada, A. R. and Showman, A. P. (2005). Jovian atmospheric dynamics: an update after *Galileo* and *Cassini*. *Reports on Progress in Physics*, 68(8):1935–1996.
- Watson, M. (1980). Shear instability of differential rotation in stars. *Geophys. and Astrophys. Fluid Dyn.*, 16(1):285–298.
- Williams, G. P. (1978). Planetary circulations: 1. barotropic representation of jovian and terrestrial turbulence. *Journal of the Atmospheric Sciences*, 35(8):1399–1426.
- Williams, G. P. (2003). Jovian dynamics. part iii: Multiple, migrating, and equatorial jets. *Journal of the Atmospheric Sciences*, 60(10):1270–1296.
- Williams, P. D. and Kelsall, C. W. (2015). The dynamics of baroclinic zonal jets. *Journal of the Atmospheric Sciences*, 72(3):1137–1151.
- Willez, E. and Bouchet, F. (2017). Theoretical prediction of reynolds stresses and velocity profiles for barotropic turbulent jets. *EPL (Europhysics Letters)*, 118(5):54002.
- Woollings, T., Hannachi, A., and Hoskins, B. (2010). Variability of the north atlantic eddy-driven jet stream. *Quarterly Journal of the Royal Meteorological Society*, 136(649):856–868.
- Young, R. M., Read, P. L., and Wang, Y. (2019). Simulating jupiter’s weather layer. part i: Jet spin-up in a dry atmosphere. *Icarus*, 326:225–252.
- Zahn, J.-P. (1974). Rotational instabilities and stellar evolution. In Ledoux, P., Noels, A., and Rodgers, A. W., editors, *Stellar Instability and Evolution*, volume 59 of *IAU Symposium*, pages 185–194.
- Zahn, J.-P. (1992). Circulation and turbulence in rotating stars. *Astronomy and Astrophysics*, 265:115–132.
- Zhou, Q. and Diamessis, P. J. (2019). Large-scale characteristics of stratified wake turbulence at varying Reynolds number. *Phys. Rev. Fluids*, 4:084802.



## Appendix A

# Shallow water quasi-geostrophic equations

Geostrophy, in which there is an approximate balance between the pressure gradient and the Coriolis force, can be exploited to simplify the equations of motion of planetary flows; this is known as *quasi-geostrophic (QG) motion*. We begin by considering the rotating shallow-water equations for a single-fluid layer of constant density, exploiting the large horizontal extent of these flows relative to their vertical extent:

$$\frac{\partial \mathbf{u}}{\partial t} + (\mathbf{u} \cdot \nabla) \mathbf{u} + \mathbf{f} \times \mathbf{u} = -g \nabla h, \quad (\text{A.1})$$

$$\frac{\partial h}{\partial t} + \nabla \cdot (h \mathbf{u}) = 0, \quad (\text{A.2})$$

where coordinates  $x$  and  $y$  correspond to the zonal and latitudinal directions respectively,  $\mathbf{u}(x, y, t) = (u, v)$  is the horizontal velocity,  $h(x, y, t)$  denotes the total fluid depth,  $\mathbf{f} = f \hat{\mathbf{z}}$  is the local vertical component of the planetary rotation vector and  $\nabla = (\partial_x, \partial_y)$  is the horizontal gradient operator. It is noted that this system can easily be generalised to include bathymetry. In addition, we approximate the Coriolis parameter,  $f$ , at latitude  $y$  with a truncated Taylor series,  $f = f_0 + \beta y$ ; this is known as the *beta-plane approximation*.

To proceed, it is necessary to scale the equations. There are three parameters required to describe a typical flow: a characteristic horizontal length scale,  $L_c$ , a characteristic horizontal velocity scale,  $U_c$ , and a characteristic Coriolis frequency,  $f_c$ . The ratio of the magnitude of the relative acceleration,  $(\mathbf{u} \cdot \nabla) \mathbf{u}$ , to the Coriolis acceleration,  $\mathbf{f} \times \mathbf{u}$ , is called the *Rossby number*,  $Ro = U_c / f_c L_c$ . Small values are indicative of the importance of rotation, such as those representing large-scale terrestrial flows.

These characteristic scales, along with an advective time scale,  $L_c / U_c$ , can be used to non-dimensionalise the Coriolis parameter,  $\hat{\mathbf{f}} = \hat{f}_0 + Ro \hat{\beta} \hat{y}$ , and the momentum equation,

$$Ro \left[ \frac{\partial \hat{\mathbf{u}}}{\partial \hat{t}} + (\hat{\mathbf{u}} \cdot \hat{\nabla}) \hat{\mathbf{u}} \right] + \hat{\mathbf{f}} \times \hat{\mathbf{u}} = -\hat{\nabla} \hat{h}, \quad (\text{A.3})$$

provided we assume that  $Ro \ll 1$  so that the flow is in near-geostrophic balance,  $\mathbf{f} \times \mathbf{u} \approx -g \nabla h$ . This latter assumption imposes that variations in fluid depth scale as  $\Delta h \sim Ro H (L_c / L_d)^2$ , where  $H$  is the mean fluid depth and  $L_d = \sqrt{gH} / f$  is the *Rossby radius of deformation*, the length scale at which the geostrophic balance becomes important. The continuity equation can be similarly non-dimensionalised:

$$Ro \left( \frac{L_c}{L_d} \right)^2 \left[ \frac{\partial \hat{h}}{\partial \hat{t}} + \hat{\nabla} \cdot (\hat{h} \hat{\mathbf{u}}) \right] + \hat{\nabla} \cdot \hat{\mathbf{u}} = 0. \quad (\text{A.4})$$

The only parameters remaining in equations (A.3) and (A.4) are the Rossby number, which we shall assume to be small, the ratio  $L_c/L_d$ , which we shall assume to be of order one, and  $\hat{\beta}$ , which we shall also assume to be of order one. Using asymptotic analysis, we can exploit these assumptions to simplify the system of equations. The idea is that variables  $\hat{\mathbf{u}}$  and  $\hat{h}$  are expanded in an asymptotic series:

$$\hat{\mathbf{u}} = \hat{\mathbf{u}}_0 + Ro \hat{\mathbf{u}}_1 + Ro^2 \hat{\mathbf{u}}_2 + \dots, \quad (\text{A.5a})$$

$$\hat{h} = \hat{h}_0 + Ro \hat{h}_1 + Ro^2 \hat{h}_2 + \dots, \quad (\text{A.5b})$$

where the Rossby number represents a small parameter, and then substituted back into the equations. Reassuringly, at zeroth order we retrieve geostrophic balance,  $\hat{\mathbf{f}}_0 \times \hat{\mathbf{u}}_0 = -\hat{\nabla} \hat{h}_0$ , and continuity,  $\hat{\nabla} \cdot \hat{\mathbf{u}}_0 = 0$ , respectively. At next order, the momentum (A.3) and continuity (A.4) equations give, respectively,

$$\frac{\partial \hat{\mathbf{u}}_0}{\partial \hat{t}} + (\hat{\mathbf{u}}_0 \cdot \hat{\nabla}) \hat{\mathbf{u}}_0 + \hat{\beta} \hat{y} \hat{\mathbf{z}} \times \hat{\mathbf{u}}_0 + \hat{f}_0 \hat{\mathbf{z}} \times \hat{\mathbf{u}}_1 = -\hat{\nabla} \hat{h}_1, \quad (\text{A.6})$$

$$\left(\frac{L_c}{L_d}\right)^2 \left[ \frac{\partial \hat{h}_0}{\partial \hat{t}} + \hat{\nabla} \cdot (\hat{h}_0 \hat{\mathbf{u}}_0) \right] + \hat{\nabla} \cdot \hat{\mathbf{u}}_1 = 0. \quad (\text{A.7})$$

These are not closed because they both involve the evaluation of a first-order quantity. Nevertheless, this can be eliminated by taking the curl of (A.6) and then substituting for the term  $\hat{\nabla} \cdot \hat{\mathbf{u}}_1$  in equation (A.7):

$$\frac{\partial}{\partial \hat{t}} \left( \hat{\zeta}_0 - \hat{f}_0 \left(\frac{L_c}{L_d}\right)^2 \hat{h}_0 \right) + (\hat{\mathbf{u}}_0 \cdot \hat{\nabla}) \left( \hat{\zeta}_0 + \hat{\beta} \hat{y} - \hat{f}_0 \left(\frac{L_c}{L_d}\right)^2 \hat{h}_0 \right) = 0, \quad (\text{A.8})$$

where the relative vorticity  $\hat{\zeta}_0 = \hat{\nabla} \times \hat{\mathbf{u}}_0$ . The final step involves recognition that  $\hat{h}_0$  and  $\hat{\mathbf{u}}_0$  are related through geostrophic balance,  $\hat{\mathbf{f}}_0 \times \hat{\mathbf{u}}_0 = -\hat{\nabla} \hat{h}_0$ . Thus, it is convenient to introduce a streamfunction,  $\hat{\psi}_0 = \hat{h}_0 / \hat{f}_0$ , such that  $\hat{\mathbf{u}}_0 = \hat{\nabla} \times (\hat{\psi}_0 \mathbf{k})$  and  $\hat{\zeta}_0 = \hat{\nabla}^2 \hat{\psi}_0$ , in order to eliminate one of the variables:

$$\frac{\partial}{\partial \hat{t}} \left( \hat{\nabla}^2 \hat{\psi}_0 - \hat{f}_0^2 \left(\frac{L_c}{L_d}\right)^2 \hat{\psi}_0 \right) + (\hat{\mathbf{u}}_0 \cdot \hat{\nabla}) \left( \hat{\nabla}^2 \hat{\psi}_0 + \hat{\beta} \hat{y} - \hat{f}_0^2 \left(\frac{L_c}{L_d}\right)^2 \hat{\psi}_0 \right) = 0. \quad (\text{A.9})$$

The horizontal velocity field can be separated into a geostrophic part,  $\mathbf{u}_g$ , and an ageostrophic part,  $\mathbf{u}_a$ , with the zeroth order components corresponding to the former. If we reinstate dimensions, noting that  $\psi = (g/f_0)h$ , then we obtain the shallow water quasi-geostrophic potential vorticity equation:

$$\frac{\partial}{\partial t} \left( \nabla^2 \psi + \beta y - \frac{1}{L_d^2} \psi \right) + (\mathbf{u}_g \cdot \nabla) \left( \nabla^2 \psi + \beta y - \frac{1}{L_d^2} \psi \right) = 0. \quad (\text{A.10})$$

The quantity inside the parentheses, given by

$$q = \nabla^2 \psi + \beta y - \frac{1}{L_d^2} \psi, \quad (\text{A.11})$$

is known as the shallow water quasi-geostrophic potential vorticity and is materially-conserved,  $Dq/Dt = 0$ . It is an approximation to the shallow water potential vorticity and is widely used in theoretical studies of the atmosphere and the ocean. For flows in which  $L_c/L_d \ll 1$ , the potential vorticity reduces to  $q = \nabla^2 \psi + \beta y$  and the motion becomes two-dimensional.

# Appendix B

## Implementation of the stochastic forcing

We parameterise the effects of small-scale eddies acting on a barotropic flow using an idealisation of two-dimensional turbulence. Specifically, we use a rapidly decorrelating, spatially homogeneous and isotropic stochastic force which is assumed to be a random function of both space and time in which energy and enstrophy are injected into a narrow annulus of wavenumbers centred around a forcing wavenumber  $k_f$ . Here we lay out the mathematical details of the forcing within a continuous formulation and then proceed to discuss discretised formulations that are numerically implemented in our DNS and DSS simulations.

### B.1 Continuous formulation

In the nonlinear and (generalised) quasilinear models, vorticity is directly forced using a stochastic force  $\xi(x, y, t)$  with mean  $\langle \xi(\mathbf{x}, t) \rangle = 0$  and two-point, two-time correlation function described by  $\Xi$ :

$$\langle \xi(\mathbf{x}_1, t_1) \xi(\mathbf{x}_2, t_2) \rangle = \Xi(\mathbf{x}_1, \mathbf{x}_2, t_2 - t_1), \quad (\text{B.1})$$

where the angular brackets denote an ensemble average and  $\mathbf{x}_i = (x_i, y_i)$ . We consider the Gaussian white noise limit in which the forcing decorrelation time  $\tau_f \rightarrow 0$  and spatial homogeneity and isotropy such that  $\Xi$  depends only on the two-point separation distance  $r = |\mathbf{x}_1 - \mathbf{x}_2|$  between points. Consequently, the correlation function becomes delta-correlated in time and takes the form

$$\langle \xi(\mathbf{x}_1, t_1) \xi(\mathbf{x}_2, t_2) \rangle = \Xi(r) \delta(t_2 - t_1), \quad (\text{B.2})$$

where  $\Xi(r)$  is related to its Fourier modes,  $\tilde{\Xi}(k)$ , according to the relations

$$\tilde{\Xi}(k) = 2\pi \int_0^\infty \Xi(r) J_0(kr) r dr, \quad \Xi(r) = \frac{1}{2\pi} \int_0^\infty \tilde{\Xi}(k) J_0(kr) k dk, \quad (\text{B.3})$$

using the fact that the two-dimensional Fourier transform of a circularly symmetric function is equivalent to a Hankel transform of order zero. Here,  $k = \sqrt{k_x^2 + k_y^2}$  is the isotropic wavenumber in Fourier space and  $J_0$  is the Bessel function of order zero. We restrict attention to narrow-band forcing distributions in which an annulus of wavevectors is excited in Fourier space with mean radius  $k = k_f$  and thickness  $2\delta k \ll k_f$ . In the idealised limit  $\delta k \rightarrow 0$ , this becomes idealised ring forcing in which energy is injected onto the circle  $k = k_f$  in Fourier space.

By assuming ergodicity such that a volume average of a single realisation is equivalent to an ensemble average over multiple realisations, we can derive an expression relating the rate of energy injection,  $\varepsilon$ , by the forcing to the spatial correlation function,  $\Xi$ . Before doing so, it is useful to re-write the vorticity equation symbolically in terms of linear and nonlinear operators:

$$\frac{\partial}{\partial t} \zeta(\mathbf{x}, t) = \mathcal{L}(\zeta(\mathbf{x}, t)) + \mathcal{N}(\zeta(\mathbf{x}, t), \zeta(\mathbf{x}, t)) + \xi(\mathbf{x}, t), \quad (\text{B.4})$$

where the vorticity at time  $t$  is then found by integrating both sides with respect to time:

$$\zeta(\mathbf{x}, t) = \zeta(\mathbf{x}, 0) + \int_0^t [\mathcal{L}(\zeta(\mathbf{x}, t')) + \mathcal{N}(\zeta(\mathbf{x}, t'), \zeta(\mathbf{x}, t')) + \xi(\mathbf{x}, t')] dt'. \quad (\text{B.5})$$

Since the energy injection rate by the forcing is given by  $\varepsilon = -\langle \xi \psi \rangle$  and the streamfunction,  $\psi$ , is related to the vorticity via the elliptic integral  $\zeta = \nabla^2 \psi$ , then we can derive an expression for  $\varepsilon$  as follows:

$$\begin{aligned} \varepsilon &= -\langle \xi(\mathbf{x}_1, t) \psi(\mathbf{x}_2, t) \rangle \Big|_{\mathbf{x}_1 = \mathbf{x}_2} \\ &= -\langle \xi(\mathbf{x}_1, t) \nabla^{-2} \zeta(\mathbf{x}_2, t) \rangle \Big|_{\mathbf{x}_1 = \mathbf{x}_2} \\ &= -\langle \xi(\mathbf{x}_1, t) \nabla^{-2} \zeta(\mathbf{x}_2, 0) \rangle - \int_0^t \langle \xi(\mathbf{x}_1, t) \nabla^{-2} [\mathcal{L}(\zeta(\mathbf{x}_2, t')) + \mathcal{N}(\zeta(\mathbf{x}_2, t'), \zeta(\mathbf{x}_2, t')) + \xi(\mathbf{x}_2, t')] \rangle dt' \Big|_{\mathbf{x}_1 = \mathbf{x}_2} \\ &= -\int_0^t \nabla_2^{-2} \langle \xi(\mathbf{x}_1, t) \xi(\mathbf{x}_2, t') \rangle dt' \Big|_{\mathbf{x}_1 = \mathbf{x}_2} \quad (\text{since the system and forcing are uncorrelated}) \\ &= -\int_0^t \nabla^{-2} \Xi(r) \delta(t - t') dt' \Big|_{r=0} \quad (\text{using (B.2) with } |\mathbf{x}_1 - \mathbf{x}_2| = r) \\ &= \frac{1}{4\pi} \int_0^\infty \frac{1}{k} \tilde{\Xi}(k) J_0(kr) dk \Big|_{r=0} \quad (\text{using (B.3) and } \int_0^t \delta(t - t') dt' = \frac{1}{2}) \\ &= \frac{1}{4\pi k_f} \tilde{\Xi}(k_f), \quad (\text{since } \tilde{\Xi}(k) = 0 \text{ unless } k = k_f) \end{aligned} \quad (\text{B.6})$$

where we note that the operator  $\nabla_2$  acts specifically on the function evaluated at point  $\mathbf{x}_2$ . Consequently, the spatial correlation function for this idealised forcing distribution can be written as

$$\tilde{\Xi}(k) = 4\pi k_f \varepsilon \delta(k - k_f), \quad \Xi(r) = 2\varepsilon k_f^2 J_0(k_f r), \quad (\text{B.7})$$

where we have used the Fourier transforms (B.3) to evaluate the physical space version.

## B.2 Discrete DNS formulation

The stochastic force  $\xi(\mathbf{x}, t)$  is numerically implemented in our DNS simulations within the NL, QL and GQL models as a first-order Markov process, approximated to be piecewise constant on discrete time steps  $t_n < t < t_{n+1}$ . Applying the discretised Fourier theorem,

$$\tilde{\xi}(\mathbf{k}, t) = \sum_{\mathbf{x}} \xi(\mathbf{x}, t) e^{-i\mathbf{k} \cdot \mathbf{x}}, \quad \xi(\mathbf{x}, t) = \frac{1}{N^2} \sum_{\mathbf{k}} \tilde{\xi}(\mathbf{k}, t) e^{i\mathbf{k} \cdot \mathbf{x}}, \quad (\text{B.8})$$

the Fourier coefficients  $\tilde{\xi}(\mathbf{k}, t)$  are given by  $\tilde{\xi}(\mathbf{k}, t) = \mathcal{A} \tilde{\eta}(\mathbf{k}, t)$  with constant amplitude  $\mathcal{A} \in \mathbb{R}$  and Markovian coefficients  $\tilde{\eta}(\mathbf{k}, t)$  satisfying the Hermitian property  $\tilde{\eta}(-\mathbf{k}, t) = \tilde{\eta}^*(\mathbf{k}, t)$  to ensure that the forcing function

$\xi(\mathbf{x}, t)$  is real. These coefficients are updated at each time step  $t_n$  using the scheme

$$\tilde{\eta}(\mathbf{k}, t_0) = X_0, \quad \tilde{\eta}(\mathbf{k}, t_n) = \gamma \tilde{\eta}(\mathbf{k}, t_{n-1}) + \sqrt{1 - \gamma^2} X_n, \quad (\text{B.9})$$

where the  $X_n$  are independent, identically distributed (IID) random variables given by  $X_n = e^{i\theta_n}$  with uniformly distributed random phase  $\theta_n \in [0, 2\pi)$  and mean and covariance given by

$$\langle X_n \rangle = 0, \quad \langle X_m X_n^* \rangle = \delta_{mn}. \quad (\text{B.10})$$

The parameter  $0 \leq \gamma \leq 1$  is related to the decorrelation time  $\tau_f$  of the forcing by  $\gamma = 1 - \Delta t / \tau_f$ , where  $\gamma = 0$  (corresponding to  $\tau_f = \Delta t$ ) approximates Gaussian white noise using a Markov process,  $\gamma = 1$  corresponds to deterministic forcing, and  $0 < \gamma < 1$  represents forcing with a Markovian time-dependence. We numerically implement idealised ring forcing by selecting only those wavevectors such that  $|k - k_f| < \delta k$  (where  $\delta k \ll k_f$ ) and specifying that their Fourier coefficients have equal amplitude.

The variance of the forced Fourier coefficients is initially unity:  $\langle \tilde{\eta}(\mathbf{k}, t_0) \tilde{\eta}^*(\mathbf{k}, t_0) \rangle = \langle X_0 X_0^* \rangle = 1$ . It is straightforward to prove that their variance remains unchanged in subsequent times. To do this, we first expand (B.9) in order to write the coefficients as a series in  $X_n$ :

$$\tilde{\eta}(\mathbf{k}, t_n) = \sum_{j=0}^n X_{n-j} \gamma^j \sqrt{1 - \gamma^2}. \quad (\text{B.11})$$

Their variance in the limit  $n \rightarrow \infty$  is then easily computed as

$$\begin{aligned} \lim_{n \rightarrow \infty} \langle \tilde{\eta}(\mathbf{k}, t_n) \tilde{\eta}^*(\mathbf{k}, t_n) \rangle &= \lim_{n \rightarrow \infty} \left\langle \left( \sum_{j=0}^n X_{n-j} \gamma^j \sqrt{1 - \gamma^2} \right) \left( \sum_{l=0}^n X_{n-l}^* \gamma^l \sqrt{1 - \gamma^2} \right) \right\rangle \\ &= \lim_{n \rightarrow \infty} (1 - \gamma^2) \sum_{j=0}^n \langle X^{(n-j)} X^{*(n-j)} \rangle \gamma^{2j} = \lim_{n \rightarrow \infty} (1 - \gamma^2) \sum_{j=0}^n \gamma^{2j} = 1, \end{aligned} \quad (\text{B.12})$$

using (B.10) and the summation property of an infinite geometric series. When  $\gamma \neq 0$ , the correlation between the forcing coefficients at different time steps is non-zero and can be computed analogously:

$$\begin{aligned} \lim_{n \rightarrow \infty} \langle \tilde{\eta}(\mathbf{k}, t_n) \tilde{\eta}^*(\mathbf{k}, t_{n-m}) \rangle &= \lim_{n \rightarrow \infty} \left\langle \left( \sum_{j=0}^n X_{n-j} \gamma^j \sqrt{1 - \gamma^2} \right) \left( \sum_{l=0}^{n-m} X_{n-m-l}^* \gamma^l \sqrt{1 - \gamma^2} \right) \right\rangle \\ &= \lim_{n \rightarrow \infty} (1 - \gamma^2) \sum_{j=m}^n \langle X_{n-j} X_{n-j}^* \rangle \gamma^{2j-m} = \lim_{n \rightarrow \infty} (1 - \gamma^2) \gamma^m \sum_{j=0}^{n-m} \gamma^{2j} = \gamma^m. \end{aligned} \quad (\text{B.13})$$

For short decorrelation times  $\tau_f$ , we can assume that the stochastic forcing is independent of the state of the system, allowing the rate of energy injection,  $\varepsilon$ , to be prescribed *a priori*. Consequently, we can derive an expression for  $\varepsilon$  using an analogous procedure to the one described for the continuous formulation:

$$\begin{aligned} \varepsilon &= -\langle \xi(\mathbf{x}_1, t) \psi(\mathbf{x}_2, t) \rangle \Big|_{\mathbf{x}_1 = \mathbf{x}_2} \\ &= -\langle \xi(\mathbf{x}_1, t) \nabla^{-2} \zeta(\mathbf{x}_2, t) \rangle \Big|_{\mathbf{x}_1 = \mathbf{x}_2} \\ &= -\langle \xi(\mathbf{x}_1, t) \nabla^{-2} \zeta(\mathbf{x}_2, 0) \rangle - \int_0^t \langle \xi(\mathbf{x}_1, t) \nabla^{-2} [\mathcal{L}(\zeta(\mathbf{x}_2, t')) + \mathcal{N}(\zeta(\mathbf{x}_2, t'), \zeta(\mathbf{x}_2, t')) + \xi(\mathbf{x}_2, t')] \rangle dt' \Big|_{\mathbf{x}_1 = \mathbf{x}_2} \end{aligned}$$

$$\begin{aligned}
&= - \int_0^t \left\langle \xi(\mathbf{x}_1, t) \nabla^{-2} \xi(\mathbf{x}_2, t') \right\rangle dt' \Big|_{\mathbf{x}_1=\mathbf{x}_2} \quad (\text{since the system and forcing are uncorrelated}) \\
&= \int_0^t \left\langle \left( \frac{1}{N^2} \sum_{\mathbf{k}} \tilde{\xi}(\mathbf{k}, t) e^{i\mathbf{k}\cdot\mathbf{x}_1} \right) \left( \frac{1}{N^2} \sum_{\mathbf{p}} |\mathbf{p}^{-2}| \tilde{\xi}(\mathbf{p}, t') e^{i\mathbf{p}\cdot\mathbf{x}_2} \right) \right\rangle dt' \Big|_{\mathbf{x}_1=\mathbf{x}_2} \\
&= \frac{1}{N^4} \int_0^t \sum_{\mathbf{k}} |\mathbf{k}^{-2}| \left\langle \tilde{\xi}(\mathbf{k}, t) \tilde{\xi}(-\mathbf{k}, t') \right\rangle dt' \quad (\text{since all terms are zero unless } \mathbf{k} + \mathbf{p} = 0) \\
&= \frac{N}{N^4 k_f^2} \int_0^t \left\langle \tilde{\xi}(\mathbf{k}, t) \tilde{\xi}^*(\mathbf{k}, t') \right\rangle dt'. \quad (\text{since } \tilde{\xi} \text{ is Hermitian and we force only } k \approx k_f) \quad (\text{B.14})
\end{aligned}$$

Here,  $N$  is the spatial resolution in the zonal and latitudinal directions and  $\mathcal{N}$  is the number of wavevectors that are forced in Fourier space. In order to evaluate this integral, we note that it can be decomposed into discrete time steps of length  $\Delta t = t_n - t_{n-1}$  as follows:

$$\varepsilon = \frac{N}{N^4 k_f^2} \left( \int_0^{t_1} \left\langle \tilde{\xi}(\mathbf{k}, t) \tilde{\xi}^*(\mathbf{k}, t') \right\rangle dt' + \dots + \int_{t_j}^{t_{j+1}} \left\langle \tilde{\xi}(\mathbf{k}, t) \tilde{\xi}^*(\mathbf{k}, t') \right\rangle dt' + \dots + \int_{t_n}^t \left\langle \tilde{\xi}(\mathbf{k}, t) \tilde{\xi}^*(\mathbf{k}, t') \right\rangle dt' \right). \quad (\text{B.15})$$

When  $\gamma = 0$ , only the final integral is non-zero, however, when  $\gamma \neq 0$ , all integrals are non-zero. In this latter case, all but the final integral can be evaluated using result (B.13), where we find that

$$\int_{t_j}^{t_{j+1}} \left\langle \tilde{\xi}(\mathbf{k}, t) \tilde{\xi}^*(\mathbf{k}, t') \right\rangle dt' = (t_{j+1} - t_j) \left\langle \tilde{\xi}(\mathbf{k}, t_n) \tilde{\xi}^*(\mathbf{k}, t_{n-(n-j)}) \right\rangle = \gamma^{n-j} \mathcal{A}^2 \Delta t. \quad (\text{B.16})$$

The final integral can instead be evaluated using result (B.12), giving

$$\int_{t_n}^t \left\langle \tilde{\xi}(\mathbf{k}, t) \tilde{\xi}^*(\mathbf{k}, t') \right\rangle dt' = (t - t_n) \left\langle \tilde{\xi}(\mathbf{k}, t_n) \tilde{\xi}^*(\mathbf{k}, t_n) \right\rangle = \frac{1}{2} \mathcal{A}^2 (t - t_n), \quad (\text{B.17})$$

where the factor of  $\frac{1}{2}$  arises due to the fact that the relevant contribution of this integral to  $\varepsilon$  is its average value as  $t$  varies over the final time-step. Summing these contributions, the rate of energy injection is

$$\varepsilon = \frac{N}{N^4 k_f^2} \left( \frac{1}{2} \mathcal{A}^2 \Delta t + \sum_{j=0}^n \gamma^{n-j} \mathcal{A}^2 \Delta t \right) = \frac{N \mathcal{A}^2 \Delta t}{N^4 k_f^2} \left( \frac{1}{2} + \sum_{j=0}^n \gamma^{n-j} \right). \quad (\text{B.18})$$

In the limit  $n \rightarrow \infty$ , or equivalently  $t \rightarrow \infty$ , the summation becomes an infinite geometric series with sum  $(1 - \gamma)^{-1}$ , hence the rate of energy injection and the forcing amplitude are related as

$$\varepsilon = \frac{1}{2} \left( \frac{1 + \gamma}{1 - \gamma} \right) \frac{N \mathcal{A}^2 \Delta t}{N^4 k_f^2}, \quad \mathcal{A} = \sqrt{\frac{2 \varepsilon N^4 k_f^2}{N \Delta t} \left( \frac{1 - \gamma}{1 + \gamma} \right)}. \quad (\text{B.19})$$

Consequently, the stochastic forcing function is defined as

$$\xi(\mathbf{x}, t) = \sqrt{\frac{2 \varepsilon k_f^2}{N \Delta t} \left( \frac{1 - \gamma}{1 + \gamma} \right)} \sum_{|k - k_f| < \delta k} \tilde{\eta}(\mathbf{k}, t) e^{i\mathbf{k}\cdot\mathbf{x}}, \quad (\text{B.20})$$

where we note for completeness that we choose not to force wavevectors of the form  $\mathbf{k} = (0, k)$  and  $\mathbf{k} = (k, 0)$  to avoid forcing purely zonal or purely meridional flows.

### B.3 Discrete DSS formulation

Our DSS (CE2) simulations are forced using the statistical properties of an infinite ensemble of forcing fields defined by the two-point correlation function,  $\Xi$ , associated with the stochastic force,  $\xi$ . The discretisation of  $\Xi$  can be derived by integrating (B.2) with respect to one of the time variables, as we now proceed to demonstrate. Without loss of generality, we shall assume that  $\gamma = 0$  in (B.20), thereby ensuring that  $\xi(\mathbf{x}, t)$  is completely regenerated at each time step with no memory. The resulting calculation gives

$$\begin{aligned}
\Xi(\mathbf{x}_1, \mathbf{y}_1) &= \int_0^\infty \langle \xi(\mathbf{x}_1, t_1) \xi(\mathbf{x}_2, t_2) \rangle dt_2 \\
&= \frac{2\epsilon k_f^2}{N\Delta t} \int_0^\infty \left\langle \left( \sum_{|k-k_f| < \delta k} \tilde{\eta}(\mathbf{k}, t_1) e^{i\mathbf{k}\cdot\mathbf{x}_1} \right) \left( \sum_{|p-k_f| < \delta k} \tilde{\eta}(\mathbf{p}, t_2) e^{i\mathbf{p}\cdot\mathbf{x}_2} \right) \right\rangle dt_2 \\
&= \frac{2\epsilon k_f^2}{N\Delta t} \int_0^\infty \sum_{|k-k_f| < \delta k} \langle \tilde{\eta}(\mathbf{k}, t_1) \tilde{\eta}(-\mathbf{k}, t_2) \rangle e^{i(\mathbf{k}\cdot(\mathbf{x}_1-\mathbf{x}_2))} dt_2 \quad (\text{since the distribution is homogeneous}) \\
&= \frac{2\epsilon k_f^2}{N\Delta t} \int_0^\infty \sum_{|k-k_f| < \delta k} \langle \tilde{\eta}(\mathbf{k}, t_1) \tilde{\eta}^*(\mathbf{k}, t_2) \rangle e^{i(\mathbf{k}\cdot(\mathbf{x}_1-\mathbf{x}_2))} dt_2 \quad (\text{since } \tilde{\eta} \text{ is Hermitian}) \\
&= \frac{2\epsilon k_f^2}{N} \sum_{|k-k_f| < \delta k} e^{i(\mathbf{k}\cdot(\mathbf{x}_1-\mathbf{x}_2))}, \quad (\text{since } \langle \tilde{\eta}(\mathbf{k}, t_m) \tilde{\eta}^*(\mathbf{k}, t_n) \rangle = \delta_{mn}) \quad (\text{B.21})
\end{aligned}$$

where we deduce that the Fourier coefficients are given by

$$\tilde{\Xi}(\mathbf{k}_1, \mathbf{k}_2) = \frac{2\epsilon k_f^2 N^4}{N}, \quad (\text{B.22})$$

provided that  $\mathbf{k}_1 + \mathbf{k}_2 = 0$  and  $|k - k_f| < \delta k$ , where  $k = \sqrt{k_{x_i}^2 + k_{y_i}^2}$  for  $i \in \{1, 2\}$ .

In a zonally symmetric system, such as that described by the zonal CE2 equations derived in Chapter 6, the number of spatial dimensions reduces from four to three due to the fact that the two zonal coordinates,  $x_1$  and  $x_2$ , are reduced to a zonal separation coordinate,  $x = x_2 - x_1$ . Accordingly, the spatial correlation function,  $\Xi$ , and its Fourier transform,  $\tilde{\Xi}$ , are given by

$$\Xi(x, y_1, y_2) = \frac{2\epsilon k_f^2}{N} \sum_{|k-k_f| < \delta k} e^{i(k_x x + k_{y_1} y_1 + k_{y_2} y_2)}, \quad \tilde{\Xi}(k_x, k_{y_1}, k_{y_2}) = \frac{2\epsilon k_f^2 N^3}{N}, \quad (\text{B.23})$$

provided that  $k_{y_1} + k_{y_2} = 0$  and  $|k - k_f| < \delta k$ , where  $k = \sqrt{k_x^2 + k_{y_i}^2}$  for  $i \in \{1, 2\}$ .

### B.4 Proof of the relation $\overline{\zeta'_1 \xi_2} + \overline{\zeta'_2 \xi_1} = \Xi$

The derivation of the CE2 equations in Chapter 6 produces a pair of coupled equations governing the evolution of the first two cumulants. Equation (6.18) for the evolution of the second cumulant involves a pair of terms given by  $\overline{\zeta'_1 \xi_2} + \overline{\zeta'_2 \xi_1}$ , which, as we now proceed to demonstrate, is statistically equivalent to the two-point correlation function,  $\Xi$ , of the stochastic forcing, under certain assumptions.

The zonal CE2 equations are formulated using a standard Reynolds decomposition of the flow variables into their zonal mean and fluctuations, or eddies, about the mean, i.e.  $\psi = \bar{\psi} + \psi'$ . Corresponding evolution equations for these individual constituents can be derived from the original vorticity equation. After applying the quasilinear approximation in order to eliminate eddy-eddy interactions, the eddy vorticity equation (6.9) can be re-written symbolically in terms of linear and nonlinear operators:

$$\frac{\partial}{\partial t} \zeta'(\mathbf{x}, t) = \mathcal{L}(\zeta'(\mathbf{x}, t)) + \mathcal{N}(U(y, t), \zeta'(\mathbf{x}, t)) + \xi(\mathbf{x}, t), \quad (\text{B.24})$$

where the eddy vorticity at time  $t$  is then found by integrating both sides with respect to time:

$$\zeta'(\mathbf{x}, t) = \zeta'(\mathbf{x}, 0) + \int_0^t [\mathcal{L}(\zeta'(\mathbf{x}, t')) + \mathcal{N}(U(y, t'), \zeta'(\mathbf{x}, t')) + \xi(\mathbf{x}, t')] dt'. \quad (\text{B.25})$$

We are now in a position to consider the term  $\overline{\zeta'_1 \xi_2}$ , where the numerical subscripts denote the point at which the variable is evaluated, i.e.  $\zeta'_1 = \zeta'(\mathbf{x}_1, t)$ . By substituting for  $\zeta'_1$  using expression (B.25) evaluated at point  $\mathbf{x}_1$ , and by assuming ergodicity such that a zonal average of a single realisation is equivalent to an ensemble average over multiple realisations, it follows that

$$\begin{aligned} \overline{\zeta'_1 \xi_2} &= \overline{\zeta'(\mathbf{x}_1, 0) \xi(\mathbf{x}_2, t)} + \int_0^t \overline{[\mathcal{L}(\zeta'(\mathbf{x}, t')) + \mathcal{N}(U(y, t'), \zeta'(\mathbf{x}, t')) + \xi(\mathbf{x}, t')] \xi(\mathbf{x}_2, t)} dt' \\ &= \int_0^t \overline{\xi(\mathbf{x}_1, t') \xi(\mathbf{x}_2, t)} dt' \quad (\text{since the system and forcing are uncorrelated}) \\ &= \int_0^t \Xi(r) \delta(t - t') dt' \quad (\text{using (B.2)}) \\ &= \frac{1}{2} \Xi(r). \quad (\text{since } \int_0^t \delta(t - t') dt' = \frac{1}{2}) \end{aligned} \quad (\text{B.26})$$

Equivalently, we can also deduce that  $\overline{\zeta'_2 \xi_1} = \frac{1}{2} \Xi(r)$ , therefore it follows that the relation is true, as required:

$$\overline{\zeta'_1 \xi_2} + \overline{\zeta'_2 \xi_1} = \Xi. \quad (\text{B.27})$$

## Appendix C

# Numerical integration of DNS and DSS

Here we present the details of the numerical methods used to integrate the DNS (NL, GQL and QL) systems and the DSS (CE2) system. In each case, we consider a square domain with doubly periodic boundary conditions. The zonal,  $x$ , and latitudinal,  $y$ , coordinates satisfy  $(x, y) \in [0, 2\pi L_D) \times [0, 2\pi L_D)$ , where  $L_D$  is the size of the domain. In practice,  $L_D$  is chosen to be unity in all simulations, however, we explicitly retain its dependence in the following formulation. Each coordinate is discretised with  $N$  grid points corresponding to a grid point spacing of  $\Delta x = 2\pi L_D/N$ . Thus, the grid points in each direction are given by

$$x, y \in \frac{2\pi L_D}{N} (0, 1, \dots, N-1). \quad (\text{C.1})$$

Each of the variables can be written in terms of its discretised Fourier transform relating spatial coordinates  $\mathbf{x} = (x, y)$  to wavevectors  $\mathbf{k} = (k_x, k_y)$ . For the case of vorticity, this is given by:

$$\tilde{\zeta}(\mathbf{k}, t) = \sum_{\mathbf{x}} \zeta(\mathbf{x}, t) e^{-i\mathbf{k}\cdot\mathbf{x}}, \quad \zeta(\mathbf{x}, t) = \frac{1}{N^2} \sum_{\mathbf{k}} \tilde{\zeta}(\mathbf{k}, t) e^{i\mathbf{k}\cdot\mathbf{x}}, \quad (\text{C.2})$$

with corresponding transforms of other variables. The allowed wavenumbers in each direction are

$$k_x, k_y \in \frac{1}{L_D} \left( -\frac{N}{2} + 1, -\frac{N}{2} + 2, \dots, 0, 1, \dots, \frac{N}{2} \right), \quad (\text{C.3})$$

where it is assumed that  $N$  is even.

### C.1 Numerical integration of the NL, GQL and QL systems

DNS of the NL, GQL and QL vorticity equations is implemented using a pseudo-spectral algorithm together with a standard 2/3 dealiasing rule. Time integration is performed in Fourier space while nonlinear terms are evaluated in physical space, as we now describe. Each vorticity equation is a stochastic partial differential equation that can be written symbolically in terms of linear and nonlinear operators:

$$\frac{\partial}{\partial t} \zeta(\mathbf{x}, t) = \mathcal{L}(\zeta(\mathbf{x}, t)) + \mathcal{N}(\zeta(\mathbf{x}, t), \zeta(\mathbf{x}, t)) + \xi(\mathbf{x}, t). \quad (\text{C.4})$$

This equation is used to integrate the vorticity forwards in time while the elliptic equation  $\zeta(\mathbf{x}, t) = \nabla^2 \psi(\mathbf{x}, t)$  is used to determine the streamfunction from the vorticity field. Applying the Fourier transform (C.2) to

both of these equations, we obtain the transformed pair:

$$\frac{\partial}{\partial t} \tilde{\zeta}(\mathbf{k}, t) = \mathcal{L}(\tilde{\zeta}(\mathbf{k}, t)) + \mathcal{N}(\tilde{\zeta}, \tilde{\zeta})(\mathbf{k}, t) + \tilde{\xi}(\mathbf{k}, t), \quad (\text{C.5})$$

$$\tilde{\zeta}(\mathbf{k}, t) = -k^2 \tilde{\psi}(\mathbf{k}, t), \quad (\text{C.6})$$

where we note that the Fourier transform commutes with the linear operator but does not commute with the nonlinear operator. Consequently, the linear and stochastic terms can be time-stepped entirely in Fourier space using standard schemes, however, the nonlinear terms must be computed in physical space before being transformed back to Fourier space. The scheme that we use is a second-order Runge-Kutta algorithm:

$$\frac{\tilde{\zeta}(\mathbf{k}, t + \Delta t) - \tilde{\zeta}(\mathbf{k}, t)}{\Delta t} = \frac{1}{2} \mathcal{L}(\tilde{\zeta}(\mathbf{k}, t) + \tilde{\zeta}(\mathbf{k}, t + \Delta t)) + \mathcal{N}(\tilde{\zeta}, \tilde{\zeta})(\mathbf{k}, t + \frac{1}{2} \Delta t) + \tilde{\xi}(\mathbf{k}, t), \quad (\text{C.7})$$

in which the stochastic term is piecewise constant on discrete time steps as described in Appendix B.2. In order to compute the nonlinear terms at the mid-point  $t + \frac{1}{2} \Delta t$  between time steps, we first compute an estimate of the vorticity at time  $t + \Delta t$  in which the nonlinear terms are evaluated at time  $t$ :

$$\tilde{\zeta}_{\text{est}}(\mathbf{k}, t + \Delta t) = \frac{(1 + \frac{1}{2} \Delta t \mathcal{L}) \tilde{\zeta}(\mathbf{k}, t) + [\mathcal{N}(\tilde{\zeta}, \tilde{\zeta})(\mathbf{k}, t) + \tilde{\xi}(\mathbf{k}, t)] \Delta t}{1 - \frac{1}{2} \Delta t \mathcal{L}}. \quad (\text{C.8})$$

An estimate of the Fourier-transformed vorticity field at the mid-point  $t + \frac{1}{2} \Delta t$  is then computed as

$$\tilde{\zeta}(\mathbf{k}, t + \frac{1}{2} \Delta t) = \frac{1}{2} (\tilde{\zeta}_{\text{est}}(\mathbf{k}, t + \Delta t) + \tilde{\zeta}(\mathbf{k}, t)), \quad (\text{C.9})$$

from which we can re-evaluate the nonlinear terms after reverting to physical space. Finally, the algorithm permits the computation of the vorticity field at the new time  $t + \Delta t$  using a rearrangement of (C.7):

$$\tilde{\zeta}(\mathbf{k}, t + \Delta t) = \frac{(1 + \frac{1}{2} \Delta t \mathcal{L}) \tilde{\zeta}(\mathbf{k}, t) + [\mathcal{N}(\tilde{\zeta}, \tilde{\zeta})(\mathbf{k}, t + \frac{1}{2} \Delta t) + \tilde{\xi}(\mathbf{k}, t)] \Delta t}{1 - \frac{1}{2} \Delta t \mathcal{L}}. \quad (\text{C.10})$$

## C.2 Numerical integration of the CE2 system

DSS of the CE2 equations is implemented analogously to the DNS systems using a pseudo-spectral algorithm. Time integration is performed in Fourier space while nonlinear terms are evaluated in physical space. The added complication is the requirement to solve a pair of coupled equations simultaneously, governing the evolution of the first cumulant,  $U(y, t)$ , and the second cumulant,  $\mathcal{Z}(x, y_1, y_2, t)$ :

$$\frac{\partial U}{\partial t} = \frac{1}{2} (\nabla_2^{-2} - \nabla_1^{-2}) \frac{\partial \mathcal{Z}}{\partial x}(0, y, y, t) - \mu U + \nu_n \frac{\partial^{2n}}{\partial y^{2n}} U, \quad (\text{C.11})$$

$$\frac{\partial \mathcal{Z}}{\partial t} + \left( U_1 + \nabla_1^{-2} \left( \beta - \frac{\partial^2 U_1}{\partial y_1^2} \right) - U_2 - \nabla_2^{-2} \left( \beta - \frac{\partial^2 U_2}{\partial y_2^2} \right) \right) \frac{\partial \mathcal{Z}}{\partial x} = \Xi - 2\mu \mathcal{Z} + \nu_n (\nabla_1^{2n} + \nabla_2^{2n}) \mathcal{Z}. \quad (\text{C.12})$$

In order to simplify the notation, we shall write these equations symbolically in terms of linear and nonlinear operators, where it is understood that the linear operators used here are not the same as the operator (6.10)

introduced in Chapter 6. Accordingly, the equations become

$$\frac{\partial}{\partial t} U(y, t) = \mathcal{L}_1(\mathcal{Z}(x, y_1, y_2, t)) \Big|_{\substack{x=0 \\ y_1=y_2=y}} + \mathcal{L}_2(U(y, t)), \quad (\text{C.13})$$

$$\frac{\partial}{\partial t} \mathcal{Z}(x, y_1, y_2, t) = \mathcal{L}_3(\mathcal{Z}(x, y_1, y_2, t)) + \mathcal{N}_n(U(y_n, t) \mathcal{Z}(x, y_1, y_2, t)) + \Xi(x, y_1, y_2), \quad (\text{C.14})$$

where we have represented the two different nonlinear operators in (C.12) using subscripts  $n \in \{1, 2\}$  for brevity, noting that  $\mathcal{N}_n(U(y_n, t) \mathcal{Z}(x, y_1, y_2, t)) = \mathcal{N}_1(U(y_1, t) \mathcal{Z}(x, y_1, y_2, t)) + \mathcal{N}_2(U(y_2, t) \mathcal{Z}(x, y_1, y_2, t))$ . After generalising the Fourier transform (C.2) to one and three spatial dimensions respectively, and letting  $U_1 = U(y_1, t)$  etc, we can transform equations (C.13) and (C.14) to obtain the pair:

$$\frac{\partial}{\partial t} \tilde{U}(k_y, t) = \mathcal{L}_1(\tilde{\mathcal{Z}}(k_x, k_{y_1}, k_{y_2}, t)) \Big|_{\substack{x=0 \\ y_1=y_2=y}} + \mathcal{L}_2(\tilde{U}(k_y, t)), \quad (\text{C.15})$$

$$\frac{\partial}{\partial t} \tilde{\mathcal{Z}}(k_x, k_{y_1}, k_{y_2}, t) = \mathcal{L}_3(\tilde{\mathcal{Z}}(k_x, k_{y_1}, k_{y_2}, t)) + \mathcal{N}_n(\widetilde{U_n, \mathcal{Z}})(k_x, k_{y_1}, k_{y_2}, t) + \tilde{\Xi}(k_x, k_{y_1}, k_{y_2}). \quad (\text{C.16})$$

The two-point forcing correlation function,  $\Xi$ , and its Fourier transform,  $\tilde{\Xi}$ , represent the statistical properties of an infinite ensemble of forcing fields and are therefore independent of time in the numerical integration. Discretised formulations are derived in Appendix B.3.

Whilst these equations comprise three spatial dimensions, in contrast to the two dimensions involved in the DNS models, there are some important properties that can be exploited in order to speed up their numerical integration. Firstly, these equations are linear in the zonal separation coordinate,  $x$ , or equivalently the zonal wavenumber,  $k_x$ , permitting the system to be solved entirely in spectral space for each  $k_x$ . This means that since we only force zonal wavevectors satisfying  $1 \leq |k_x| \leq k_f + \delta k$ , then zonal wavenumbers outside of this range are redundant and can be ignored. Secondly, the structure of the Fourier coefficients of the correlation functions,  $\tilde{\Xi}$  and  $\tilde{\mathcal{Z}}$ , must ensure that these functions are real in physical space, i.e.  $\tilde{\Xi}(k_x, k_{y_1}, k_{y_2}) = \tilde{\Xi}^*(-k_x, -k_{y_1}, -k_{y_2})$ , in addition to being symmetric with respect to  $\mathbf{x}_1 \leftrightarrow \mathbf{x}_2$ , i.e.  $\tilde{\Xi}(k_x, k_{y_1}, k_{y_2}) = \tilde{\Xi}(-k_x, k_{y_2}, k_{y_1})$ . Combined, these conditions require that  $\tilde{\Xi}(k_x, k_{y_1}, k_{y_2}) = \tilde{\Xi}^*(k_x, -k_{y_2}, -k_{y_1})$ , which permits the construction of these correlation functions using only the positive or negative  $k_x$  components. Consequently, it is sufficient to solve for the zonal wavenumbers

$$k_x \in \{1, 2, 3, \dots, k_f + \delta k\}, \quad (\text{C.17})$$

thereby reducing the system to a set of  $k_f + \delta k$  pairs of equations governing the nonlinear evolution of the two  $y$ -coordinates. This greatly reduces the size of the problem, particularly when  $k_f + \delta k$  is not large.

Due to their deterministic nature, the CE2 equations require the initialisation of a small amount of noise, which we choose to add to the  $U(y)$  field. In the subsequent evolution, the linear terms are time-stepped entirely in Fourier space, while the  $y$ -components of the nonlinear terms are computed in physical space before being transformed back to Fourier space. We use a second-order Runge-Kutta algorithm:

$$\frac{\tilde{U}(k_y, t + \Delta t) - \tilde{U}(k_y, t)}{\Delta t} = \mathcal{L}_1\left(\tilde{\mathcal{Z}}(\mathbf{k}, t + \frac{1}{2}\Delta t)\right) \Big|_{\substack{x=0 \\ y_1=y_2=y}} + \frac{1}{2}\mathcal{L}_2\left(\tilde{U}(k_y, t) + \tilde{U}(k_y, t + \Delta t)\right), \quad (\text{C.18})$$

$$\frac{\tilde{\mathcal{Z}}(\mathbf{k}, t + \Delta t) - \tilde{\mathcal{Z}}(\mathbf{k}, t)}{\Delta t} = \frac{1}{2}\mathcal{L}_3\left(\tilde{\mathcal{Z}}(\mathbf{k}, t) + \tilde{\mathcal{Z}}(\mathbf{k}, t + \Delta t)\right) + \mathcal{N}_n(\widetilde{U_n, \mathcal{Z}})(\mathbf{k}, t + \frac{1}{2}\Delta t) + \tilde{\Xi}(\mathbf{k}), \quad (\text{C.19})$$

in which  $\mathbf{k} = (k_x, k_{y_1}, k_{y_2})$  and a standard 2/3 dealiasing rule is applied to the latitudinal wavenumbers. Special treatment is required to compute the nonlinear terms and the eddy-forcing term,  $\mathcal{L}_1(\mathcal{Z})(0, y, y, t)$ , at the mid-point  $t + \frac{1}{2}\Delta t$ , between time steps. To proceed, we first compute an estimate of  $U$  and  $\mathcal{Z}$  at time  $t + \Delta t$  in which these terms are evaluated at time  $t$ :

$$\tilde{U}_{\text{est}}(k_y, t + \Delta t) = \frac{\left(1 + \frac{1}{2}\Delta t \mathcal{L}_2\right) \tilde{U}(k_y, t) + \left[\mathcal{L}_1\left(\tilde{\mathcal{Z}}(\mathbf{k}, t)\right)\Big|_{\substack{x=0 \\ y_1=y_2=y}}\right] \Delta t}{1 - \frac{1}{2}\Delta t \mathcal{L}_2}, \quad (\text{C.20})$$

$$\tilde{\mathcal{Z}}_{\text{est}}(\mathbf{k}, t + \Delta t) = \frac{\left(1 + \frac{1}{2}\Delta t \mathcal{L}_3\right) \tilde{\mathcal{Z}}(\mathbf{k}, t) + \left[\mathcal{N}_n(\widetilde{U}_n, \mathcal{Z})(\mathbf{k}, t) + \tilde{\Xi}(\mathbf{k})\right] \Delta t}{1 - \frac{1}{2}\Delta t \mathcal{L}_3}. \quad (\text{C.21})$$

An estimate of the Fourier-transformed  $U$  and  $\mathcal{Z}$  fields at the mid-point  $t + \frac{1}{2}\Delta t$  are then computed as

$$\tilde{U}\left(k_y, t + \frac{1}{2}\Delta t\right) = \frac{1}{2} \left(\tilde{U}_{\text{est}}(k_y, t + \Delta t) + \tilde{U}(k_y, t)\right), \quad (\text{C.22})$$

$$\tilde{\mathcal{Z}}\left(\mathbf{k}, t + \frac{1}{2}\Delta t\right) = \frac{1}{2} \left(\tilde{\mathcal{Z}}_{\text{est}}(\mathbf{k}, t + \Delta t) + \tilde{\mathcal{Z}}(\mathbf{k}, t)\right), \quad (\text{C.23})$$

from which we can re-evaluate the nonlinear and eddy-forcing terms after reverting to physical space. Finally, the algorithm permits the computation of  $U$  and  $\mathcal{Z}$  at the new time  $t + \Delta t$  using these updates:

$$\tilde{U}_{\text{est}}(k_y, t + \Delta t) = \frac{\left(1 + \frac{1}{2}\Delta t \mathcal{L}_2\right) \tilde{U}(k_y, t) + \left[\mathcal{L}_1\left(\tilde{\mathcal{Z}}(\mathbf{k}, t + \frac{1}{2}\Delta t)\right)\Big|_{\substack{x=0 \\ y_1=y_2=y}}\right] \Delta t}{1 - \frac{1}{2}\Delta t \mathcal{L}_2}, \quad (\text{C.24})$$

$$\tilde{\mathcal{Z}}_{\text{est}}(\mathbf{k}, t + \Delta t) = \frac{\left(1 + \frac{1}{2}\Delta t \mathcal{L}_3\right) \tilde{\mathcal{Z}}(\mathbf{k}, t) + \left[\mathcal{N}_n(\widetilde{U}_n, \mathcal{Z})(\mathbf{k}, t + \frac{1}{2}\Delta t) + \tilde{\Xi}(\mathbf{k})\right] \Delta t}{1 - \frac{1}{2}\Delta t \mathcal{L}_3}. \quad (\text{C.25})$$

## Appendix D

# Zonal jet migration in the presence of strong vortices

A small number of numerical simulations (using the NL model) reveal the coexistence of a strong vortex with a single zonal jet. In these cases the vortex is positioned at a fixed latitude relative to the jet core, propagating westwards throughout the domain. As can be seen in Figure D.1, the presence of the vortex gives rise to a co-located positive spike in the eddy momentum flux convergence, breaking the north-south symmetry of the jet velocity profile. As a result, the jet-vortex pair migrate in tandem at a speed that is greater than that observed in the other simulations. Aside from the presence of the vortex, the  $\psi$  and  $\psi'$  fields otherwise bear some resemblance to those in Figure 4.8(a), where we observe that the eddy field has a large-scale structure that is dominated by a coherent  $\mathbf{k} = (1, 0)$  wave.

This phenomenon appears to occur for small values of  $\beta$  when the domain is marginally large enough to accommodate a single jet. It has never been observed in multiple-jet configurations, and a small increase in  $\beta$  results in the disappearance of the vortex structure, leaving a single jet migrating as described in Chapters 4 and 5. Given the possibility that this behaviour is associated with a geometrical constraint in the system, we choose to exclude these simulations from our analysis.

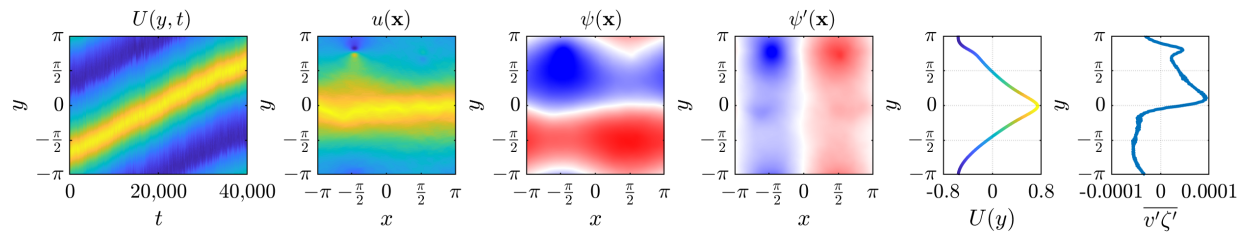


**Figure D.1** Zonal jet migration in the presence of strong vortices. From left to right we show a latitude-time plot of the zonal mean zonal velocity field  $U(y, t)$ , a single snapshot of the zonal velocity field  $u(\mathbf{x})$ , the corresponding streamfunction  $\psi(\mathbf{x})$  and streamfunction perturbation field  $\psi'(\mathbf{x})$ , the time-averaged jet velocity profile  $U(y)$  and the time-averaged eddy momentum flux convergence  $\overline{v'\zeta'}$ . A single zonal jet migrates in the direction of a strong vortex (parameters:  $\beta = 0.3$ ,  $\mu = 0.00005$ ,  $\varepsilon = 10^{-5}$ ,  $k_f = 16$ ,  $N = 256$ ,  $R_\beta = 4.70$ ).



## Appendix E

# Generalisation of linear stability analyses

It is sometimes of interest, particularly when comparing theoretical results with data from direct numerical simulations, to consider the linear stability of a laminar flow with a different amplitude to that of the basic laminar solution, such as that given by (8.17). Consequently, in the context of horizontal shear instabilities, we explain in this appendix how the linear stability of such flows can be computed from the results presented in Section 8.3. We will focus on the standard system of equations (8.6)-(8.8), although an equivalent procedure can also be applied straightforwardly to the LPN equations (8.15)-(8.16).

We begin by considering a laminar flow  $a\mathbf{u}_L(y)$  given by

$$a\mathbf{u}_L(y) = aRe \sin(y)\mathbf{e}_x, \quad (\text{E.1})$$

with amplitude  $aRe$  where  $a \in \mathbb{R}$ , and without loss of generality  $a > 0$ . For small perturbations  $\mathbf{u}'(x, y, z, t)$  away from this laminar flow, i.e. letting  $\mathbf{u} = a\mathbf{u}_L(y) + \mathbf{u}'(x, y, z, t)$ , and using the assumption that the growth rates of instabilities are significantly larger than the rate at which the background flow is evolving due to the uncompensated forcing, the linearised perturbation equations are

$$\frac{\partial \mathbf{u}'}{\partial t} + aRe \cos(y)v' \mathbf{e}_x + aRe \sin(y) \frac{\partial \mathbf{u}'}{\partial x} + \nabla p = \frac{1}{Re} \nabla^2 \mathbf{u}' + BT' \mathbf{e}_z, \quad (\text{E.2})$$

$$\frac{\partial T'}{\partial t} + aRe \sin(y) \frac{\partial T'}{\partial x} + w' = \frac{1}{RePr} \nabla^2 T', \quad (\text{E.3})$$

$$\nabla \cdot \mathbf{u}' = 0. \quad (\text{E.4})$$

Rescaling the velocity field according to  $\mathbf{u}' = a^{1/2} \hat{\mathbf{u}}'$  leads to the transformed set

$$a^{-1/2} \frac{\partial \hat{\mathbf{u}}'}{\partial t} + a^{1/2} Re \cos(y) \hat{v}' \mathbf{e}_x + a^{1/2} Re \sin(y) \frac{\partial \hat{\mathbf{u}}'}{\partial x} + a^{-1} \nabla p = \frac{1}{a^{1/2} Re} \nabla^2 \hat{\mathbf{u}}' + \frac{B}{a} T' \mathbf{e}_z, \quad (\text{E.5})$$

$$a^{-1/2} \frac{\partial T'}{\partial t} + a^{1/2} Re \sin(y) \frac{\partial T'}{\partial x} + \hat{w}' = \frac{1}{a^{1/2} RePr} \nabla^2 T', \quad (\text{E.6})$$

$$\nabla \cdot \hat{\mathbf{u}}' = 0. \quad (\text{E.7})$$

By considering normal mode disturbances of the form  $q(x, y, z, t) = \tilde{q}(y) e^{ik_x x + ik_z z + \sigma t}$  for variables  $q \in (\hat{u}', \hat{v}', \hat{w}', T', p)$ , and rescaling the parameters and growth rates using the relations

$$\hat{\sigma} = \frac{\sigma}{a^{1/2}}, \quad \hat{Re} = a^{1/2} Re, \quad \hat{B} = \frac{B}{a}, \quad \hat{Pr} = Pr, \quad (\text{E.8})$$

the resulting system is identical to the set of equations (8.23)-(8.27), except for the rescaling that is implicit in the hats on the parameters and growth rates. Consequently, it can be re-formulated as a generalised eigenvalue problem for the complex growth rates  $\hat{\sigma}$ ,

$$\mathbf{A}(k_x, k_z, \hat{Re}, \hat{B}, \hat{Pr})\mathbf{X} = \hat{\sigma}\mathbf{B}\mathbf{X}, \quad (\text{E.9})$$

and solved numerically using the method described in Section 8.3.

The linear stability analysis presented in Section 8.3 considered  $a = 1$  (i.e. the laminar background state), where  $\hat{Re} = Re$ ,  $\hat{B} = B$ ,  $\hat{Pr} = Pr$  and  $\hat{\sigma} = \sigma$ . For  $a \neq 1$ , relations (E.8) provide a transformation between the original analysis and the linear stability of flows with a generic amplitude  $a\mathbf{u}_L(y)$ , such as those that evolve from an initial state of rest.